PERFORMANCE MODELING AND EXPERIMENTAL INVESTIGATIONS OF ROTATING DETONATION ENGINES

by

ANDREW R. MIZENER

Presented to the Faculty of the Graduate School of
The University of Texas at Arlington in Partial Fulfillment
of the Requirements
for the Degree of

DOCTOR OF PHILOSOPHY

THE UNIVERSITY OF TEXAS AT ARLINGTON

December 2018

To everyone who told me I could.

ACKNOWLEDGEMENTS

I would like to thank my advisor, Dr. Frank K. Lu, for his first taking a chance on me and then believing in me to see this to its finish. I would also like to thank the members of my committee, Dr. Donald R. Wilson, Dr. Zhen Xue Han, Dr. Rasool Kenarangui, and Dr. Daejong Kim, for their interest in my research and willingness to accommodate last-minute scheduling. I would also like to extend my appreciation to Dr. Luca Maddalena for his frank advice and counsel and commitment to upholding high standards and quality research. Additionally, many thanks are in order to Dr. Andrew Makeev and Dr. Brian Shonkwiler of the Advanced Materials and Structures Lab (AMSL) for the loan of the high speed camera used in the experimental phase of the research plan, and to Dr. Patrick E. Rodi for the suggestion of and collaboration on the RDE-Waverider integration study.

I am grateful to the entire ARC family, and in particular Dr. Eric Braun and James Peace, for their friendship, moral support, and willingness to lend a hand or an ear when I needed one. I am also very grateful to David Carter for the many times I needed his advice, suggestions, answers to random questions, and small parts machined, and to Nirmal Umapathy for his assistance with assembling the Arthur test facility. I am especially appreciative of the tireless efforts of my undergraduate assistant, Cooper Green, for going above and beyond what could ever have been expected from a student in his position. I could not have done it without him.

I am indebted beyond words for my friends and family, and in particular my parents, Ellen and Jeff Mizener, for carrying me when I could not carry myself. I would like to pay special thanks to my father for all of the assistance with the

various electrical and computational components of the Arthur test facility, up to and including building subsystems of the engine control system and providing me with the circuit diagrams of these newly-designed components so that others could do the same for themselves in the future.

It would be unbecoming of me if I did not also thank the teachers who made me who I am today. In particular, Sister Virginia Scherer and Ms. Susan Zapata: thank you. I would not be here if not for you.

Finally, to φ, for never failing to be there for me when I needed someone.

September 7, 2018

ABSTRACT

PERFORMANCE MODELING AND EXPERIMENTAL INVESTIGATIONS OF ROTATING DETONATION ENGINES

Andrew R. Mizener, Ph.D.

The University of Texas at Arlington, 2018

Supervising Professor: Frank K. Lu

The rotating detonation engine (RDE) is a promising propulsion concept that has the potential to offer increased thermodynamic performance in a compact package with no moving parts. A series of analytical and experimental investigations was carried out on RDEs with the joint goal of investigating swirl, torque, and a range of other design parameters of interest. The model and experimental facility were then applied to related problems with the goal of advancing the understanding of RDE applications.

A flexible, low-order, semi-empirical model for a rotating detonation engine was presented. The model was formulated to be able to run broad parametric analyses more efficiently than numerical modeling. The presence of swirl at the exit plane of RDEs is still debated, so the model was formulated to leave open this possibility. Parametric analysis was conducted to determine the effect of a range of engine design parameters on performance. Exit swirl and torque were shown to be small but not uniquely zero.

The model was combined with a waverider forebody model. Together, these were used to conduct parametric analysis of the sensitivity of integrated performance to freestream, waverider forebody, and RDE design parameters. Practical limitations on the Mach number of detonation engines operating in supersonic flows were presented and discussed. Peak performance was seen at the point of maximum forebody pressure recovery. Thrust and torque were shown to be sensitive to body shape and freestream parameters, while specific impulse and thrust-specific fuel consumption were not.

The design of a rotating detonation engine and experimental test facility were presented and discussed. The facility was designed and instrumented to allow the measurement of resultant torque on the engine as well as take thrust and pressure readings. A series of tests was conducted using the engine, with no steadily-propagating detonation waves detected. Pressure, torque, thrust, and frequency data were presented and discussed. A high-speed camera was used to visualize the exhaust plume and the flame structure inside the annulus, which similarly failed to detect a detonation wave. The camera was then used to conduct high-speed visualizations of the ignition process inside the engine for both spark plug and predetonator igniters. Both methods showed the creation of two counter-rotating detonation waves which intersected and canceled each other out on the far side of the annulus. Pressure waves were observed to continue to rotate for several periods before dying out. The qualitative observations from the visualizations were supported by the pressure data. Detailed visualizations were performed to quantitatively investigate the propagation of the initial combustion front around the annulus for varying degrees of injector swirl. Predetonator ignition was observed to directly initiate a detonation, whereas deflagration-to-detonation transition was observed for spark plug ignition. Injector swirl promoted transition in combustion waves propagating into the swirl

and depressed it in waves propagating with the swirl. Overdriven detonations were observed for both ignition methods. A discussion of the possible causes for the failure to sustain a detonation wave was presented and discussed.

TABLE OF CONTENTS

LIST OF ILLUSTRATIONS

LIST OF TABLES

NOMENCLATURE

A	Area
a	Speed of sound, 2^{nd}-order polynomial regression coefficient
B	Blockage ratio
b	2^{nd}-order polynomial regression coefficient
C	Circumference
c	2^{nd}-order polynomial regression coefficient
c_d	Discharge coefficient
$\mathscr{D}$	Drag
d	Diameter
E	Error
F	Total resultant force
f	Specific resultant force, frequency, fuel/oxidizer ratio
f_b	Specific body force
GF	Gauge factor
g_0	Gravitational acceleration at sea level
h	Enthalpy
I_{sp}	Specific impulse
K	Nut factor
L	Length
$\mathscr{L}$	Lift
l	Propellant injection distance
M	Mach number

$\dot{m}$	Mass flow rate
n	Normal vector, power-law body exponent
n_{inj}	Number of injection holes
P	Pressure
$\boldsymbol{P}_{ij}$	Pressure (normal stress) tensor
Q	Heat transfer, total detonation heat release
q	Heat flux, specific detonation heat release, dynamic pressure
R	Gas constant, resistance
$\mathscr{R}$	Range
$\hat{\mathscr{R}}$	Normalized range metric
r	Radial coordinate, power-law body radius
r_b	Power-law body radius at Waverider forebody base
r_m	Mean annular radius
S	Control surface
T	Temperature
$\mathscr{T}$	Torque
t	Time
U	Velocity of noninertial reference frame
u	Velocity, uncertainty
V	Inertial velocity
$\mathscr{V}$	Volume, control volume
$\dot{\mathscr{V}}$	Volumetric flow rate
W	Noninertial velocity
x	Waverider axial coordinate
z	Axial coordinate

α Empirical correction factor, linear regression coefficient

β Linear regression coefficient

γ Ratio of specific heats

δ_a Annulus thickness

ε Strain

ϵ Error tolerance, eccentricity

ζ Expansion area height

θ Circumferential coordinate/angle, sensitivity index

θ_{cone} Waverider forebody cone angle

θ_e Ellipse orientation angle

θ_s Waverider forebody initial turning angle

Λ Detonation wave height

ν Prandtl–Meyer function

Ξ Injector hole area ratio

ρ Density

$\boldsymbol{\sigma}_{ij}$ Cauchy stress tensor

$\boldsymbol{\tau}_{ij}$ Viscous shear stress tensor

Υ Relative z-θ force ratio

ψ Flow angle

Subscripts

A Property upstream of oblique shock wave

B Property downstream of oblique shock wave

CJ Chapman–Jouguet property

c Chamber property

ch Choked property

cr	Critical property
det	Detonation property
$hole$	Injection hole property
g	Gauge property
HS	High-speed DAQ property
i	Index
id	Ideal poperty
in	Injection point property
ig	Ignition property
inj	Injection mixture property
LS	Low-speed DAQ property
r	Property in r-direction
sh	Shock property
she	Shock exit property
sl	Slipline property
sle	Slipline exit property
st	Stoichiometric property
V	Inertial property
W	Noninertial property
z	Property in z-direction
θ	Property in θ-direction
0	Stagnation property
1	Injection plane property, property upstream of CJ detonation
2	Exhaust plane property, property downstream of CJ detonation
2π	Property at θ equal to 2π

3	Inner annular wall property
4	Outer annular wall property
I	Property upstream of detonation wave
II	Property downstream of detonation wave
III	Property after Prandtl–Meyer expansion wave
IV	Property behind oblique shock
∞	Freestream property

Superscripts

$\hat{}$	Unit vector
$\bar{}$	Average property
$*$	Sonic property

CHAPTER 1

INTRODUCTION

1.1 On Detonations

Before we can begin our explanation of their applications, it is necessary to first establish the fundamentals of detonations, their basic structure, and how they form.

Detonation is the supersonic mode of combustion. It is, at its most fundamental level, a shock wave coupled to and sustained by a trailing combustion front [1, 2]. Detonations can be constrasted with deflagrations, which are the subsonic mode of combustion and consist of a subsonic diffusion wave sustained by combustion [3]. Due to the presence of the shock wave, detonations propagate at speeds on the order of thousands of meters per second, and are accompanied by a sharp increase in pressure and density. In contrast, a deflagration propagates on the order of tens of meters per second, and is an approximately isobaric process [3].

In vernacular usage, "detonation" is often used interchangably with "explosion." The latter is a qualitative term, and refers to any rapid energy release, usually accompanied by a pressure increase, independent of the presence of a combustion front [1]. An explosion which sustains a subsonic combustion wave is a deflagration, and a mixture which permits this is termed a low explosive; an explosion which sustains a supersonic combustion wave is detonation, such mixtures are called high explosives [4]. Detonations may be initiated in either gaseous or condensed media; the former are more useful for aerospace propulsion applications and are therefore the focus of this dissertation.

1.1.1 History and Theory of Detonations

The word *detonation* derives, through the French *détonation*, from the Latin *dētōnare*, meaning "to thunder down" [5]. Though the phenomenon has been known in the West since the Renaissance [3], the scientific study of detonations began in France in the early 1880s, with the work of Berthelot and Vieille [6, 7] and Mallard and Le Châtlier [8] into the flame speeds of various gaseous fuels in a range of diluted and undiluted oxidizers. Their early experiments observed detonation-to-deflagration transition, measured detonation velocities (and identified a maximum propagation velocity), and identified shock wave compression as a key component in initiating the combustion process [3, 9]. These experimental observations, published 1881–1883, predate slightly Hugoniot's 1887 postumous publication of the theory of shock waves [10–12]. However, almost immediately after Hugoniot's work was released, a quantative theory of detonations was developed by Chapman (1889) in England [13], Mikelson (1890) in Russia [14], and Jouguet (1904, 1905/1906) in France [15–17].

1.1.1.1 Chapman–Jouguet Theory

The Chapman–Jouguet (CJ) theory, as it is now known (Mikkelson's work did not receive recognition outside his home country), derives from the work of Rankine (1870) in Scotland [18] in addition to that of Hugoniot [3], and assumes that the detonation wave is steady, one-dimensional, and treats the detonation front as a planar discontinuity. Further, it is assumed that the gas is calorically perfect and at thermochemical equilibrium, with no body forces or heat lost to the surroundings. The derivation is given in many sources including Refs. [1], [3], and [19], so it shall suffice to give only an outline here. It is convenient, though not required, to pose the problem in a detonation-fixed reference frame, whereby the only velocities are the (unknown) upstream and downstream velocities u_1 and u_2.

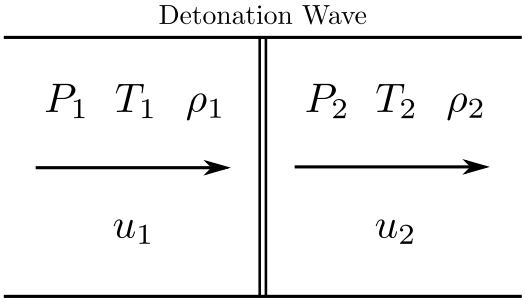

Figure 1.1. Chapman–Jouguet states.

For a given upstream state (density ρ_1, pressure P_1, and temperature T_1) and heat release q, the CJ theory uses the conservation equations of mass, momentum, and energy

$$\rho_1 u_1 = \rho_2 u_2 \tag{1.1}$$

$$P_1 + \rho_1 u_1^2 = P_2 + \rho_2 u_2^2 \tag{1.2}$$

$$c_{p_1} T_1 + \frac{1}{2} u_1^2 + q = c_{p_2} T_2 + \frac{1}{2} u_2^2 \tag{1.3}$$

and the ideal gas equation of state

$$P = \rho R T \tag{1.4}$$

to derive expressions for the unknown velocities and the thermodynamic properties downstream of the detonation wave (ρ_2, P_2, T_2). However, from these expressions alone, the problem is underdetermined: there are only four equations for five unknowns.

To determine this final constraint, we must introduce the so-called Rankine–Hugoniot equations. The first of these, the Rayleigh line, defines the thermodynamic path along which the gas must follow through the combustion process

$$u_1^2 = \frac{1}{\rho_1^2} \left[\frac{P_2 - P_1}{1/\rho_1 - 1/\rho_2} \right] \tag{1.5}$$

Note that the special cases of $\rho_2 = \rho_1$ and $P_1 = P_2$ define constant volume and constant pressure combustion, respectively. As u_1^2 and ρ_1^2 are both by definition positive, so must the quantity $(P_2 - P_1)/(1/\rho_1 - 1/\rho_2)$ also be positive: if $P_2 > P_1$, $\rho_2 > \rho_1$ and vice versa.

The second, the Hugoniot curve, characterizes the loci of possible values of P_2 and ρ_2 (usually expressed as $1/\rho_2$) for a given upstream state P_1 and ρ_1 (again, usually as $1/\rho_1$) and specific heat release q for a detonation

$$\frac{\gamma}{\gamma - 1}\left(\frac{P_2}{\rho_2} - \frac{P_1}{\rho_1}\right) - \frac{1}{2}\left(P_2 - P_1\right)\left(\frac{1}{\rho_1} + \frac{1}{\rho_2}\right) = q \tag{1.6}$$

Note that the case of $q = 0$ holds for shock waves, and is called the "shock Hugoniot".

In order to satisfy the conservation equations, any possible physical state of the gas must lie on both the Rayleigh line and the Hugoniot curve. Therefore, their points of intersection define the possible final states of any possible detonation process. The points above the constant-pressure case (that is, for which $P_2 > P_1$ and $\rho_2 > \rho_1$) represent pressure-gain combustion, and are detonations. The points below the constant-volume combustion case (that is, for which $P_2 < P_1$ and $\rho_2 < \rho_1$) represent pressure-loss combustion, and are deflagrations.

Chapman further showed that at the slopes of the Rayleigh line and the Hugoniot curve at their points of tangency are identically equal to the slope of the adiabat [1], these points are referred to as the upper and lower Chapman–Jouguet points. The upper point is the case for which $P_2 > P_1$ and $\rho_2 > \rho_1$ (a detonation), the lower point represents the opposite case (a deflagration). These points correspond to entropy extrema: at the upper CJ point, the slope of the entropy curve is positive, corresponding to an entropy minimum; for the lower CJ point, the slope of the entropy point is negative, corresponding to an entropy maximum. Therefore, a CJ detonation is the minimum-entropy case, while a CJ deflagration is the entropy

maximum. As a further consequence of this result, it can be shown that at the Chapman–Jouguet points the Mach number behind the wave is unity. Therefore, for both CJ deflagrations and CJ detonations

$$u_2 = a_2 \tag{1.7}$$

where a_2 is the speed of sound in the burned gas. It is this result, formulated by Jouguet when investigating entropy across the Hugoniot curve [3] and now called the Chapman–Jouguet condition, that fully determines the system of equations and allows the calculation of the velocities and downstream thermodynamic properties of a Chapman–Jouguet detonation.

Chapman also observed that the upper CJ point corresponds to the case of minimum detonation velocity. Any Rayleigh line yielding a solution of u_1 greater than this would intersect the Hugoniot curve at two points, indicating two possible solutions. As this poses a paradox, he postulated that the minimum-velocity case must be the physical solution [3]. Though based on intuition and not a mathematical proof, this assumption has been shown to correspond very closely to physically-measured detonation solutions. For example, for the case of stoichiometric hydrogen–oxygen combustion initially at $P_1 = 1\,\text{atm}$ and $T_1 = 291\,\text{K}$, Chapman–Jouguet theory predicts a detonation velocity of $u_1 = 2{,}806\,\text{m/s}$, whereas experimental observations have yielded $u_1 = 2{,}819\,\text{m/s}$ [1], an error of only $0.107\,\text{percent}$.

The discussion of Chapman–Jouguet theory would not be complete without mentioning the contributions of Crussard (1907) [20], who was the first to graphically apply the Rankine–Hugoniot equations [9] and linked Chapman and Jouguet's results by showing that the minimum-velocity and the minimum-entropy cases are identical, and also correspond to the case of sonic flow behind the detonation [3]. The graphical representation of this theory, a further contribution of Crussard, is given in Figure 1.2,

which shows the shock and detonation Hugoniot curves, Rayleigh lines, and upper and lower CJ points; the axes are normalized by the initial conditions P_1 and $1/\rho_1$.

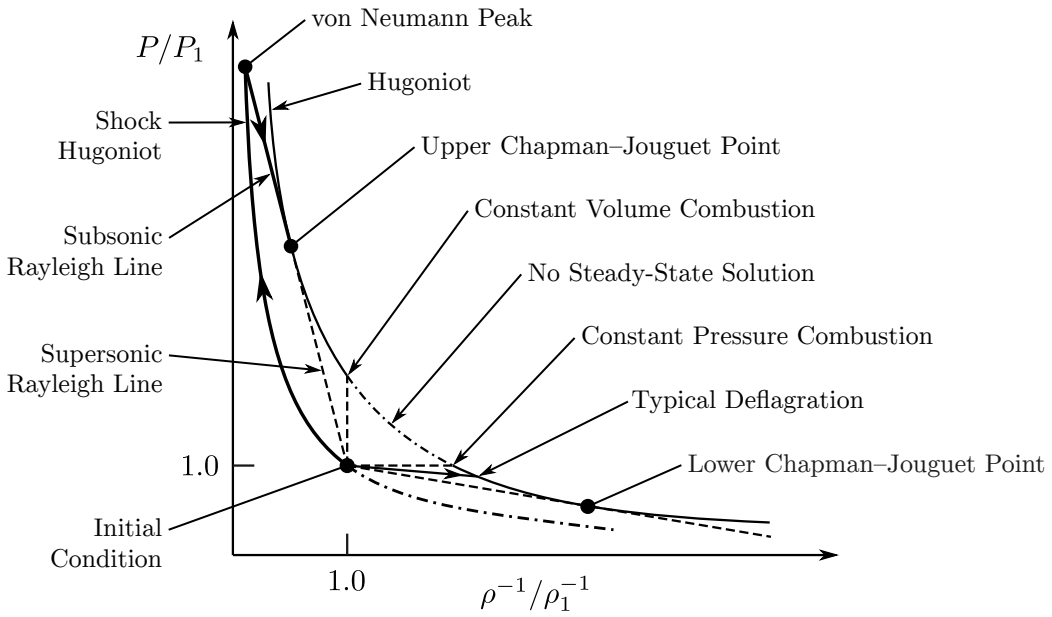

Figure 1.2. Hugoniot curve, adapted from [21].

1.1.1.2 The Zel'dovich–Von Neumann–Döring Model

Though CJ theory is a useful approximation of the behavior of a simple detonation wave, and predicts actual observed velocities remarkably well under ideal conditions, it does not attempt to describe the structure of the detonation, or attempt to understand the physical mechanisms by which it propagates. It was not until the 1940s that the next significant leap forward in detonation theory came, when Zel'dovich (1940) in Russia [22, 23], von Neumann (1942) in the United States [24], and Döring (1943) in Germany [25] independently described the structure of a detonation wave. The model that jointly bears their name (often shortened simply to ZND) treats the shock wave and the combustion front separately and recognizes that

chemical reactions occur on a finite time scale. Instead of a single-step process, the ZND model characterizes a detonation wave in three phases [1]:

1. A leading shock wave, described as a planar discontinuity which adiabatically compresses the gas to point above the CJ pressure, referred to as the von Neumann peak. Density and temperature are also increased through the shock.
2. An induction period, prior to the onset of chemical reactions. Pressure, temperature, and density remain constant in this phase.
3. A reaction zone, during which the gas undergoes exothermic chemical reactions. In this phase, the temperature increases and the pressure and density decrease, finishing at the upper CJ point.

The second and third phases are often combined, as the induction period is physical but makes no significant contribution to the overall behavior of the detonation wave. It is the expansion of the combustion products behind the shock (in the reaction zone and behind the wave itself) that provides the mechanism for the detonation to propagate forward. The behavior of a ZND detonation is therefore heavily dependent on the chemical reaction rate [1].

Additionally, the existence of a finite reaction rate led von Neumann to apply a reaction progress variable (given various symbols in the literature, including ε [1], n [3, 24] and λ [19, 26]), which ranges from 0 (no reactions yet) to 1 (reactions fully complete). The gas remains in local thermodynamic equilibrium, but the precise equilibrium state is a function of the reaction progress variable. Therefore, as the gas state passes down the Rayleigh line between the von Neumann peak and the upper CJ point, Fig. 1.2, a Hugionot curve can be defined for each intermediate state. The behavior of these intermediate Hugoniot curves was used by von Neumann to draw several interesting conclusions, including disproving the existence of weak detonations (a detonation in which the gas behind the wave is supersonic) and demonstrating the

existence of pathological detonations (in which the detonation wave propagates at a velocity greater than the hypothesized CJ velocity) [3].

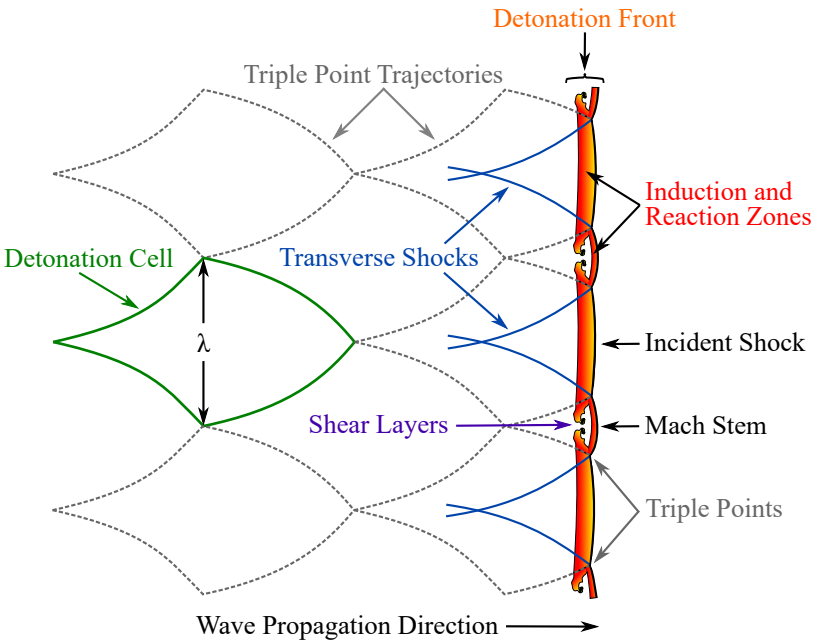

Figure 1.3. Detonation front, showing shock structure and triple point trajectories and their relation to the detonation cell [27], adapted from [28].

1.1.2 The Structure of the Detonation Wave Front

While the ZND model is an improvement over Chapman–Jouguet theory in that it accounts for the finite rate of the chemical reactions and provides a physical mechanism for the detonation to propagate and sustain itself, it still models the detonation wave front as a steady, one-dimensional discontinuity. However, observations of the detonation wave front have shown conclusively that the detonation wave is an inherently unstable, complex, three-dimensional structure [29]. The leading shock front interacts with transverse waves shock waves to form a characteristic triple-shock structure. The trajectories of the triple points corresponding to the intersection of the

leading shock structure and the traverse waves forms a distinct diamond or fish-scale cellular pattern, Fig. 1.3 [2, 3, 30].

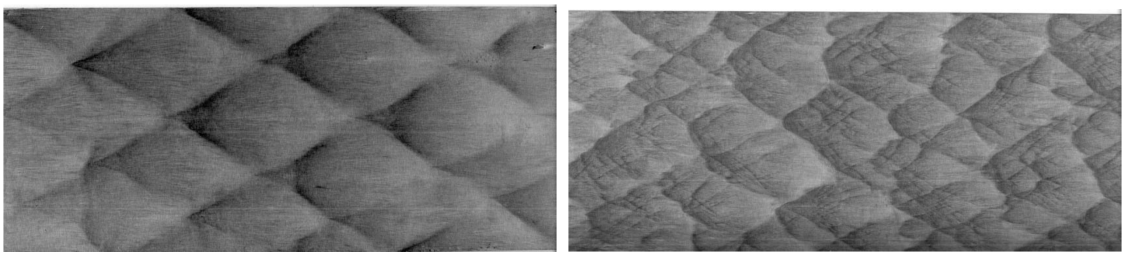

(a) Weakly unstable detonation (b) Strongly unstable detonation

Figure 1.4. Soot-foil traces of detonation wavefronts [30].

Observations of this cell structure can be made using a technique first used by Mach and Sommer [31] to study shock interactions, applied first to observations of the strcture of detonations by Denisov and Troshin [32–34]. A metal foil is lightly covered with soot and a detonation wave passed over it, leaving the triple-shock cellular structure imprinted on the foil. This "soot foil" technique is widely used to experimentally characterize the size of these cells, dubbed the "detonation cell size" (or occasionally more precisely as the "detonation cell width"), commonly denoted by λ. The cellular structure is not always regular, however. The more stable the detonation front, the more regular the observed cells. (It should be noted that as detonations are always unstable, this distinction is between so-called "weakly unstable" and "strongly unstable" detonation waves.) Figure 1.4, from Ref. [30], shows two soot-foil traces of mixtures with varying degrees of stability: Fig. 1.4a is taken from a weakly unstable detonation ($2\,H_2 - O_2 - 12\,Ar$), and shows a well-defined, regular cellular pattern. This is in contrast with Fig. 1.4b, from a strongly unstable detonation ($C_3H_8 - 5\,O_2 - 9\,N_2$): this foil shows a complex, irregular cellular structure with internal substructures and

a range of length scales. Within the pattern, though, a dominant set of larger-scale cells can be observed; the average size of these is used to characterize λ [3].

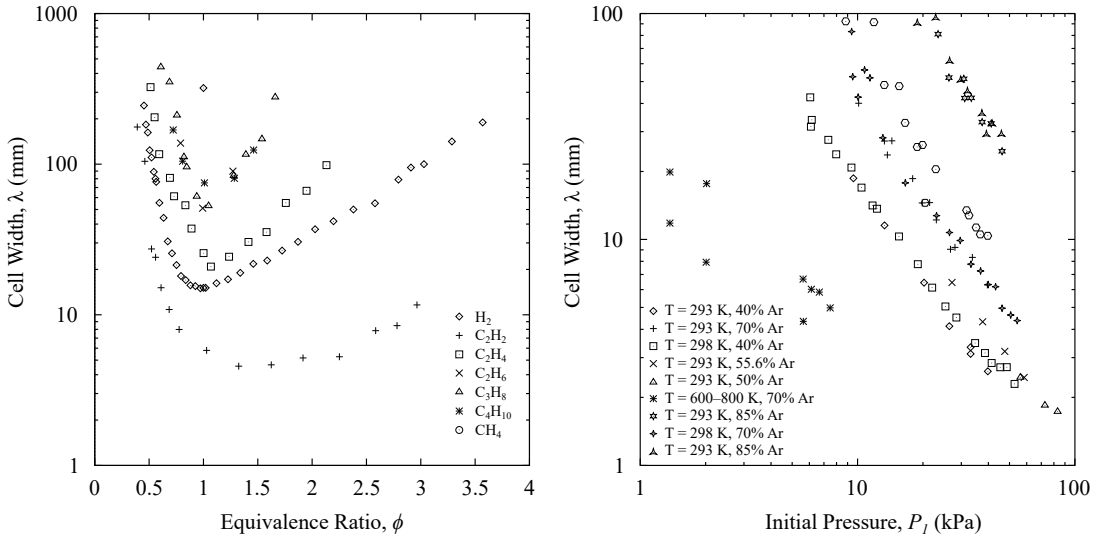

(a) Variation in ϕ for hydrocarbon-air mixtures at 101.3 kPa

(b) Variation in P_1 for stoichiometric H_2-O_2 mixtures with argon diluent

Figure 1.5. Detonation cell widths as a function of initial state [35].

The detonation cell size has been experimentally observed to correlate strongly to a range of other detonation parameters, in particular its ability to maintain its structure and continue to propagate. In this capacity, it can be thought of as the sensitivity of the mixture [29], and therefore represents a useful characteristic length scale against which to characterize the effect of external (tube diameter, orifices, boundary type) or internal (propellant composition, initial gas state) effects on the detonation wave [29].

The detonation cell size is not fixed, however. It is instead strongly a function of the propellant composition and the initial gas state. Minimum cell size is generally observed at equivalence ratio $\phi \approx 1$, increasing sharply as mixtures become more fuel- or oxidizer-rich, or as diluent increases [29, 36]; Fig. 1.5a. Cell size is also strongly

dependent on the initial pressure, with increases in P_1 corresponding to decreases in λ; Fig 1.5b.

At the moment, the only way of determining the cell width of a given gas at a given initial state is by experiment. Databases of this data are available, in particular the excellent Detonation Database begun by Shepherd at Cal Tech [35, 36], from which the data for Fig. 1.5 was obtained, but there are limitations. For example, there have been only very limited experiments on cell size for pressures greater than 1 atm (as the detonation pressure scales with the initial pressure, there are very legitimate safety reasons for this lack of data). The data is also biased towards those mixtures which have cell sizes that can be experimentally determined at laboratory scale. Reactants with low detonability and high cell sizes, such as larger-chain hydrocarbons and methane (particularly in dilute mixtures or air), have very limited data available. Additionally, databases must be kept up-to-date, which requires dedicated effort; the Detonation Database, for example, has not been updated since 2005.

Unfortunately, there exists at the moment no way to know the cell width of a given gas composition and initial state absent experiment. Some low-order correlations have been hypothesized [3], but these are empirical in nature and rely on good experimental data. There have been efforts to computationally predict cell size by chemical kinetics [37–43] and by machine learning [44, 45], but these efforts have so far had mixed success. As an understanding of the detonation cell size is key in characterizing the suitability of a reactant for practical detonation-based applications, further fundamental research in this area is therefore necessary.

1.1.3 Deflagration-to-Detonation Transition

In general, detonations may form in one of two ways. Under appropriate conditions, pressure-wave instabilities of a deflagration wave can create a positive-feedback mechanism which results in an acceleration of the flame front and a transition to a detonation wave; this process is called deflagration-to-detonation transition (DDT) [3]. Like detonations, deflagrations are inherently unstable. However, unlike detonations, there is no single stable propagating velocity for a deflagration. Instead, they tend to continuously accelerate until they either transition to a detonation or reach a quasi-stable deflagration velocity befitting the boundary conditions [46]. After combustion is initiated, the expanding products result in the creation of a compression or shock wave (the "precursor shock") which propagates into the reactants ahead of the combustion zone. Though there are many modes by which the DDT process can be initiated [47], the mechanism which causes transition is universal: the formation of a local "auto-explosion" in the reaction zone initiates a positive feedback mechanism which results in the coupling of the flame front and precursor shock wave and formation of a detonation wave. This process occurrs rapidly (on a microsecond timescale), and causes a significant increase in the velocity of the wavefront. The mode by which these auto-ignition will be initiated is not predictable *a priori* [47], but factors known to aid in the transition process include [46]:

- Obstacles (such as the famous Shchelkin spiral [48]), which induce folding of the combustion front, maintaining fine-scale turbulence and thereby increasing burning rate.
- Physical boundaries, which cause interaction of the flame with reflected shocks and pressure waves, inducing Rayleigh–Taylor instabilities within the deflagration front.

- Pre-heating and pre-compression of the reactants by the precursor shock wave, amplifying the positive feedback loop between the deflagration front and the precursor shock.

However, the initation of an auto-explosion within the reaction front, while necessary, is not by itself sufficient to induce transition. Instead, that auto-explosion must create a coherent, self-amplifying shock wave and energy release; this mechanism was proposed by Lee and named SWACER: "Shock Wave Amplification by Coherent Energy Release" [49].

Alternatively, detonations may be directly initiated; that is, form spontaneously without the need for a transition process from a deflagration. This requires a substantial amount of initiation energy to generate the thermochemical conditions necessary for the detonation wave to form, and therefore is often done with an external explosive charge or by injection of an external shock wave or pre-existing detonation wave [3]. However, even in the case of direct initiation, detonation in the reactants is still induced by a local auto-explosion in the turbulent interaction between the ignition source and the reactants [50].

1.2 Detonation Propulsion

Due to the lower entropy generation in the combustion process and the significant increase in pressure through the shock wave, the potential efficiency gains from replacing deflagration-based gas turbine and rocket engines with detonation-based engines has spurred significant interest into the use of detonation waves for propulsion since the 1940s. Such research arose independently in multiple places: Hoffman tested an early pulsed detonation concept in Germany in 1941 [51], Roy proposed a detonation-powered ramjet in France in 1946 [52], and a patent for a detonation propulsion device was awarded posthumously to Robert Goddard in 1949 [53] (there

does not appear to be any evidence his invention was tested). More in-depth research efforts were conducted in the 1950s and early 1960s in the United States [51, 54–56] and the Soviet Union [57] and several patents were issued in the United States for detonation-based propulsion systems in the 1960s [58–62]. However, these initial bursts of interest were not successful in creating a practical engine concept, and research efforts waned by the early 1970s. Renewed interest in detonation propulsion began again in the late 1980s, particularly in pulse detonation engines [63–72] and oblique detonation wave engines [70, 72–81], and has continued at a high level to the present day.

The high velocity of the detonation wave with respect to the incoming propellant presents a significant design challenge to propulsion applications: in general, the detonation will propagate significantly faster than the vehicle or engine attempting to harness it for thrust. So far, three main ways have been proposed to solve this problem:

1. Match the incoming velocity of the gas to the steady detonation velocity. This is the method employed in stationary and oblique detonation engines, Fig. 1.6, and is the simplest of the three concepts. It is, however, sensitive to perturbations in incoming velocity and mass flow, and requires the engine to operate at supersonic speeds [70].

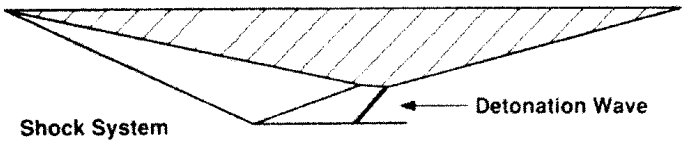

Figure 1.6. Oblique detonation wave engine concept [82].

2. Do not attempt to establish a steadily propagating detonation wave within the engine, and instead use the detonation's high velocity to perform high-frequency pulsed detonation. This is the method employed in pulse detonation engines, Fig. 1.7, and is probably the most well-studied of the detonation concepts. It is extremely simple in concept, but requires high-speed valving, and practical operation at high frequencies requires the use of a purge gas to prevent freshly-injected propellants from autoigniting (deflagrating) on contact with the hot combustion products from the previous cycle [71]. This has the effect of reducing the maximum operational frequency of the engine, and for rocket applications requires carrying an additional inert gas on board the vehicle. Additionally, such an engine does not produce steady thrust.

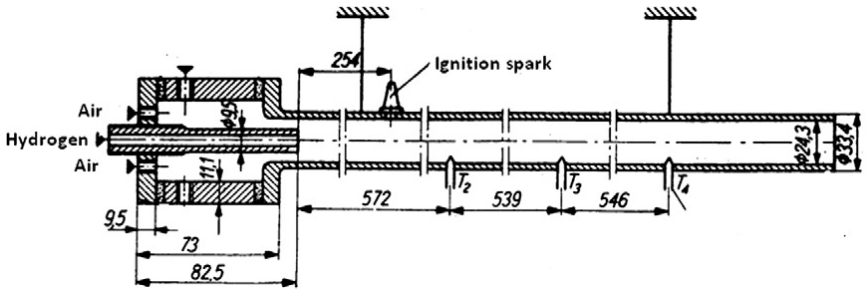

Figure 1.7. Pulse detonation engine concept [51].

3. Do not attempt to set up a steadily propagating axial detonation, but instead ignite a detonation wave in the circumferential direction around an annular combustion chamber. This is the method employed in the rotating detonation engine, and will be discussed more in depth in the following section.

1.3 The Rotating Detonation Engine

The rotating detonation engine (in the literature variously also referred to as the "rotating detonation wave engine" and "continuous detonation [wave] engine") consists of an annular combustion chamber through which a detonation wave propagates circumferentially. This detonation wave is sustained by axial propellant injection while the detonation products expand out the rear of the engine to produce thrust.

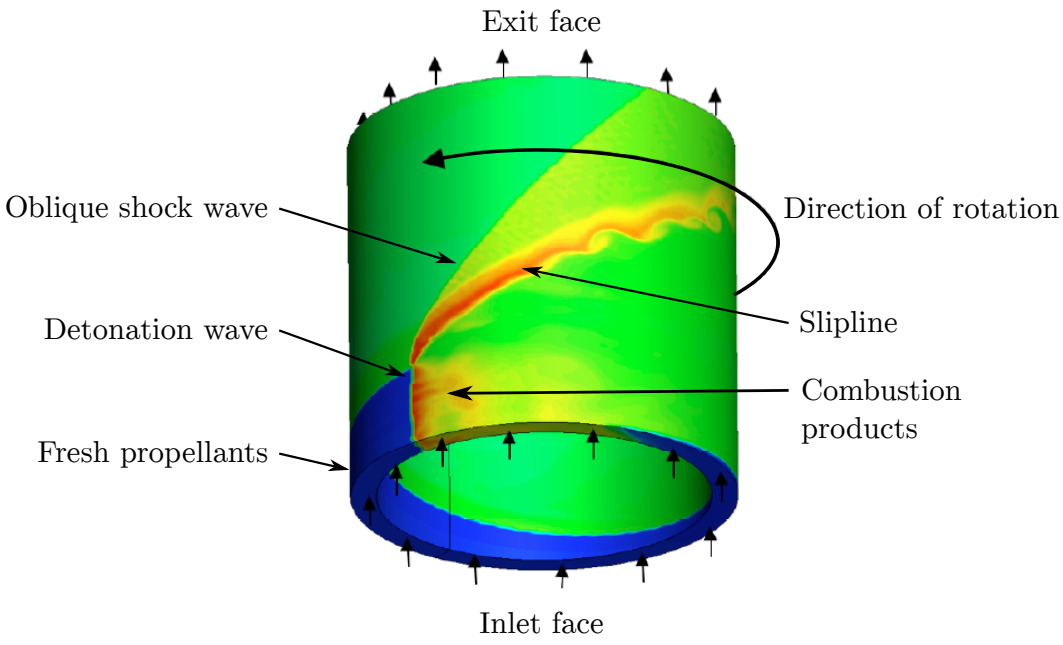

Figure 1.8. RDE temperature profile, adapted from [83].

Figure 1.8, adapted from the computational simulations of Nordeen et al. [83], shows a temperature profile of the RDE which illustrates many of its salient features. The detonation wave appears near the bottom of the annulus as a vertical red line, with the combustion products behind it in red and orange. In front of the detonation wave are the propellants injected into the head-end of the annulus (bottom), shown in blue. Combustion products (cooling from red to green) expand out the back end of the

engine (top). The curved black line indicates the direction of detonation propagation, the burned mixture expands out to the left from the detonation wave, towards the exit plane around the annulus. Expanding diagonally upwards from the top of the detonation wave as a thin yellow line is the attached oblique shock wave, this is formed by the expansion flow circulating around the annulus and interacting with the fresh burned combustion products. While not visible in Figure 1.8, computational studies also show a fraction of the propellant flow which does not detonate, but instead deflagrates on contact with the recirculating hot combustion gasses. This is termed "contact surface burning", and represents a performance loss. The slipline between the expanding fresh combustion products and the recirculating flow can be seen as a red and orange region below the shock wave. In computational studies, a Kelvin–Helmholtz instability forms along this line, elements of which are seen here.

The anuluar combustion chamber provides a compact, scalable configuration that appears to be widely scalable. This compactness and lack of moving parts, along with the significant promised gains in efficiency, make the RDE an object of significant research interest and offers significant promise in a variety of aerospace applications [21, 70, 84].

1.4 Research Efforts

RDE research originated in the late 1950s and early 1960s independently in the Soviet Union by Voitsekhovsky [85] at the Institute of Hydrodynamics (LIH, named for Mikhail Lavrentyev in 1980 [86]) in Novosibirsk and in the United States by Nicholls et al. [55] at the University of Michigan, developing jointly out of research into the rotating instability in rocket engines and the spinning instability of detonation waves. After a period of early activity in the 1960s [61, 87, 88], and despite ongoing research efforts at LIH [89–95], the RDE fell into a period of disinterest in

the West for the rest of the 20$^{\text{th}}$ Century. In the comprehensive review of propulsion applications of detonation waves by Kailasanath in 2000 [70], the RDE merits only a single passing paragraph. However, by the late 2000s, in addition to the ongoing research of Bykovskii et al. in Russia [95–102] RDE research efforts were underway in France [103–112], Poland and Japan [113–115], Korea [116], the United States [117], and other countries. Since then, research into RDEs has expanded significantly: there are currently RDE research efforts ongoing at a number of research institutions on at least three continents, and has prompted a number of recent literature reviews [118–120].

1.4.1 Engine Models

Previous computational work in RDEs has largely consisted of high-order numerical simulations, the majority of which have been two-dimensional, but three-dimensional studies are becoming more common [118, 119]. These studies are useful for understanding the RDE's complex internal fluid dynamics, with many of them considering basic performance features of the RDE on a limited range of design parameters, most commonly propellant plenum pressure or pressure ratio, for performance metrics, usually thrust and specific impulse.

Hayashi et al. performed a sensitivity analysis focused on temperature, pressure, and Mach number [115]. Schwer and Kailasanath investigated engine size [121] and inlet configuration [122]. Nordeen et al. investigated the effects of annulus area changes [123] and the impact of a downstream converging-diverging nozzle [124]. Zhdan et al. studied the effects of chamber length, pressure ratio, and expansion ratio [97], and propellant equivalence ratio [125]. These are all high-order simulations which require extensive computational time, so the number of parametric sweeps has necessarily been limited. Such numerical methods have the potential for high accu-

racy and are especially useful for modeling unsteady flow phenomena inside the RDE annulus. However, they are computationally expensive and time-consuming to set up and run, making them impractical for early design-stage parametric analysis and engine sizing, where a detailed account of flow physics might not be necessary.

Low-order models have hitherto been limited to the work of Braun et al. who published an analytical cycle analysis for the airbreathing RDE [126, 127] and performed a first- and second-law analysis [128]. These studies used the Endo–Fujiwara model [129, 130] as a basis, which was derived for pulse detonation engines. However, it is not based on RDE flow physics, and Braun's equations for circumferential property distributions derived from it could not be corroborated. Additionally, Braun's model incorporated a sizing method that limits it to an airbreathing engine. Recently, a more comprehensive parametric study of the RDE for an ethylene–air engine was published by Fievisohn and Yu, which used a method of characteristics solver [131] to determine the effect of annulus circumference, annulus width, engine length, equivalence ratio, propellant plenum temperature and pressure, and area ratio (ratio of injector nozzle to chamber cross-sectional area) on a range of engine performance parameters and detonation characteristics [132, 133]. This is still a numerical model, but a lower-order one which can be solved relatively quickly.

1.4.2 On Swirl

Within the context of RDEs, "swirl" is defined as a nonzero circumferential velocity component in the inertial frame. It is known that the high rotational velocity of the detonation wave induces a strong circumferential velocity component in the noninertial flow on the inlet plane [124], and if this velocity continues to the exhaust plane it represents a potentially significant performance loss and may induce rotation of the vehicle. Until recently, there has been little attempt to quantify the magnitude

or effect of exit flow swirl. Braun et al. [126, 127], Bykovskii [96], Yi et al. [134] and Davidenko et al. [111] did not mention it; Schwer and Kailasanath [135] showed that it is nonzero on at least part of the exit plane, but simply stated that it will decrease performance and increase wall loading. Nordeen et al. noted the presence of swirl inside the engine [83, 136], but argued for zero net swirl in the exhaust flow [83]. Hishida et al. [114] plotted V_θ/V_z as a function of time, and indicated that it is less than three percent, which they implied was effectively zero. However, in recent publications, several authors have explicitly addressed the issue of swirl, including Paxson [137] and Nordeen et al. [123, 124].

The prevailing theory in the literature is that the detonation-induced swirl component in the exhaust flow is counteracted by flow turning through the trailing oblique shock wave, resulting in zero net swirl in the exhaust flow. Furthermore, no studies have yet considered the effect of swirl imparted to the propellant flow. This is of interest for two main reasons: if exit swirl is nonzero, then inlet swirl may serve to counteract it. There may also exist situations where exit swirl is desirable (for example, turbomachinery applications, potentially reducing or eliminating the need for inlet guide vanes). In these cases, it is of interest to investigate the effect of inlet swirl as a means of controlling swirl at the exit.

While rotational ("non-axial") flow has been observed in experiments by Aerojet Rocketdyne, as reported in [120], Fig. 1.9, experimental efforts have been even more limited: Braun [117] tested two RDE designs with swirled injection or premixing to improve mixing and assist with establishing a stable rotating detonation and reported some operational success, but the engine was not instrumented to measure the effects of this swirl and swirl was not adjustable. To the author's knowledge, this is the only previous experimental investigation of swirl in RDEs in the literature.

Figure 1.9. Evidence of exit swirl on aerospike nozzle [120].

1.4.3 RDE Integration

As previously established, the RDE has long been envisioned as a propulsion system in high-speed vehicles. Wolański illustrated a hypothetical RDE installed in a hypersonic vehicle [72] and with Tobita et al. received a U.S. patent in 2010 for a flying RDE concept [138]. However, integration studies have been limited. Some experimental investigations have been performed: with gas turbine engines in Poland [72,139] and the United States [140] and with ramjets in Russia [141,142] and China [143]. The aforementioned studies involved fixed inlets and did not attempt to characterize the effect on performance due to changes in inlet or forebody design. There have hitherto been no computational studies which integrate an RDE and a supersonic inlet. Yi et al. modeled an RDE in a flow with a freestream Mach number of 1.5, but ignored inlet effects [134]. Schwer et al. modeled the diffuser upstream of an RDE for a freestream Mach number of 2.5, but inlet design was not a part of the study [144].

1.4.4 High-Speed Visualization

High-speed cameras have been used to confirm the presence of rotating detonation fronts in RDEs [118, 119], generally with frame rates on the order of tens of thousands per second. (Consideration of the frame rates and exposure times for such tests is important, as lower frame rates limit the time-resolution of the observable phenomena and higher exposure times wash out the frame, possibly obscuring detail, and can lead to blurred images of very high-speed phenomena.) These visualizations are commonly performed from a down-annulus perspective, but some studies have been performed by directly observing the visible front [145] or OH* chemiluminescence [146–149] using optically-accessible RDEs. Additionally, there have been some studies which have used curved or straight channels to observe propagating detonation waves in a manner reminiscent of rotating detonation engines [116, 150–154]. These studies focus on the behavior of steadily-propagating detonations, and not on the ignition or startup dynamics.

1.4.5 Ignition Studies

A number of methods have been used to start rotating detonation engines. Many studies, particularly early ones, used automotive spark plugs with varying degrees of success. Spark plugs are cheap, simple to install and use, and require no additional fuel or valving, but are relatively low energy (and thus less likely to successfully initiate a detonation in low-detonability mixtures), and offer no way of controlling the direction or number of detonation waves. Other techniques employed include high-voltage discharge/plasma jets [89, 155, 156], hot wire [92], and even solid energetic charges [95,155]. These methods have demonstrated moderate repeatability, but consistent success has been reported with predetonation tubes [157–160]. These predetonators usually consist of a tangential cylinder extending into the annulus which

is filled with a detonable mixture and ignited, with the intent of propagating a detonation wave into the engine to ignite the RDE propellants. To fill the tube without the need for a timing mechanism, the predetonation tube is sometimes set apart from the chamber by a diaphragm [55, 157, 161], though this is not a practical approach for operational use. More recently, a series of timed sparks was used by Kurosaka et al. to initiate a detonation wave [162, 163].

Ignition studies of RDEs have been fairly limited. Miller [158, 164] studied the design of predetonators. Bykovskii [165] investigated the ignition behavior inside an annular chamber by a unique swirled predetonator and exploding wire igniter for a range of fuel/oxidizer mixtures with side-wall visualization by falling-drum camera. Peng [166] investigated ignition by spark plug and was able to establish much more reliable ignition by that method than previously reported [157]. St. George investigated starting transients and the stability of the established detonation, including direction and speed of propagation, for predetonator ignition [167] and performed a detailed investigation into optimization of predetonator design [159]. Fotia [168] investigated ignition inside an RDE with varying degrees of back pressure, focusing on factors governing the establishment of varying modes of steady operation. The most comprehensive study to date has been by Yang [160], which investigated three ignition methods (normal spark plug, high-energy spark plug, and predetonator), and took down-engine high-speed video. These visualizations were performed with frame rates between 48,000–60,000 frames/s and exposure times between 15–20 μs. These studies have shown that there is a delay between the initial ignition event and the onset of a steadily propagating detonation wave. These delays have been observed to be stochastic, but with a predetonator generally shortening the time to onset of detonation [160]. Investigations of the ignition process and associated phenomena can help develop a better understanding the mechanisms by which the rotating det-

onation front is established, as well as factors influencing the number of detonation waves, and the direction and mode of propagation.

CHAPTER 2

CONTROL VOLUME ANALYSIS OF THE ROTATING DETONATION ENGINE

2.1 Control Volume

The rotating detonation engine control volume $\mathscr{V}$ is defined as the annulus of the engine and consists of four surfaces: the injection (head-end) plane S_1, the exit (exhaust) plane S_2, and two co-annular cylindrical walls S_3 (inner) and S_4 (outer). These surfaces and their outward-pointing normal vectors are shown in Fig. 2.1.

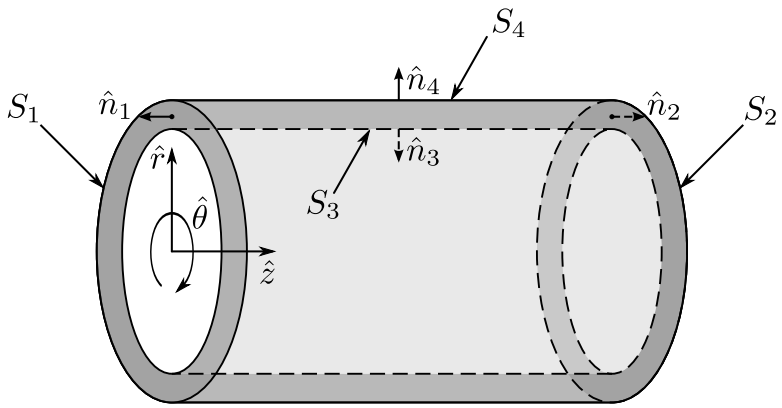

Figure 2.1. RDE control volume surfaces and normal vectors.

The control volume is fixed in space, and flow within it is assumed to be cyclic and inviscid with no body forces. Property variations in the r-direction are neglected.

2.2 Velocity Definitions

To convert between the inertial (laboratory-fixed) and noninertial (detonation-fixed) coordinate frames, a Galilean transformation is necessary. This is a common

technique in turbomachinery [169,170], and has been successfully applied to the RDE by Nordeen et al. [21,83,136,171] This transformation is defined as

$$\vec{W} = \vec{V} - \vec{U} \tag{2.1}$$

where $\vec{V}$ is the velocity in the inertial reference frame, $\vec{W}$ is the velocity in the noninertial reference frame, and $\vec{U}$ is the velocity of the noninertial frame with respect to the inertial frame. For an RDE, the detonation wave velocity

$$\vec{U} = \vec{U}_{det} = 0\ \hat{r} \pm U_{det}\ \hat{\theta} + 0\ \hat{z} \tag{2.2}$$

where U_{det} is positive when the detonation wave rotates in the $+\theta$ direction and negative when it rotates in the $-\theta$ direction. The vector sum of these components is illustrated in Fig. 2.2. To make its components easier to see, $\vec{V}$ has been illustrated with swirl (that is, $V_\theta \neq 0$).

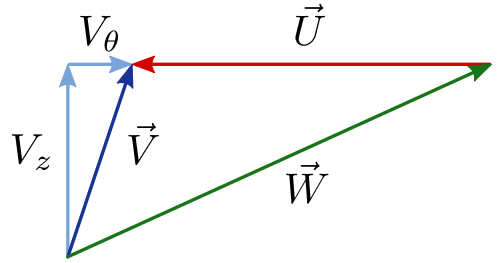

Figure 2.2. Velocity components and definitions.

Note that in the present studies, swirl is deemed positive when oriented in the $+\theta$-direction, and negative when in the $-\theta$-direction.

2.3 Internal Flow Model

The internal flowfield of an RDE is complex and has been the subject of considerable study. High-order models are widely used to investigate detailed aspects

of the internal flow characteristics, but as previously established, are too computationally expensive for low-order parametric analysis. Therefore, a simplified internal flow model was created in order to compute the inlet and exit flow conditions for control-volume analysis. Fig. 2.3 illustrates this model.

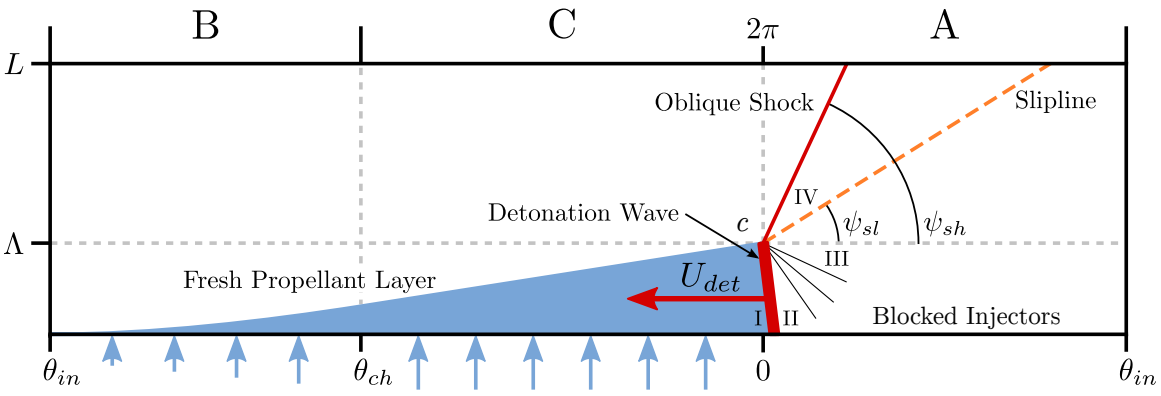

Figure 2.3. Unrolled RDE annulus with major features labeled.

The detonation wave propagates circumferentially around the annulus, sustained by continuous injection of fresh propellants. This model assumes only a single detonation wave, which can be configured to rotate in either the positive or negative θ-direction. Figure 2.3 illustrates the latter. A two-γ model is assumed, with propellant mixture properties used upstream of the detonation wave and detonation values used in the expansion and on the exit plane. Propellant flow is assumed to be premixed. In reality, operational engines will likely require separate fuel and oxidizer flows with incomplete mixing, which cause a performance loss.

Previous numerical studies [21, 83, 121, 122, 136, 172] indicated a region of propellant flow which does not pass through the detonation wave and instead deflagrates on the contact surface between the fresh propellant flow and the expanding combustion products. This contact surface burning likewise represents a performance loss.

Incomplete mixing and contact surface burning are neglected in this model. Mixture properties of the unburned fuel–oxidizer mixture are calculated using properties from Refs. [173] and [174] and the 1976 U.S. Standard Atmosphere [175]. Detonation properties are calculated using Cantera [176] with the Caltech Shock & Detonation Toolbox [177], assuming choked injector flow upstream of the detonation wave and equilibrium conditions.

Numerical models indicate that the detonation wave inclines somewhat towards the injector flow. This inclination is due to the axial velocity of the injector flow, and can be estimated by assuming the detonation wave is normal to the noninertial velocity vector of the injection flow immediately upstream of the detonation wave, as shown in Fig. 2.4, where

$$\psi_{det} = \psi_{\mathrm{I}} = \tan^{-1} \frac{W_{\mathrm{I}_z}}{W_{\mathrm{I}_\theta}} \tag{2.3}$$

is the detonation wave inclination angle

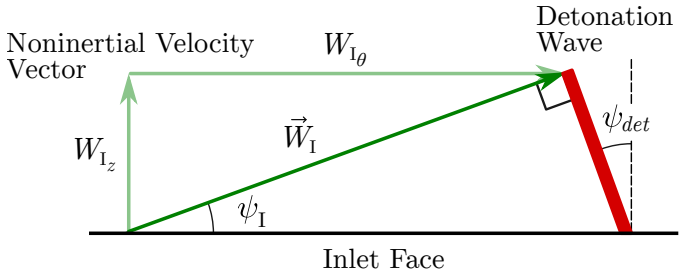

Figure 2.4. Inclination of detonation wave due to axial velocity of injector flow.

As illustrated in the experimental results of Bykovskii et al. [96] and the detailed flowfield simulations of Nordeen et al. [21, 83, 136, 171], Schwer and Kailasanath [121, 122, 135, 172, 178], the rotating detonation wave is coupled to an attached oblique shock wave. This shock wave and the slipline (shear layer) between the expansion products passing through the shock wave and those passing through the detonation

wave defines an area into which the detonation products can expand, as illustrated in Fig. 2.3. Numerical simulations have shown that both the oblique shock wave and the slipline curve somewhat around the annulus. However, as a first-order approximation, the present analysis neglects this curvature and models both the oblique shock wave and slipline as linear.

Design parameters for the engine consist of the annulus outer and inner diameters d_o and d_i and length L; the injector hole area ratio $\Xi = A_{inj}/S_1$, where A_{inj} is the total area of the injector holes on the annulus face; the propellant plenum stagnation pressure and temperature $P_{0_{inj}}$ and $T_{0_{inj}}$; the injector flow angle ψ_{inj}; the propellants (fuel and oxidizer); and the equivalence ratio ϕ. This model considers only a straight annulus with no cross-sectional area change or nozzle. The effect of nozzles and annulus contouring, as well as advanced cooling techniques (such as transpiration cooling, ablative linings, cooling by propellant pre-heat, or cryogenics) are beyond the scope of this analysis.

2.3.1 Injector Conditions

Flow into the control volume is governed by the pressure decay behind the detonation wave, and is divided into three flow regimes, illustrated in Fig. 2.3.

A. $P_c \geq P_{0_{inj}}$: No injection. Counter-flow into the injector is neglected in this model.

B. $P_{0_{inj}} > P_c > P_{cr}$: Flow entering the chamber is subsonic, $P_{inj} = P_c$.

C. $P_c \leq P_{cr}$: Flow entering the chamber is sonic, $P_{inj} = P_{cr}$.

where P_c is the chamber static pressure, P_{inj} is the static pressure of the injected propellant flow, and

$$P_{cr} = P_{0_{inj}} \left(\frac{2}{\gamma_{inj} + 1} \right)^{\gamma_{inj}/(\gamma_{inj}-1)} \tag{2.4}$$

is the critical pressure.

The injection temperature and velocity in regimes B and C are given by

$$T_{inj} = T_{0_{inj}} \left(\frac{P_{inj}}{P_{0_{inj}}} \right)^{(\gamma_{inj}-1)/\gamma_{inj}} \tag{2.5}$$

$$V_{inj} = \sqrt{\frac{2\gamma_{inj}}{\gamma_{inj}-1} R_{inj} T_{0_{inj}} \left[1 - \left(\frac{P_{inj}}{P_{0_{inj}}} \right)^{(\gamma_{inj}-1)/\gamma_{inj}} \right]} \tag{2.6}$$

The points at which injection begins (separating regime A from regime B) and chokes (separating regime B from regime C) have been designated θ_{in} and θ_{ch}, respectively.

2.3.2 Shock and Slipline Angles

Sichel and Foster [179] derived a method to determine the oblique shock wave and slipline angles for a detonation wave bounded on one side by a wall and the other by an inert mixture, which was applied by Fievisohn and Yu [131] to calculate the oblique shock and slipline angles inside an RDE. The states for this analysis are given as Roman numerals in Fig. 2.3: I and II are immediately in front of and behind the detonation wave, III is behind the Prandtl–Meyer expansion fan, and IV is the inert products behind the oblique shock wave. Again, c denotes the (inert) gas chamber properties.

The derivation of this method is given in both Sichel and Foster [179] and Fievisohn and Yu [131]. First, the oblique shock relation links the oblique shock angle, slipline angle, and the chamber Mach number M_c

$$\tan \psi_{sl} = 2 \cot \psi_{sh} \left[\frac{M_c^2 \sin^2 \psi_{sh} - 1}{M_c^2 \left(\gamma_c + \cos 2\psi_{sh} \right) + 2} \right] \tag{2.7}$$

Secondly, the slipline angle is given by

$$\psi_{sl} = \nu \left(M_{\mathrm{III}} \right) - \nu \left(M_{\mathrm{II}} \right) \tag{2.8}$$

where $\nu(M)$ is the Prandtl–Meyer function. However, from Chapman–Jouguet theory, $M_{\mathrm{II}} = 1$, which yields $\nu(M_{\mathrm{II}}) = 0$. Thus, Eq. (2.8) simplifies to

$$\psi_{sl} = \sqrt{\frac{\gamma_{\mathrm{II}}+1}{\gamma_{\mathrm{II}}-1}}\tan^{-1}\sqrt{\frac{\gamma_{\mathrm{II}}-1}{\gamma_{\mathrm{II}}+1}\left(M_{\mathrm{III}}^2-1\right)} - \tan^{-1}\sqrt{M_{\mathrm{III}}^2-1} \tag{2.9}$$

Finally, the pressures on both sides of the slipline, P_{III} and P_{IV}, are equal. Using pressure ratios, they are related by

$$\frac{P_{\mathrm{IV}}}{P_c} = \frac{P_{\mathrm{I}}}{P_c}\frac{P_{\mathrm{II}}}{P_I}\frac{P_{\mathrm{III}}}{P_{\mathrm{II}}} \tag{2.10}$$

where the pressure ratio across the oblique shock wave P_{IV}/P_c is given by

$$\frac{P_{\mathrm{IV}}}{P_c} = 1 + \frac{2\gamma_c}{\gamma_c+1}\left(M_c^2\sin^2\psi_{sh} - 1\right) \tag{2.11}$$

the pressure ratio across the Prandtl–Meyer expansion wave $P_{\mathrm{III}}/P_{\mathrm{II}}$ is

$$\frac{P_{\mathrm{III}}}{P_{\mathrm{II}}} = \left[\frac{\frac{1}{2}(\gamma_{\mathrm{II}}+1)}{1+\frac{1}{2}(\gamma_{\mathrm{II}}-1)M_{\mathrm{III}}^2}\right]^{\gamma_{\mathrm{II}}/(\gamma_{\mathrm{II}}-1)} \tag{2.12}$$

and $P_{\mathrm{II}}/P_{\mathrm{I}}$ is the pressure ratio across the detonation wave. Note that M_c, M_{II}, and M_{III} in Eqs. (2.7)–(2.12) are the noninertial Mach number

$$M_W = \frac{\|\vec{W}\|}{a} \tag{2.13}$$

where $\vec{W}$ is the velocity in the noninertial frame and is a the speed of sound, calculated as outlined in Sec. 2.3.3.

Eqs. (2.7), (2.9), and (2.10) form a numerical scheme with three unknowns: the shock and slipline angles ψ_{sh} and ψ_{sl}, and the Mach number behind the Prandtl–Meyer expansion M_{III}. In general, the chamber conditions must be determined iteratively. First, an initial value of chamber Mach number M_{c_i} is guessed and used to calculate P_{c_i} by isentropic flow expansion. (For these calculations, $P_c = P_c\,|_{\theta=2\pi}$.) This allows the calculation of ψ_{sh_i} and ψ_{sl_i} by Eqs. (2.7)–(2.10), and then the detonation wave

height Λ_i is computed by the method outlined in Sec. 2.3.3. Finally, Λ_i is used to calculate the value of chamber pressure and Mach number around the annulus $P_{2\pi_i}$ and $M_{2\pi_i}$. If $M_{2\pi_i}$ and M_{c_i} agree to within a specified tolerance, chosen as $\epsilon = 10^{-6}$, the values of ψ_{sh} and ψ_{sl}, as well as the detonation wave height, are passed on to the rest of the engine model and used in the performance parameter calculations. If not, a new value of chamber Mach number $M_{c_{i+1}}$ is calculated by the secant method using the recurrence relation

$$M_{c_{i+1}} = M_{c_i} - \Delta M_i \frac{M_{c_i} - M_{2\pi_{i-1}}}{\Delta M_i - \Delta M_{i-1}} \tag{2.14}$$

where $\Delta M_i = M_{c_i} - M_{2\pi_i}$. Convergence is generally achieved within five iterations. A flowchart of this solution method is given in Fig. 2.5.

This method was derived for a planar detonation wave propagating normally to the wall into a quiescent fluid. However, as previously established, the axial velocity component of the injected propellants causes the detonation to incline into the flow by angle ψ_{det}. This inclination has the effect of increasing the shock angle and sliplines with respect to the inlet face. To account for this, the shock and slipline angles computed by the method given here are adjusted by factors of the detonation wave angle

$$\psi_{sh} = \psi_{sh_i} + \psi_{det} \tag{2.15a}$$

$$\psi_{sl} = \psi_{sl_i} + \alpha\, \psi_{det} \tag{2.15b}$$

where α is an empirical constant determined by inspection of published high-order numerical simulations. For the present analysis, $\alpha = 0.5$.

2.3.3 Flow Expansion and Detonation Wave Height

Chapman–Jouguet theory states that the Mach number of the flow immediately behind a detonation wave is unity. Additionally, as previously mentioned, the deto-

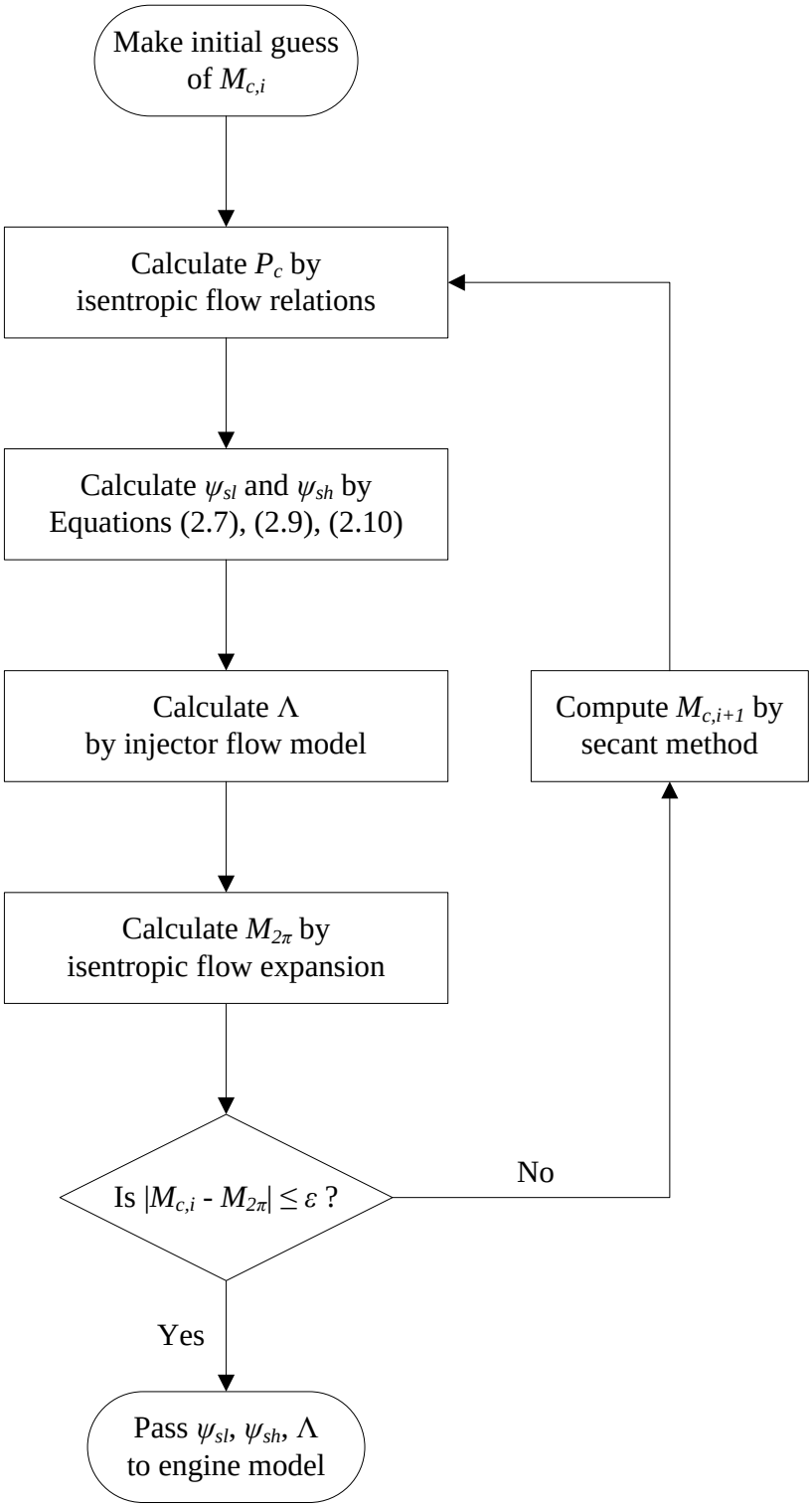

Figure 2.5. Internal flow model flowchart.

nation product expansion region is bounded above by the slipline and below by the injector face and fresh propellant layer, as seen in Fig. 2.6. The area of this region is given by

$$A(\theta) = \delta_a \zeta(\theta) \tag{2.16}$$

where, approximating the propellant injection region as triangular, the expansion area height ζ is

$$\zeta(\theta) = \begin{cases} \Lambda + r_m \theta \tan\psi_{sl} & 0 \leqslant \theta \leqslant \theta_{in} \\ \Lambda + r_m \theta \tan\psi_{sl} - \Lambda \dfrac{\theta - \theta_{in}}{2\pi - \theta_{in}} & \theta_{in} < \theta \leqslant 2\pi \end{cases} \tag{2.17}$$

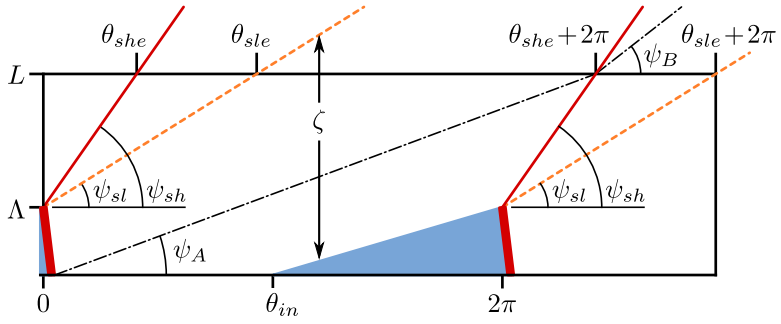

Figure 2.6. Expansion and flow turning nomenclature.

This configuration, of expansion flow bounded on one side by a wall and the other by a fluid boundary, is similar to that seen in an aerospike nozzle [180]. With the detonation wave forming a pseudo-throat and with the area change a known function of θ, the expansion region can be approximated using nozzle flow techniques. Therefore, the compressible flow Mach–area relation can be used to calculate the Mach number at any point in the expansion

$$\left(\frac{A}{A^*}\right)^2 = \frac{1}{M_W^2}\left[\frac{2 + (\gamma - 1)M_W^2}{\gamma + 1}\right]^{(\gamma+1)/(\gamma-1)} \tag{2.18}$$

where the sonic area A^* is the the detonation wave surface area

$$A^* = \Lambda \delta_a \tag{2.19}$$

The expansion area relation in Eq. (2.16) is a function of the detonation wave height, which is itself dictated by the pressure decay inside the annulus—necessitating a numerical scheme to solve for Λ. First, an initial guess was made of the detonation wave height, Λ_i. This sets the pressure distribution in the annulus, and allows the calculation of the injection and choking points θ_{in} and θ_{ch}. The axial injection velocity was then numerically integrated around the annulus, which gives the propellant axial injection distance $l_{inj_z,i}$. Iteration was performed by the secant method until $l_{inj_z,i} = \Lambda_i$ using the recurrence relation

$$\Lambda_{i+1} = \Lambda_i - (\Lambda - l_z)_i \frac{\Lambda_i - \Lambda_{i-1}}{(\Lambda - l_z)_i - (\Lambda - l_z)_{i-1}} \tag{2.20}$$

A flowchart of this scheme is given in Figure 2.7. Convergence is achieved in approximately five iterations.

2.3.4 Exit Flow Angles and Shock Wave Turning

As has been extensively documented in high-order models, a portion of the flow expansion in an RDE recirculates and passes through the oblique shock wave. This causes the flow to turn, and has been observed by Paxson [137] and Nordeen et al. [124] to cause flow reversal in the inertial frame, which counteracts the detonation-induced circumferential velocity component. A model for this flow turning is necessary, but determining the angle at which the recirculating flow impinges on the oblique shock wave requires an approximation of the variation of the flow angle on the exit plane. It is known that flow along the slipline exits the annulus at angle $\psi = \psi_{sl}$ in the nonertial frame, and the angle at which flow impinges upon the shock wave at the

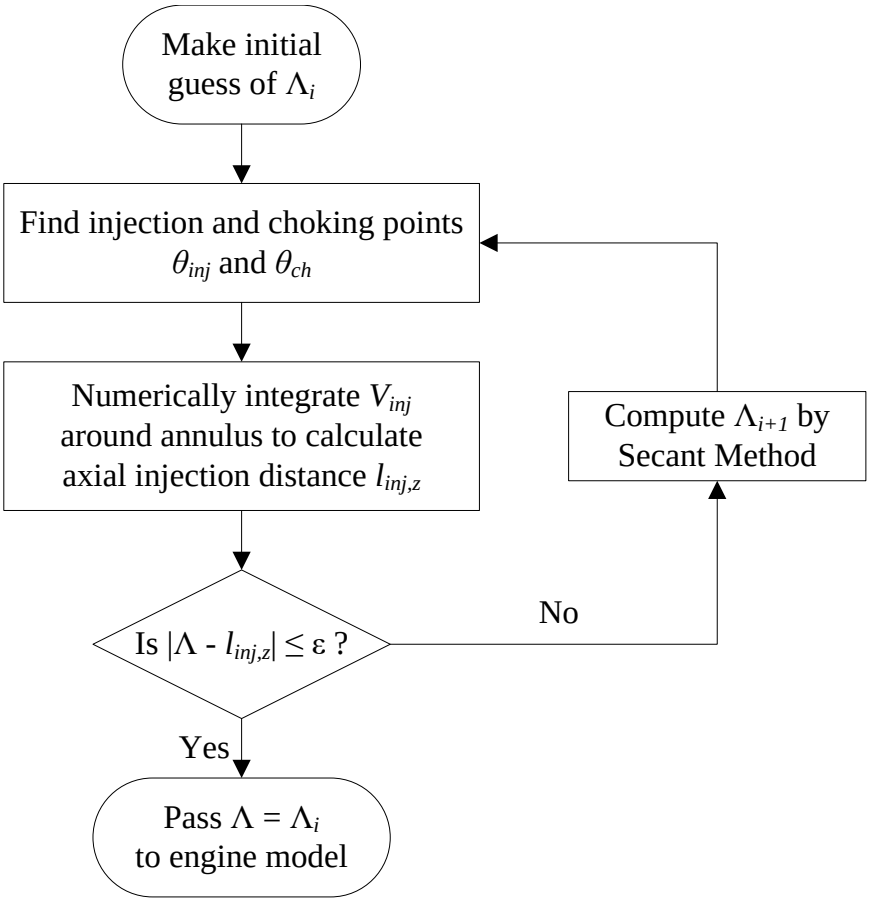

Figure 2.7. Internal flow model flowchart.

point where it exits the annulus can be approximated analytically by a streamline beginning at the base of the detonation wave

$$\psi_A = \tan^{-1}\left(\frac{L}{r_m\left(\theta_{she} + 2\pi\right)}\right) \tag{2.21}$$

where the shock exit point

$$\theta_{she} = \frac{L - \Lambda}{r_m \tan\psi_{sh}} \tag{2.22}$$

is shown in Fig. 2.6. Calculating $\vec{W}_A$, T_A, and P_A by flow expansion, oblique-shock relations are used to calculate the velocity $\vec{W}_B$, temperature T_B, pressure P_B, and angle of the turned flow ψ_B, as well as A^*_B for the turned-flow region.

Properties on the exit plane are determined by considering the expansion flow over the interval $\theta = [\theta_{sle},\ \theta_{sle} + 2\pi]$, where

$$\theta_{sle} = \frac{L - \Lambda}{r_m \tan \psi_{sl}} \tag{2.23}$$

is the point at which the slipline exits the annulus. To calculate the flow expansion past $\theta = 2\pi$, an extension of Eq. (2.17) is required. For $\theta = [2\pi,\ \theta_{sle} + 2\pi]$, the lower bound of the expansion area is approximated by the mean of the shock and slipline angles, and for $\theta = [\theta_{she} + 2\pi,\ \theta_{sle} + 2\pi]$ the upper and lower bounds are the shock wave and slipline, respectively

$$\zeta(\theta) = \begin{cases} r_m \theta \tan \psi_{sl} - r_m (\theta - 2\pi) \tan \frac{1}{2} (\psi_{sh} + \psi_{sl}) & 2\pi < \theta \leqslant \theta_{she} + 2\pi \\ r_m (\theta - 2\pi) (\tan \psi_{sh} - \tan \psi_{sl}) & \theta_{she} + 2\pi < \theta \leqslant \theta_{sle} + 2\pi \end{cases} \tag{2.24}$$

At a given angle θ_i along the exit plane, the Mach-area relation is used to calculate the noninertial Mach number M_{W_i}, which is in turn used to calculate static thermodynamic properties and speed of sound a_i. These are used to calculate the magnitude of the inertial velocity $||\vec{W}_i|| = M_{w_i} a_i$. A flow-angle constraint is applied to this to determine the z- and θ-components W_{z_i} and W_{θ_i}, with the exit angle ψ_{e_i} determined by

$$\psi_{e_i} = \begin{cases} \psi_{sl} + (\theta_i - \theta_{sle}) \dfrac{\psi_A - \psi_{sl}}{(\theta_{she} + 2\pi) - \theta_{sle}} & \theta_{sle} < \theta \leqslant \theta_{she} + 2\pi \\ \psi_B + (\theta_i - \theta_{she} - 2\pi) \dfrac{\psi_B - \psi_{sl}}{\theta_{she} - \theta_{sle}} & \theta_{she} + 2\pi < \theta \leqslant \theta_{sle} + 2\pi \end{cases} \tag{2.25}$$

Finally, once the components of $\vec{W}_{e_i}$ are known, the exit velocity in the inertial frame $\vec{V}_{e_i}$ is calculated by the Galilean transformation, Eq. (2.1).

2.4 Conservation Equations

The control volume analysis begins with the differential, compressible forms of the three conservation equations: continuity, energy, and momentum.

2.4.1 Continuity

In vector notation, the differential form of the continuity equation is

$$\frac{\partial \rho}{\partial t} + \nabla \cdot (\rho \vec{V}) = 0 \tag{2.26}$$

Integrating Eq. (2.26) over the control volume yields

$$\delta_a r_m \left[\int_0^{2\pi} (\rho V_z)_2 \, d\theta - \int_0^{2\pi} (\rho V_z)_1 \, d\theta \right] = 0 \tag{2.27}$$

2.4.2 Energy

Nordeen [21, 83, 123, 124] applied the conservation of rothalpy ("rotating enthalpy") to RDEs with great success. However, it is primarily of interest when analyzing internal flows in the noninertial frame, and is not necessary when considering the control volume as a whole, in the inertial frame. For that, the conventional energy equation is sufficient. In differential form it is

$$\rho \frac{D h_0}{D t} = \frac{\partial P}{\partial t} + \nabla \cdot \left(\boldsymbol{\tau}_{ij} \cdot \vec{V} - \vec{q} + \vec{q}_{det} \right) + \rho \vec{f} \cdot \vec{V} \tag{2.28}$$

where a source term $\vec{q}_{det}$ has been added to account for the internal heat release of the detonation wave. Integrating over the control volume and applying the assumptions from Sec. 2.1, Eq. (2.28) simplifies to

$$\int_S \rho h_0 \vec{V} \cdot \hat{n} \, dS = - \int_S \vec{q} \cdot \hat{n} \, dS + Q_{det} \tag{2.29}$$

Heat losses through the annular walls (S_3 and S_4) are computed by separate heat-transfer analyses and can simply be expressed as Q_3 and Q_4. Since ρ, h_0, and V_z on

the inlet and exit faces are functions only of θ, the surface integrals can be simplified, yielding

$$\delta_a r_m \left[\int_0^{2\pi} (\rho h_0 V_z)_2 \, d\theta - \int_0^{2\pi} (\rho h_0 V_z)_1 \, d\theta \right] = Q_{det} - Q_3 - Q_4 \tag{2.30}$$

2.4.3 Momentum

The differential form of the Navier–Stokes equation is

$$\rho \frac{D\vec{V}}{Dt} = -\nabla \cdot (\boldsymbol{P}_{ij} + \boldsymbol{\tau}_{ij}) + \vec{f_b} + \vec{f} \tag{2.31}$$

Integrating over the control volume $\mathscr{V}$ and simplifying, expressions are derived for the axial and circumferential forces

$$F_z = \delta_a r_m \left[\int_0^{2\pi} \left(\rho V_z^2 + P - P_\infty \right)_2 d\theta - \int_0^{2\pi} \left(\rho V_z^2 + P \right)_1 d\theta \right] \tag{2.32}$$

$$F_\theta = \delta_a r_m \left[\int_0^{2\pi} (\rho V_\theta V_z)_2 \, d\theta - \int_0^{2\pi} (\rho V_\theta V_z)_1 \, d\theta \right] \tag{2.33}$$

where P_∞ is the freestream (back) pressure.

However, it is convention in rocket propulsion contexts to draw the control volume such that mass flux into the system is zero. If the control volume in Figure 2.1 is extended to encompass the propellant plenum (at stagnation conditions), Eqs. (2.32) and (2.33) reduce to

$$F_z = \delta_a r_m \int_0^{2\pi} \left(\rho V_z^2 + P - P_\infty \right)_2 d\theta \tag{2.34}$$

$$F_\theta = \delta_a r_m \int_0^{2\pi} (\rho V_\theta V_z)_2 \, d\theta \tag{2.35}$$

The resultant force in the radial direction F_r is assumed to be negligible.

2.4.4 Performance Parameters

Equation (2.34) represents the thrust, and Eq. (2.35) represents the circumferential force exerted on the control volume due to swirl at the exit plane. Numerical

integration is performed by the trapezoid rule, over the interval $\theta = [0,\ 2\pi]$ on the inlet plane and $\theta = [\theta_{sle},\ \theta_{sle} + 2\pi]$ on the exit plane.

Expansion is assumed to continue beyond the exit plane of the engine. For a given point θ on either the inlet or exit plane, the computation proceeds as follows: first, the expansion area and noninertial Mach number are calculated, followed by (chamber) static temperature, pressure, density, and speed of sound. These are used to determine the injection velocity, pressure, temperature, and density of the injection or exit flow as outlined in Sec. 2.3.

Several additional performance parameters are also calculated. First, the relative ratio between circumferential force and thrust is of importance, and should be as close to unity as possible

$$\Upsilon = 1 - \frac{F_\theta}{F_z} \tag{2.36}$$

Secondly, the resultant torque caused by exit swirl, computed about the mean annular radius

$$\mathcal{T} = r_m F_\theta \tag{2.37}$$

Next, specific impulse is calculated using the thrust and full propellant flow rate $\dot{m}_{inj}$

$$I_{sp_z} = \frac{F_z}{\dot{m}_{inj} g_0} \tag{2.38}$$

However, many RDE studies, including those by Braun et al. [127], Hishida et al. [114], Hayashi et al. [115], Schwer and Kailasanath [135,181], Nordeen et al. [123], and Fievisohn and Yu [132], report fuel-based total specific impulse, instead of (or sometimes in addition to) one using the total propellant flow rate (that is, fuel and oxidizer)

$$I_{sp_f} = \frac{\|\vec{F}_z + \vec{F}_\theta\|}{\dot{m}_f g_0} \tag{2.39}$$

Additionally, while not explicitly performance metrics, several parameters of the RDE are tracked for analysis. These include the detonation wave height, Λ, the injector

condition at $\theta = 2\pi$ (A, B, or C, from Sec. 2.3.1), the propellant flow rate, $\dot{m}_{inj}$, and the mean exhaust flow angle

$$\overline{\psi}_e = \tan^{-1} \frac{\overline{V}_{\theta_2}}{\overline{V}_{z_2}} \tag{2.40}$$

where $\overline{V}_{\theta_2}$ and $\overline{V}_{z_2}$ are the spatially-averaged circumferential and axial velocity components on the exit plane, respectively.

2.5 Results

2.5.1 Design Condition

A baseline design, typical of many small experimental RDEs, was chosen to provide a point from which to vary the design parameters for parametric analysis. The engine has an outer annulus diameter of 100 mm and an inner diameter of 80 mm ($\delta_a = 10\,\text{mm}$, $r_m = 45\,\text{mm}$), and a length of 120 mm. The injector area ratio is 0.50, and propellants are stoichiometric hydrogen and oxygen with plenum stagnation properties of 5 atm and 300 K, injected with zero swirl. Back pressure is 1 atm. The analytical model was run on this design, the results of which are given in Table 2.1.

Table 2.1. Base engine performance

Property	Value
Thrust, F_z	1,890 N
Circumferential force, F_θ	127 N
Torque at mean radius, $\mathcal{T}$	$5.74\,\text{N} \cdot \text{m}$
Relative force ratio, Υ	0.933
Z-specific impulse, I_{sp_z}	313 s
Fuel-based total specific impulse, I_{sp_f}	2,800 s
Detonation wave height, Λ	25.0 mm
Propellant mass flow rate, $\dot{m}_{inj}$	0.617 kg/s
Mean exit swirl angle, $\overline{\psi}_e$	6.73°

This analysis was conducted prior to the implementation of Eq. (2.3) to calculate the detonation wave inclination angle ψ_{det}. For these calculations, the computed oblique shock angles from Sec. 2.3.2 were adjusted by a constant factor of 7°, estimated from the numerical simulations of Nordeen [21] and Fievisohn and Yu [131] (the slipline angle was not adjusted). This yields angles of $\psi_{sh} = 61°$ and $\psi_{sl} = 37°$, almost identical to those observed in the numerical results of Nordeen [21]

Of note is that the model predicts a nonzero circumferential force and therefore allows for a resultant torque on the control volume. The assumption of zero net swirl in the exhaust of an RDE is predicated on the oblique shock wave counteracting the circumferential velocity component on the exit plane of the engine. However, as the present results indicate, this is not uniquely true: variation in a range of design parameters causes the exit velocity and momentum profiles to change, resulting in varying degrees of exit swirl. The exit velocity profile for the baseline design is given in Fig. 2.8; the x-axis has been normalized to set $\theta_{sle} = 0$, but $\theta = 2\pi$ and θ_{sle} are indicated. Flow turning through the oblique shock wave causes reversal in the noninertial frame, as observed in prior numerical models [21, 123, 124, 137]. However, this does not necessarily result in $\overline{V}_{\theta_2} = 0$ or zero net exit momentum. Indeed, as parametric analysis will show, the increase in density through the oblique shock wave results in the $F_\theta = 0$ case occurring separately from the $\overline{\psi}_e = 0$ case. Additionally, as seen in Eq. (2.35), the torque is a function of the product of V_z and V_θ, so that even a small amount of swirl in the inertial-frame exit flow will cause a resultant torque on the control volume. The presence of any nonzero circumferential velocity component represents a twofold performance loss: it results in decreased total thrust, and the resultant torque poses a structural and design challenge, particularly in space applications. As a result, the possibility of engine swirl should be incorporated into engine design studies, and methods of deswirling employed if necessary.

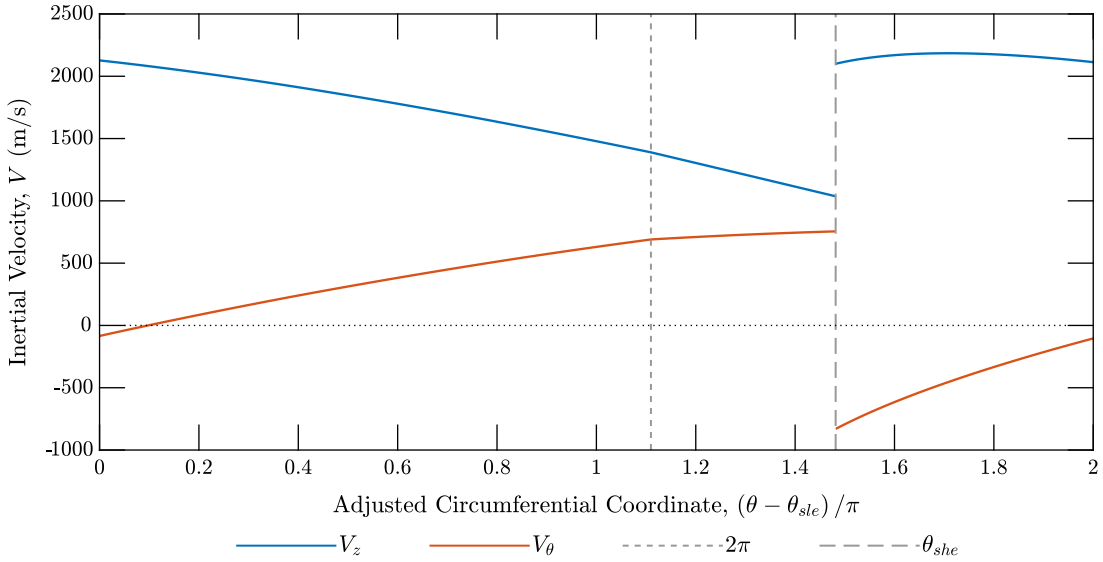

Figure 2.8. Exit-plane inertial velocity profile of baseline design.

2.5.2 Parametric Analysis

Parametric analyses consisted of sweeps performed on six engine design parameters: propellant plenum pressure $P_{0_{inj}}$ and temperature $T_{0_{inj}}$, injection swirl angle ψ_{inj}, annulus width δ_a and length L, and equivalence ratio ϕ. The range of each is given in Table 2.2. For all cases, the propellant was taken as hydrogen and oxygen, and all cases were performed without coolant flow (the adiabatic wall condition was assumed, $Q_3 = Q_4 = 0$). The detonation wave was assumed to rotate in the $-\theta$-direction.

Five sweeps of 101 data points each were calculated, and carpet plots created, for each pair of design parameters. The variation in performance for each parameter (except $P_{0_{inj}}$ and $T_{0_{inj}}$) was investigated against propellant plenum stagnation pressure; pressure is plotted against plenum stagnation temperature. Additionally, to investigate the effect of various engine size parameters, annulus length is also plotted against annulus width.

Table 2.2. Ranges of engine design parameters

Property	Range
Propellant plenum pressure, $P_{0_{inj}}$	2 – 20 atm
Propellant plenum temperature, $T_{0_{inj}}$	250 – 400 K
Propellant swirl angle, ψ_{inj}	-50 – $+50°$
Annulus width, δ_a	1 – 50 mm
Engine length, L	50 – 300 mm
Equivalence ratio, ϕ	0.75 – 1.50

Figure 2.9 shows the variation in performance for varying propellant plenum stagnation pressure and temperature. As expected, higher propellant pressures and lower temperatures are beneficial to performance. Thrust and torque scale linearly with $P_{0_{inj}}$, but $\dot{m}_{inj}$ does not, resulting in specific impulses which appear to asymptote to maxima as $P \to 20\,\text{atm}$. This same asymptotic behavior is also seen in the force ratio Υ. Higher propellant pressures also result in a lower value of the exit swirl angle, but the effect is not a strong one; over the range of pressures tested, exit swirl decreases an average of 0.34°. Propellant temperature has a much lower effect on performance than pressure (particularly for torque), and in all cases, increased propellant temperature decreases performance: it increases torque and mean exit swirl angle and decreases thrust, specific impulse, and force ratio. This is due to several factors: for a given value of $P_{0_{inj}}$, increased $T_{0_{inj}}$ decreases the both the pressure and temperature across the detonation wave, as well as the Chapman–Jouguet detonation velocity and the mass flow rate of propellants into the chamber. These all contribute to decreased RDE performance, and indicate that whenever possible, a lower propellant temperature should be used.

Variation in performance for injector swirl angle is shown in Fig. 2.10. Thrust is symmetrical about and maximum at $\psi_{inj} = 0°$, but paradoxically, torque decreases

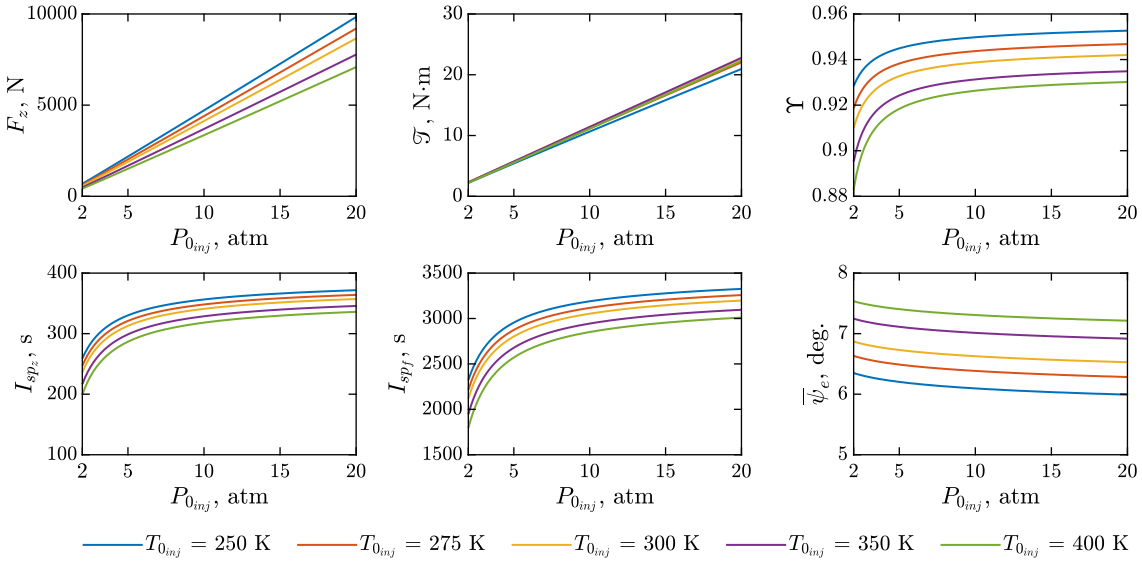

Figure 2.9. RDE parametric performance, injector stagnation pressure $P_{0_{inj}}$ vs. injector stagnation temperature $T_{0_{inj}}$.

with increased injection swirl. This is not due to the effect of circumferential velocity: $\overline{V}_{\theta_2}$ is maximized at $\psi_{inj} = \pm 40°$, with the zero-injection-swirl condition representing a relative minimum. However, swirl in the injectors, positive or negative, increases the expansion inside the annulus, which results in a marked decrease in $\overline{\rho}_2$ and with it the exit circumferential momentum. This increased expansion also results in lower chamber pressures and thus increased propellant mass flow rates, meaning that the $\psi_{inj} = 0°$ condition maximizes specific impulse. These results indicate that for maximum propulsive performance, zero injector swirl is desirable. However, if reduced torque is desired, some value of injection swirl may be beneficial. There may also be some other potential uses of swirled injection, such as biasing the injection flow to force the detonation wave to rotate in a proscribed direction (a technique successfully demonstrated by Braun et al. [117]), but this will always come with a commensurate decrease in thrust and I_{sp}.

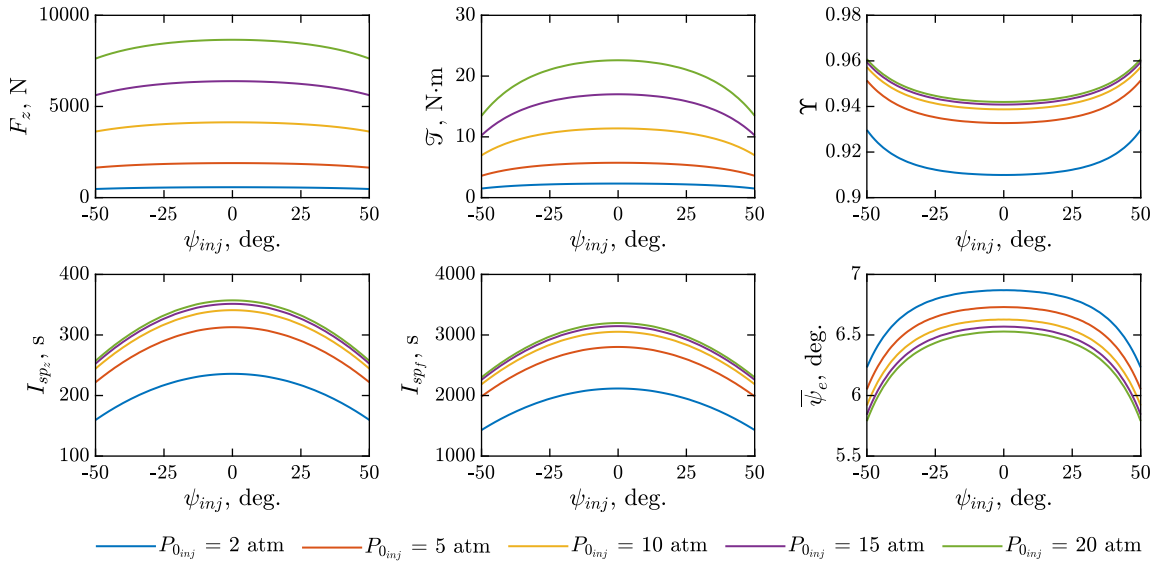

Figure 2.10. RDE parametric performance, injector swirl angle ψ_{inj} vs. injector stagnation pressure $P_{0_{inj}}$.

Annulus width results are shown in Fig. 2.11. Thrust and torque increase, but not linearly with each other: force ratio increases, indicating that thrust increases at a greater rate. Higher injection pressures increase Υ, especially for narrower annuli. Propellant mass flow rate and thrust scale nearly identically with each other, so increases in annulus width result in much less dramatic gains in specific impulse: increasing δ_a from 1 to 50 mm results in a 100-fold increase in thrust but an increase in I_{sp_f} of only about 60 s. Therefore, for a given engine diameter, a wider annulus is generally preferred to a narrower one.

Performance for varying annulus lengths is shown in Fig. 2.12. Thrust and specific impulse decrease with increasing L. This is due to the effect of increased expansion on both density and pressure: as the expansion area increases with increasing L, $\overline{P}_2$ and $\overline{\rho}_2$ both decrease, resulting in a decrease in both the both the momentum and pressure thrust terms; the latter much more than the former. However, the same

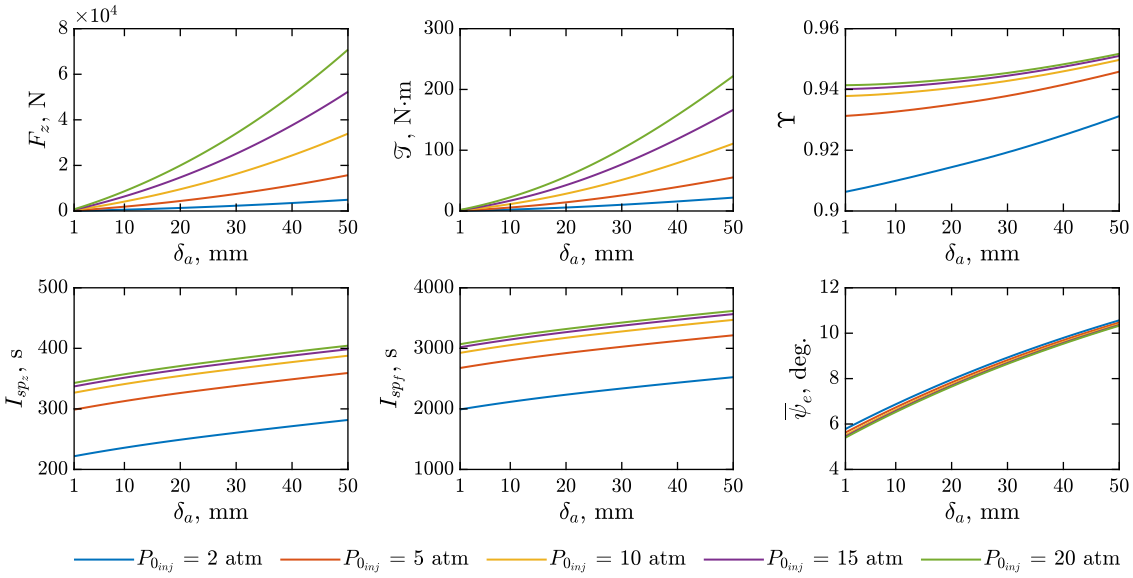

Figure 2.11. RDE parametric performance, annulus width δ_a vs. injector stagnation pressure $P_{0_{inj}}$.

is not true for F_θ. As annulus length increases, a greater percentage of the mass flow passes through and is turned by the oblique shock wave, resulting in a torque-maximum condition between $L = 105$ and 110 mm (increasing slightly with increasing injection pressure). Below this point, flow turning through the oblique shock wave is insufficient to counteract the additional velocity due to flow expansion; above it, increased L results in sufficient turning to reduce torque.

Force ratio is maximized for very short annuli and very long ones, with a relative minimum between $L = 135$ and 168 mm (asymptotically decreasing with increasing injection pressure). As annulus length has no effect on propellant mass flow rate, increased L also decreases specific impulse. These results indicate that shorter annuli are preferred to longer ones. There is an additional benefit to this: engine length (and other size parameters such as δ_a) are tied closely to mass. While investigations of weight on the RDE is beyond the scope of this model, in general, for a given

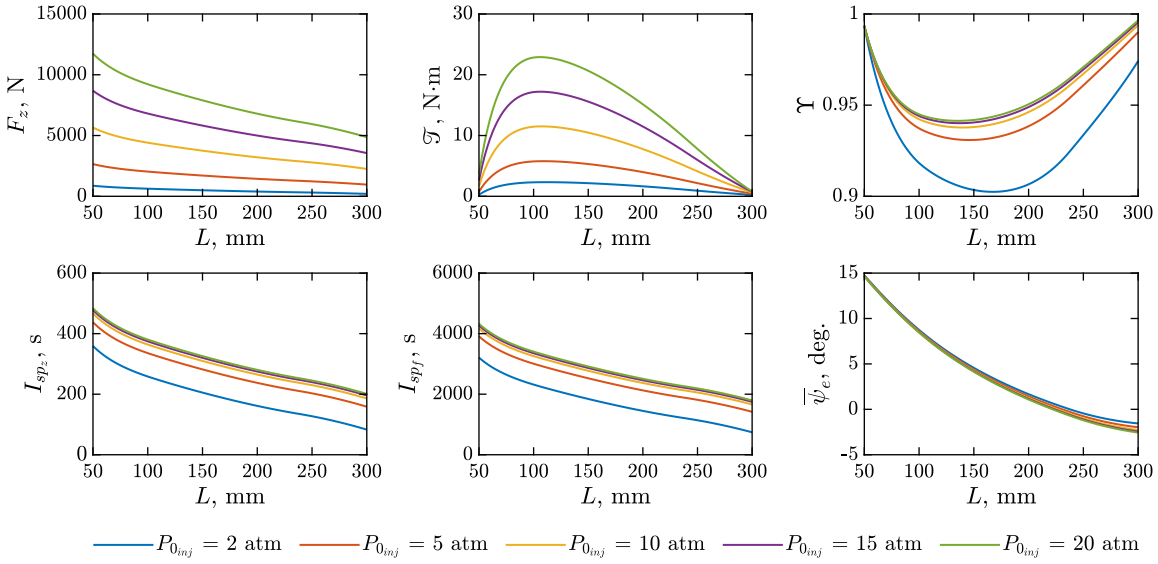

Figure 2.12. RDE parametric performance, annulus length L vs. injector stagnation pressure $P_{0_{inj}}$.

performance requirement, reduced engine mass is advantageous. Additionally, the exit flow remains underexpanded ($\overline{P}_2 > 1\,\text{atm}$) for the vast majority of engine lengths tested (indeed, for the vast majority of all parametric sweeps in the present analysis) for $P_{0_{inj}} > 2\,\text{atm}$, indicating that RDEs can derive significant benefit from integration with nozzles. Finally, it is worth noting that the flow-turning model used in the present results is only valid until the point at which the oblique shock and slipline intersect. This point can be determined analytically by

$$L_{max} = \Lambda + 2\pi r_m \frac{\tan\psi_{sh}\tan\psi_{sl}}{\tan\psi_{sh} - \tan\psi_{sl}} \tag{2.41}$$

For the design engine (Sec. 2.5.1), with $\psi_{sh} = 61°$, $\psi_{sl} = 37°$, and $\Lambda = 25.04\,\text{mm}$, this maximum length is 390.9 mm.

It is also worthwhile to understand the effect of equivalence ratio on performance. The results of this analysis are given in Fig. 2.13. Notably, it can be seen that, excepting specific impulse, any equivalence ratio effects are minimal compared to

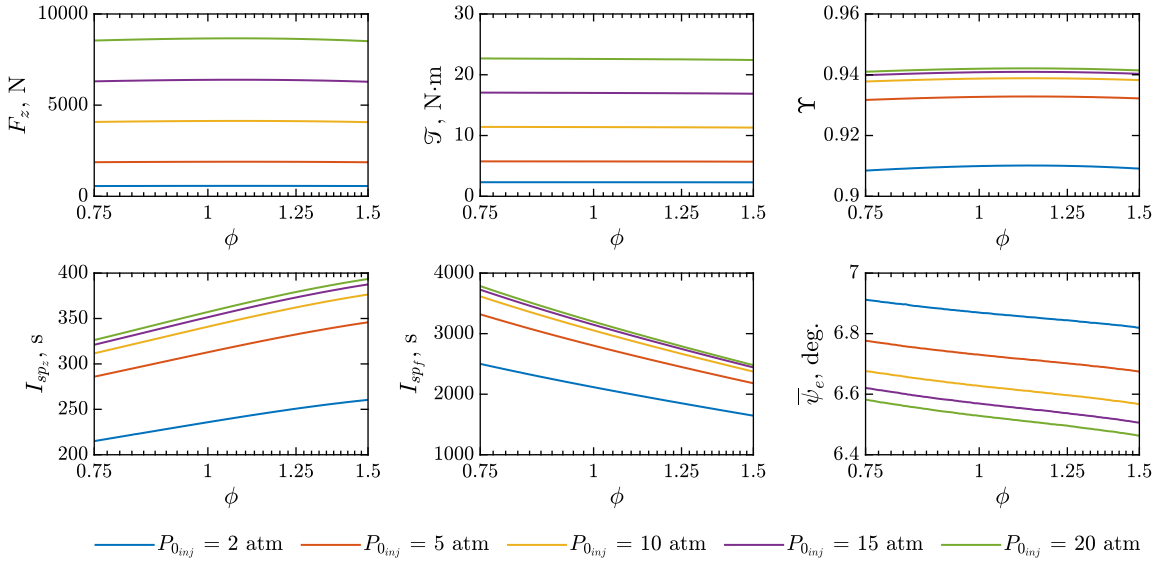

Figure 2.13. RDE parametric performance, equivalence ratio ϕ vs. injector stagnation pressure $P_{0_{inj}}$.

the effect of propellant stagnation pressure. There is some variation, though: thrust is maximized at an equivalence ratio of approximately 1.08, whereas torque is almost completely unaffected (at a given pressure, total change in $\mathcal{T}$ over the range of ϕ is approximately 1 percent). Force ratio is maximized at approximately $\phi = 1.14$; exit swirl angle is is minimized for fuel-rich mixtures, but the variation in $\overline{\psi}_e$ is only 0.107° on average. The most significant effects of equivalence ratio are on I_{sp}. If the full propellant mass flow rate (including both fuel and oxidizer) is considered, specific impulse is maximized for fuel-rich mixtures; if only the fuel flow is considered, the maximum is for fuel-lean mixtures. Which is preferred in an analysis will likely depend largely on the mode the engine will operate in: engines operating in rocket mode (such as the one considered in this analysis), which must carry fuel and oxidizer onboard, will likely prefer to consider I_{sp_z} and are best served by a fuel-rich propellant mixture. On the other hand, airbreathing RDEs, which can use atmospheric oxygen

and are constrained only by fuel flow, will certainly prefer to consider I_{sp_f} and are best served by fuel-lean mixtures. There are heat transfer factors for equivalence ratio as well: fuel-lean detonations have a lower heat release, which aids somewhat in the active cooling design problem.

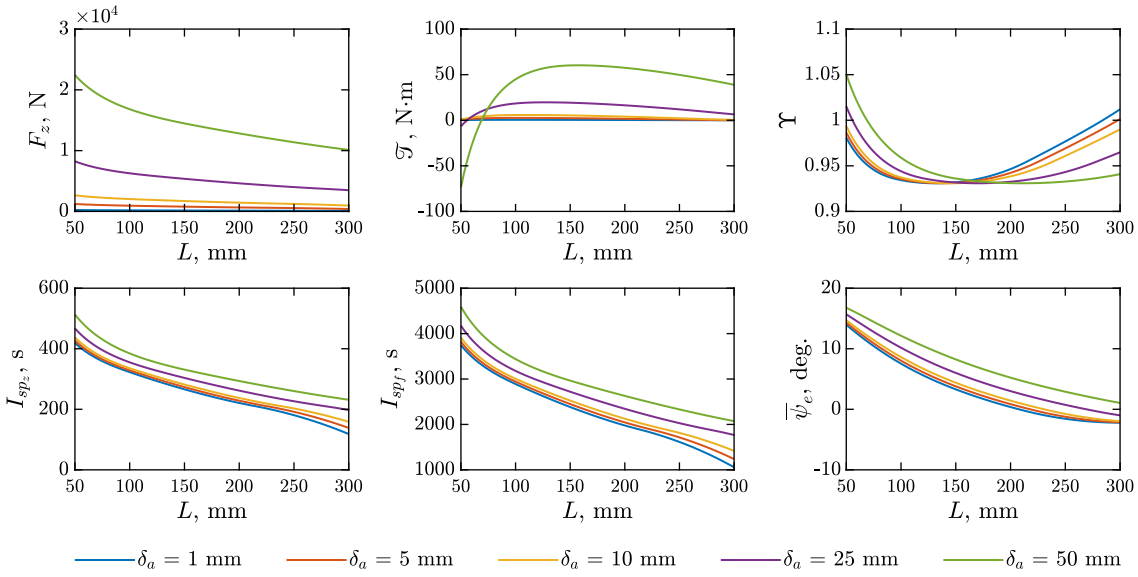

Figure 2.14. RDE parametric performance, annulus length L vs. annulus width δ_a.

Finally, it is of interest to investigate the effect of parametric variation of the two engine size parameters: annulus width δ_a and length L. These results are shown in Fig. 2.14. Shorter and wider annuli have greater thrust and specific impulse, but of particular interest are the results in torque: there are configurations which show zero net torque, especially for very short and very wide annuli. For $\delta_a = 50\,\text{mm}$, this occurs at $L \approx 68.9\,\text{mm}$; for $\delta_a = 25\,\text{mm}$, it occurs at $L \approx 55.1\,\text{mm}$. Curves of Υ indicate a zero-F_θ condition for narrower annuli at values of L slightly below 50 mm. Very narrow annuli also show zero-torque results for very large values of L: for $\delta_a = 5\,\text{mm}$, this condition occurs at $L \approx 298.3\,\text{mm}$, increasing with increasing annulus width.

Therefore, while wider and shorter annuli give better absolute performance, there exists a zero-net-torque condition which can be designed for.

2.5.3 Comparison to Existing Models

The most commonly-reported performance result in the literature is specific impulse, usually fuel-based I_{sp}. Table 2.3 gives the approximate rage of specific impulses reported by a variety prior models: Braun et al. [126, 127] and Fievisohn and Yu [132, 133] are low-order models, and Hayashi et al. [115], Schwer and Kailasanath [135], and Zhdan et al. [97] presented numerical results. None, however, are control-volume based, and none explicitly consider engine swirl in their computations. (Note that Zhdan reported specific impulse in meters per second; it has been converted to seconds by dividing by g_0.)

Table 2.3. Summary of results

Authors	Propellants	Reported	Specific Impulse (s)
Mizener and Lu [182]	H_2 – O_2	I_{sp_f}	2,000 – 3,500
		I_{sp_z}	250 – 420
Braun et al. [126, 127]	H_2 – Air	I_{sp_f}	2,000 – 3,500
Hayashi et al. [115]	H_2 – O_2	I_{sp_f}	2,300 – 3,500
		I_{sp_z}	360 – 380
Schwer and Kailasanath [135]	H_2 – Air	I_{sp_f}	2,900 – 5,400
Zhdan et al. [97]	H_2 – O_2	I_{sp_z}	250 – 330
Fievisohn and Yu [132, 133]	C_2H_4 – O_2	I_{sp_f}	2,000 – 5,200

Fuel-based specific impulses predicted in the present model are in the range of 2,000–3,500 s for most configurations (excepting very short and very wide annuli, which extend the upper limit into the 4,500 s range). For mixture-based specific impulse, the range is 250–420 s. Both compare favorably to those in the above studies,

in particular I_{sp_f}. Moreover, the present model is significantly more flexible than full numerical simulations at a substantial computational savings.

2.5.4 Limitations of Low-Order RDE Analysis

As with all low-order and control-volume analyses, there are limitations to this model. A number of phenomena known to be present in RDE flows are neglected, including viscosity, turbulence, contact surface burning, incomplete combustion, injector lag due to backflow of detonation products, heat transfer losses, and radial effects. The oblique shock and slipline were assumed to be straight. For the former, this is a reasonable assumption, especially for shorter annulus lengths: the curvature seen in the simulations is slight, and the shock is approximated well by a straight line. However, the slipline curvature is more pronounced, and simulations show a Kelvin–Helmholtz instability forming along it, which cannot be properly accounted for in control-volume analysis. The linear approximation also tends to slightly underestimate the expansion area immediately behind the detonation wave, and slightly overestimate the shock and slipline exit angles. Combined, these tend to somewhat overpredict the exit angles of the noninertial flow and therefore swirl in the inertial frame. Additionally, the torque computed here is the resultant forces on the control volume itself. The mechanism for transferring this force to the surrounding system is not explored in this model. A further consideration is that the present results consider the rocket mode only, and omit mass flow into the control volume. In airbreathing applications, the axial and circumferential momenta of the inlet flows have significant effects on thrust, torque, and specific impulse. These effects are beyond the scope of this analysis, but are important topics for future investigation into the operational capabilities of RDEs.

It is also worth noting that the system described by this model—a single detonation wave with an idealized flowfield, rotating in a fixed direction around the annulus—represents a hypothetical "worst-case" scenario for torque. The model does not account for the experimentally-observed tendency for the detonation wave to split into multiple waves in larger annuli and at higher injection pressures/propellant mass flow rates, or of the so-called "slapping" mode of detonation propagation in RDEs (whereby an even number of detonation waves propagate around the annulus in opposite directions, likely producing no net swirl in the exhaust flow). As with all low-order analyses, once a broader range of experimental data is available, coefficients can be calculated and applied to the model or its output to bring its results more in line with observed performance, enhancing its predictive capabilities.

CHAPTER 3

APPLICATION OF THE ANALYTICAL MODEL: RDE–WAVERIDER INTEGRATION

While rocket-mode applications represent the bulk of RDE research to date, the RDE has drawn interest in air-breathing applications as well. Indeed, this promise has led to active research into the RDE as a cruise missile propulsion system [120,183].

The study outlined in this chapter was performed in collaboration with Dr. Patrick E. Rodi, combining his model for generating waverider forebodies by the osculating flowfield method with a modified version of the low-order rotating detonation engines outlined in Ch. 2. The study focuses on aspects of engine/airframe integration and performance interactions for integrated RDE–waverider systems. Parametric studies were performed to investigate a range of OFWR forebody and RDE engine design parameters on propulsive performance of waverider-RDE vehicles and to determine first-order descriminators affecting integrated performance. Sections dealing with waveriders (3.1, 3.2, 3.2.2, and the first paragraph of 3.8) were primarily authored by Dr. Rodi; sections dealing with rotating detonation engines and overall performance were primarily authored by myself. Section 3.7 was jointly authored.

3.1 Some Brief Notes on Waveriders

Air-breathing propulsion at hypersonic Mach numbers has received much attention over the years. Such propulsion systems generally focus upon highly-integrated scramjets; recent flight test examples include the X-43 and X-51A. Airframe–propulsion integration is a key design consideration for airbreathing hypersonic vehicles, in

which the forebody functions as part of the inlet of the propulsion system. Such an integrated scramjet is illustrated in Fig. 3.1, where the forebody compression surface processes the air being fed into the engine. In the current work, this forebody compression surface is a waverider geometry. In addition to providing compression, the forebody must also have good aerodynamic and volumetric properties to maximize overall vehicle performance. Investigations of overall performance characteristics have been made using a variety of inlet geometries over a range of conditions [184–186].

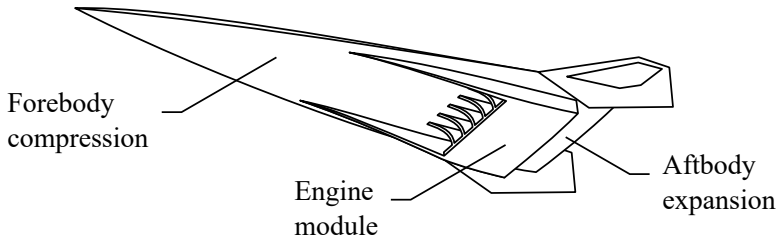

Figure 3.1. Hypersonic vehicle with an airframe-integrated air-breathing propulsion system, adapted from [187].

The related pursuit of high lift-to-drag ratio ($\mathscr{L}/\mathscr{D}$) supersonic/hypersonic bodies has been underway for decades. By taking into account the hyperbolic nature of the supersonic inviscid flowfield during the design process, vehicle aerodynamic performance can be greatly increased. One such utilization of this approach is in waverider design. By utilizing body shapes created from known supersonic flowfields, waveriders effectively increase the lift generated from a supersonic vehicle by riding the shock wave that the vehicle itself has created. This leading shock wave is attached to the leading edge of the body, preventing spillage from the high-pressure lower surface of the vehicle to the low-pressure upper surface, and thereby reducing the induced drag [188]. The combination of increased aerodynamic performance, decreased flow spillage, and shock-induced compression makes waveriders a good choice

for scramjet-powered vehicles, wherein the waverider forebody also functions as part of the engine inlet.

Various waverider concepts have been developed since the 1950s [189–191]. The conical waverider method has been extensively developed [192, 193] for axisymmetric shock shapes; however limits to vehicle $\mathscr{L}/\mathscr{D}$ ratios exist with this approach. To further increase the $\mathscr{L}/\mathscr{D}$ of waveriders at useful lift coefficients, the osculating cones method was developed. This approach permits a more general definition of the possible shock wave shapes, yielding a significant improvement in waverider $\mathscr{L}/\mathscr{D}$ [194–196]. A recent evolution of the osculating cones method is the osculating flowfield method [197]. Both methods employ a series of planes that are created normal to the local shock wave shape defined at the trailing edge of the waverider geometry, but the osculating flowfield method improves performance and design flexibility by permitting flowfields from geometries beyond simple right angle-angle cones. Vehicles generated with the osculating flowfield method have demonstrated modestly superior $\mathscr{L}/\mathscr{D}$ performance over those created using the osculating cones method [198], with additional improvements in volumetric efficiency, trimmed $\mathscr{L}/\mathscr{D}$ ratio, and delayed boundary layer transition.

Considerations for a forebody design as part of a high-speed, air-breathing propulsion system include inlet mass capture, compression efficiency, inlet contraction ratio, inlet flow distortion, flow spillage, boundary-layer state, and flow separation. Such factors were explored using osculating flowfield-based waverider (OFWRs) forebodies in [199]. The forebody also influences overall vehicle design through propulsion component size and weight, propulsion system packaging, angle-of-attack/sideslip performance sensitivities, longitudinal stability, and lateral/directional stability. It can be noted here that the integration of ramjets and scramjets onto high-speed vehicles is complex, involving a variety of potentially conflicting requirements such as propul-

sion efficiency, aerodynamic performance, thermodynamic balance, and structural loading [184, 200, 201].

3.2 OFWR Forebody Modeling

In the osculating flowfield method, a series of "power-law body"-based flowfields is employed on each osculating plane, where the local power-law body radius r is a function of position along the body defined by

$$\frac{r}{r_b} = \left(\frac{x}{L}\right)^n \tag{3.1}$$

where r_b is the radius of the power-law body at its base, x is the vehicle axis measured from the nose, L is the total forebody length, and n is the exponent in the power-law body expression. Typically, the exponent varies between $0.75 \leq n \leq 1.1$. (Note that a conical geometry is produced when $n = 1$.) A power-law body-based flowfield was selected for use on the osculating planes in the method due to the pressure drag reduction observed in power-law bodies when compared to cones [189, 190]. Much of this pressure drag reduction benefit can now be incorporated into waveriders to improve the lift-to-drag ratio.

The forebody cone angle θ_{cone} can vary across the span of the vehicle, using the effective shock wave angle β_{eff} to define the streamwise distance between the leading edge and the traces in the waverider baseplane. The local surface turning angle at any point x on an osculating plane

$$\theta_s = \tan^{-1}\left[n \sin\theta_{cone}\left(\frac{x}{L}\right)^{n-1}\right] \tag{3.2}$$

is derived from Eq. (3.1) [199] and is used to define the initial turning angle of the flow at the leading edge, along with the final turning at the rear of the osculating plane (that is, just before the cowl shock). To minimize total pressure losses due

to the initial shock at the leading edge, a small initial turning angle is desired. To determine this angle, x/L is set to a small value and Eq. (3.2) is used to generate the local turning. For non-conical bodies ($n \neq 1$), x/L must have values very close to 0.0 to produce the desired small initial turning angles. For a physically realistic example, a 1 in radius leading edge on a 100 ft long osculating plane, $x/L = 8.33 \cdot 10^{-4}$. For this value of x/L, and with $\theta_{cone} = 11°$ and $n = 1.1$, the initial flow turning angle $\theta_s = 5.90°$. Therefore, this initial turning, and the shock wave generated at the freestream Mach number to induce it, are calculated and used to define the air properties entering the engine. Local air properties just downstream of the leading edge are calculated using the initial turning angle for the given osculating plane using the Rankine–Hugoniot relations.

Downstream of the leading edge, the flow is then considered to be turned isentropically to the turning angle at the downstream end of the osculating plane, immediately before the engine. At $x/L = 1$ for this geometry, the final flow turning angle is $\theta_s = 11.85°$. This flow is then turned back to the freestream direction by an oblique shock wave, resulting in the conditions entering the engine. This flowfield model is sketched in Fig. 3.2. In this study, any flowfield non-uniformities normal to the forebody surface have been ignored.

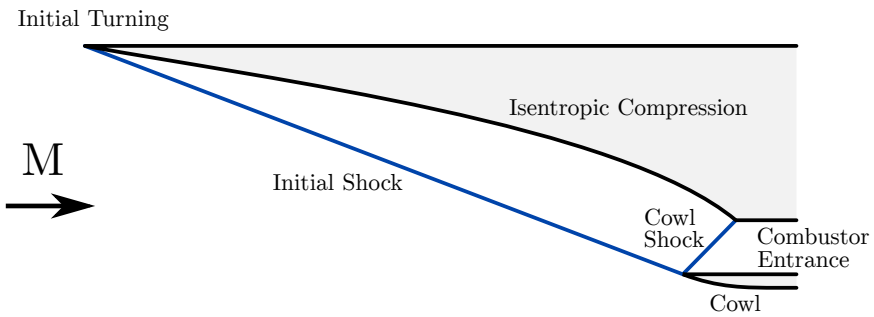

Figure 3.2. Assumed forebody flowfield [199].

3.2.1 Mach Number Limits

For generation of the RDE flowfield input variables, freestream conditions are chosen to match the dynamic pressure $\overline{q}$ of 1,000 psf (47.88 kPa). This value of dynamic pressure is commonly used in air-breathing aerospace vehicle design. To quantify sensitivities to freestream condition, input variables at $\overline{q} = 500$ psf (23.94 kPa) and 1,500 psf (71.82 kPa) are also calculated. However, it remains to determine the incoming Mach numbers to pair with these dynamic pressures.

A key consideration for RDE operation is that the propellants must not ignite (that is, deflagrate) prior to encountering the detonation wave. The autoignition characteristics of flowing gaseous mixtures are complex and depend on several factors including fluid velocity, density (particularly in the boundary layer), the wall temperature, and the stagnation temperature [202]. A full investigation of these factors is beyond the scope of this analysis. For this low-order, inviscid analysis, the autoignition condition is approximated as the stagnation temperature of the flow at the RDE inlet, $T_{0_{inj}}$. As stagnation temperature is constant through a shock wave, the temperature at the RDE inlet is only a function of freestream Mach number and dynamic pressure, and not the inlet design. Autoignition temperatures (AITs) for some selected fuels ($P = 1$ atm, $\phi = 1$) are given in Table 3.1. These temperatures are only very weakly dependent on pressure [202–204]; propellant composition (fuel, oxidizer, equivalence ratio) is the primary driver of autoignition temperatures.

Using this condition, we observe that $T_{0_{inj}} > 900$ K for all of these cases, implying that $M \geq 4$ is unsuitable for detonation applications. A freestream Mach number of 3 represents a viable condition, with $T_{0_{inj}}$ between 606.6 K at $\overline{q} = 1{,}500$ psf and 613.1 K at $\overline{q} = 500$ psf. The case of $M = 3.5$ may also represent a viable option: $T_{0_{inj}}$ is between 747.4 K at $\overline{q} = 1{,}500$ and 1,000 psf and 762.3 K at $\overline{q} = 500$ psf. These are similar to or slightly above the autoignition temperatures of most hydrocarbon

Table 3.1. Autoignition temperatures of selected fuels

Name	Formula	AIT Range (K)	Reference
Hydrogen	H_2	773–793	[203]
Methane	CH_4	810–905	[205]
Propane	C_3H_8	739–766	[205]
Ethylene	C_2H_4	723–763	[206]
Methanol	CH_3OH	698–715	[207]
JP-8		500–550	[208]

fuels, but with consideration of ignition delay times and careful design, an RDE can certainly be constructed such that the detonation wave arrives before the propellants autoignite. To attempt to better quantify this autoignition limit under this constraint, the Mach numbers at which the freestream stagnation pressure reaches the autoignition temperature (using the minimum of the AIT range in Table 3.1 and the 1976 U.S. Standard Atmosphere [175]) have been calculated; these are given in Table 3.2. Additionally, as the autoignition temperature appears to decrease with increasing hydrocarbon molecular mass, operation with more practical jet fuels may be limited to Mach numbers less than 3.

Table 3.2. Maximum freestream Mach number at lower autoignition limit of selected fuels

	Dynamic pressure, $\overline{q}$		
Fuel	500 psf	1,000 psf	1,500 psf
Hydrogen	3.53	3.58	3.58
Methane	3.65	3.69	3.70
Propane	3.43	3.47	3.47
Ethylene	3.34	3.38	3.38
Methanol	3.29	3.33	3.33
JP-8	2.55	2.56	2.56

3.2.2 Forebody Performance Models

To achieve subsonic flow into the RDE, the flowfield model in Fig. 3.2 was modified to include a normal shock wave at the conditions behind the cowl shock. This approach is known as Performance Model #1 and is illustrated in Fig. 3.3. The greatest performance losses with this approach occur in the post-cowl normal shock, due to the high local Mach number before this shock wave.

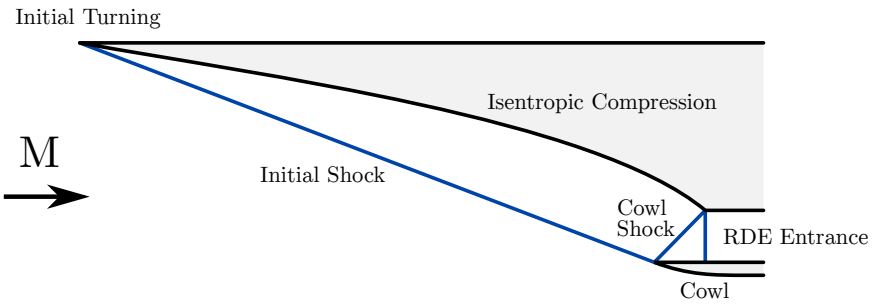

Figure 3.3. Model #1 flowfield.

A parametric sweep of typical osculating flowfield waverider forebodies was made using this model at freestream Mach numbers of 3 and 3.5, assuming $\gamma = 1.4$. The total pressures behind the final normal shock, normalized by the freestream total pressure, are shown in Figs. 3.4 and 3.5. These data were calculated by using the Rankine–Hugoniot equations across the shock waves present for each waverider geometry. For every case, the initial shock, the flow angle before the cowl shock, the cowl shock angle, and the strength of the normal shock before the RDE were uniquely calculated. The forebody cone angle was varied from 5° to 8° for $M = 3$ and from 5° to 9° for $M = 3.5$; the power-law exponent n varied from 0.75 (convex) to 1.1 (concave).

A number of observations can be made from these results. Most obvious is the overall low final total pressure at both Mach numbers. At Mach 3, the best

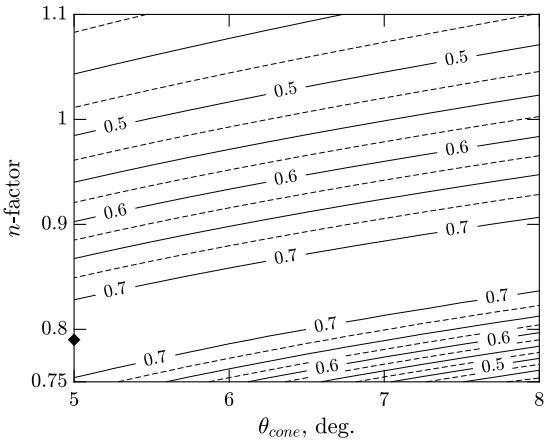

Figure 3.4. Total pressure ratio for model #1 at M = 3.

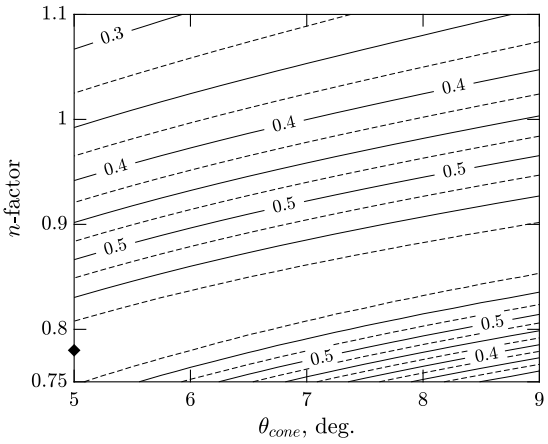

Figure 3.5. Total pressure ratio for model #1 at M = 3.5.

performing Model #1 forebodies have a total pressure ratio of approximately 0.72, found from numerous configurations in a swath from $\theta_{cone} = 5°$ and $n = 0.79$, to $\theta_{cone} = 8°$ and $n = 0.87$. At Mach 3.5, the best performing Model #1 forebodies have a lower total pressure ratio of approximately 0.59, for configurations from $\theta_{cone} = 5°$ and $n = 0.78$, to $\theta_{cone} = 8°$ and $n = 0.88$. These results for the Model #1 inlet model are consistent with the isentropic compression with a single turning cowl shock performance reported in [209].

In an effort to improve inlet pressure recovery, the flowfield model in Fig. 3.2 was modified to include a crossing shock inlet between the cowl shock and the normal shock before the RDE. This model is known as Performance Model #2, and is shown in Fig. 3.6. As was conducted with Performance Model #1, a parametric sweep of typical osculating flowfield waverider forebodies was made using Performance Model #2 at freestream Mach numbers of 3 and 3.5. The total pressures for the Model #2 inlet behind the final normal shock, normalized by the freestream total pressure, are

shown in Figs. 3.7 and 3.8. As for Model #1 data, the forebody cone angle was varied from 5° to 8° ($M = 3$) or 9° ($M = 3.5$), with the n-factor varied from 0.75 to 1.1.

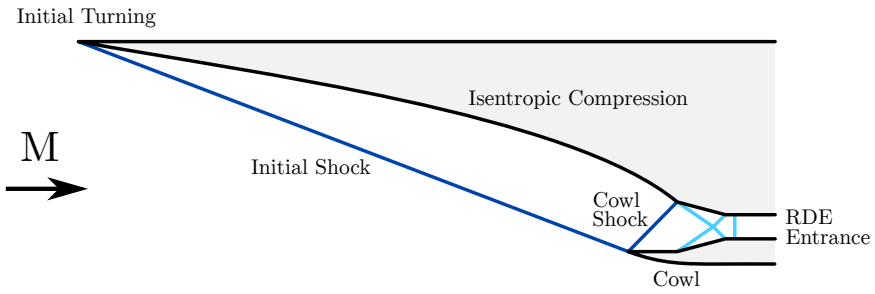

Figure 3.6. Model #2 flowfield.

As with the Model #1 configurations, these data were calculated by using the Rankine-Hugoniot equations across the specific shock waves present for each waverider geometry. In a number of extreme cases with very blunt geometries (low values of n), a solution using this model was not possible due to shock wave detachment at the low Mach numbers within the crossing shock inlet. These cases were excluded, and are shown as gray regions in Figs. 3.7 and 3.8. The additional oblique shock waves significantly increase the total pressure of the flow entering the RDE. At Mach 3, the best performing Model #2 forebodies have a total pressure ratio of approximately 0.88, found along a region from $\theta_{cone} = 5°$ and $n = 0.86$, to $\theta_{cone} = 8°$ and $n = 0.95$. At Mach 3.5, the best performing forebodies have a lower total pressure ratio of approximately 0.78, for configurations from $\theta_{cone} = 5°$ and $n = 0.84$, to $\theta_{cone} = 9°$ and $n = 0.94$. These results for the Model #2 inlet model are consistent with performance result for similar inlets in [210]. Due to the substantially superior pressure recovery, Model #2 was selected as the inlet design for all further analysis.

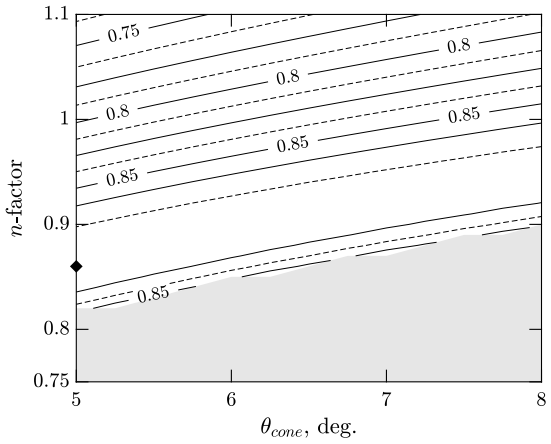

Figure 3.7. Total pressure ratio for model #2 at M = 3.

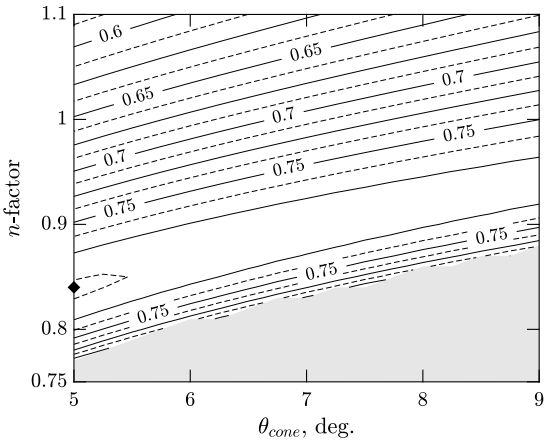

Figure 3.8. Total pressure ratio for model #2 at M = 3.5.

3.3 Model Interactions

The challenge of integrating a high-speed air-breathing propulsion system with an aircraft vehicle increases with Mach number [211]. In the current work, the integrated system performance is predicted by employing separate forebody performance and RDE performance models. The flowfield exiting the forebody model defines the inflow conditions (stagnation pressure $P_{0_{inj}}$ and stagnation temperature $T_{0_{inj}}$) for the RDE model. No additional interactions between these two components are modeled. At the entrance to the RDE, the propellant mixture is assumed to consist of a stoichiometric mixture of fuel and air; the effects of mixing are beyond the scope of this analysis.

3.4 Modifications to the Rotating Detonation Engine Model

This study employs a version of the low-order analytical performance model for a rotating detonation engine outlined in Ch. 2. However, some modifications were necessary to accommodate the airbreathing nature of the study. The most significant

difference in the analysis was the definition of the control volume for determining performance parameters: airbreathing engines must accommodate the mass flux into the system when performing a momentum balance. To that effect, the modified control volume used for this analysis is shown in Fig. 3.9. The inlet is defined as surface 1, and consists of uniform flow at freestream conditions. The exit, surface 2, is defined as the RDE exit plane, and properties are determined by the RDE model outlined previously. Further surfaces are drawn such as to follow streamlines, assuming an ideal streamtube.

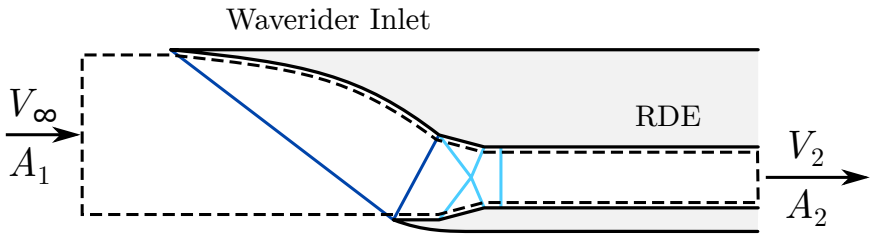

Figure 3.9. Integrated RDE/waverider control volume.

The momentum balance, simplifying from Eq. (2.31) accounting for the incoming uniform flow, yields the following expressions for thrust

$$F_z = \delta_a r_m \int_0^{2\pi} \left(\rho V_z^2 + P - P_\infty\right)_2 d\theta - \rho_\infty V_\infty^2 A_1 \tag{3.3}$$

and circumferential force

$$F_\theta = \delta_a r_m \int_0^{2\pi} \left(\rho V_\theta V_z\right)_2 d\theta \tag{3.4}$$

noting that the latter is unchanged. The ambient back pressure is calculated from the freestream Mach number M, the inlet pressure ratio $P_{0_{inj}}/P_{0_\infty}$, and the RDE inlet stagnation pressure (for the freestream, $\gamma_\infty = 1.4$)

$$P_\infty = P_{0_{inj}} \left(\frac{P_{0_{inj}}}{P_{0_\infty}}\right)^{-1} \left(1 + \frac{\gamma_\infty - 1}{2} M^2\right)^{-\gamma_\infty/(\gamma_\infty - 1)} \tag{3.5}$$

The inlet area A_1 is determined from continuity, Eq. (2.26), and is defined as

$$A_1 = \frac{1}{\rho_\infty V_\infty} \int_2 (\rho V)_2 \, dA_2 \tag{3.6}$$

Additionally, this analysis does include the analytical determination of ψ_{det} by Eq. 2.3, as detailed in Section 2.3

Details of inlet design are not explored in this analysis. While important to ramjet and scramjet design, and aspects such as rectangular-to-circular transition inlets are an active area of research [212–214], such impacts are not expected to be a significant discriminator in integrated waverider forebody–RDE performance and are beyond the scope of this preliminary analysis. Excepting those outlined here, no additional changes or modifications have been made to the model, and the assumptions made in the previous analysis are carried over.

3.5 RDE Sizing

While waveriders are most commonly associated with the hypersonic realm, lower supersonic Mach numbers were proposed in some of the original research into the subject [215]. Additionally, the $M = 3$–4 region is of interest for air-breathing cruise missiles. Although there are some hypersonic cruise missiles in development, there are none currently operational. There are, however, long-to-medium range cruise missiles operating in the $M = 2$–4 range [216–219]. Many of these are powered by ramjets, though there are some gas turbine-powered systems, and as previously mentioned, there is at least one effort to produce an RDE-powered cruise missile [120, 183].

There are also physical constraints to RDE propellant selection. Detonation waves have been observed to fail to propagate in narrow channels, and a limit for

RDE operation as a function of detonation cell size λ was proposed by Bykovskii [96] as

$$\delta_{a_{min}} \gtrsim (2.4 \pm 1)\,\lambda \tag{3.7}$$

where $\delta_{a_{min}}$ is the minimum annulus thickness. Therefore, the detonation cell size of the propellants must be considered when sizing a practical rotating detonation engine. To establish the relative detonability of various fuels, Table 3.3 lists the detonation cell size for stoichiometric combustion in air of several fuels at or near standard temperature and pressure. Notably, methane is not a practical option for RDE operation. Even at the lower end of Bykovskii's estimate, it would require $\delta_a \gtrsim 0.67\,\text{m}$. It is worth noting again that detonation cell size is strongly a function of pressure, indicating that greater pressure recovery may open up design space to less-detonable fuels such as methane. (In the present analysis, the static pressure at the waverider exit varies between 0.58 atm and 2.59 atm, increasing for higher Mach numbers, higher dynamic pressures, and lower values of n.)

Table 3.3. Stoichiometric detonation cell sizes for selected fuels in air at standard conditions

Name	Formula	Detonation Cell Size λ (mm)	Reference
Hydrogen	H_2	15.1	[220]
Methane	CH_4	280–320	[220]
Propane	C_3H_8	69	[220]
Ethylene	C_2H_4	21.2–28	[36, 220]
Methanol	CH_3OH	26	[221]
JP-4		46.0	[36]

For this preliminary analysis, two propellants were investigated: hydrogen and propane. Hydrogen has very small cell sizes, even in air mixtures, and offers excellent

performance. However, hydrogen is extremely difficult to store and is volumetrically inefficient. Propane was selected as a model hydrocarbon. It is not a perfect substitute for kerosene-based aviation propellants (Jet-A, JP-8, JP-10, etc.) but is better documented in the detonation literature, is easily storable, and offers a moderately high autoignition temperature. Though its cell size is on the higher end of desirable, it represents a useful starting point for this analysis.

With the choice of a hydrocarbon fuel, a mechanism that can accomodate light hydrocarbons was required for use in Cantera. The USC-II mechanism [222], which can accommodate hydrogen and hydrocarbons with up to four carbons, was chosen for this purpose. For consistency, it was used for both the hydrogen and propane cases in this study.

To determine a design point for the RDE and provide a point of reference for performance, a literature search of cruise missiles and their propulsion systems was conducted. While information on small military powerplants is not often publicly available, some size and performance data can be found for several well-known cruise missile engines: the Williams F107 (used in the BGM-109/AGM-109 Tomahawk [223]), the Teledyne CAE J402 (Harpoon, SLAM [223]), and the Microturbo TRI 40 (KDA NSM, Exocet Block 3 [224]) and TRI 60 (MBDA Apache, MBDA Storm Shadow [224]). These are all subsonic systems, but provide a useful benchmark in the absence of better data. This information is summarized in Table 3.4.

All four of these engines have outer diameters around 0.3 m, so this dimension was chosen for the RDE used in this analysis. With $d_o = 0.3\,\mathrm{m}$, parametric analysis was performed for both hydrogen and propane fuels to determine the remaining engine size parameters: annulus width δ_a and length L. Parametric performance results for hydrogen are shown in Fig. 3.10, and those for propane in Fig. 3.11. For both cases,

Table 3.4. Cruise missile propulsion systems

Engine	Type	Diameter (m)	Length (m)	Thrust (kN)	TSFC (kg/kN·h)
Williams F107	Turbofan	0.305	0.938	2.65	—
Teledyne CAE J402	Turbojet	0.318	0.737	2.94	122
Microturbo TRI 40	Turbojet	0.280	0.680	3.40	120
Microturbo TRI 60	Turbojet	0.348	0.851	5.33	110

the inlet conditions are taken from a conical forebody ($\theta_{cone} = 5°$, $n = 1.0$) at the central design case ($M = 3$, $\overline{q} = 1{,}000\,\text{psf}$).

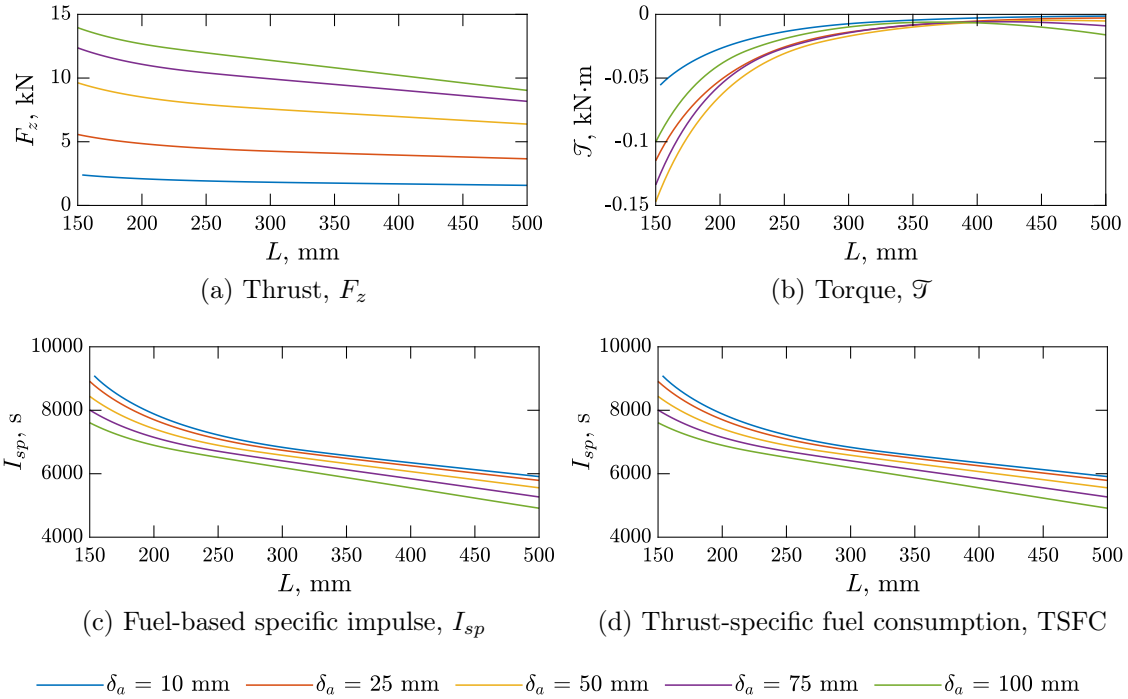

(a) Thrust, F_z

(b) Torque, $\mathcal{T}$

(c) Fuel-based specific impulse, I_{sp}

(d) Thrust-specific fuel consumption, TSFC

Figure 3.10. RDE sizing results, hydrogen fuel.

For both hydrogen and propane fuels, parametric analysis reveals that wider annuli offer greater thrust at the cost of lower specific impulse. Longer annuli decrease

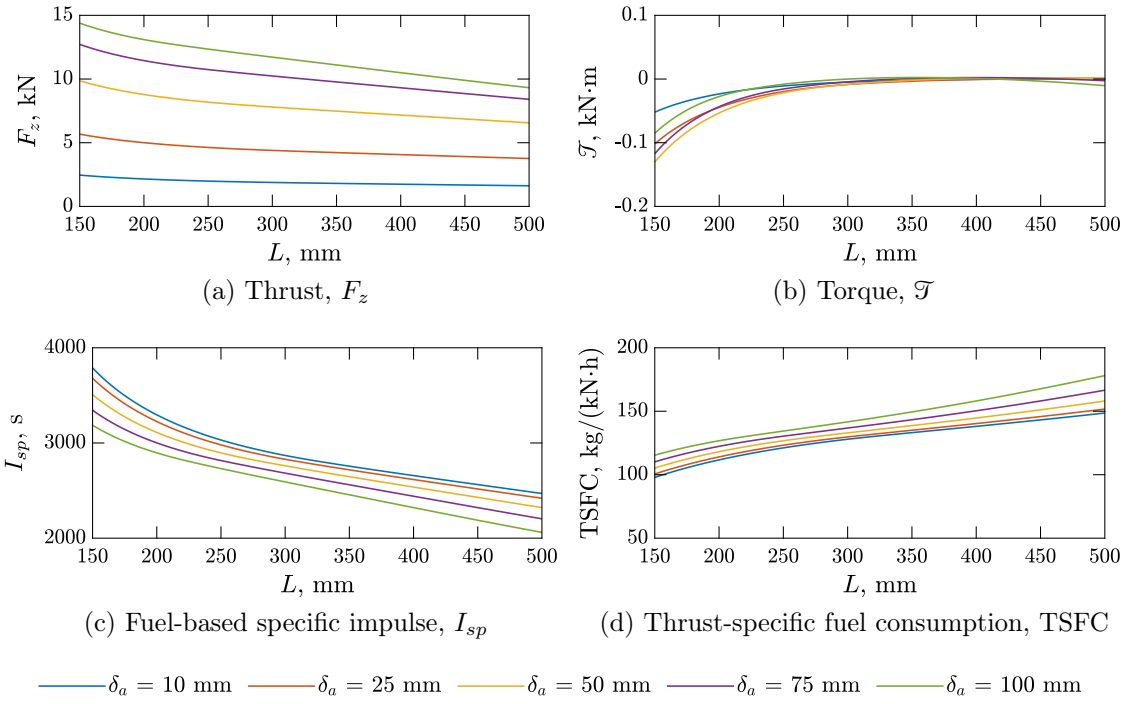

(a) Thrust, F_z (b) Torque, $\mathcal{T}$

(c) Fuel-based specific impulse, I_{sp} (d) Thrust-specific fuel consumption, TSFC

Figure 3.11. RDE sizing results, propane fuel.

both thrust and specific impulse, but result in less resultant torque on the control volume. Therefore, a compromise was made: annulus width δ_a was chosen as 50 mm ($d_i = 0.2$ m) and annulus length L as 0.3 m.

3.6 Parametric Analysis of Forebody/RDE Integrated Performance

The design condition for this analysis was selected as $M = 3$ at $\overline{q} = 1{,}000$ psf. To investigate the effect of dynamic pressure and Mach number perturbations from this design condition, further cases were run at $M = 3$ for $\overline{q} = 500$ and 1,500 psf, and $M = 3.5$ at $\overline{q} = 1{,}000$ psf. The input values for these conditions result in a set of four input conditions for each propellant for RDE analysis, summarized in Table 3.5. As previously mentioned, due to the substantially superior pressure recovery, only inlet Model #2 was considered in this analysis. Likewise, all cases used air as the oxidizer.

Table 3.5. Summary of design cases

Mach number M	Dynamic pressure $\overline{q}$, psf	Fuel
3	500	H_2
3	1000	H_2
3	1500	H_2
3.5	1000	H_2
3	500	C_3H_8
3	1000	C_3H_8
3	1500	C_3H_8
3.5	1000	C_3H_8

RDE propulsive performance with waverider cone angle θ_{cone} and power-law body exponent n are rendered as contour plots of thrust F_z, torque $\mathcal{T}$, fuel-based specific impulse I_{sp}, and thrust-specific fuel consumption TSFC. As mentioned previously, certain combinations of n and θ_{cone} at a given freestream Mach number M cause shock detachment in the inlet, invalidating the model. This occurs for blunt convex body profiles ($n \leq 0.9$), especially for larger values of θ_{cone}. Mach 3 cases are limited to a maximum cone angle of 8° and no solutions are possible below $n = 0.82$; $M = 3.5$ cases are limited to 9°, and no solutions exist below $n = 0.77$. Regions where no solution exists are shaded gray on the contour plots. For every plot, the point of maximum performance is marked with a black diamond.

Figures 3.12 and 3.13 give the performance results for $M = 3$, $\overline{q} = 1{,}000\,\text{psf}$, with hydrogen and propane fuel, respectively. In both cases, maximum performance occurs at $\theta_{cone} = 5°$ and $n = 0.86$, which is the point of greatest pressure recovery. Indeed, because stagnation temperature is constant through the shock system and engine dimensions remain constant, the key variable to engine performance is pressure recovery in the inlet system, which is greatest for low cone angles and, more

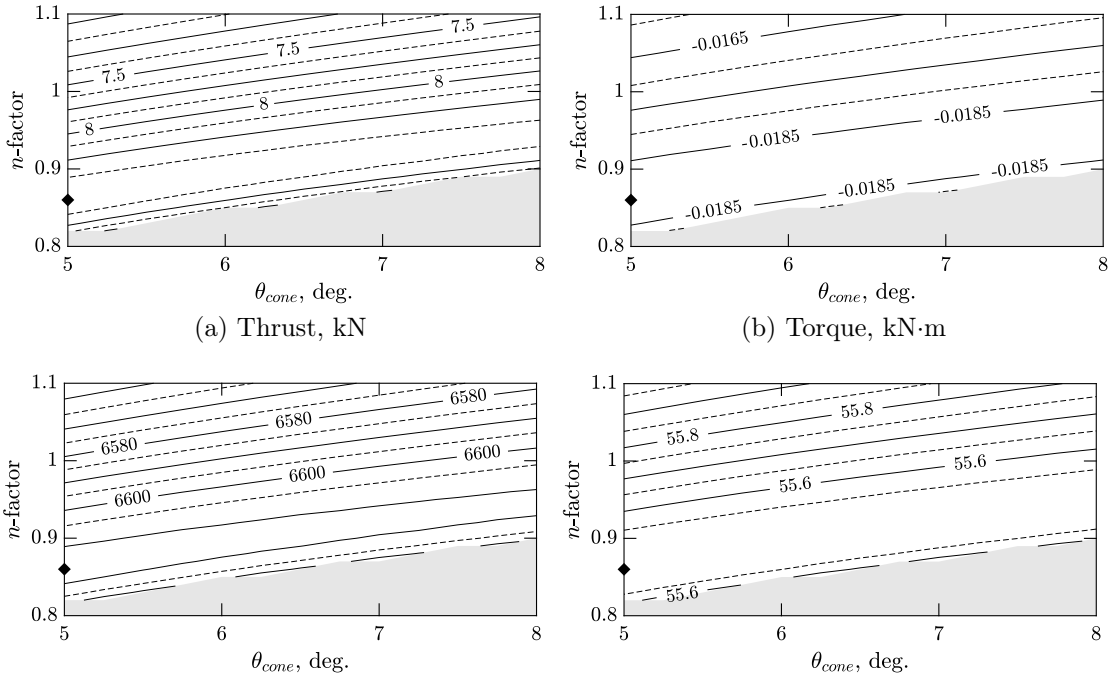

(a) Thrust, kN

(b) Torque, kN·m

(c) Fuel-based I_{sp}, s

(d) TSFC, kg/(kN·h)

Figure 3.12. Integrated RDE performance map, Mach 3, $\overline{q} = 1000$ psf, hydrogen fuel.

significantly, convex body profiles. As θ_{cone} increases, the optimum n-factor increases to $n = 0.95$ at $\theta_{cone} = 8°$. Performance is relatively insensitive to cone angle: increasing θ_{cone} along the performance peak from 5°–8° results in a decrease in thrust of only 0.39 percent for both hydrogen and propane fuels; this decrease in performance is roughly equivalent to an increase of 0.022 or decrease of 0.013 in n for both fuels. Propane offers a 3.13 percent increase in thrust and a 51 percent decrease in torque over hydrogen, but decreases specific impulse (and increases TSFC) by a factor of 2.4. The latter is due to the substantially higher weight of propane over hydrogen, which results in higher mass flow rates of fuel to maintain stoichiometric combustion.

To conserve space, performance maps for other conditions are placed in Appendix B. Inlet performance is dependent on freestream Mach number, so performance maps have identical shape for a given value of M, differing only in magnitude.

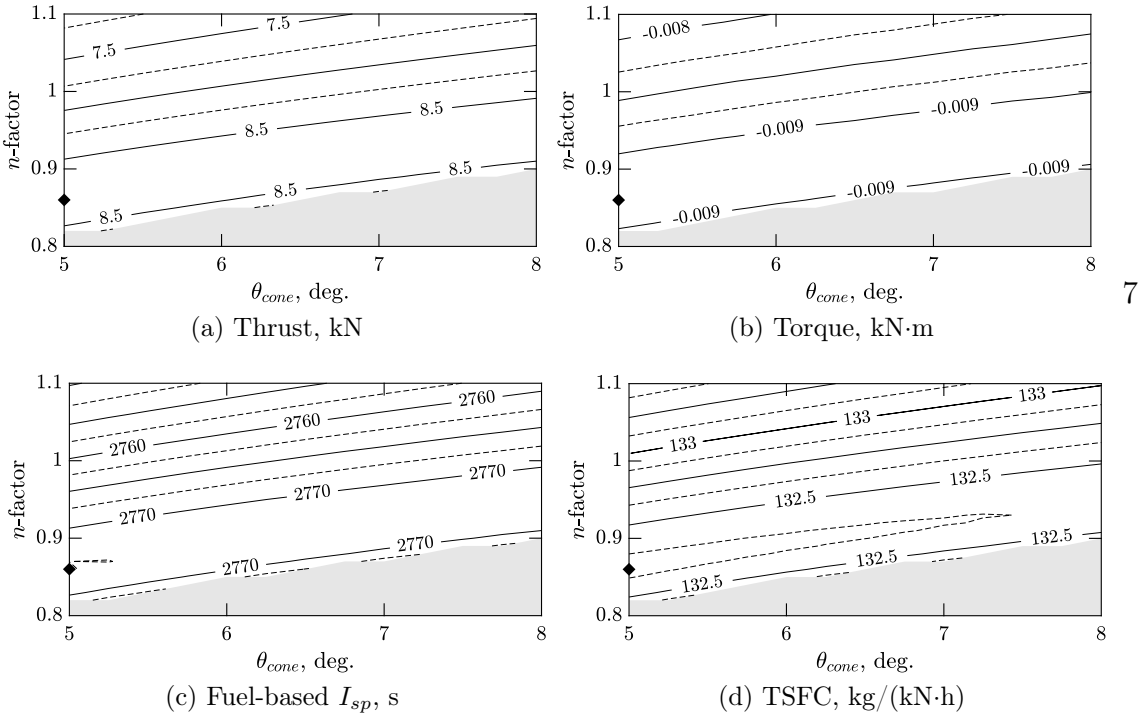

(a) Thrust, kN

(b) Torque, kN·m

(c) Fuel-based I_{sp}, s

(d) TSFC, kg/(kN·h)

Figure 3.13. Integrated RDE performance map, Mach 3, $\overline{q} = 1000$ psf, propane fuel.

While the point of peak performance ($\theta_{cone} = 5°$, $n = 0.86$) does not change, decreasing $\overline{q}$ to 500 psf at $M = 3$ (Figs. B.1 and B.2) reduces inlet pressure, resulting in a substantial decrease in thrust vs. the $\overline{q} = 1{,}000$ psf case: by a factor of 2.02 for both fuels. Torque is decreased proportionally less, by a factor of 1.8 for hydrogen and 1.7 for propane. Specific impulse and TSFC are not significantly affected: the former decreases by only 0.62 percent for hydrogen and 0.67 percent for propane; the latter increases by only 0.63 percent for hydrogen and 0.67 percent for propane.

For $M = 3$, $\overline{q} = 1{,}500$ psf (Figs. B.3 and B.4) the point of peak performance again does not change, but inlet pressure does, resulting in a 50 percent increase in thrust for both fuels. Torque increases proportionally less, by 45.5 percent for hydrogen and 50.3 percent for propane. Again, specific impulse and TSFC are not

significantly affected: they increase (I_{sp}) and decrease (TSFC) by 0.25 percent for hydrogen and 0.23 percent for propane.

Finally, increasing the freestream Mach number to $M = 3.5$ with $\overline{q} = 1{,}000$ psf (Figs. B.5 and B.6) does change the optimum forebody characteristics: peak performance occurs at $\theta_{cone} = 5^\circ$ and $n = 0.84$. Additionally, while the performance maps have the same shape, they no longer scale identically. Due to the to the increased pressure at the RDE inlet and shifted pressure recovery profile, performance gains over the baseline case increase with increasing n-factor (again, these trends are relatively insensitive to cone angle). Peak thrust, relative to the maximum performance of the baseline case, increases 20.3 percent for hydrogen and 18.8 percent for propane. Torque increases at a proportionally greater rate, particularly for propane: by a factor of 2.04 for hydrogen vs. a factor of 2.73 for propane. Specific impulse and TSFC are again not significantly affected: the former decreases by 3.06 percent (hydrogen) and 4.08 percent (propane), the latter decreases by 3.15 percent (hydrogen) and 4.25 percent (propane), respectively.

From these results, it can be seen that thrust is very sensitive to both body shape (θ_{cone}, n) and freestream (M, $\overline{q}$) parameters, and scales with the pressure at the RDE inlet. Torque scales similarly with thrust (though proportionally somewhat less in $\overline{q}$, and somewhat more in M). Fuel-based specific impulse and TSFC follow the same trends as thrust, but are much less sensitive to perturbations in either body shape or freestream parameters; this is due to mass flow rate and thrust scaling very similarly with changes in $P_{0_{inj}}$. Greater performance is achieved at higher Mach numbers and dynamic pressures. Autoignition temperature limits may present a barrier to operation at $M > 3.5$. This temperature limit is eased somewhat at higher dynamic pressures ($T_{0_{inj}}$ decreases with increasing $\overline{q}$), indicating that higher Mach number operation may be easier to accomplish at higher dynamic pressures.

3.7 Range Impacts

Beyond impacts to the performance of the propulsion system inlet due to employing an OFWR forebody, it is possible to explore vehicle range as well. The aerodynamic improvements possible with the OFWRs were illustrated in [198]. These results, and more recent experience, show that the OFWRs demonstrate up to 13 percent superior $\mathscr{L}/\mathscr{D}$ ratio at a given volumetric efficiency. The combined effects on total range from both the propulsion efficiency increase and lift-to-drag ratio improvement from using OFWR forebodies can be calculated using the Breguet range equation

$$\mathscr{R} = I_{sp_f} V \frac{\mathscr{L}}{\mathscr{D}} \ln\left(\frac{m_i}{m_f}\right) \tag{3.8}$$

where $\mathscr{R}$ is the range, I_{sp_f} is the fuel-based specific impulse from the RDE model, V is the velocity, $\mathscr{L}/\mathscr{D}$ is the forebody's lift-to-drag ratio, and m_i and m_f are the vehicle masses at the start and end of cruise [225]. While the exact range would be influenced by factors not presently included in the modeling, a simple mass-independent range metric $\hat{\mathscr{R}}$ can be defined for relative comparison between the forebody geometries and RDE engines studied. This metric is defined here as

$$\hat{\mathscr{R}} = I_{sp} V \frac{\mathscr{L}}{\mathscr{D}} \tag{3.9}$$

By calculating the inviscid forebody $\mathscr{L}/\mathscr{D}$ and using the engine performance, this range metric has been quantified across the design space. Figure 3.14 shows the range metric as a function of cone angle and n-factor, at $M = 3$, and $\overline{q} = 1{,}000$ psf for H_2/air. Without data regarding the vehicle empty and gross weights, an absolute measure of the range cannot be calculated. Consequently, the range metric data have been normalized by the maximum value for theH_2/air case to produce a relative measure of waverider forebody–RDE performance. For these conditions, the best normalized range metric occurs at $\theta_{cone} = 5°$, and $n = 0.98$. A large plateau exists in

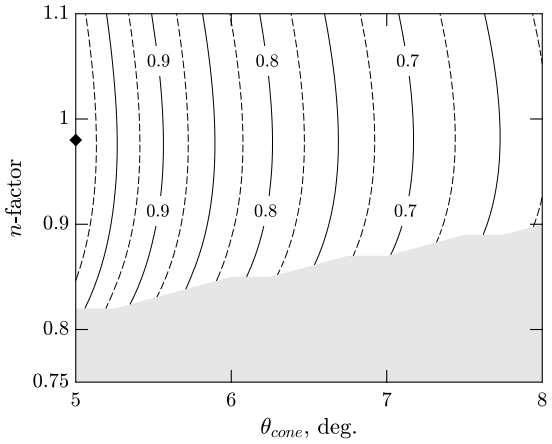

Figure 3.14. Normalized range metric for Mach 3, $\overline{q} = 1000\,\text{psf}$, hydrogen–air.

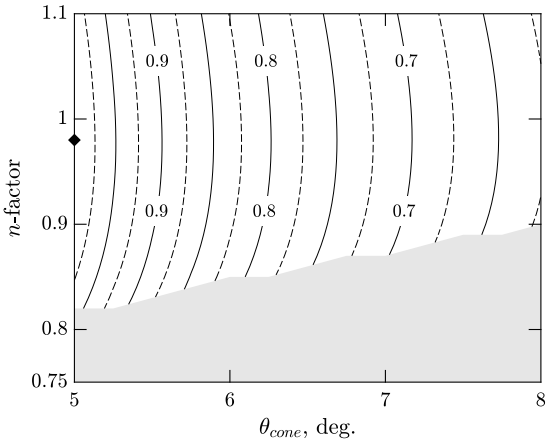

Figure 3.15. Normalized range metric for Mach 3, $\overline{q} = 1000\,\text{psf}$, propane–air.

the peak performance around $n = 1$. This trend is present across the range of cone angles. Smaller cone angles produce superior range metrics over larger cone angle due to the greater inviscid lift-to-drag ratios.

Figure 3.15 shows range metric data for at Mach 3, and $\overline{q} = 1{,}000\,\text{psf}$ for C_3H_8/air. Again, the data have been normalized by the best range metric using C_3H_8 at these conditions. As with H_2/air, the best normalized range metric occurs at $\theta_{cone} = 5°$, and $n = 0.98$. While Figs. 3.14 and 3.15 look similar, the absolute values are quite different; only the normalized distributions look so alike. Normalized range metric data for the other values of dynamic pressure at $M = 3$ are nearly identical to those above, when normalized by the maximum value obtained for each fuel: they differ by less than one percent from the $\overline{q} = 1{,}000\,\text{psf}$ case, with $\overline{q} = 1{,}500\,\text{psf}$ providing a minute increase (0.26 percent) and $\overline{q} = 500\,\text{psf}$ providing an even smaller decrease (0.084 percent). As such, these data are not plotted. At a fixed Mach number, changes in the dynamic pressure will not alter the waverider inviscid $\mathscr{L}/\mathscr{D}$.

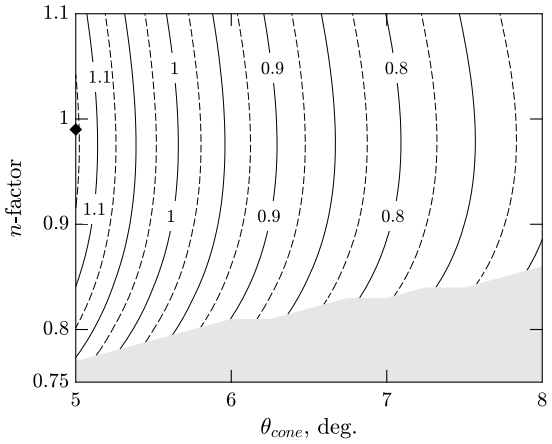

Figure 3.16. Normalized range metric, Mach 3.5, $\overline{q} = 1000\,\text{psf}$, hydrogen–air.

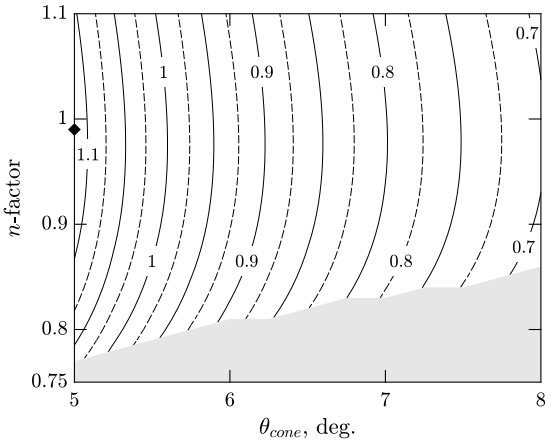

Figure 3.17. Normalized range metric, Mach 3.5, $\overline{q} = 1000\,\text{psf}$, propane–air.

Figures 3.16 and 3.17 show the normalized range metric data for Mach 3.5, and $\overline{q} = 1{,}000\,\text{psf}$ for H_2/air and C_3H_8/air, respectively. Values greater than unity are possible, due to the normalization by the peak metric value from the $M = 3$ and $\overline{q} = 1{,}000\,\text{psf}$ data. The peak range metric at $M = 3.5$ is 1.13 for H_2/air and 1.18 for C_3H_8/air (13 and 18 percent improvements over $M = 3$, respectively); these peaks occur at $\theta_{cone} = 5^\circ$ and $n = 0.97$. As observed at $M = 3$, the normalized distributions for H_2/air and C_3H_8/air look very similar. However, the absolute values are quite different.

The normalized range metric contour plots show a relative performance among the examined waverider forebody geometries. The overall similarity in the plots indicate that the best performing waveriders for hydrogen are also the best performing waveriders for propane, showing an independence from the fuels used by the RDE. This result is observed at both freestream Mach numbers. Additionally, a given vehicle configuration will have similar relative performance over the range of Mach

numbers examined. Therefore, the optimum waverider design is robust with superior performance over a range of conditions.

3.8 Limitations of the Analysis

The osculating flowfield method is an extension of the osculating cones method. In both methods, it is assumed that the three-dimensional shock wave shape of the inviscid flowfield can be obtained by incorporating a series of known flowfields orientated on planes normal to the user defined shock wave trace in the base plane of the flowfield. The applicability of this approach has been confirmed by numerous wind tunnel tests and numerical investigations [191,195]. Limits do exist regarding the permitted variability between adjoining osculating planes. As long as these variations remain sufficiently small so as not to impact the pressure on the forebody surface, the method is sound. Additional assumptions include that the radius of the waverider's leading edge is negligibly small as to not impact the flowfield structure. A similar assumption is made regarding the leading edge radius of the cowl. Also, any shock wave displacement effects due to viscous effects are ignored, including those due to local areas of separation.

The autoignition condition in this study is estimated using the stagnation temperature of the freestream flow. However, as noted previously, autoignition is a complex phenomenon with many governing factors. Indeed, Frolov [142] et al. have reported successful operation of a hydrogen-fueled RDE-powered ramjet in a Mach 5.7 freestream with flow stagnation temperatures of 1,500 K. The autoignition condition used in this study therefore represents a first-order estimate of the upper Mach number limit, and further experiments are required to explore these limits in practical operation.

The present analysis does not model the RDE inlet or a diffuser between the waverider forebody. Flow into the RDE is approximated by a model developed for rocket-mode engines, so the RDE performance is only a function of the waverider exit stagnation pressure, not the inlet Mach number (or velocity or dynamic pressure). As thrust and mass flow rate both scale strongly with this parameter, this is potentially the cause of the insensitivity of specific impulse and TSFC to freestream and body shape parameters. Furthermore, each configuration is considered as an on-design configuration, with the inlet size (i.e. capture area) being dictated by continuity through the RDE model. The inlet is not sized for any one condition, but is instead re-sized for each successive condition. A detailed discussion of the limitations of the RDE model is given in Ch. 2.5.4, but it is worth reiterating that this model assumes only a single detonation wave. Previous experimental studies have shown that the the number of detonation waves has been shown to be dependent on a number of parameters including the mass flow rate through the engine [118]. However, Yi et al. showed computationally that specific impulse is unaffected by the number of propagating detonation fronts [134]. Additionally, no nozzle is modeled in this analysis. An inspection of the magnitude of the respective terms in Eq. (3.3) reveals that pressure thrust is a significant component of the overall thrust generated. This indicates that the RDE exit flow is strongly underexpanded and significant benefit could be obtained from aft-body expansion or a nozzle.

This is a preliminary, first-order integration study looking for design discriminators. Both the waverider forebody and RDE models were run on conventional personal computers, with computation times for both on the order of seconds. The most computationally intense component of either model is Cantera, which takes 30–40 s to converge on the detonation properties (this is heavily mechanism- and

propellant-dependent). Though each model was computed separately, this is many orders of magnitude faster than high-order computational solutions would require.

CHAPTER 4

DESIGN AND CONSTRUCTION OF THE RDE AND EXPERIMENTAL FACILITY

4.1 A Brief History of RDEs at UT Arlington

The University of Texas at Arlington has built two previous RDEs, experimentally investigated by Braun and Dunn in 2009 and 2010 [117]. The first, officially referred to in the literature as CDE001 but nicknamed "Hershey" due to its prominent aerospike nozzle (reminiscent of Hershey's Kisses® chocolates, Fig. 4.1), had small injector ports and proved unable to sustain a detonation wave [117].

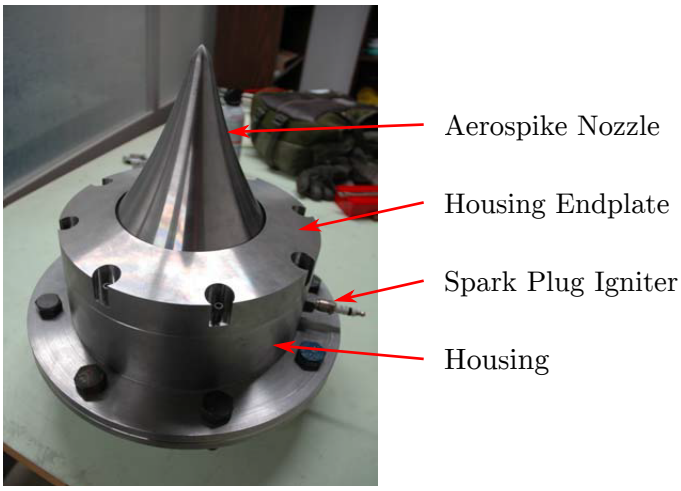

Figure 4.1. CDE001, "Hershey" (rear view) [117].

The second RDE, CDE002 (nicknamed "Skittle", for its brightly-colored assembly drawings, Fig. 4.2, similar to Skittles® candies), showed clear detonations for one rotation around the annulus, but deteriorating for the second rotation [117]. It

is hypothesized that this was due to insufficent propellant flow. This engine was also designed with active cooling of its outer annular surface, leading to U.S. Patent 8,544,280 B2, "Continuous Detonation Wave Engine with Quenching Structure" [226].

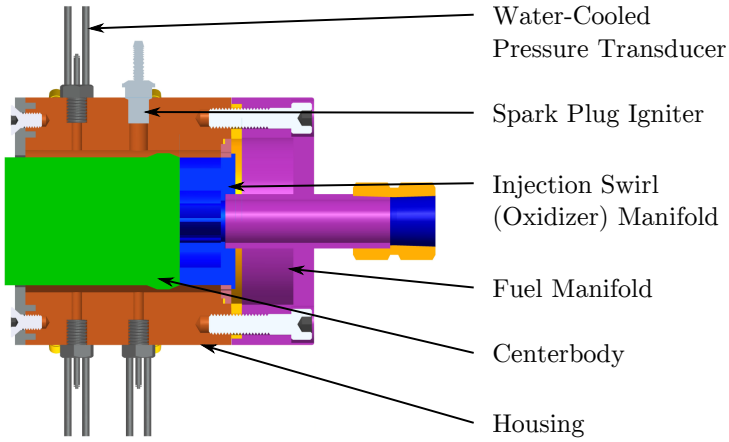

Figure 4.2. CDE002, "Skittle" (assembly drawing).

Following the completion of the original test plan, both Hershey and Skittle were disassembled and stored.

4.2 Engine Design

A new RDE (officially designated CDE003) was created for the current round of experiments. This engine uses Skittle as a base design, and a number of new features were incorporated with the intent of improving the RDE's operational use, increasing its useful lifespan, and exploring new design space. Funds for this conversion were provided in part by a NIST/UTA Technology Acceleration Program grant. CDE003 has been named "Arthur" (because "RDE" sounds like "Artie;" short for Arthur). An exploded, labeled assembly view of this engine is shown in Fig. 4.3.

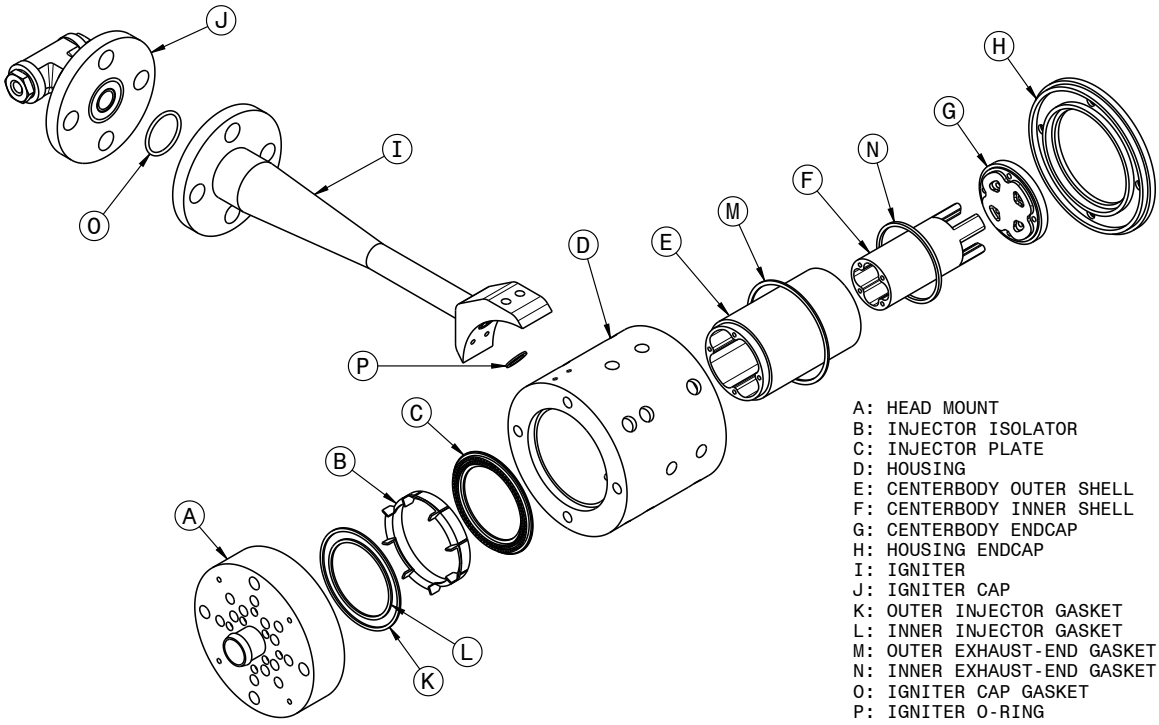

Figure 4.3. Exploded assembly view of RDE "Arthur".

There are eight primary components, the majority of which are new; Arthur shares only the housing and housing endcap with Skittle. However, the re-use of these two components (especially the housing) saved considerable material and manufacturing expense. Arthur was specifically designed to be modular, with the intent of enabling a broad range of testing capabilities. A number of significant design features will be highlighted in the following subsections. The components are:

A. Head mount. Contains the mounting points for the housing and centerbodies, as well as the propellant injector ports and inner coolant in- and outflow ports. Contains a fluidic valve/propellant mixing chamber, further details of which are given in Section 4.2.3.

B. Injector isolator. This sits inside the fluidic valve/propellant mixing chamber, and is designed to separate the propellant flows from each other. It can be removed for premixed operation; further details are given in Section 4.2.3.

C. Injector plate. Can be removed and swapped out for alternate designs. More information is given in Section 4.2.4.

D. Housing. This is the external shell of the RDE and contains the pressure transducer and thermocouple ports, the spark plug igniter, the PDE igniter interface, and the outer coolant flow ports. Modified slightly from its Skittle configuration, the details of which are given in Section 4.2.1.

E. Centerbody outer shell. Forms the inner boundary of the combustion annulus. Inner coolant flow travels along its inner surface. Details of the inner annulus cooling system design are given in Section 4.2.2.

F. Centerbody inner shell. Designed to allow inner-shell coolant flow to recirculate. Coolant flow travels axially along its outer surface, recirculates through the square ports at the end, and returns down its center. Details of the inner annulus cooling system are given in Section 4.2.2.

G. Centerbody endcap. Forms the aft end of the centerbody; the end face forces coolant recirculation.

H. Housing endcap. Forms the aft-end of the housing, allows access to the outer coolant flow ports. Braun [117] tested Skittle both with and without this on, the former was found to increase performance. Outer-annular wall cooling is not possible with this removed.

I. Igniter. A tangential predetonator with a high blockage ratio to provide deflagration-to-detonation transition. Further details are given in Section 4.2.5.

J. Igniter cap. Caps the igniter, provides predetonator propellant injection ports and a spark plug for ignition. Further details are given in Section 4.2.5.

K.-P. (Excepting O) Copper gaskets for high-temperature sealing. Copper was chosen (as opposed to rubber or another polymer material) for its high temperature resistance, malleability, and coefficient of thermal expansion (equivalent to or slightly greater than that stainless steel [227], meaning that the seal will tighten with temperature). The igniter gasket, part O, is rubber.

4.2.1 Annulus Width

The original Skittle annulus was narrow: 0.18 in (4.45 mm), with a throat downstream of the swirled propellant injection of 0.08 in (1.9 mm). Detonations have been shown to fail to propagate in sufficiently small tubes [228, 229], and narrow channels (that is, annuli) are believed to present a risk of inducing the same effect [230]. Bykovskii [96] suggests a minimum annulus width as a function of the detonation cell size λ (see Sec. 3.5), which for stoichiometric hydrogen–oxygen at 1 atmosphere is approximately 2.1 mm [96]. Though highly pressure dependent, this gives a rough estimate of the lower end annulus dimensions: δ_a between 7.07 and 2.91 mm. The annulus width of Skittle lies within this range, but stoichiometric H_2–O_2 is also a highly detonable mixture with a small cell size. Less-detonable mixtures (hydrogen–air, methane–oxygen, lean mixtures) have larger cell sizes [36] and would likely require wider annuli to operate well.

Increasing the annulus width would allow a broader range of operating conditions, both in terms of equivalence ratio and propellant composition. As a result, the inner diameter of the housing and endcap were increased from 3.45 in (87.6 mm) to 3.76 in (95.5 mm). The new centerbody (Section 4.2.2) has an outer diameter of 3.14 in (79.8 mm), giving a new annulus width of $\delta_a = 0.31$ in (7.87 mm). A front and sectional view of Arthur, indicating annulus dimensions, as well as overall length and diameter is given in Fig. 4.4.

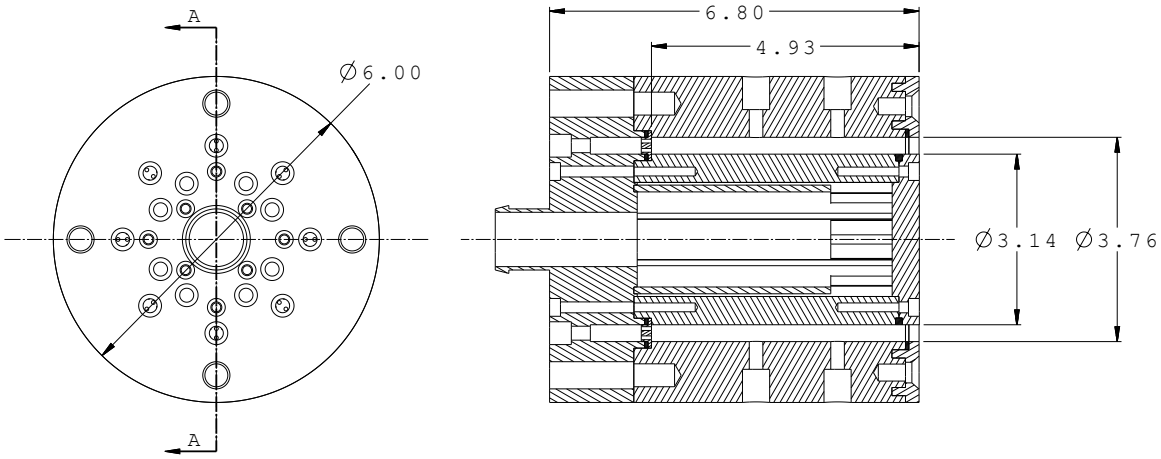

Figure 4.4. Front and section views of Arthur engine core (dimensions in inches).

4.2.2 Active Cooling of Inner Annular Surface

One of the main problems in the design of operational RDEs is dealing with the extremely high heat release of the detonation wave. High-temperature materials have been hypothesized as a possible solution to the heating problem [231], but these are not believed to represent a viable solution [118], as they can heat up to greater than the autoignition temperature of the propellant mixture and cause deflagration prior to the detonation wave, thus compromising the entire RDE concept. Skittle was already actively cooled on its outer annular wall (one of the main subjects of the patent on its design [226]), but it employs heat sink cooling on its inner annular surface: its centerbody is solid bronze. Active cooling of the inner surface presents a design challenge. It is possible to use heat-sink cooling methods for short runtimes, but there is no free surface on the inner annulus to dump waste heat during longer-duration tests; it *must* be actively cooled. Additionally, due to the confined nature of the centerbody, coolant flow must either return through the same face it enters (the head-end surface), be exhausted into the annulus (for example, as transpiration coolant), or be exhausted out the aft end of the centerbody.

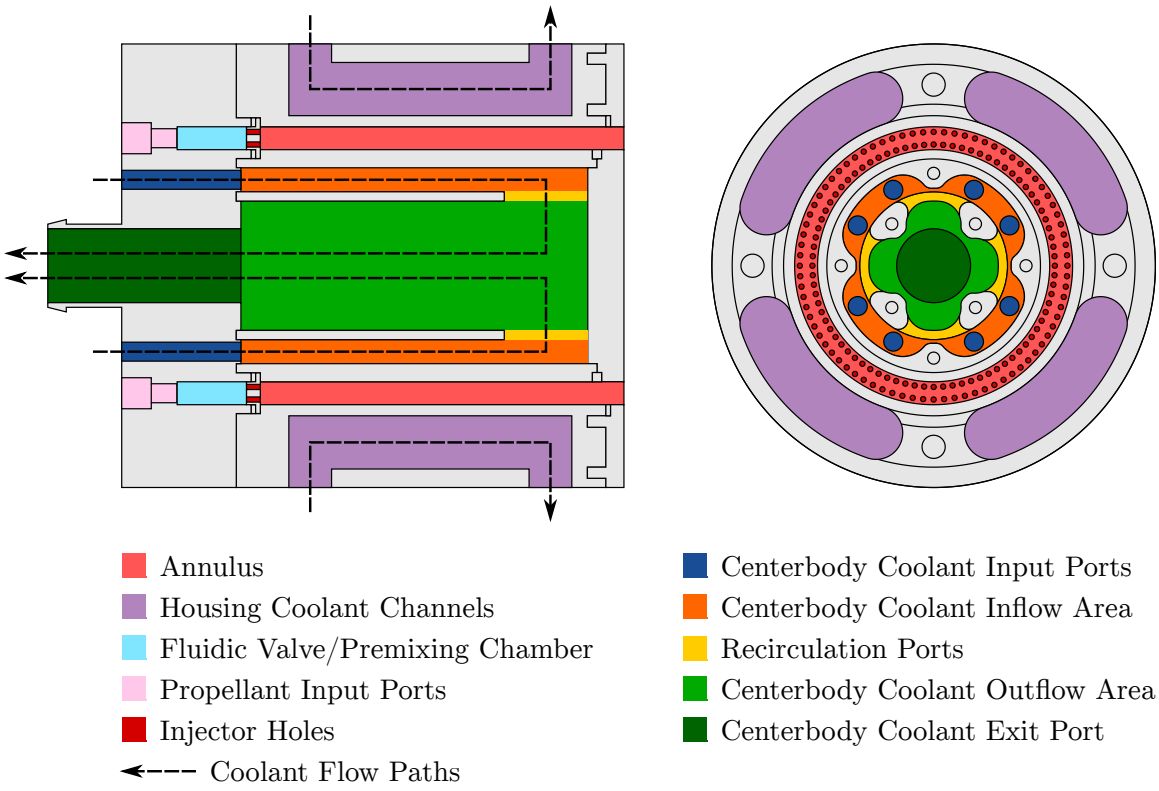

Figure 4.5. Major flow regions of Arthur.

Therefore, a two-shell design was used in the centerbody. Coolant enters through eight evenly-distributed ports on the head mount and passes axially down the length of the engine through the gap between the outer and inner shells, turns through the recirculation ports, and returns through the center of the inner shell and out through the machined barbed fitting at the center of the head mount. A schematic sectional and aft view of Arthur is shown in Fig. 4.5, color-coded by flow area. Coolant flow paths are shown by dashed dotted lines, coolant input ports for the centerbody are dark blue, the inflow area is orange, recirculation ports are indicated in yellow, the outflow area is green, and the centerbody exit port is in dark green, exiting through the head mount hose barb. Housing coolant channels are purple.

Additionally, Fig. 4.6 shows the the outer and inner shells from the rear, with the recirculation ports indicated.

Figure 4.6. Outer and inner centerbody shells, aft view, showing recirculation ports.

To allow for even coolant flow, the centerbody inflow and outflow areas and the total recirculation port area are all equal. The machined hose barb on the head mount was as large as could be allowed while still having clearance for the mounting screws for the inner centerbody. It has an inner diameter of 1.00 in (25.4 mm) and an outer diameter of 1.13 in (28.7 mm). The barb has an outer diameter of 1.25 in (31.8 mm) at the barb and was designed to fit a 1 in nylon hose as a tight compression fit: the end of the hose is warmed in hot water to make it soft, and then forced over the barbed fitting. The coolant flow system is described in more detail in Section 4.3.4.

4.2.3 Fluidic Valve Injector System and Injector Isolator

A key operational consideration of an RDE is the ability of the injectors to recover quickly from the high pressure region immediately following the detonation wave. This is termed “interruption time”, and the possiblility of using a fluidic valve

to reduce this time was experimentially investigated with good success by Braun et al. [232] and Peace et al. [233]. Fluidic valves use fluid dynamics principles (instead of mechanical parts) to control fluid flow. The fluidic valve investigated by Braun and Peace et al. consists of a generally rectangular cross-section plenum cavity between the detonation chamber and the injector face. It functions by providing a sudden area increase which attenuates the shock wave entering the cavity, allowing the supply pressure of the propellants to more quickly push the contact surface between combustion products and propellants back out of the injectors and refuel the RDE.

A fluidic valve of this type can also serve as a premixing chamber. Incomplete combustion due to poor mixing in the chamber represents a potentially significant performance loss in RDE design, as detonation velocities on the order of 2,000–3,000 m/s [1] provide on the order of 10 µs for separate propellant streams to mix prior to the arrival of the detonation wave. These losses can be avoided if the propellants are mixed prior to injection into the annulus. Therefore, Arthur was designed with a joint fluidic valve/mixing chamber, an annular groove 1.00 in deep and 0.31 in wide, as seen in seen in Fig. 4.7. It is illustrated in light blue in Fig. 4.5. At the base of the fluidic valve are the eight evenly-distributed propellant injection ports, which are alternated between fuel and oxidizer.

However, premixed propellant flow presents a design challenge for RDEs. Though the fluidic valve has been shown to attenuate the effect of the shock wave entering the injector cavity, and narrow tube diameters (such as those in the injector plate) have been shown to inhibit detonation propagation [228, 229, 234], there is no impediment to the high-temperature combustion products entering the cavity. These combustion products can ignite premixed propellants, with potentially catastrophic consequences. Therefore, an isolator to separate the fuel and oxidizer flow was designed and manufactured to fit into the fluidic valve chamber of Arthur. When

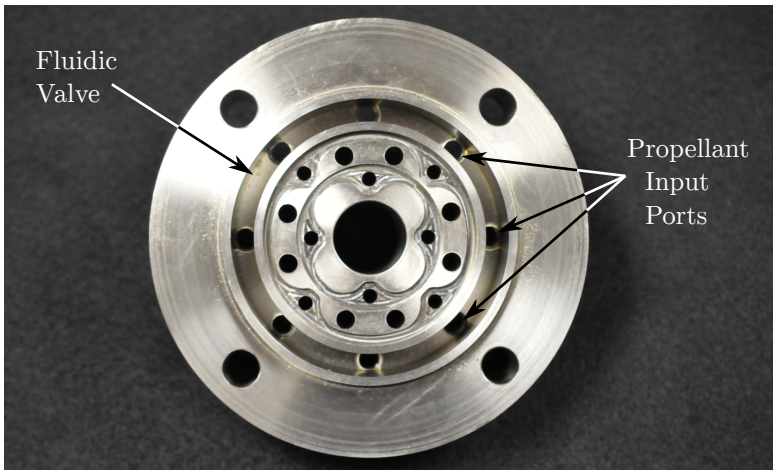

Figure 4.7. Downstream view of head mount, showing fluidic valve.

installed, the propellants are separated; when removed, it enables premixed operation. A labeled image of the injector isolator can be seen in Fig. 4.8.

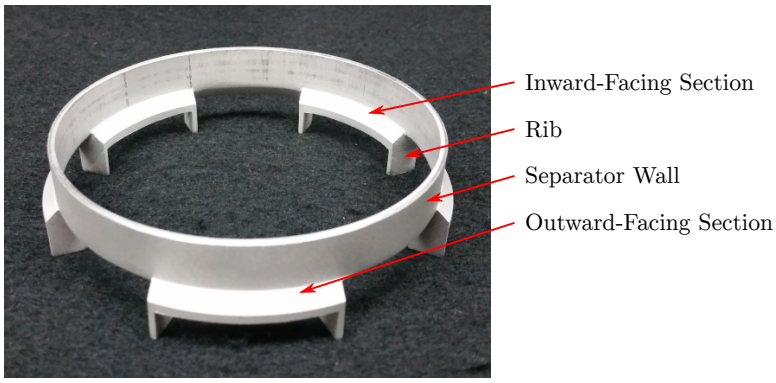

Figure 4.8. Injector isolator.

The isolator separates the injection chamber into eight regions, each of which is centered over a propellant injector port: four outward-facing regions (directing propellants toward the inner half of the chamber) and four inward-facing regions (directing propellants towards the outer half of the chamber), separated by ribs and a central separator wall. With injector ports alternated between fuel and oxidizer,

this serves to direct all fuel flow towards one half of the annulus, and all oxidizer flow towards the other half, as seen in Fig. 4.9. For all of the tests described in Chapter 5, the injector isolator has been installed in the fluidic valve cavity. A bead of high-temperature silicone is applied along all internal edges to ensure that there is no leakage or mixing of propellants inside the injector cavity.

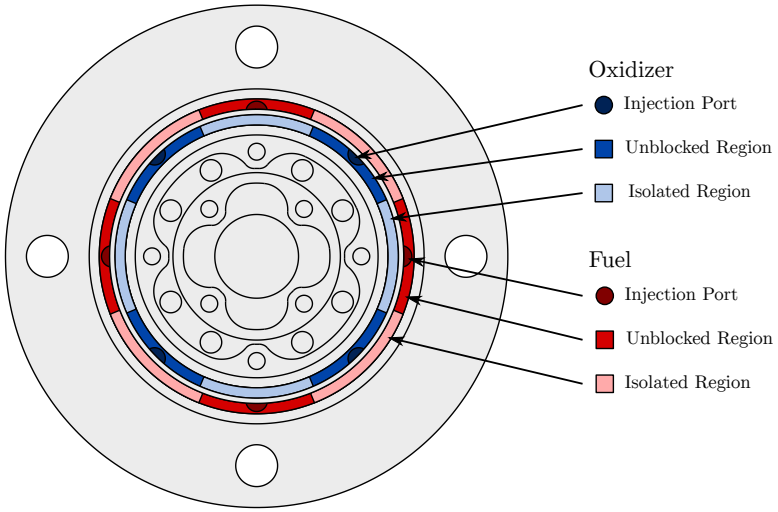

Figure 4.9. Injector isolator, assembly view.

4.2.4 Injector Plates

One of the modular features of Arthur is the ability to exchange injector plates, which makes variation of the injection characteristics (especially swirl) easy. A number of injector plates were manufactured, including ones with simple straight injection, with impinging injection without swirl, and ones designed to induce both positive and negative swirl. Fig. 4.10 shows a front and section view of the the straight-injection injector plate. There is a groove in the bottom surface of the injector plate, which was designed to mesh with the central separator wall of the injector isolator. A thin bead

of high-temperature silicone is applied in this groove as an additional countermeasure against propellant leakage between the regions.

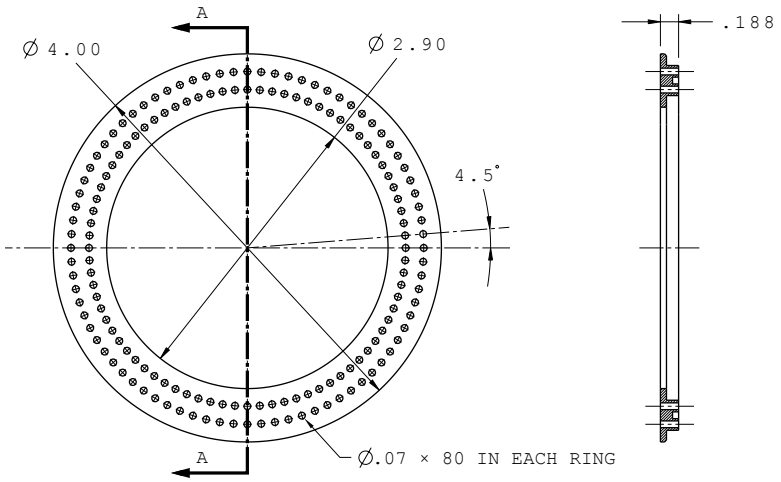

Figure 4.10. Injector plate, front and section view (dimensions in inches).

4.2.5 Ignition Systems

As previously discussed, there is as of yet no consensus on the best way to ignite an RDE. While many methods have been explored, the two most popular are automotive spark plugs and tangential predetonators. The latter consists of a tangential tube extending into the annulus which is filled with a detonable mixture and ignited, with the intent of directly initiating a detonation wave in the chamber (that is, without the need for a deflagration-to-detonation transition). The criteria by which an ignition method is judged are twofold: first, can it initiate a detonation wave inside the annulus; second, does it do so repeatably? Previous studies have reported moderate success with spark plugs, whereas reliable ignition has been reported with tangential predetonators [118]. Only when reliable, repeatable ignition is achieved can more advanced topics such as the number of detonation waves, their

direction of propagation, and their stability under various on- and off-design conditions be investigated. Therefore, Arthur has been designed with two possible ignition methods: a Champion® spark plug mounted along the circumference of the engine and a tangential predetonator.

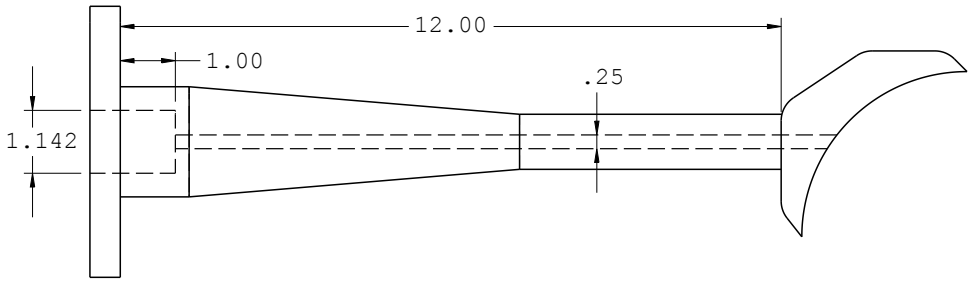

Figure 4.11. PDE coupling/predetonator igniter (dimensions in inches).

The predetonator was originally concieved as a pulse detonation engine (PDE) igniter. PDEs are designed and valved to be refilled quickly and easily, have precise fill timing to control the equivalence ratio of the propellants, can be ignited repeatably, and achieve the detonation-to-deflagration process before the detonation wave exhausts the engine. During the design process, UTA's only operational PDE was the one used by Joshi [235] and Bello [236], and a coupling was designed to interface between this PDE and Arthur, Fig. 4.11. The entrance diameter matches the PDE's inner diameter (1.142 in); this decreases to 0.25 in (6.35 mm) diameter 1.0 in (25.4 mm) past the flange. The original version of this pulse detonation ignition concept, including a vertically-fired Arthur, is shown in Fig. 4.12. As can be seen, the ultimately unwieldy length of this coupling was dictated by the several inches of mounting rails extending past the exit flange.

The primary intent for the use of the full PDE as the igniter was to make use of existing systems and hardware, but in the time between the engine design and

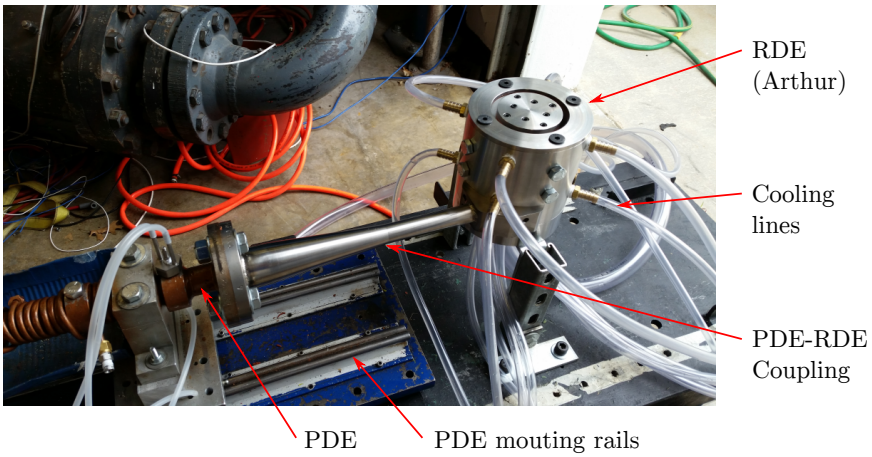

Figure 4.12. Original PDE–RDE assembly (with cooling lines installed).

the assembly of the experimental facility, the PDE research facility was disassembled. While not the original intent of the step diameter change in the coupling design, obstacles which change the effective diameter of the tube have been shown to induce deflagration-to-detonation transition in detonation tubes and pulse detonation engines [237, 238]. The blockage ratio B of the coupling, here defined for a circular cross-section tube and blocking orifice as

$$B = 1 - \left(\frac{d_i}{d_e}\right)^2 \tag{4.1}$$

where d_i is the initial (upstream) tube diameter and d_e is the downstream (narrowed) tube diameter, is higher than those considered in previous studies ($B = 0.95$), but Porel [238] reported that higher blockage-ratio orifices should be located towards the beginning of the tube, as is the case for the present coupling. Therefore, the pulse detonation engine was omitted from the design, and the coupling itself was used as the predetonator igniter, and is listed as such as part I in Fig. 4.3.

To supply propellants and provide a means of ignition, a fueling and igniter head was manufactured for the predetonator, indicated as part J in Fig. 4.3. The body of the igniter head is a 3/4 in FNPT tee. Propellant inputs are supplied by

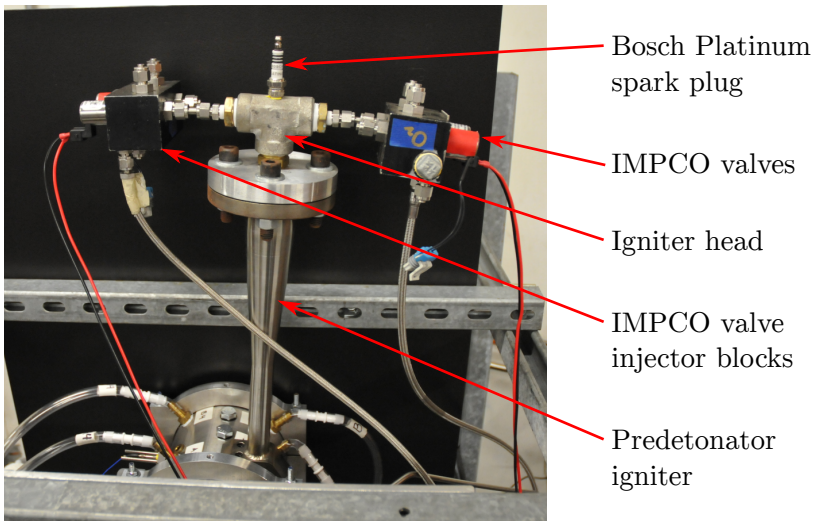

Figure 4.13. Mounted igniter assembly.

1/4 in Swagelok® connections, entering through opposing sides of the tee. The tee connects to the flange by means of a 3/4 in NPT pipe nipple. Ignition is supplied by a spark plug threaded through a hole at the top of the tee. The flange mates with the end of the coupling, and seals with a 1.5 in ID o-ring (on the bottom surface of the flange, not shown). The full igniter assembly, including igniter cap, fuel control valves, and spark plug (Bosch® Platinum), is shown in Fig. 4.13. To save space and minimize the torque on the engine, the igniter is mounted vertically. Further details of the fuel control system for the predetonator are given in Section 4.3.3.1. Both the engine and predetonator spark plugs are triggered by an existing spark box and power supply. For safety purposes, a remote cutoff switch was located in the ARC control room. This switch must be flipped to close the circuit and enable the spark.

Finally, for situations where spark plug ignition alone is sufficient, an igniter hole cap was manufactured, Fig. 4.14. This covers the predetonator hole so that testing can be conducted without the predetonator mounted, relieving the system of the torque preload imposed by the igniter. To minimize any residual torque effect

from the igniter hole cap it has been been manufactured from aluminum, but to reduce the risk of sustaining damage from exposure to combustion, the hole cap has been designed with a stainless steel insert covering the ignition hole. This insert can easily be removed and swapped should it sustain any damage.

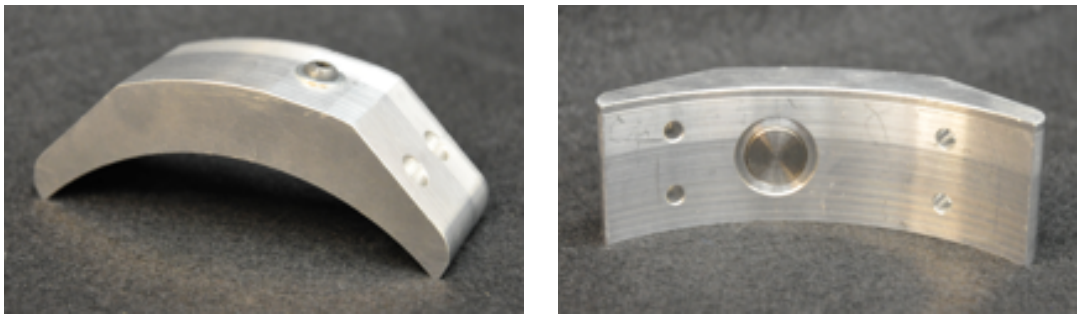

(a) Side view (b) Underside, showing stainless insert

Figure 4.14. Igniter hole cap.

4.2.6 Nozzles

Unlike Skittle, Arthur does not incorporate a nozzle. This was an intentional design decision, as the effect of nozzles on RDEs is a topic of ongoing research, and—as with the analytical model—a decision was made to attempt to characterize base RDE performance independent of nozzle effects. However, the modular design of Arthur allows nozzles of various types to be incorporated as a future research step.

4.3 Testing Facility

The operational experimental facility is illustrated in Fig. 4.15. While the original experimental setup (Fig. 4.12) had the engine firing vertically, that arrangement was due to the need to share test space with an existing PDE setup. The PDE test facility was disassembled, so a new test facility was designed for the RDE experimen-

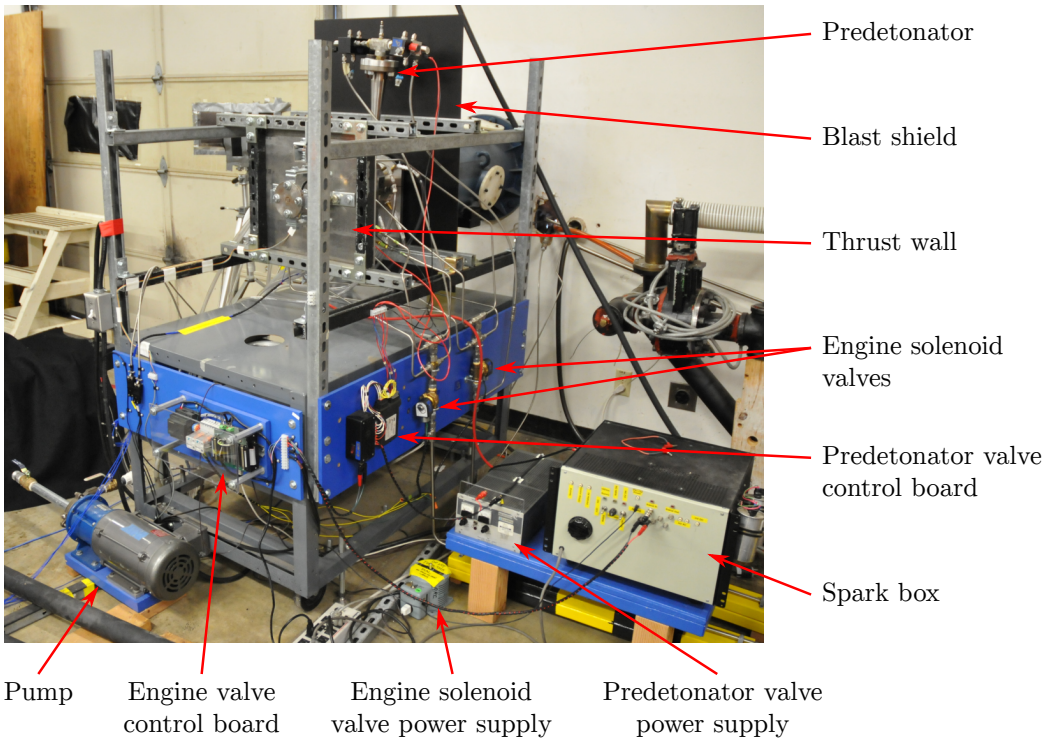

Figure 4.15. Experimental test facility.

tal test plan. Instead, Arthur is fired horizontally into a dump tank. Firing into the dump tank is preferred for several reasons:

1. It locates the engine closer to the propellant bottles, reducing the tubing length required to plumb the engine.
2. It locates the engine closer to the high-speed DAQ system, significantly reducing the distance the DAQ must be moved to switch between experiments.
3. It allows the engine to be fired indoors, enabling testing during poor weather and avoiding a need to roll the test stand outside (as would be required if firing vertically).

Additionally, firing the engine indoors made it easier to operate the high-speed camera (Section 5.7) for extended durations, and allowed testing with the laboratory lights turned off. The testing platform was constructed by mounting a truss to a wheeled

table. The table was leveled with the use of jack screws and is quite stable. If necessary there are hardpoints on the floor for tiedown chains that can be employed to further restrain it, though such restraint was not necessary during the testing plan.

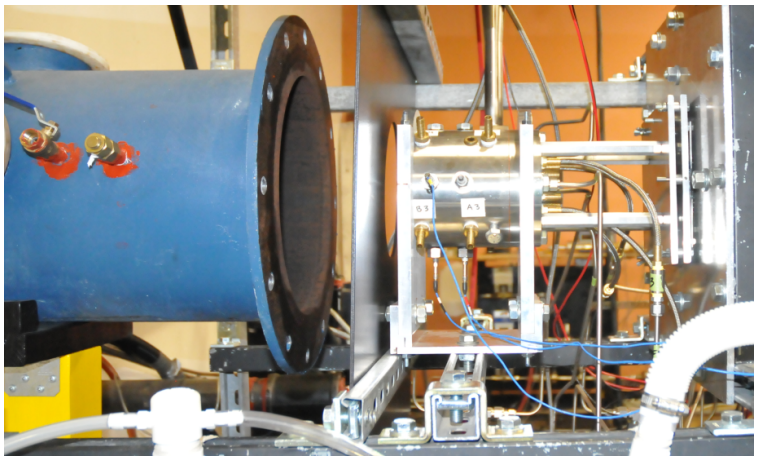

Figure 4.16. Positioning of Tunnel Extension.

To prevent the possibility of damage to the lab wall, a segment of the wind tunnel into whose vacuum tank Arthur is firing was mounted to the wall flange. This brought the exit plane of the engine closer to the tunnel, reducing the risk of damaging the wall, particularly before the startup process was understood or the exhaust plume had been observed. Figure 4.16 shows the tunnel extension's position relative to the engine exit plane. The extension was left in place for the early testing plan, but was removed to enable the installation of the mirror assembly prior to the down-engine high-speed camera tests, after it had been established that there was no risk to the wall.

4.3.1 Experimental Setup

A scale schematic of the experimental setup is given in Fig. 4.17. For clarity, fasteners have been omitted.

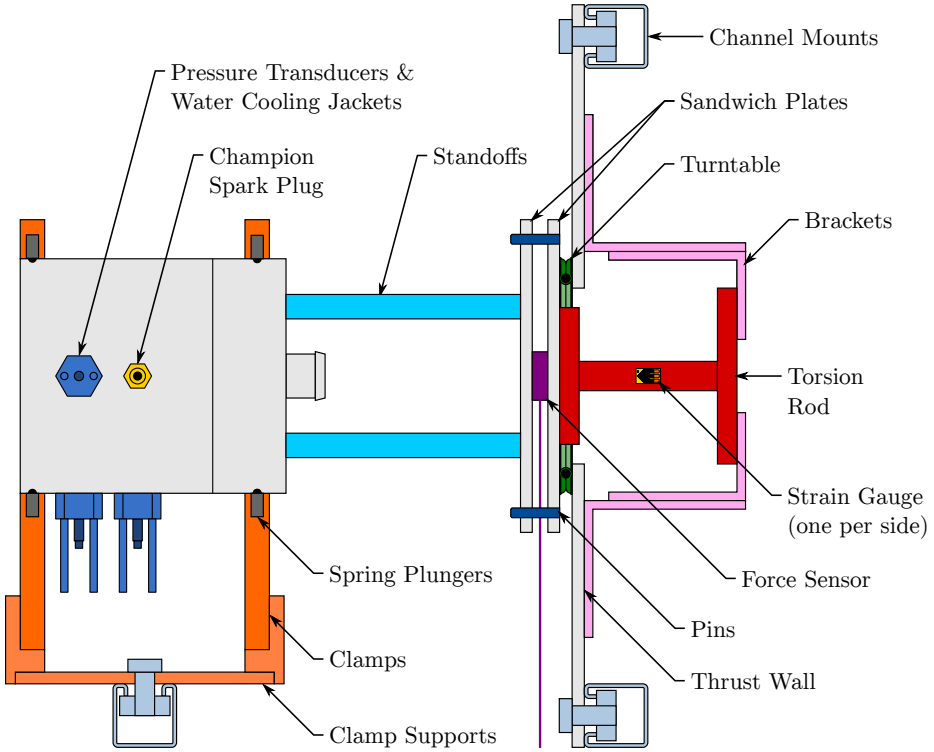

Figure 4.17. Annotated schematic of experimental setup.

In order to measure both thrust and torque, the experimental setup must allow for both translation and rotation. Rather than using frictionless rails (which only allow translation), Arthur is supported at the front and back by circular clamps, Fig. 4.18, each of which is lined with six spring-nose ball plungers. Ball-nose spring plungers were reported by Bello [236] to reduce friction in a PDE-Linear Power Generator system; their use here allows the engine to both translate and rotate. The upper and lower ball plungers have different spring forces, as the lower plungers must support the weight of the engine, but the upper ones serve only to keep the engine

in place. Additionally, if thrust measurements are not necessary, the plungers can be either removed or screwed into the clamps so that the balls are below the surface, and the clamps tightened around the engine to fix it in place.

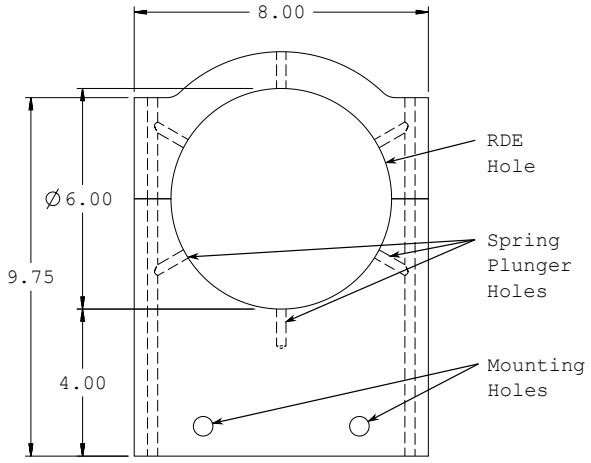

Figure 4.18. RDE clamp (dimensions in inches).

The clamps were originally designed to mount to separate channel supports, but this configuration made alignment difficult. Instead, the clamps are mounted to a supporting plate, which attaches to a single supporting channel member, as seen in Fig. 4.17.

4.3.2 Thrust and Torque Measurements

Thrust is measured by a PCB® 201B03 dynamic quartz force sensor. To accommodate the propellant and coolant lines at the head end of the engine (in particular the centerbody coolant return hose, which has a large diameter and cannot bend tightly), four 6 in long, 5/8 in hex standoffs are used to offset the thrust sensor from the face of the engine. PCB quartz force sensors must be preloaded to function properly. However, as the full engine must be free to rotate, the sensor cannot be

preloaded against the thrust wall. Instead, the sensor is placed between two 8 in diameter sandwich plates, with the preloading provided by tightening the force sensor between them. The preload force is determined by tightening two 1/4 in bolts. The tightening torque $\mathcal{T}$ necessary to provide a given clamping force F is given by

$$\mathcal{T} = K \cdot d \cdot F \tag{4.2}$$

where d is the nominal bolt diameter and K is an empirical constant termed the "nut factor", representing the friction between the nut and the bolt [239]. For a clean, dry (non-lubricated), zinc-plated bolt, $K = 0.2$ is typical. Therefore, to provide the necessary 200 lb preload with a 1/4 in, a torque of $10\,\text{in} \cdot \text{lb}$ is necessary. As there are two bolts, each bolt was loaded to half of this value, $5\,\text{in} \cdot \text{lb}$. Torque preload to the bolts is provided by a CDI® (Consolidated Devices Inc.) 361SM torque screwdriver. To prevent excessive preloading of the force sensor, the closest available setting on the torque screwdriver that did not exceed $5\,\text{in} \cdot \text{lb}$ was used: $4.8\,\text{in} \cdot \text{lb}$. Therefore, the total preload applied was $192\,\text{in} \cdot \text{lb}$. To prevent rotation of the plates with respect to each other, they are connected by two pins in addition to the bolts for preloading. Rotational freedom between the plates and the thrust wall is provided by a lubricated corrosion-resistant turntable.

Torque measurements are taken by measuring the strain in a rod with one end fixed in the engine and the other to the thrust wall. The rod is attached at the front to the second sandwich plate, which—due to the spring plungers and turntable—rotates with Arthur. It passes through a central hole in the thrust wall, and is fixed at the back with brackets attached to the thrust wall. This arrangement can be seen at the right side of Fig. 4.17, and was chosen to prevent the torsion rod from being subjected to any additional stresses which would need compensation. As the engine experiences torque, the rod is subjected to torsion, which is measured by a

pair of Micro–Measurements® 187UV shear/torque strain gauges. Each strain gauge contains two shear-measuring elements. The use of two gauges, one on each side of the the rod, forms a full Wheatstone bridge and also serves to compensate for any bending stress which might be present in the rod. The strain gauge system connects to a National Instruments® SCC-SG04 Full Bridge Strain Gauge module. The module includes trimming potentiometers for calibration and to zero the system offset and plugs into a NI SC-2345 signal conditioning connector block. The calibration of the strain gauge measurements to applied torque is discussed in Section 5.3.

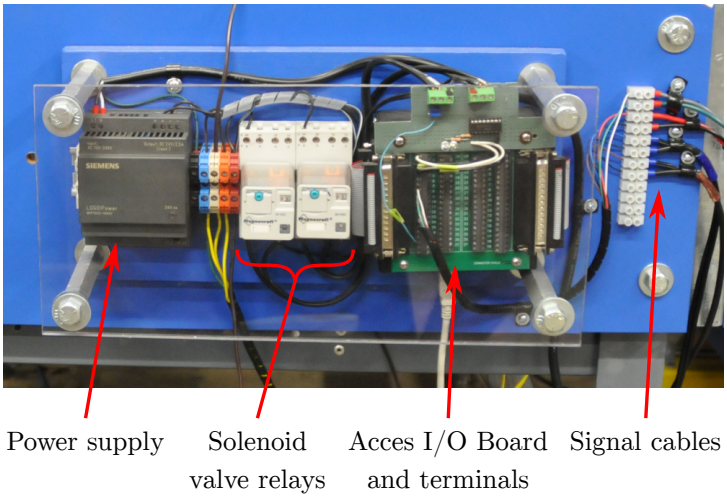

Figure 4.19. Engine valve control board.

4.3.3 Engine Control System

The engine operational cycle, including engine and igniter valve opening, DAQ triggering, and the spark signal, is controlled by an Acces® USB-A012-8E I/O board via a LabVIEW® control program. The engine control board, including both I/O board and engine valve relays can be seen in Fig. 4.19, and its circuit diagram is given as Fig. D.2 in Appendix D. The operational cycle timing diagram is given as

Fig. C.1 in Appendix C; cycle timings are given as Table C.1 in the same appendix. The method for calculating the engine fill times is given in Section 5.1.4.

4.3.3.1 Propellant Supply & Control

Propellants are supplied by a single fuel or oxidizer bottle per line and are controlled by an existing gas cart. For each line, the gas cart provides a pneumatic valve for master flow control, a straight-tube "flowmeter" with an Omega® PX302–200AV static pressure transducer and type T thermocouple, a check valve, and a flash arrestor. Pressure and temperature measurements are used to determine stagnation properties and mass flow rates. Details of the flow rate calibration are given in Section 5.1. All lines from the propellant bottles to the distribution manifolds are 1/2 in; lines from the manifolds are 1/4 in. Like the spark cutoff switch, the pneumatic valves are remotely operated from the ARC control room. To provide an additional safety precaution and prevent accidental propellant flow through the system, they are opened just prior to every test and closed immediately thereafter. When blowing down the line after testing to relieve pressure, the bottles are always closed and the spark box is turned off.

Engine propellant injection is governed by two 300 psi Parker® 1/2 in port two-way brass solenoid valves, which are independently controlled through the Acces I/O board. The propellant distribution panel can be seen in Fig. 4.20. Fuel lines connect to the engine by flexlines; oxidizer lines are hardlines from the manifolds to the engine. This was done for cost reasons; oxygen-rated flexlines were not available for this project. The routing of the oxygen lines was done so as to provide as much play as possible.

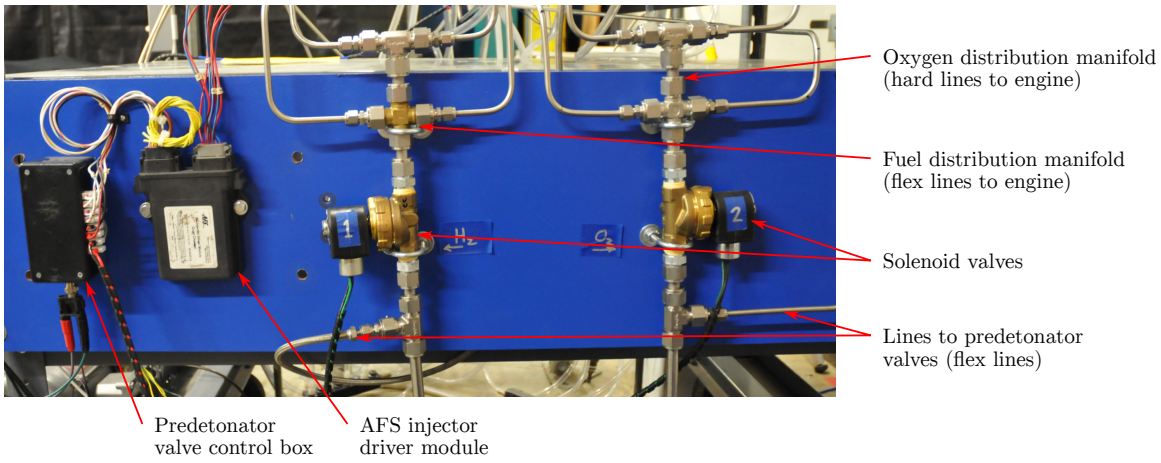

Figure 4.20. Propellant distribution panel and AFS valve control modules.

4.3.3.2 Igniter Control System

Igniter propellant is controlled by two IMPCO® Gs2 gaseous fuel injectors, controlled by a 4-channel AFS® Injector Driver Module. The details of the igniter flow rate calibration are given in Section 5.1. To trigger injector valves, a new trigger box was built, which significantly improves on the previous ones used at the ARC. The circuit diagram for this new trigger box is given as Fig. D.1 in Appendix D. The trigger box and injector driver are mounted to the propellant distribution panel, and can be seen in Fig. 4.20.

4.3.4 Coolant System

Coolant flow for the RDE consists of water provided by a Liquiflo® 620 series centrifugal pump. This pump is capable of a maximum flowate of 45 gal/ min and a maximum differential head of 65 ft. To allow long-duration tests (greater than 1 min in duration at maximum water flowrate), a coolant storage tank of approx 100 gal is required. A disused detonation tube dump tank was found to be the correct size. It was located outside (where there is more room), and the pump inside (away from the

elements, where the floor is level and it can be secured to the ground if necessary). The two are linked by a 1 in ID suction hose, with a ball valve at each end. This allows the suction hose to be detached so the overhead door can be closed when not testing, while not draining the tank or losing prime on the pump. Before being moved into place, the coolant tank was washed out to remove any old dirt or grime from the inside.

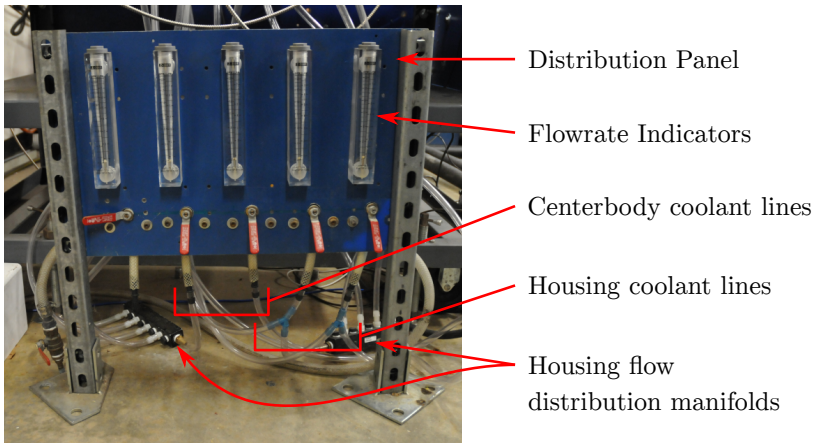

Figure 4.21. Coolant distribution system.

The coolant distribution system is shown in Fig. 4.21. The two rightmost ports on the blue distribution panel each split in two with a blue barbed wye connector, these four lines supply the housing coolant flow channels. The two ports to the right of these each connect to a centerbody coolant distribution manifold, seen in black with white plastic fittings. Lines are 1/2 in OD $\times$ 3/8 in ID nylon hose for both the inflow and return flow (except the centerbody return flow line, which is 1 in OD, as previously described). Steady-state flowrates for each line are read off the distribution panel (to a maximum of 2 gal/ min).

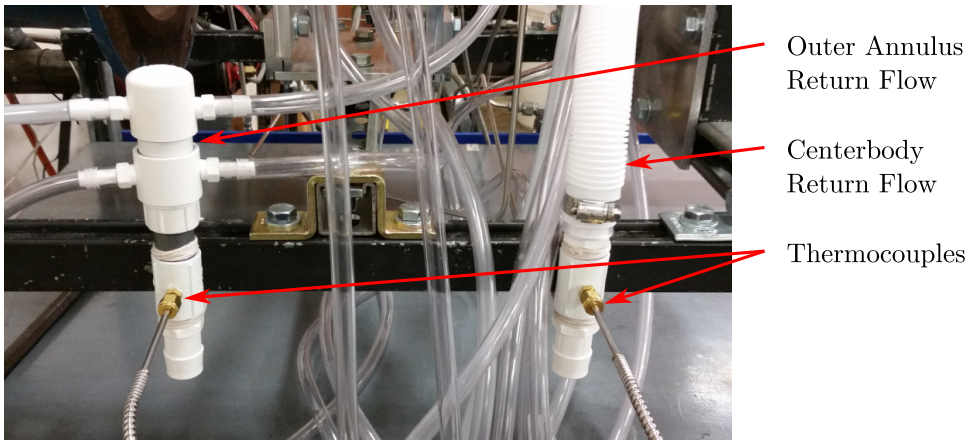

Figure 4.22. Instrumented coolant return system.

The engine is instrumented to be able to determine heat transfer calorimetrically using the coolant mass flow rate and the input and exit temperatures. Coolant flow input temperature is measured at the pump exit, and exit flow temperature for the inner and outer annuli are measured separately by thermocouples on the return flow. The centerbody coolant return flow, which comes through a single hose, is measured directly. However, coolant flow through the four outer-annulus channels returns separately. These four return flows are mixed together, and the temperature of this mixed flow is measured by a thermocouple. The configuration of this return flow is seen in Fig. 4.22. All thermocouples are type J.

4.3.5 Plumbing and Instrumentation Diagrams

The plumbing and instrumentation diagrams for the experimental setup are given in Appendix E.

4.3.6 Engine Instrumentation

The engine is instrumented with three PCB 111A24 pressure transducers, numbered P_1–P_3, mounted in PCB 064B02 flush-mounted water-cooling adaptors. Trans-

ducers P_1 and P_2 are at the same axial distance from the injector face at a 90° offset, with the third (P_3) aligned circumferentially with P_2 but spaced 1.5 in closer to the injection plane. The axial and circumferential placements of the transducers and igniters are illustrated in Fig. 4.23.

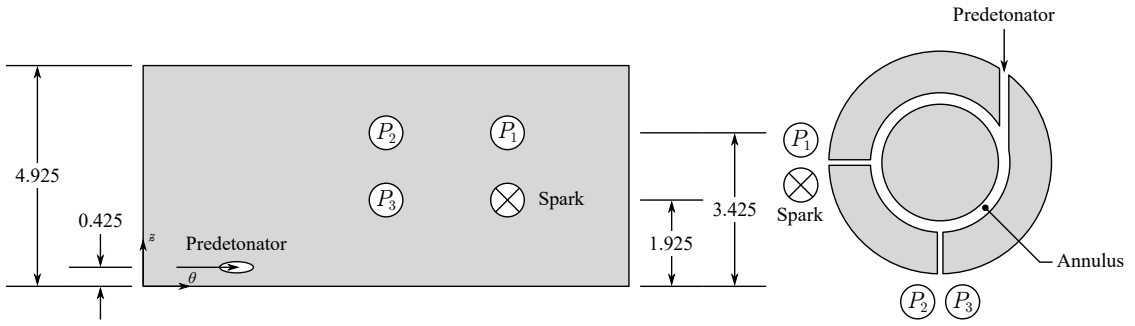

(a) Axial placement (unrolled annulus, dimensions in inches) (b) Circumferential placement

Figure 4.23. Instrumentation and igniter locations.

4.3.7 Data Acquisition Systems

Data are acquired using two data acquisition systems: a high-speed system for engine pressure and thrust measurements, and a low-speed system for gas cart, coolant temperature, and strain measurements. Both DAQ systems are triggered by the LabVIEW control program according to the pre-specified timing (Appendix C). For ease of organization, all data files use a date-time string file name convention.

High-speed data acquisition is conducted by a National Instruments PXI system. High-speed data signals are conditioned by a PCB Model 483A ICP® signal conditioner and sent to a National Instruments TB-2709 terminal base, which connects to a NI PXI-6133 S-series multifunction DAQ module mounted in a PXIe-1065 chassis (a second TB-2709/PXI-6133 unit receives the high-speed DAQ trigger). The

data acquisition is controlled by a NI PXIe-8130 Embedded Controller; data are written to an external NI HDD-8263 RAID array.

The PXI-6133 DAQ module is capable of sampling at 2.5 MHz, but early tests revealed a memory limitation. High sampling rates resulted in files too large to be written to the RAID drive. After consultation with engineers at National Instruments, the culprit was found to be the DAQ Assistant (and `lvm` file format) in the high-speed LabVIEW DAQ program. The LabVIEW program was then rewritten using base DAQmx functions and the `tdms` (Technical Data Management Streaming) file format: base DAQmx functions are more memory-efficient (and allow for more customization), and `tdms` is a National Instruments file format optimized for saving large amounts of data to a disk [240]. The rewritten LabVIEW program is capable of taking data at $f_{HS} = 1\,\text{MHz}$ for test durations of up to 2 s or $f_{HS} = 2\,\text{MHz}$ for test durations of 1 s or less.

The low-speed DAQ system is run on the same Dell Optiplex 7010 PC that runs the experimental control program. Data cables for pressure and temperature measurements as well as the low-speed trigger are connected to a National Instruments SCB-68 shielded signal conditioning block which connects to a PCI 6024E DAQ card. Strain data are conditioned by the aforementioned NI SC-2345 connector block connected to a PCI 6023E DAQ card. However, the number of PCI ports on the Optiplex PC motherboard is limited, so the 6023E DAQ card connects to the test PC through a StarTech PEX2PCI4 PCI Express-to-4 Slot PCI expansion box. Sampling parameters are entered and data results displayed in a dedicated LabVIEW program for the low-speed measurements. Both the low-speed DAQ cards are capable of a maximum sampling rate of 200 kHz, but a downside of using the StarTech PCI expansion box is that it limits data transfer rates. Therefore, to prevent the data acquisition program from crashing, a much lower sampling rate was used; generally

$f_{LS} = 1\,\text{kHz}$. All low-speed data traces are saved to a single `lvm` file per experiment. Additionally, to provide a zero reading for the strain gauge, gas cart stagnation pressure and temperature, and coolant line temperature measurements, a "gas cart" file was taken prior to every test at 5 kHz for 1 s.

4.3.8 Reflected Shock Attenuation

Early experiments revealed that a starting shock wave is generated upon RDE ignition. This starting shock wave reflected off the back of the dump tank and back out on the engine itself. This had the effect of pushing the exit flame back towards the front of the engine and onto the coolant tubes and instrument cables. To prevent the flame impinging on the instrument cables, a blast shield is mounted behind the engine exhaust plane. The blast shield is constructed from 1/4 in thick aluminum with a 7 in hole for the engine to fire through, and coated with high-temperature paint. It is sized to shield the predetonator in addition to the RDE itself, and can be seen as the black screen behind the mounted igniter assembly in Fig. 4.13

Additionally, to attenuate the shock wave reflecting off the back of the dump tank, a triangular shock wave deflector is constructed and mounted inside the dump tank. The first deflector is constructed from 1/4 in plywood and is 4 ft tall, the top 3 ft of which are covered with 1 in thick triangular-ridged acoustic foam. It works extremely well and almost completely eliminates the effects of the reflected shock wave, but the repeated shock impacts caused it to fall apart after several months of use, totaling 54 tests. A second deflector is therefore constructed out of 1/2 in plywood and significantly reinforced. It is constructed to the same approximate dimensions, but to make it easier to replace the acoustic foam in the event of future damage, it is mounted to removable panels. For additional shock absorption, rubber washers are placed between the removable panels and the body of the deflector. At the conclusion

of the test plan, the updated shock wave deflector has withstood 513 tests without any noticeable damage. Figure 4.24 shows this deflector installed in the dump tank.

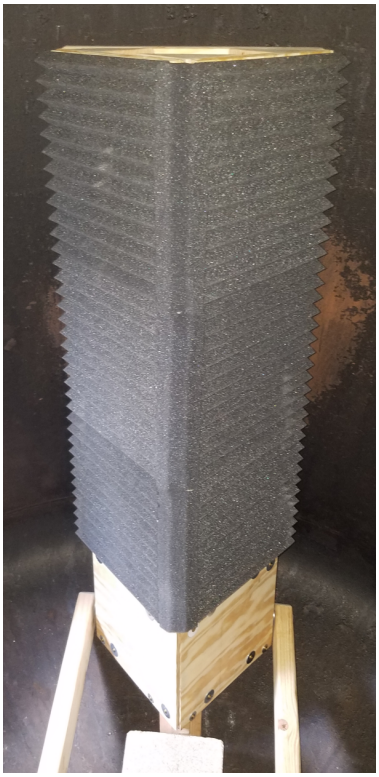

Figure 4.24. Shock wave deflector.

CHAPTER 5

TESTING OF A ROTATING DETONATION ENGINE

5.1 Propellant Flow Calibrations

As propellant flows are governed entirely by propellant bottle regulator pressures it is necessary to calibrate the propellant mass flow rates to set equivalence ratios and determine cycle timings. Calibration is accomplished by connecting an Omega FMA-1623A-VOL flowmeter in each successive line between the gas cart and the propellant control valves. Pressure and temperature measurements are obtained from the pressure transducers and thermocouples on the gas cart. Separate calibrations are run for both the fuel (hydrogen) and oxidizer (oxygen) lines for each of the main engine and the predetonator igniter lines. However, for safety reasons, nitrogen is used for all flow rate calibration tests.

Engine flow calibrations are performed with the engine solenoid valves open. A ball valve is placed after the mass flow meter to control gas flow. The data acquisition program is started and data are collected for five seconds, at which point the ball valve is opened. Gas is allowed to flow until the flow meter reading stabilizes (an additional 15–25 s, increasing with line stagnation pressure), at which point the ball valve is closed. Data are collected from the gas cart pressure transducer and thermocouple for the appropriate line at 5 kHz per channel. The stagnation pressures and temperatures in the lines are obtained by averaging the first 4 s of the data files (before the ball valve is opened); the steady-state static properties are obtained by averaging the final 4 s of the pressure and temperature data. A DIN-8 cable to connect the flow meter to a computer is not available, so stabilized flow rates are manually read from the

display and recorded. The predetonator igniter tests are performed similarly, but without the need to use the ball valve. For consistency, it is left on the line, but left open. Instead, the igniter valves are programmatically triggered by the control program after an initial 5 s delay; steady flow rate readings are obtained after 15–20 s.

As the critical condition for choked flow

$$P_0 \geq P_b \left(\frac{\gamma + 1}{2} \right)^{\frac{\gamma}{\gamma - 1}} \tag{5.1}$$

is met for line stagnation pressures greater than 13.13 psig (for diatomic gases with back pressure $P_b = 14.7$ psia), flow measurements are made at bottle regulator pressures from 15–100 psi in 5 psig increments. Calibrations for both fuel lines are performed in two full low-to-high sweeps, conducted consecutively on the same day. However, the higher flow rates through the engine oxygen line depleted the propellant bottles much faster than the others and required higher bottle pressures to maintain steady flow rates. Limited nitrogen supplies prevented two full sweeps from being conducted in one day for the oxygen lines. Instead, partial sweeps conducted over three days are combined into a single dataset for the engine flow, and only a single sweep is possible for the predetonator flow.

The ideal steady mass flow rate is computed using the choked mass flow parameter

$$\dot{m}_{id} = A \frac{P_0}{\sqrt{T_0}} \sqrt{\frac{\gamma}{R}} \left(\frac{\gamma + 1}{2} \right)^{-\frac{\gamma + 1}{2(\gamma - 1)}} \tag{5.2}$$

where the critical area for sonic flow is calculated using the smallest measurable diameter between the propellant bottles and the solenoid valves on the flow distribution panel. For the oxygen line, this is the bottle nipple (for the nitrogen bottle, inner diameter $d_i = 0.237$ in); for the hydrogen line, this is a short length of 1/4 in tube just after the pressure regulator ($d_i = 0.155$ in).

The ratio between the actual measured mass flow rate $\dot{m}_{act}$ and the ideal mass flow rate yields the discharge coefficient of the line, which is pressure-dependent

$$c_d = \frac{\dot{m}_{act}}{\dot{m}_{id}} \tag{5.3}$$

The discharge coefficients for the fuel and oxidizer lines for each calibration are shown in Fig. 5.1. The oxygen line discharge is higher than those for the hydrogen lines for both engine and predetonator tests (with the exception of $P_0 \lesssim 20\,\text{psig}$). Of note, however, is that there is significantly more variation to the oxygen line data, particularly in the range $50\,\text{psig} < P_0 < 65\,\text{psig}$; the reasons for this variation are unknown. An outlier detection test is performed using Chauvanet's criterion on the linear-region engine oxygen line data (see Section 5.1.2); no points met the criterion for elimination.

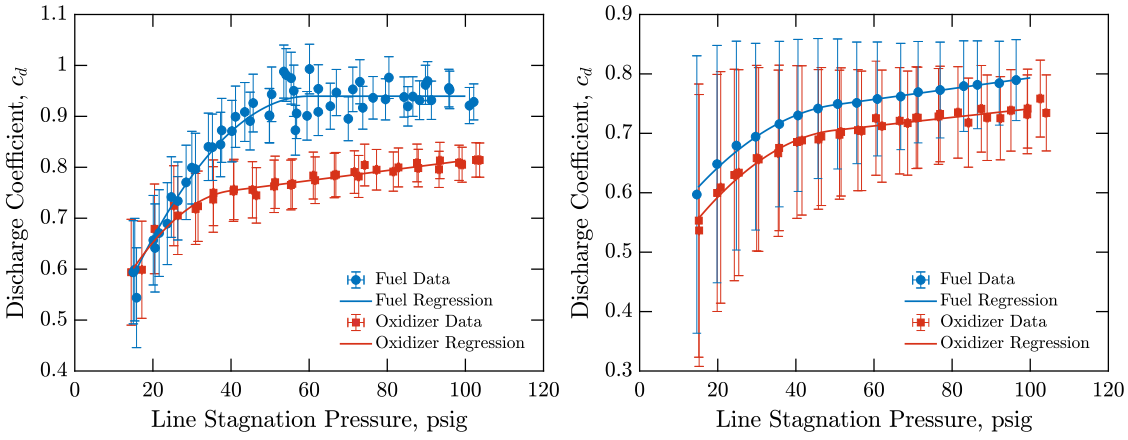

(a) Engine lines (b) Predetonator igniter lines

Figure 5.1. Calibrated steady-flow discharge coefficients.

5.1.1 Uncertainty Analysis of Flow Rate Calibrations

An uncertainty analysis is performed on the flow rate calibration data. Component uncertainties are obtained for each term in Eq. (5.2) and propagated to the ideal mass flow rate by Taylor series expansion [241]

$$u_{\dot{m}_{id}} = \pm \left[(\theta_{P_0} u_{P_0})^2 + (\theta_A u_A)^2 + (\theta_{T_0} u_{T_0})^2 \right]^{1/2} \tag{5.4}$$

where θ_i is the sensitivity index for variable x_i

$$\theta_i = \frac{\partial \dot{m}_{id}}{\partial x_i} \tag{5.5}$$

As the stagnation properties P_0 and T_0 are determined by averaging a range of data, the second-order uncertainties $u_{P_0} = u_{2_{T_0}}$ and $u_{T_0} = u_{2_{T_0}}$ are used; the uncertainty in area u_A is determined by uncertainty propagation using the uncertainty in choking diameter measurements.

The design-stage uncertainty in the actual mass flow rate $u_{\dot{m}_{act}}$ is obtained from the mass flow meter specifications and combined with the ideal mass flow rate uncertainty to determine an uncertainty in the discharge coefficients

$$u_{c_d} = \pm \left[(\theta_{\dot{m}_{act}} u_{\dot{m}_{act}})^2 + (\theta_{\dot{m}_{id}} u_{\dot{m}_{id}})^2 \right]^{1/2} \tag{5.6}$$

The uncertainties in line stagnation pressure u_{P_0} and discharge coefficient u_{c_d} are plotted as error bars in Fig. 5.1. The uncertainties in pressure are very small, and in general not visible behind the data markers. However, the uncertainties in discharge coefficients are large, especially for the igniter flow calibrations. This is driven almost entirely by the uncertainty in actual mass flow rate. The zero-order uncertainty of the flowmeter is relatively large (display resolution of 0.001 kg/min), but much more significant is the instrument uncertainty. The flowmeter accuracy is specified as 0.8 percent of the reading, plus 0.2 percent of the full-scale range of

the instrument. The flowmeter employed in these calibrations is the largest of the Omega FMA-1600 series, with a full-scale range of 15.880 kg/min of nitrogen; observed flow rates are between 0.2 and 1.22 kg/min for the engine lines and 0.08 and 0.4 kg/min for predetonator lines. Therefore, the observed flow rates (particularly for the predetonator) are in the extreme low range of the flowmeter, resulting in an extremely large contribution to the measurement uncertainty due to these effects: between 53.2 and 90.2percent of the total uncertainty for engine lines measurements and between 53.2 and 94.5percent for predetonator measurements.

5.1.2 Regressions

To enable prediction of discharge coefficients (and therefore mass flow rates and equivalence ratios), a least-squares regression is fitted to the data. The data indicate that for both the oxygen and hydrogen lines, the discharge coefficient increases non-linearly until a critical pressure P_{cr} is reached, at which point the increase becomes linear. A piecewise regression is therefore employed: above the critical pressure, a linear regression is utilized

$$c_d = \alpha P_g + \beta \tag{5.7}$$

and below the critical pressure, a second-order polynomial regression is employed

$$c_d = aP_g^2 + bP_g + c \tag{5.8}$$

To compute the coefficients of the second-order polynomial, three constraints are required. These are taken as

1. $c_d(P_{g_2}) = c_{d_2}$
2. $c'_d(P_{g_2}) = \alpha$
3. $c_d(P_{g_1}) = c_{d_1}$

where points 1 and 2 correspond to the lower and upper bounds of the nonlinear pressure region, respectively ($P_{g_1} = 15\,\text{psig}$ and $P_{g_2} = P_{cr}$) and α is the slope of the function at the upper bound. The first two constraints are chosen to prevent discontinuities: the magnitude and slope of the nonlinear region at the critical pressure should be identical to that of the linear region. Therefore, the regression of the linear region is performed first, and once the coefficients α and β are determined, $c_d(P_{cr})$ can easily be calculated by Eq. (5.8). Note that while both igniter lines and the fuel engine line both showed linear regions with positive slopes, no such trend is apparent in the engine oxidizer calibration. Instead, though noisy, the discharge coefficient appears to be approximately constant above the critical pressure. Therefore, for that case, $\alpha = 0$ and β is simply the average of the discharge coefficients in the linear region.

The final constraint, the magnitude of the discharge coefficient at the lower pressure boundary P_{g_1}, is determined by finding the value of $c_d(P_{g_1})$ which gives the minimum residual sum of squares (RSS) for the second-order polynomial regression. This is computed numerically using the Golden-Section Search method [242] (convergence by golden-section search is linear, and is achieved in approximately 50 iterations). Once obtained, the coefficients of the nonlinear regression are given by Eqs. (5.9a)–(5.9c)

$$a = \frac{(c_{d_1} - c_{d_2}) - \alpha\,(P_{g_1} - P_{g_2})}{(P_1 - P_{g_2})^2} \tag{5.9a}$$

$$b = \alpha - 2aP_{g_2} \tag{5.9b}$$

$$c = c_{d_2} + P_2\,(aP_{g_2} - \alpha) \tag{5.9c}$$

The coefficients for each regression are given in Table 5.1 and the critical pressures and goodness-of-fit parameters are given in Table 5.2.

Table 5.1. Regression coefficients

		Nonlinear			Linear	
Type	Line	a (psig^{-2})	b (psig^{-1})	c	α (psig^{-1})	β
Engine	Oxidizer	-1.740×10^{-4}	2.088×10^{-2}	0.313	0	0.940
	Fuel	-2.049×10^{-4}	1.738×10^{-2}	0.387	9.893×10^{-4}	0.714
Igniter	Oxidizer	-8.732×10^{-5}	9.639×10^{-3}	0.484	9.063×10^{-4}	0.703
	Fuel	-1.011×10^{-4}	1.084×10^{-2}	0.416	7.216×10^{-4}	0.669

Table 5.2. Critical pressures and goodness-of-fit parameters

			Nonlinear		Linear	
Type	Line	P_{cr} (psig)	RSS	R^2	RSS	R^2
Engine	Oxidizer	60	2.400×10^{-2}	0.952	5.878×10^{-4}	0.952
	Fuel	40	2.295×10^{-3}	0.931	4.553×10^{-5}	0.896
Igniter	Oxidizer	50	2.486×10^{-4}	0.987	1.957×10^{-6}	0.990
	Fuel	50	1.091×10^{-3}	0.967	6.569×10^{-5}	0.696

5.1.3 Equivalence Ratio and Flow Rate Maps

Using the regressions obtained in Section 5.1.2, steady-state engine flow rates and equivalence ratios could be determined. Using Eq. (5.2) and the discharge coefficients, fuel (hydrogen) and oxidizer (oxygen) flowrates are determined for a range of line stagnation pressures by

$$\dot{m} = c_d A \frac{P_0}{\sqrt{T_0}} \sqrt{\frac{\gamma}{R}} \left(\frac{\gamma + 1}{2} \right)^{-\frac{\gamma+1}{2(\gamma-1)}} \tag{5.10}$$

The resulting equivalence ratio and total propellant mass flow rate maps are given in Fig. 5.2 and Fig. 5.3, respectively. For these maps, the stagnation temperature is taken as 85 °F (302.6 K).

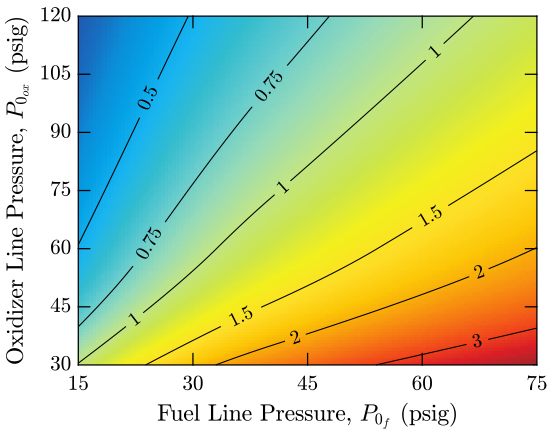

Figure 5.2. Equivalence ratio map.

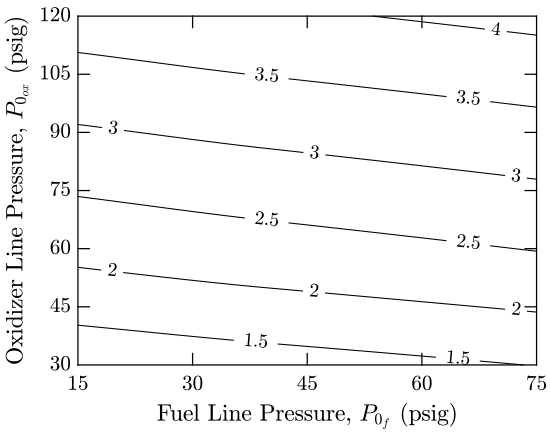

Figure 5.3. Total propellant mass flow rates in kg/min.

5.1.4 Determination of Cycle Timings

The flow rate calibrations outlined here are used to determine the engine cycle timings seen in Fig. C.1 in Appendix C. Given a specified fuel and oxidizer pressure, mass flow rates for each propellant are determined by Eq. (5.10). Then, the volumentric flow rate is obtained by

$$\dot{\mathscr{V}} = \frac{\dot{m}}{\rho} \tag{5.11}$$

where the propellant density is computed assuming choked flow of an ideal gas

$$\rho = \frac{P_0}{RT_0}\left(\frac{\gamma+1}{2}\right)^{\frac{1}{1-\gamma}} \tag{5.12}$$

Fill times are determined from the volumetric flow rate and the sum of the maximum line volume between the engine control valves and the injection plenum and one-half of the fluidic valve plenum volume (engine, Eq. (5.13)) or one-half of the predetonator internal volume (predetonator igniter, Eq. (5.14)):

$$t_{fill,\,eng} = \frac{\mathscr{V}_{line} + 0.5\,\mathscr{V}_{plenum}}{\dot{\mathscr{V}}} \tag{5.13}$$

$$t_{fill,\,ig} = \frac{0.5\,\mathscr{V}_{igniter}}{\dot{\mathscr{V}}} \tag{5.14}$$

Though the engine control valves can be independently operated, the fuel valve is hardwired to open first. Therefore, the cycle timing is dependent on which engine fill time (oxidizer or fuel) is greater:

- If $t_{fill,\,eng_{ox}} \geq t_{fill,\,eng_f}$

$$t_{evd} = 0\,\text{ms}$$

$$t_{ivd} = t_{fill,\,eng_{ox}} - t_{iot}$$

$$t_{iot} = t_{fill,\,ig_{max}}$$

- If $t_{fill,\,eng_{ox}} < t_{fill,\,eng_f}$

$$t_{evd} = t_{fill,\,eng_f} - t_{fill_{ox,ig}}$$

$$t_{ivd} = t_{fill,\,eng_f} - t_{iot}$$

$$t_{iot} = t_{fill,\,ig_{max}}$$

where $t_{fill,\,ig_{max}}$ is the maximum of $t_{fill,\,ig_f}$ and $t_{fill,\,ig_{ox}}$. For spark plug operation, where the igniter valves remain closed throughout the cycle, the times are

- If $t_{fill,\,eng_{ox}} \geq t_{fill,\,eng_f}$

$$t_{evd} = 0$$

$$t_{ivd} = t_{fill,\,eng_{ox}}$$

$$t_{iot} = 0\,\text{ms}$$

- If $t_{fill,\,eng_{ox}} < t_{fill,\,eng_f}$

$$t_{evd} = t_{fill,\,eng_f} - t_{fill_{ox,ig}}$$

$$t_{ivd} = t_{fill,\,eng_f}$$

$$t_{iot} = 0\,\text{ms}$$

Table C.1 in Appendix C lists test pressures and cycle timings used in the test plan, as well as a labeled cycle diagram showing the definition of each cycle time variable, Fig. C.1. Those times use the raw times computed by the method outlined here, with the following empirical adjustments:

- Predetonator Igniter
  - Igniter Valve Delay Time (t_{ivd}): round up to the nearest millisecond and add 5 ms.
  - Igniter Valve Open Time (t_{iot}): round up to the nearest millisecond and add 1 ms.
- Spark Plug Igniter
  - Igniter Valve Delay Time (t_{ivd}): add 2 ms to the sum of the predetonator times.

5.2 Determination of Expected Detonation Properties

The detonation properties are strongly dependent on the properties upstream of the detonation wave, which are themselves a function of the Mach number of the flow in the chamber. Most RDE models, including the one detailed in Chapter 2, assume sonic flow through the injectors and in front of the detonation wave. However, unless the injectors are the full width of the annulus, the area change experienced by the flow downstream of the injectors will change the Mach number. It remains, then, to have a method of estimating the chamber properties so that the expected detonation properties can be predicted. In the analysis here, the assumption of choked injection ports is retained, but expansion into the chamber is accounted for by the Mach-area relation

$$\left(\frac{A}{A^*}\right)^2 = \frac{1}{M^2}\left[\frac{2}{\gamma+1}\left(1+\frac{\gamma-1}{2}M^2\right)\right]^{(\gamma+1)/(\gamma-1)} \tag{5.15}$$

where the total injector port area $A_{inj} = n_{inj}A_{hole}$ is taken as the sonic area A^* and the annular cross-sectional area is taken as A. For Arthur, $A/A^* = 5.46$ yields $M_{\mathrm{I}} = 3.27$. Once the chamber Mach number has been determined, the static pressure is obtained from the choked isentropic flow equation

$$P_{\mathrm{I}} = \overline{P}_0 \left(\frac{\gamma + 1}{2} \right)^{-\frac{\gamma}{\gamma - 1}} \tag{5.16}$$

in which $\overline{P}_0$ is defined as the mole-weighted average of the line stagnation pressures

$$\overline{P}_0 = \frac{P_{0_f} + \phi f_{st} P_{0_{ox}}}{1 + \phi f_{st}} \tag{5.17}$$

where f_{st} is the stoichiometric molar fuel-oxidizer ratio (note that this method is only valid for cases where both fuel and oxidizer have the same ratio of specific heats γ). The Chapman–Jouguet pressure P_{CJ} and velocity U_{CJ} are then determined from Cantera. The characteristic detonation frequency f_{CJ} is determined from the engine dimensions

$$f_{CJ} = \frac{C_m}{U_{CJ}} \tag{5.18}$$

where $C_m = 2\pi r_m$ is the circumference of the engine at mean radius.

5.3 Strain Gauge Calibration

Strain gauge calibration is performed with the engine dismounted by attaching a calibration flange head to the engine-side of the torque rod. The calibration flange has a hex nut welded at its center, and torque is applied to the this flange, via a socket over the hex nut, with a Husky® 625319 micrometer-adjustable torque wrench (40–200 $\mathrm{in \cdot lb}$ range, calibrated and accurate to ± 3 percent of clockwise reading). Torque is applied to the calibration flange, alternating clockwise and counterclockwise directions, in 100 $\mathrm{in \cdot lb}$ increments, over the full range of the torque wrench, 40 to 200 $\mathrm{in \cdot lb}$. Torque is designated as positive when it is clockwise about the axis of the engine, and negative when counterclockwise about the engine's central axis.

To capture the strain corresponding to the applied torque, data are taken at 1,000 Hz during the loading process. An unloaded measurement is taken immediately prior to taking each loaded data set; the zeroed strain readings are then determined by subtracting the mean unloaded reading from the loaded data file. The maximum (absolute) strain observed in the zeroed strain file before the torque wrench released is extracted and recorded as the loaded strain. Three sweeps are conducted over the full range of the torque wrench; these data are plotted in Fig. 5.4. A least-squares linear regression (vertical intercept set to 0; $r^2 = 0.9982$) is fit to the data yielding

$$\mathcal{T} = -8.7386\,\varepsilon \tag{5.19}$$

where torque has units of in · lb and strain has units of με.

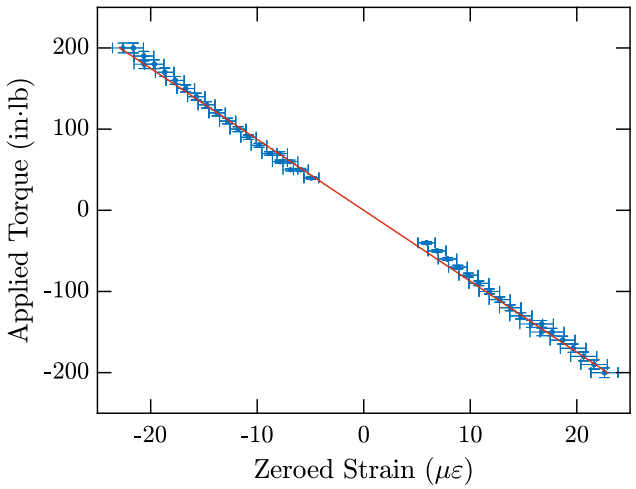

Figure 5.4. Strain gauge calibration.

As with the flow rate calibrations, an uncertainty analysis has been performed on this data. From the definition of the gauge factor GF, the strain is given as

$$\varepsilon = \frac{\Delta R}{GF \cdot R} \tag{5.20}$$

where R and ΔR here are the gauge resistance and elemental change in resistance due to the application of strain ε. Therefore, by error propagation, the instrument uncertainty in strain is determined by

$$u_{c_\varepsilon} = \pm \left[(\theta_{GF} u_{GF})^2 + (\theta_{\Delta R} u_{\Delta R})^2 + (\theta_R u_R)^2 \right]^{1/2} \tag{5.21}$$

The component uncertainties u_{GF} and u_R are given by the strain gauge specifications; $u_{\Delta R}$ is assumed negligible. In order to compute the sensitivity indicies θ_i, the values of each variable in Eq. (5.20) must be known, and ΔR is not. However, R, ε, and GF are known, so ΔR can be determined by rearranging Eq. (5.20) and using the known nominal values

$$\Delta R = \varepsilon \cdot GF \cdot R \tag{5.22}$$

The zero-order uncertainty in strain measurements is determined from the resolution of the DAQ as

$$u_{0_\varepsilon} = \pm \frac{1}{\sqrt{2}} \,\text{resolution} \tag{5.23}$$

where the factor of $1/\sqrt{2}$ is due to each zeroed strain measurement being determined from two un-zeroed measurements, each with identical resolution ($0.9829\,\mu\varepsilon$). It is worth noting that, despite maxing out the DAQ gain, the resolution remains poor, leading to relatively high uncertainty in strain measurements. This is due to the thickness of the torque rod: it is sized based on an early, erroneous version of the RDE model from Chapter 2, which predicted much higher torque values than the final model. The safety factor chosen for these higher torques ultimately led to the rod being too thick to have good response to the final required application. Compared to the relatively high strain uncertainty, the torque uncertainty is low and dominated by the instrument error (± 3 percent of wrench setting).

5.4 Test Matrix

For the experimental test plan, four primary experimental variables to consider are chosen. These are

1. Propellant flow pressure
2. Equivalence ratio
3. Injection swirl angle
4. Ignition method

The governing variable for propellant flow pressure is chosen as the fuel line stagnation pressure, which, combined with equivalence ratio, determines the necessary oxidizer line pressure. The fuel pressures chosen are 15–60 psig in increments of 15 psig (each increment therefore corresponding to an increase of approximately 1 atm). Equivalence ratios chosen are 0.50, 0.75, 1.0, 1.5, and 2.0, with a focus on the middle three values. Injection swirl angle is governed by injection plate: 0°, +30°, or −30°.

Table C.1 in Appendix C outlines the test pressures and cycle timings used for each injector plate. Note that, at higher fuel pressures, some test conditions are marked as not possible. This is due to the limitations of the pressure gauge on the oxygen regulator, which has a maximum range of 150 psig, and of the IMPCO injector valves, which have a rated maximum operational pressure of 116 psia.

5.5 Experimental Test Plan

Between October 17, 2017, and October 31, 2018, the engine was fired 625 times. The testing campaign can be broken down into 6 phases:

1. Preliminary shakedown testing (tests 1–41, October 2017–February 2018)
2. Early extended-duration testing (tests 42–55, March–April 2018)
3. Equivalence ratio variation testing (tests 46–89, April–May 2018)

4. Revised timing calibration testing (tests 90–112, June 2018)
5. Initial high-speed camera testing (test 113–350, June–August 2018)
6. Improved high-speed ignition visualization (test 351–625, October 2018)

The majority of these tests are conducted with a duration of $t_{test} = 500\,\text{ms}$, though tests are conducted at up to $t_{test} = 2\,\text{s}$ during Phase 2. Phases 1–4 are conducted using a Victor® regulator on the fuel line, which broke between tests 112 and 113. This is replaced with a Matheson® regulator, on which the final two-thirds of the experiments are conducted. This regulator is the one for which the fuel line calibration in Sections 5.1.2 is performed, and for which the largest quantity of data is taken. Considering this fact, and that there are no qualitative differences between the Phase 5 and 6 data and those from earlier testing, the analysis of the results will focus on these final two phases.

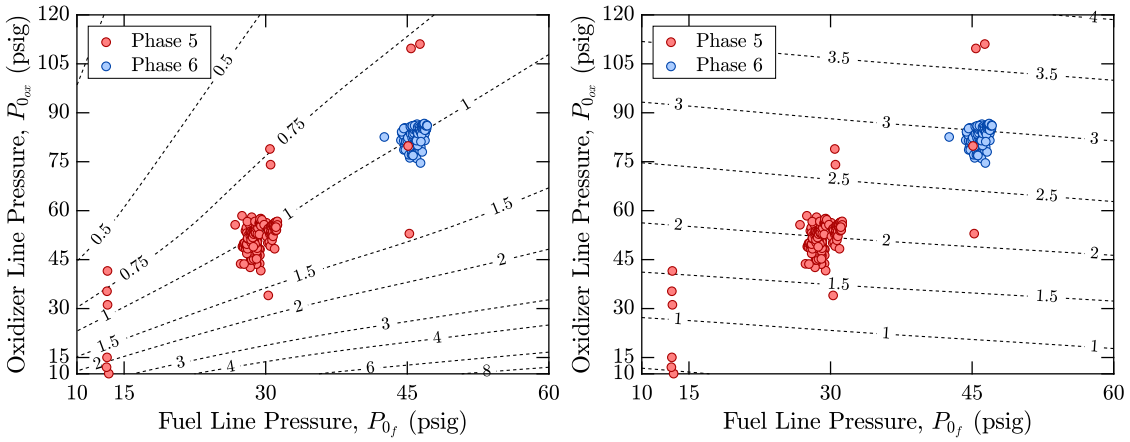

(a) On equivalence ratio

(b) On mass flow rate (kg/min)

Figure 5.5. Actual conditions of tests conducted in Phases 5 and 6.

Figure 5.5 shows the actual test conditions of each of the 513 tests in Phases 5 and 6, superimposed on contours of equivalence ratio ϕ (Fig. 5.5(a)) and total propellant mass flow rate $\dot{m}_{tot}$ (Fig. 5.5(b)). Phase 5 tests are largely conducted at fuel

stagnation pressure $P_{0_f} \approx 30\,\text{psig}$ and equivalence ratios near unity, with some exploration of the effect of varying equivalence ratio and injector pressure. Phase 6 tests are conducted at fuel stagnation pressure $P_{0_f} \approx 45\,\text{psig}$ and $\phi \approx 1.0$.

5.6 Analysis of Engine Performance Data

Throughout the test plan, very little qualitative difference is observed in the engine performance data. Therefore, in the following analysis, two tests characteristic of those seen during the experimental phase have been selected as representative: one where ignition is performed using the predetonator igniter (test 246) and one which uses the spark plug for ignition (test 302). Both tests are conducted at the same nominal conditions, $P_{0_f} = 30\,\text{psig}$ and $\phi = 1.0$; the actual conditions, as well as the the expected detonation properties (P_{CJ}, U_{CJ}, and f_{CJ}) computed by the method of Sec. 5.2, are given in Table 5.3. The results from these tests are characteristic of those observed throughout the test plan, but exceptions will be mentioned.

Table 5.3. Conditions of representative tests

Property	Units	Test 246	Test 302
Ignition method		Predetonator	Spark plug
Low-speed DAQ sampling rate f_{LS}	Hz	1,000	1,000
High-speed DAQ sampling rate f_{HS}	MHz	2.0	2.0
Fuel stagnation pressure P_{0_f}	psig	27.92	29.16
Oxidizer stagnation pressure $P_{0_{ox}}$	psig	49.56	55.59
Equivalence ratio ϕ		1.022	0.955
Total propellant mass flow rate $\dot{m}_{tot}$	kg/min	1.934	2.133
Detonation pressure P_{CJ}	atm	21.03	22.48
Detonation velocity U_{CJ}	m/s	2,876	2,823
Detonation frequency f_{CJ}	kHz	10.45	10.25

5.6.1 Pressure Measurements

As discussed in Sec. 4.3.6, pressure measurements within the annulus are taken using three PCB 111A24 high-frequency pressure transducers; Fig. 4.23. The intent of these transducers is to detect the rotating detonation front, and attempt to ascertain the number and direction of propagation of the waves. However, no steady rotating detonation is observed in any of the tests conducted during the test plan.

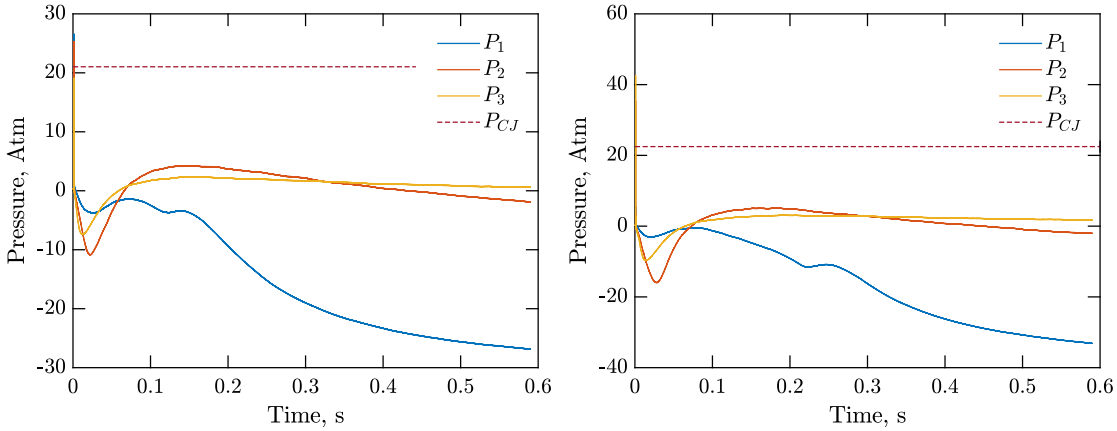

(a) Predetonator ignition

(b) Spark plug ignition

Figure 5.6. Full high-speed pressure traces.

Figure 5.6 shows the full pressure traces for both representative tests. Past an initial spike at ignition, there are no further significant pressure spikes throughout the test. These initial pressure spikes can be seen better in Fig. 5.7, which have been zoomed in to the time of and immediately after ignition. In both, the estimated Chapman–Jouguet pressure P_{CJ} has been overlaid. By inspection of Figs. 5.6 and 5.7, a detonation wave is clearly experienced by a majority of the pressure transducers in each test. This is the case for the majority of tests using both ignition types, particular for the predetonator. However, under some conditions, the spark plug failed to ignite a detonation detected by one or more transducers. Such a case can be seen in the P_1

trace in Fig. 5.7(b); more discussion of this behavior is in Section 5.7.2.3.2. However, in all cases, even when a detonation is observed, it does not continue to propagate, but instead decays into a deflagration.

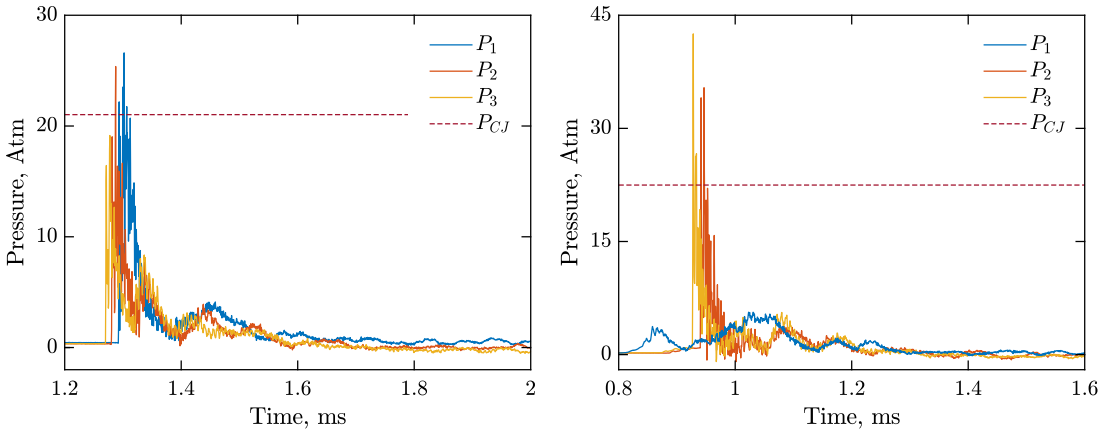

(a) Predetonator ignition

(b) Spark plug ignition

Figure 5.7. Zoomed pressure traces of ignition process.

Though no sustained detonations are directly observed in the pressure traces, it is nevertheless of interest to see if there are any characteristic frequencies present in data which might hint at underlying behavior. Therefore, spectrograms are created using the pressure data for both tests. To eliminate low-frequency noise and compensate for thermal drift, a 2$^{\text{nd}}$-order high-pass Butterworth filter with a cutoff frequency of 500 Hz is applied to the data; Fig. 5.8 presents the spectrograms for the predetonator test and Fig. 5.9 those for the spark plug test.

In both tests, a distinct band of frequencies can be seen in the 10 kHz range, particularly for the predetonator-ignition data; the band is much less well defined for the spark-ignition test, excepting P_1 (particularly interesting, considering that this transducer saw no detonation at all in the raw pressure data). This frequency corresponds precisely to the expected detonation frequencies from Table 5.3. It is also

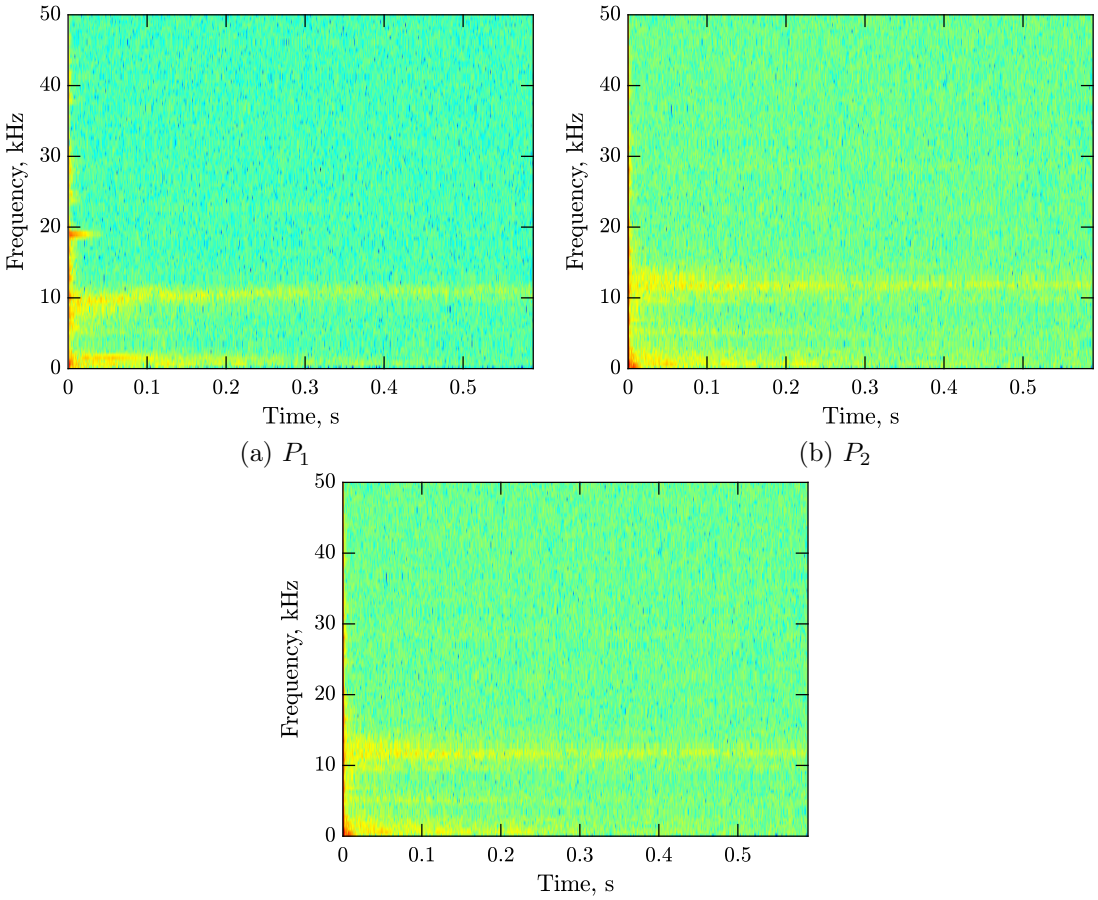

Figure 5.8. Spectrograms of filtered pressure data, predetonator ignition.

worth noting that in both P_1 spectrograms—but particularly for the spark test—the observed frequency appears to start below that frequency and increase towards it for the first 0.1–0.2 s of the test before steadying out. Though no periodic detonation is observed at the pressure transducers, these results indicate that there is a weak wave propagating around the annulus at the expected detonation frequency. Further investigations are necessary to determine the nature of this phenomenon.

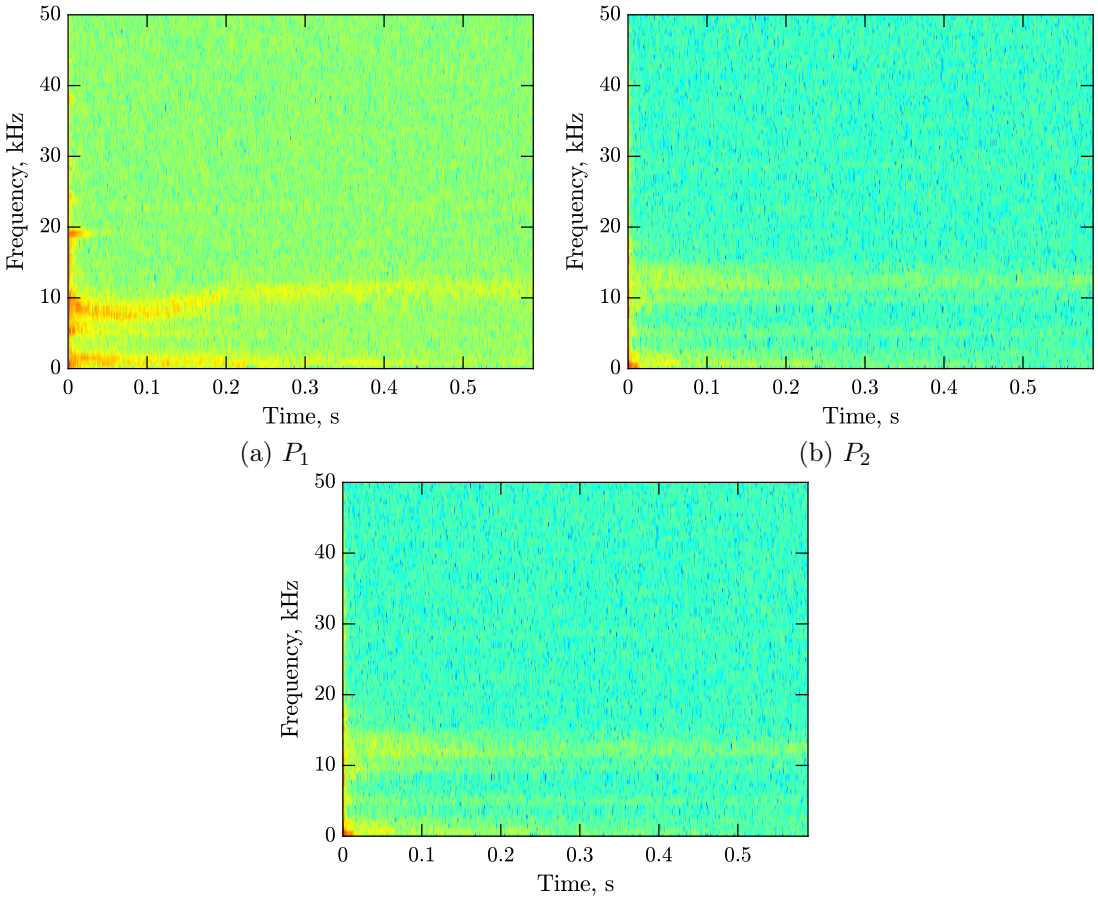

(a) P_1 (b) P_2

(c) P_3

Figure 5.9. Spectrograms of filtered pressure data, spark plug ignition.

5.6.2 Thrust and Torque Data

One of the stated goals of the research plan is to determine whether the rotating detonation phenomenon caused a torque, as detailed in Section 4.3.2. Torque is determined by measuring the strain in the strain gauges during the test. As with the strain calibrations, these readings are then zeroed using a reading taken immediately before every test; these zeroed strain readings are then converted to torque using Eq. (5.19). The torque readings measured for the two representative tests are shown in Fig. 5.10.

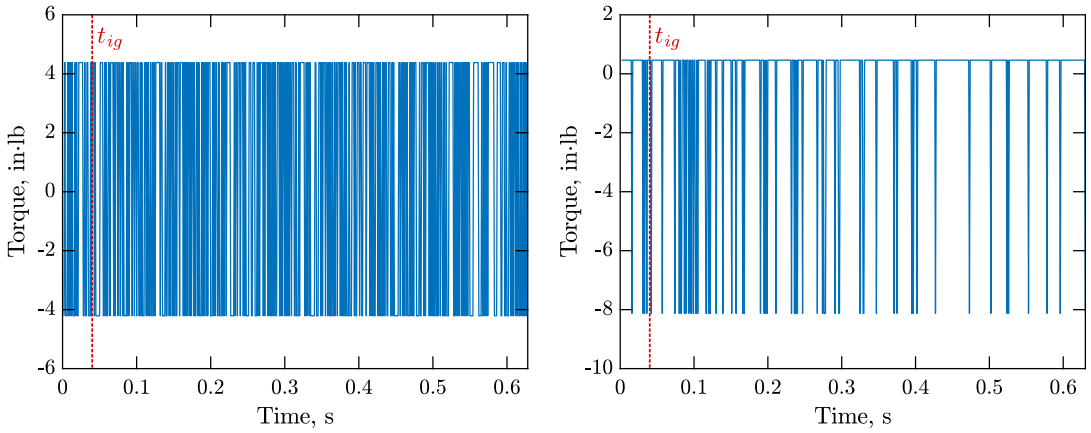

(a) Predetonator ignition (b) Spark plug ignition

Figure 5.10. Torque measurements.

The predetonator ignition case (Fig. 5.10(a)) shows no appreciable amount of torque. The signal is stationary within a single count of the DAQ symmetric about $0\,\text{in}\cdot\text{lb}$, and the average torque over the test is $0.326\,\text{in}\cdot\text{lb}$. The spark plug ignition case (Fig. 5.10(b)) appears to have some nonzero negative torque, but the signal is likewise stationary within a single count, and the average is also near zero, $-0.412\,\text{in}\cdot\text{lb}$. It is worth mentioning that as the strain signal is sampled on the low-speed data acquisition system, ignition occurs at approximately 40 ms; this point is labeled as t_{ig} on both figures. There is notably no apparent change in torque reading at or after the ignition time. These results are characteristic of those observed through the entire test plan. Some tests showed some occasional spikes outside of a single count, but those results are not repeatable.

There are multiple possible causes for the failure to record any useful torque readings. As previously mentioned, due to the thickness of the torque rod, the resolution of the strain readings is poor; future tests should use a thinner torque rod and/or one manufactured from a material with lower torsional stiffness (such as aluminum). Additionally, the ball-spring plungers, though reported by Bello [236] as

having reduced friction, did not do so nearly as expected. While the ball does reduce the contact area between the engine and its mounts, the bearing does not rotate, and therefore does not aid in transmitting rotation. These, and the aforementioned lack of flexible oxygen lines, combined to cause the engine facility to have significant internal friction, thereby substantially reducing the sensitivity of the torque measurements. It is also worth reiterating that the strain calibrations are designed to calibrate the strain gauges alone, and are therefore made by applying torque directly to the torque rod with the engine dismounted. They are not intended to quantify the internal resistance to rotation.

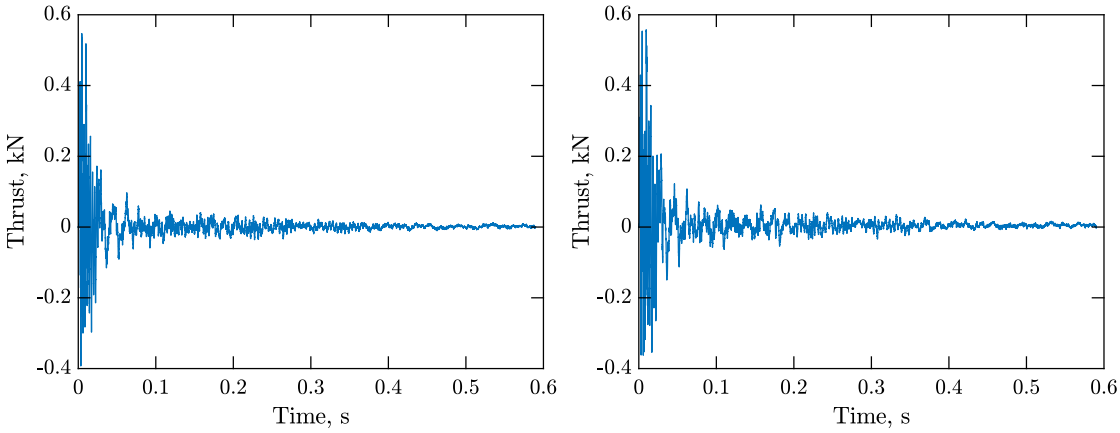

(a) Predetonator ignition

(b) Spark plug ignition

Figure 5.11. Thrust measurements.

For likely the same reasons as the failure to obtain good torque readings, the thrust measurements are similarly unenlightening. Figure 5.11 shows the thrust readings for the two representative tests. In both cases, the initial ignition causes a high-magnitude, noisy response, which rapidly dies out by the first 0.1 s. Damped oscillations are clearly present in the data, so the same 2^{nd}-order high-pass Butterworth

filter (cutoff frequency 500 Hz) is applied to the thrust data as is used on the pressure data. Spectrograms of this filtered signal are generated and displayed in Fig. 5.12.

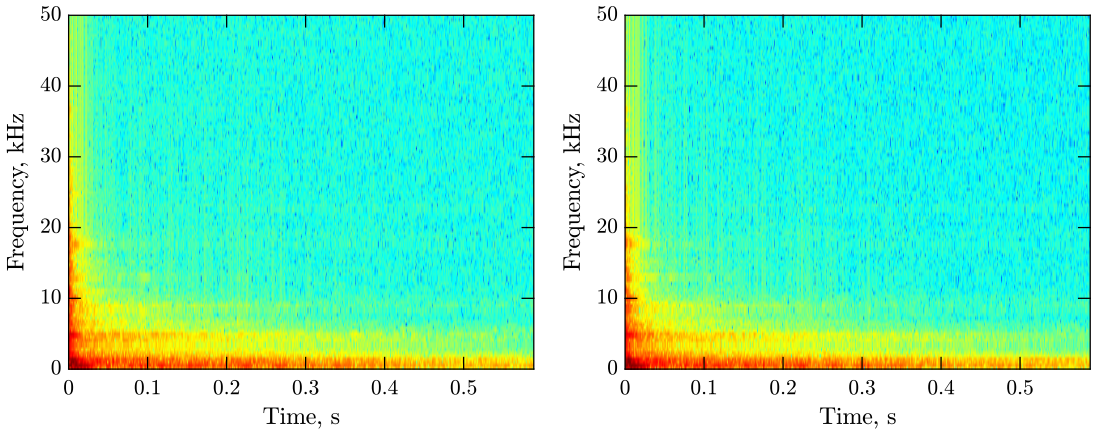

(a) Predetonator ignition

(b) Spark plug ignition

Figure 5.12. Spectrograms of filtered thrust measurements.

The oscillation in the thrust data is primarily relatively low-frequency noise (< 3 kHz). There is no significant frequency present in the 10 kHz range as seen in the pressure spectrograms. This provides further evidence in favor of the 10 kHz signal in the pressure data being a fluidic phenomenon, and not due to any vibration or motion of the structure itself. Steady thrust (taken as the average of the thrust data after the initial 0.1 s oscillation) is 1.007 N for the predetonator ignition test and 4.760 N for the spark plug ignition test. These are reduced even further after the low-frequency noise is removed. Steady thrust for the filtered data is effectively zero: 6.101×10^{-3} N for the predetonator test and 7.945×10^{-4} N for the spark test.

5.7 Engine Cycle Visualizations

5.7.1 Low-Speed Video Observations of Exhaust Plume

A "low-speed" camera (so named to contrast it with the high-speed camera used in subsequent sections) is used to document the exhaust plume. For most of the test plan, this is a Nikon® D300S DSLR used in video mode with a tripod. (Early tests used a Sony® HDR-CX260V Handycam, but this had decidedly inferior video quality and is replaced prior to test 42.). Figure 5.13 shows frames from three tests conducted at the same fuel-line pressure ($P_{0_f} = 45\,\text{psig}$) and different equivalence ratios.

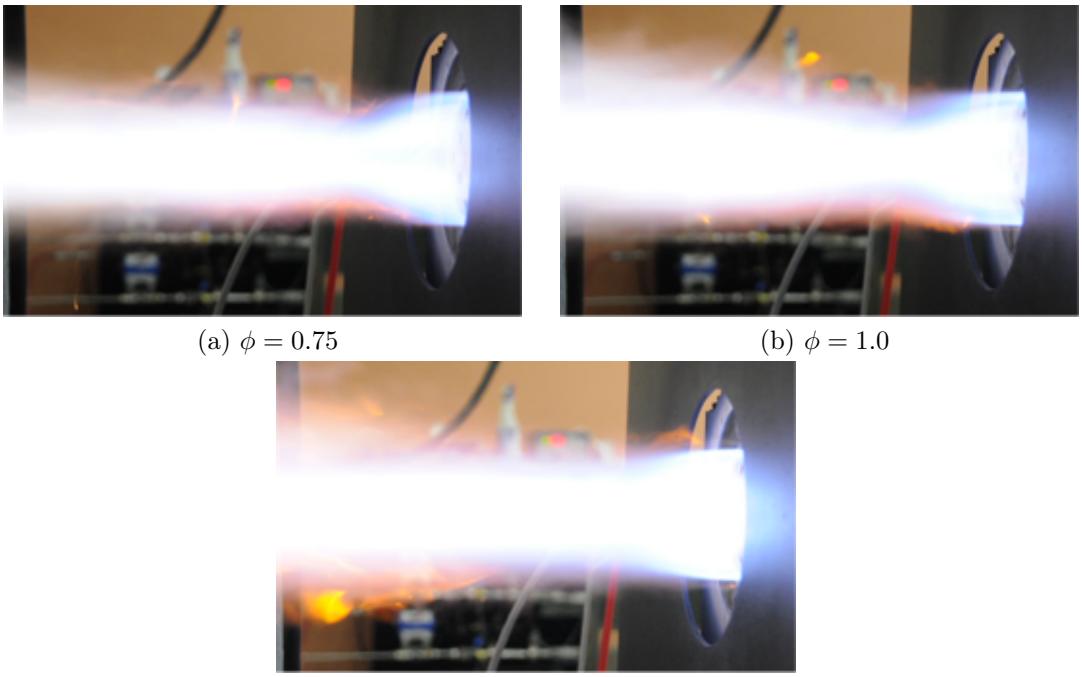

(a) $\phi = 0.75$ (b) $\phi = 1.0$

(c) $\phi = 1.5$

Figure 5.13. Visualizations of exhaust plume from lows-speed camera.

All three tests exhibit the characteristic bright white/blue expected of a hydrogen/oxygen flame, with the flame becoming slightly less bright and somewhat more transparent as equivalence ratio is reduced (that is, becomes more oxygen-rich).

However, there are also regions of the flame, visible along the upper and lower boundary, that show the yellow-orange color that is expected from a hydrogen-rich flame. These yellow-orange regions increase in size and visibility as the equivalence ratio is increased (that is, becomes more fuel-rich), which appears to indicate that the local equivalence ratio varies around the annulus; this is discussed in detail in Sec. 5.7.2.2. The exhaust plume is also notably overexpanded, as evidenced by its impinging after the flow exits the annulus. The oxygen-rich (fuel-lean) tests appear to be more overexpanded than the fuel-rich ones, though no quantitative analysis is performed on this effect.

5.7.2 Initial High-Speed Visualizations

Having failed to observe detonation phenomena by pressure or torque measurements, a high-speed camera is employed to visualize of the combustion process both from the side (to observe the exhaust plume) and using a down-engine view (to observe the behavior of the combustion process during testing).

High-speed visualization is performed using a Shimadzu® HPV-X2 Hyper Vision high-speed video camera. This camera is capable of up to 1,000,000 frames/s and exposure times as short as 200 ns for either 128 or 256 frames. A flat mirror is set up downstream of the engine to enable visualization down the annulus without exposing the camera to the hot combustion gases. Figure 5.14 shows the camera; the mirror assembly is visible at the left side of Fig. 5.14(a). A dedicated computer is used to operate the camera. Camera settings (number of frames, frame rate, exposure time, trigger delay) are entered into this computer, and the camera is triggered by the same signal which triggered the high-speed DAQ. No external light sources are employed, the only source of illumination during these tests is the combustion occurring within the annulus. Most of these tests are conducted with the laboratory

lights on, but during the startup visualization phase of testing (Sec. 5.7.2.3), several experiments are conducted with the the laboratory lights turned off. No difference in image quality is observed between these two sets of tests. Exposure times used in these experiments, on the order of 1,000–10,000 ns, are too low to be noticeably affected by external laboratory illumination.

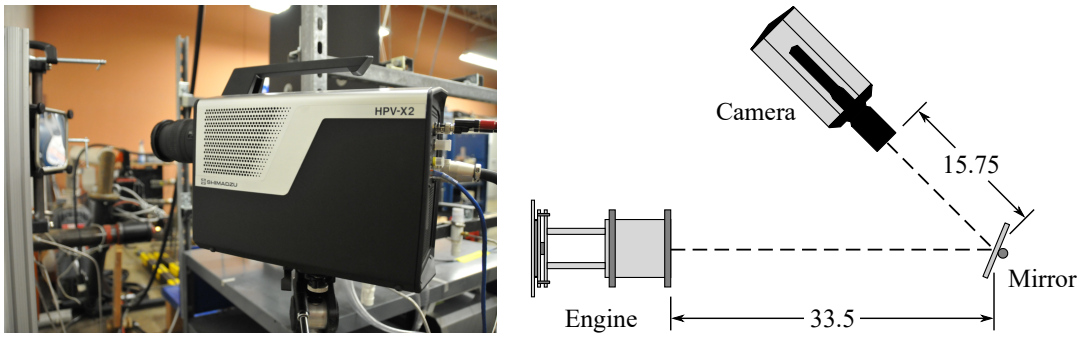

(a) Shimadzu HPV-X2 camera (b) Camera-mirror layout (dimensions in inches)

Figure 5.14. High-speed camera and setup.

5.7.2.1 Side-View Visualization of Exhaust Plume

The first set of high-speed camera visualizations is conducted to establish timing requirements and explore frame rates and exposure times for the high-speed camera tests. These tests are conducted using a side-view of the exhaust plume, prior to the installation of the downstream mirror. An example still from one such test, conducted at 100,000 frames/s with an exposure time of 10,000 ns is given in Fig. 5.15. No discernible rotating flow component is detected in these videos, so the mirror is added downstream of the annulus and the camera reoriented to the position shown in Fig. 5.14(b).

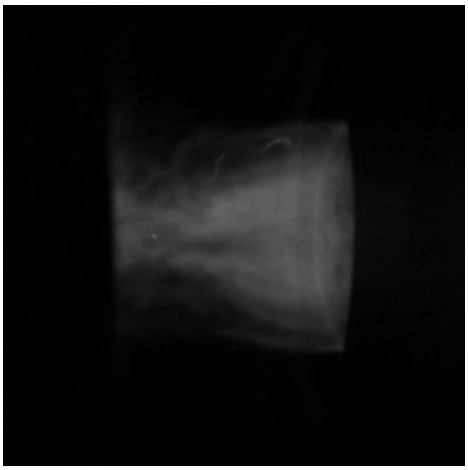

Figure 5.15. High-speed visualization of exhaust plume.

5.7.2.2 Down-Engine Visualization

Two sets of tests are conducted to attempt to visualize the steady operation of the engine from a down-engine perspective. The delay on the high-speed camera trigger is to avoid any ignition or startup transients. Successful visualizations are achieved at frame rates between 25,000 and 100,000 frames/s and exposure times between 5,000 and 20,000 ns. The first set of tests is performed at $P_{0_f} = 30$ psig and $\phi = 1.0$; the second set is conducted to determine if varying propellant composition or pressure has any effect and are conducted at a range of propellant pressures and equivalence ratios.

Figure 5.16 shows four frames from four different steady-operation tests. Figures 5.16(a) and 5.16(b) have identical propellant composition but varying frame rates (40,000 and 25,000 frames/s, respectively). Figures 5.16(c) and 5.16(d) are conducted with identical camera settings (50,000 frames/s), but varying propellant composition: Fig. 5.16(c) is conducted at a lower propellant pressure and is fuel-lean, Fig. 5.16(d) is conducted at an increased propellant pressure and is fuel-rich. These settings are summarized in Table 5.4.

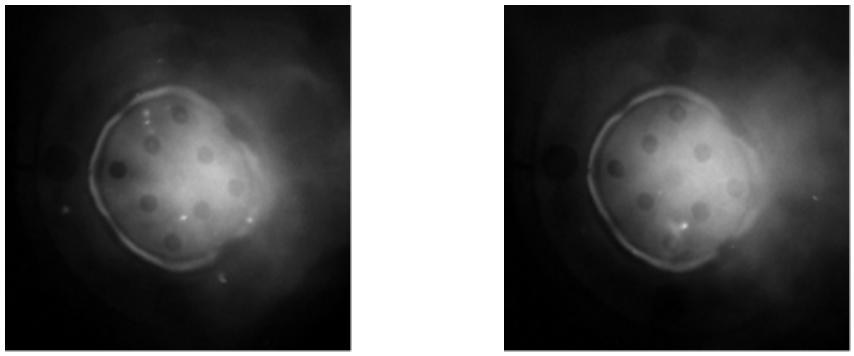

(a) Test 138 (b) Test 139

(c) Test 204 (d) Test 208

Figure 5.16. Comparison of steady-state operation tests.

Aside from brightness (oxygen-rich flames are dimmer than fuel-rich flames), there are no significant differences between the tests. There is no detectable swirled component to the flow, and no bright detonation wavefronts are observed. The annulus appears to be divided into alternating bright and dark segments, but those segments are not observed to move. Indeed, on further inspection, a probable reason for this presents itself rapidly: these points correspond to the parts of the annulus immediately above the propellant injection ports. Figure 5.17 shows the locations of the hydrogen ports (red) and the oxygen ports (blue).

The bright and dark areas around the annulus are therefore most likely due to local variations in the equivalence ratio, and not a propagating wave of any sort. This indicates that while the injector isolator (Section 4.2.3) is in fact separating

Table 5.4. Conditions of steady-state operation visualization tests

		Test Settings		Camera Settings	
Figure	Test No.	P_{0_f} (psig)	ϕ	Frame Rate (fps)	Exposure Time (ns)
5.16(a)	138	30	1.0	40,000	10,000
5.16(b)	139	30	1.0	25,000	10,000
5.16(c)	204	15	0.75	50,000	10,000
5.16(d)	208	45	1.5	50,000	10,000

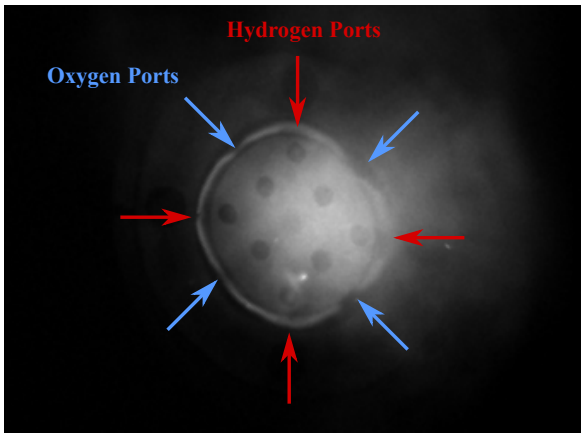

Figure 5.17. Steady-operation frame with injector port locations.

the propellants as it is designed to do (an observation confirmed by inspections of the fluidic valve cavity when the engine is disassembled to change injector plates), it is not doing so evenly. This is very likely the cause of the yellow-orange regions of the exhaust flame seen in the low-speed test videos in Fig. 5.13. As discussed in Section 1.1.2, detonations have widely been observed to have the lowest cell size (that is, most stable) in the region near $\phi = 1.0$, with cell size increasing rapidly and then failing to form at all as equivalence ratio strays further from unity. Therefore, having failed to observe a detonation front in the range $0.75 \leq \phi \leq 1.5$, there is no reason to believe that any success would be achieved by testing at the more extreme equivalence ratios ($\phi = 0.50$ and 2.0) and those points are abandoned.

5.7.2.3 Visualization of Engine Startup Phenomena

The steady-operation tests having failed to show any propagating detonation, a further series of tests is conducted to visualize the engine startup process, to shed some light on the failure to establish a detonation wave. Successful capture is achieved at frame rates up to 500,000 frames/s and exposure times down to 500 ns; the two selected representative tests are among them. For these results, the ignition time t_{ig} is taken as the first frame at which light is seen in the high-speed video.

5.7.2.3.1 Predetonator Ignition

A series of frames of the ignition process from the predetonator test is shown in Fig. 5.18. (The lack of circularity in the images is due to positioning of the mirror and camera as well as warping of the mirror.) This test is conducted with a camera frame rate of 500,000 frames/s and exposure time of 500 ns. The selected frames show the initial propagation around the annulus of the starting combustion front and the immediate aftermath. Figure 5.18(a) shows the first frame in which combustion can be observed; the white arrow indicates the location and direction of the tangential predetonator exit. The predetonator is observed to directly initiate two concurrent detonation waves which propagated around the annulus in opposite directions, Figs. 5.18(b)–5.18(d), reminiscent of the "bifurcation" or "slapping" mode of operation observed by Shank [243], Smith [244], Blüemner [245] and others. These waves intersected and merged on the opposite side of the annulus, Fig. 5.18(e), where they appeare to self-cancel. Sub-detonative pressure waves continue to propagate around the annulus, Fig. 5.18(f), again in a "slapping" mode, but these die down rapidly. After the initial ignition transient has passed, flow inside the annulus has an observable clockwise rotation (in the direction of tangential predetonator), though ul-

timately no steady rotating detonation is observed to form. As previously mentioned, the reasons for this failure to initiate a detonation wave remain unknown and under investigation.

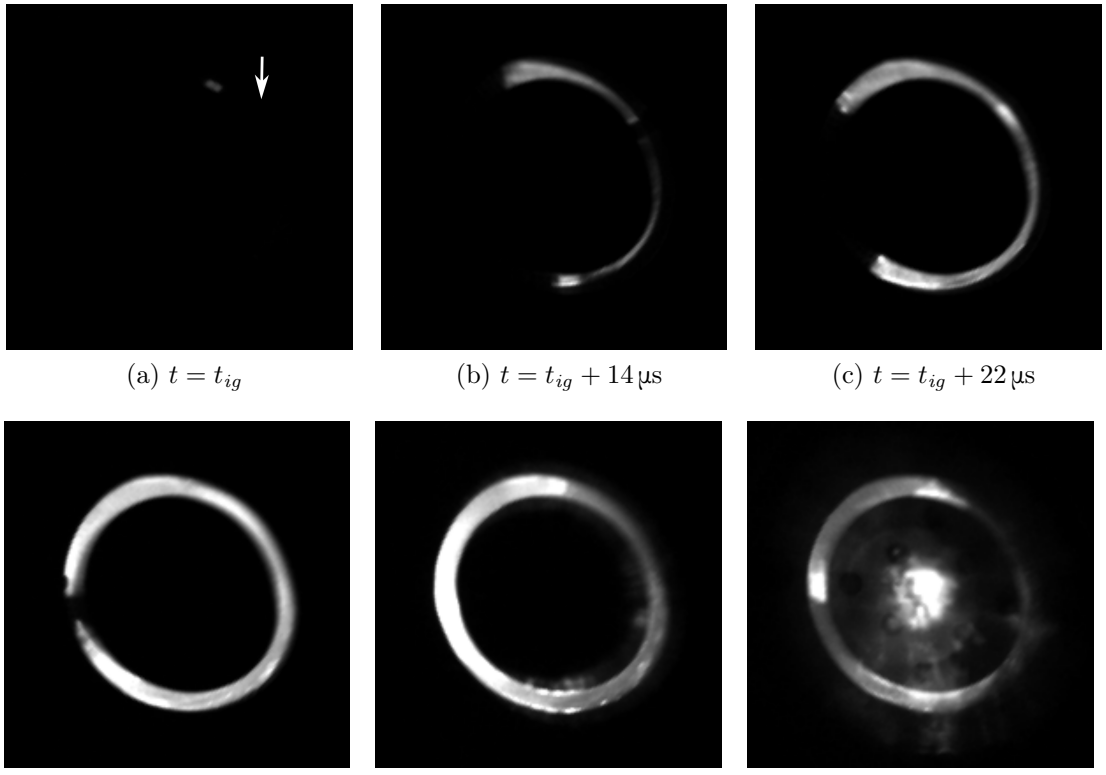

(a) $t = t_{ig}$ (b) $t = t_{ig} + 14\,\mu s$ (c) $t = t_{ig} + 22\,\mu s$

(d) $t = t_{ig} + 34\,\mu s$ (e) $t = t_{ig} + 50\,\mu s$ (f) $t = t_{ig} + 92\,\mu s$

Figure 5.18. Predetonator ignition: 500,000 frames/s, 500 ns exposure.

5.7.2.3.2 Spark Plug Ignition

A series of frames from the spark plug test is shown in Fig. 5.18. This test is conducted with a camera frame rate of 200,000 frames/s and an exposure time of 500 ns. Unlike for the predetonator, t_{ig} for the spark plug case is difficult to determine. Figure 5.19(a) illustrates the assigned ignition time, corresponding to the first moment at which illumination can be perceived in the frame; the white arrow

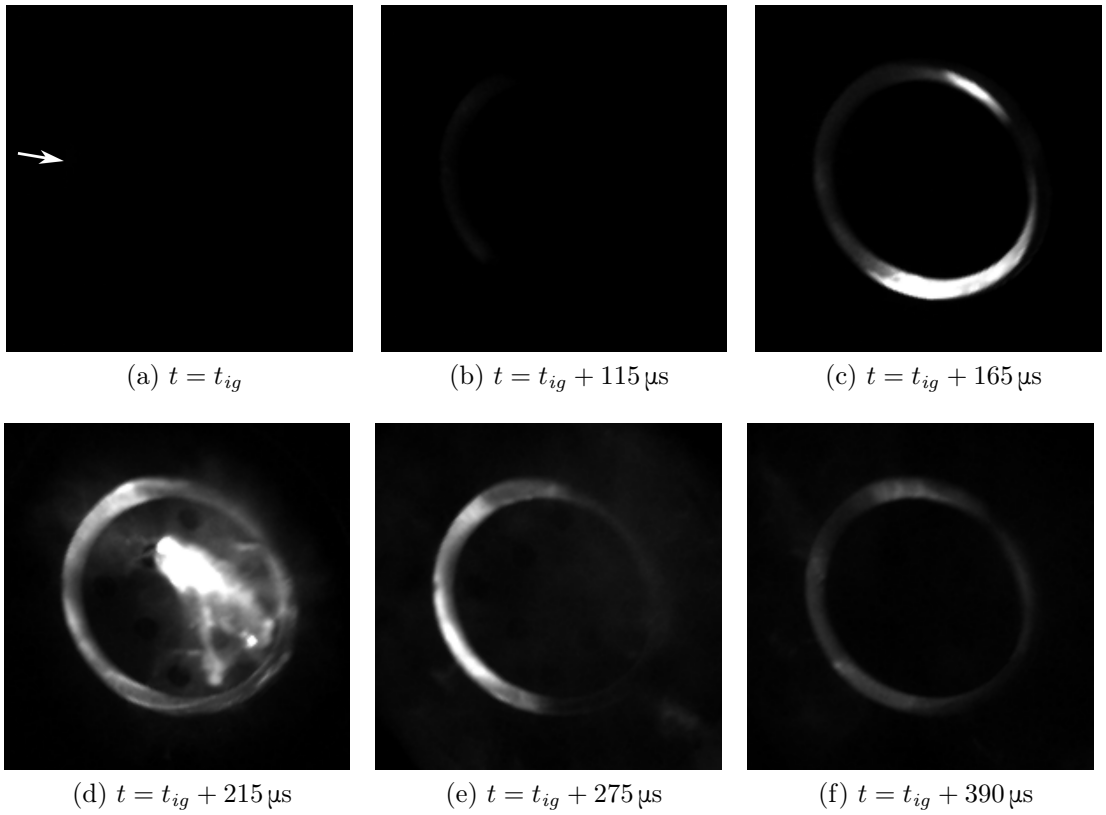

(a) $t = t_{ig}$ (b) $t = t_{ig} + 115\,\mu s$ (c) $t = t_{ig} + 165\,\mu s$

(d) $t = t_{ig} + 215\,\mu s$ (e) $t = t_{ig} + 275\,\mu s$ (f) $t = t_{ig} + 390\,\mu s$

Figure 5.19. Spark plug ignition: 200,000 frames/s, 500 ns exposure.

indicates the spark plug location. The low-energy spark induced a deflagration which propagates relatively slowly (compared to predetonator ignition) in both directions around the annulus, Fig. 5.19(b). Each branch of this initial deflagration transitioned to a detonation approximately 90° around the annulus, Fig. 5.19(c), which intersects and merges on the opposite side of the chamber. Like the predetonator case, the detonation waves appear to largely self-cancel, but unlike for the predetonator, the subsequent sub-detonative pressure waves continue to propagate for several rotations around the annulus; Fig. 5.19(d) shows these waves as they approach the initial spark point, and Fig. 5.19(e) shortly after they have completed their first revolution and passed through each other. These waves continue to propagate at decreasing magnitude for several revolutions; Fig. 5.19(f) shows them after they have completed

approximately one-and-three-quarter revolutions and are returning back toward the point of initial spark again. Also unlike the predetonator ignition cases, after the initial ignition transients have completed, there is no observable rotational component to the subsequent flowfield inside the annulus. Again, no steady rotating detonation is observed to form.

5.7.2.3.3 Comparisons with Pressure Data

The pressure data in Fig. 5.7 confirmed the observations from the high-speed camera. In the predetonator ignition test, Fig. 5.7(a), each pressure transducer shows an initial characteristic detonation pressure trace, but only a series of sub-detonative pressure waves thereafter, decreasing rapidly in magnitude. After 1.6 ms, some oscillation appear to remain in the pressure data (particularly in transducer P_1), but the discrete identifiable pressure waves have almost completely died out. In contrast, the spark ignition test, Fig. 5.7(b), shows an an initial sub-detonation pressure rise at the transducer circumferentially coincident with the spark plug (P_1) that transitions to a detonation by the time the wave reaches transducers P_3 and P_2, which are offset 90° from the spark plug. The pressure waves remain larger in magnitude for a greater number of periods than the detonator ignition case (approximately four distinct pulses are observable after the detonation, in contrast to the predetonator's 2-3), but die out with little apparent oscillation after the final pressure pulse.

5.7.3 Improved High-Speed Ignition Visualization

The mirror used to provide the down-engine view warped somewhat when mounted and partially delaminated over the course of the initial testing phase. This results in the distortion that can be seen in Figs. 5.16–5.19, rendering them unsuitable for qualtitative analysis of the ignition process. Additionally, approximately 1.3–

1.9 ms after the initial ignition event a wobble is observed in the high-speed videos. This is due to oscillation of the mirror and render down-engine imaging impossible for approximately 50 ms. Therefore, following the conclusion of Phase 5, the mirror assembly is modified to provide a better, more stable image for improved analysis. A higher-quality mirror is combined with a stronger, more rigid aluminum mounting plate. The overall setup in Fig. 5.14 is unchanged, but cross-line laser and digital levels are employed to position and align the mirror and camera both vertically and horizontally. These modifications result in a significant improvement in image quality and the complete elimination of wobble.

5.7.3.1 Procedure

For this phase of testing, the text matrix outlined in Sec. 5.4 is narrowed: only injection swirl angle and ignition method are varied. Propellant conditions are kept constant at $P_{0_f} \approx 45$ psig and $\phi \approx 1.0$ (fuel pressure is increased from Phase 5 to increase propellant flow rate to the engine). Three injector plates are employed, with injector holes angled 0°, +30°, and −30° circumferentially around the annulus. For improved mixing, a "half-impinging" injector plate (so named because the outer ring of injector holes is angled 15° towards the center, with the inner ring of holes remaining un-angled) is used for the 0° swirl condition. Each injector plate is tested with both predetonator and spark plug igniter systems. Engine performance data (pressure, thrust, and torque) are taken during this phase, but are not qualitatively different from those in previous phases.

High-speed camera settings for the improved ignition visualizations are standardized on a frame rate of 200,000 frames/s and an exposure time of 500 ns. The exposure time is chosen to enable observation of the sub-detonation pressure waves which are observed to propagate around the annulus after the merging of the initial

combustion fronts. While the high-speed camera is capable of frame rates of up to 500,000 frames/s at this exposure, Phase 5 showed that the 256-frame limitation made capture of the initial ignition event extremely difficult at that rate.

The camera trigger delay for each test condition is determined by testing at a lower frame rate (5,000 frames/s) several times and noting the time of ignition capture. Testing then proceeded until a minimum of three successful captures of the ignition and subsequent transients is obtained (as a rule of thumb, this is assessed as ignition being observed by frame 100). High-speed camera data are saved in `bmp` (still image) and 24-bit `avi` (video) format.

Before each testing session, two reference (calibration) images are taken: one with a 5 mm calibration grid (with angle markings at every 45°) affixed to the end of the engine, and a second with this grid removed simply showing a down-engine view of the position of the engine in the frame. An example of each of these reference images is shown in Fig. 5.20.

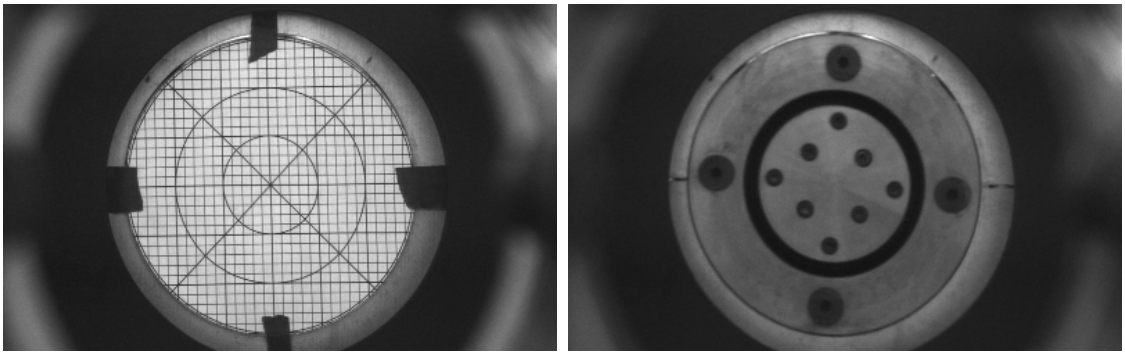

(a) Calibration grid (b) Down-image

Figure 5.20. Example reference images.

These images are used to focus the high-speed camera (it is not equipped with autofocus) and to align the image in the frame.

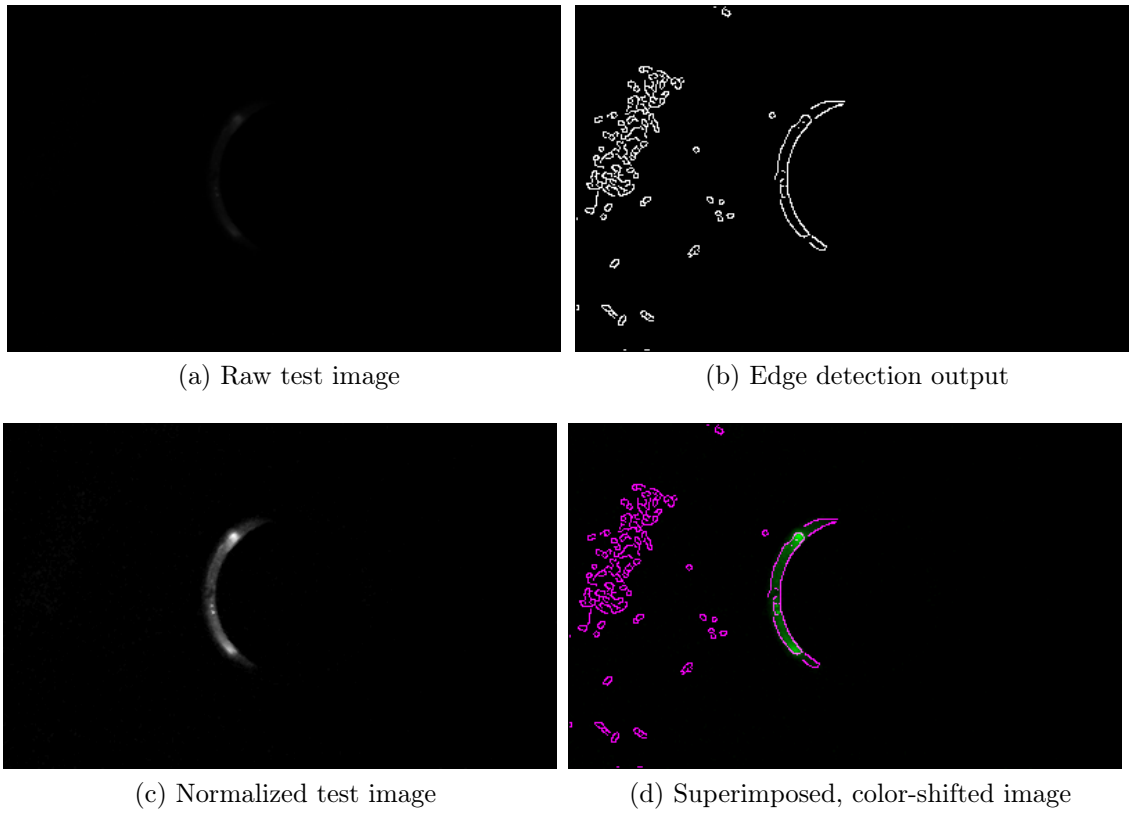

(a) Raw test image (b) Edge detection output

(c) Normalized test image (d) Superimposed, color-shifted image

Figure 5.21. Example of image processing method.

5.7.3.2 Image Processing & Calibration

The progress of the combustion front along the annulus is tracked by applying an edge-detection algorithm (the `edge` function in the MATLAB Image Processing Toolbox) using the two-threshold Canny method [246]. This image is superimposed on a test image which has been normalized to set the brightest pixel to white and the darkest to black. The superimposed images are color-shifted: the edge-detection output to magenta and the normalized test image frame to green. This method of display allows manual inspection of the image detection results to eliminate false positives and negatives (especially for the deflagration frames in the spark plug ignition

tests, which are dimmer and more prone to noise). An illustration of each of these images is given in Fig. 5.21.

The edge detection method is only able to detect the combustion front on its initial transit around the annulus after ignition. Though the sub-detonation pressure waves are once again visible in the testing, there is insufficient contrast between these waves and the surrounding combustion for them to be identified by the edge detection method. Therefore, the analysis is focused on the initial ignition event, from its genesis to the point at which the two combustion waves merge on the opposite side of the annulus. The number of successful tests for each condition is given in Table 5.5.

Table 5.5. Successful ignition captures per test configuration

Swirl (deg)	Igniter	Successful Tests
0	Predetonator	3
	Spark Plug	8
+30	Predetonator	8
	Spark Plug	7
−30	Predetonator	6
	Spark Plug	11

To calibrate the test images and determine the location of the center of the engine, the Canny edge-detection algorithm is applied to the down-engine reference images (Fig. 5.20(b)). The output of the edge-detection algorithm is then masked to leave only the inner and outer wall edges, and the eccentricity ϵ and orientation θ_e with respect to the x-axis of each ellipse determined (using the MATLAB function `regionprops`). Additionally, the circular error, defined as the deviation of the major and minor axes from equality, is calculated as

$$E = 1 - \sqrt{1 - \epsilon^2} \tag{5.24}$$

and expressed as a percent. The eccentricities, errors, and elliptical orientations of each wall boundary are given in Table 5.6. The wall edges are very close to true circles: $\epsilon < 0.3$ for all cases, with less than a 4.5 percent difference between the major and minor axes.

Table 5.6. Eccentricities and orientation of annular wall edges in down-engine reference images

Swirl (deg)	Igniter	For Tests	Inner Wall			Outer Wall		
			ϵ	E (%)	θ_e (deg)	ϵ	E (%)	θ_e (deg)
0	Predetonator	351–385	0.274	3.84	−85.87	0.224	2.53	−83.48
	Spark Plug	386–420	0.292	4.35	−85.07	0.226	2.58	−81.91
+30	Predetonator	421–435	0.263	3.52	−77.74	0.269	3.69	−83.96
	Predetonator	436–460	0.196	1.94	89.02	0.223	2.51	−86.87
	Spark Plug	461–520	0.279	3.97	−77.62	0.254	3.27	87.58
−30	Predetonator	521–575	0.247	3.10	−73.49	0.238	2.87	−76.16
	Spark Plug	576–625	0.262	3.48	−86.69	0.286	4.19	−81.96

The masked, edge-detected images are loaded into a vector-graphics utility and a circle is fit to the inner annular wall boundary for each down-engine reference frame. This circle is then located in place with respect to the edges of the frame and its center—representing the center of the annulus—is located. This reference guide is then transferred to each frame of the test (using the superimposed, color-shifted images) in which combustion is observed. Angle guides are placed with their origin at the center of each circle and rotated about this origin to align with the leading edge of the combustion front, and these angles are recorded. Angles are measured from the x-axis, with positive angles along the upper half of the annulus and negative angles along the lower half. This method is performed for each successful visualization of

the combustion process for each test condition, from the initial ignition capture frame until the combustion waves merge.

5.7.3.3 Observations of Ignition Phenomena

As with the Phase 5 results detailed in Sec. 5.7.2.3, both the predetonator and spark plug initiate two counter-rotating combustion fronts beginning at the ignition source. However, the superior image quality allows a much more detailed look at the propagation of the combustion fronts.

5.7.3.3.1 Analysis of Selected Frames

A series of frames, beginning with the first frame in which combustion is detected and ending with the final frame before the combustion waves merge, have been selected from a representative test for each test condition. The direction of injector swirl is indicated by a gray arrow on each frame, and the approximate location of the igniter (predetonator or spark plug) is indicated with a white arrow in the first frame. To save space, these figures have been placed in Appendix F.

Firstly, we note that the ignition dynamics for the predetonator tests appear to be largely insensitive to injection swirl angle. Figures F.2, F.6, and F.10 give the selected frames for the predetonator ignition for $0°$, $+30°$, and $-30°$ injector swirl, respectively. All three show that a strong combustion wave is initiated in both directions around the annulus. There is little if any time to transition to a detonation wave (determined by the appearance of a bright combustion front in the frame). When such a transition is observed, it is always seen on the upper branch and is achieved in $15\,\mu s$ or less (note that the tangential predetonator exit points in the $+\theta$ direction). The two combustion waves merge slightly less than $180°$ around the annulus from the predetonator exit in most cases; this is likely due to the brief transition period on the

upper branch. In some cases, the $-30°$ swirl is observed result in merging at angles greater than 180° (as seen in Fig. F.10(f), where the spark plug is silhouetted against the combustion front), but this did not occur in all cases. With one exception, all predetonator cases show that the two combustion waves waves merged in 11 or 12 frames (55 or 60 μs).

In contrast, the predetonator tests show much more interesting and complex behavior. As observed in Sec. 5.7.2.3.2, the spark plug initiates a faint primary combustion wave (an apparent deflagration) which propagates slowly around the annulus, building in intensity, until a brighter, faster-propagating secondary wave combustion wave (an apparent detonation) appears and accelerates quickly around the annulus until the wavefronts merge. However, more detailed observations show that only in very rare cases does the leading edge of the deflagration wave transition to a detonation. Instead, the secondary wave forms behind the leading edge of the primary wave after approximately 100–150 μs, accelerates rapidly, and overtakes the leading wave. The point at which this secondary wave appears (and its distance behind the primary wave upon becoming visible) varies considerably from test to test, and appears to be strongly dependent on injector swirl angle.

In the case of 0° swirl, seen in Fig. F.4, the secondary wave appears significantly behind the leading edge of the primary wave (though not yet distinct enough for a wave front to be captured by edge detection, the beginnings of this secondary wave can be observed in Fig. F.4(c)), with both top and bottom secondary waves being visible at approximately the same time. However, in both $+30°$ and $-30°$ cases (Figs. F.8 and F.12, respectively), the primary combustion front propagates slightly quicker in the direction of the swirled injection, this branch develops a secondary wave significantly later the branch propagating into the swirled flow. In the case of Fig. F.8 ($+30°$ swirl), the transition to an apparent detonation occurs at the leading

edge of the upper branch only in the very last frame before the combustion branches are observed to merge. In another +30° swirl case, no transition is observed in the upper branch prior to merging. Additionally, while the branch propagating into the swirled flow does not appear to develop a secondary wave earlier (110–150 µs, in the same range as the unswirled injection cases), it does appear noticeably closer to the leading edge of the primary wave; the observable overlap is only 1–2 frames (5–10 µs) on average, in contrast to an average of 4 frames (20 µs) for the unswirled injection. Due to the secondary wave developing much earlier in the branch propagating into the swirled flow, the point of merging occurs most often on the side of the branch propagating with the flow ($> 180°$ in the +30° swirl tests and $< 180°$ in the −30° swirl tests).

5.7.3.3.2 Quantitative Analysis of Wave Propagation

Using the angle data and the camera frame rate, θ–t wave diagrams are generated of the successful tests for each experimental condition. The differential angle $\Delta\theta$ is determined by subtracting the angle recorded in the first frame at which illumination is seen θ_1 from the angle in each subsequent frame θ. To more effectively compare the wave propagation on the two combustion branches, this is given as a magnitude

$$\Delta\theta_i = |\theta_i - \theta_1| \tag{5.25}$$

Additionally, by taking the angular distance traveled between frames, the camera frame rate, and the mean annular radius, an approximation of the mean wave speed U_m is obtained

$$U_{m_i} = r_m f_{HS} \left(\Delta\theta_{i+1} - \Delta\theta_i\right) \frac{\pi}{180°} \tag{5.26}$$

where f_{HS} is the high-speed camera frame rate and $\Delta\theta$ is measured in degrees. The θ–t wave diagrams and wave velocity figures are grouped by test condition and likewise placed in Appendix F. In these figures, solid lines indicate the upper combustion branch and dashed lines indicate the lower branch.

The wave diagrams support the qualitative observations from the selected frames. In the case of predetonator ignition, for 0° swirl (Fig. F.1), the lower branch fronts propagate at an approximately steady rate of 3 km/s immediately upon ignition, whereas the upper branches accelerate for approximately 20 ms before stabilizing at the same velocity as the lower branch. These observations are tempered somewhat by the small data record, as only two of the three tests follow this behavior. Test 378 is a clear outlier, particularly with respect to the upper branch; it propagates significantly slower than for any other test. However, while there is an approximately 30 ms acceleration period, the lower branch does reach the same steady velocity of approximately 3 km/s.

In contrast, the imposition of swirl does appear to have some effect on the initial propagation of both wave branches: positive 30° swirl (Fig. F.5) retards somewhat the upper branch (propagating into the flow), resulting in a clearer period of acceleration for the first 20–30 ms and a slightly lower final velocity (approximately 2.4 km/s), and briefly causing a sharp increase in the propagation velocity at approximately 7–12 ms and a slightly higher final velocity for the lower branch (approximately 2.9 km/s). Negative 30° swirl (Fig. F.9) does not have the same deleterious effect on the upper branch, which now propagates with the flow. Instead of a brief acceleration period followed by a constant velocity, the upper branch now accelerates (albeit at a decreasing rate) for the majority of the record before reaching a steady velocity of approximately 3 km/s only at the very end of the test. Some tests showed a brief acceleration period

for the the lower branch (propagating into the flow), where others did not. However, the final velocity is lower than that for the upper branch (approximately 2.7 km/s).

For spark plug ignition, the 0° swirl case (Fig. F.3) shows no significant difference between the upper and lower branches. There is no discernible acceleration period for the primary wave; a steady velocity of 1 km/s is observed. Additionally there is a significant period after ignition where both primary and secondary waves are observed, with the secondary waves accelerating from the point at which they are observed to a final velocity upon merging of 2.5–3.5 km/s. When swirl is introduced, however, the branches again differentiate themselves.

Under +30° swirl (Fig. F.7) the primary wave for both branches accelerates slowly as it progresses around the annulus, from an initial average velocity of slightly under 0.5 km/s to a final velocity near 0.8 km/s. The upper primary wave (moving in the flow direction) initially propagates faster, before being overtaken by the lower wave in speed after an average of 50 ms and in angle after 80–100 ms. Additionally, while there is a substantially smaller period of overlap between the primary and secondary waves (particularly, as noted previously, for the upper branch), there is no notable period of acceleration; once the secondary wave appears, it travels at an average of 2.8 km/s for both the upper and lower branches.

In contrast, the −30° swirl case (Fig. F.11) shows distinct acceleration in the primary wave for both the upper and lower branches, but noticeably more for the former, from an initial average velocity of 0.3–0.5 km/s to a final velocity of 0.8–1 km/s. The lower primary branch (propagating with the flow) initially outpaces the upper primary wave branch, but the latter develops a secondary wave 15–20 μs earlier. Like the positive swirl case, once the secondary wave appears, there is very little observed acceleration: both upper and lower branch secondary waves travel at an average of 3 km/s.

5.7.3.3.3 On Primary and Secondary Waves

In the previous sections, the two waves have largely referred to as "primary" and "secondary", rather than as "deflagration" or "detonation". As the physical structures are not observable and the existence and propagation of the wave is only determined from the light released by the combustion reactions, the presence of a deflagration or detonation can not be conclusively diagnosed. However, it is readily apparent that the secondary wave travels on the order of a factor of six faster than the primary wave, and releases more energy (as determined from the combustion light release intensity). Using the method of Sec. 5.2, the Chapman–Jouguet detonation velocity for the nominal $P_{0_f} = 45\,\text{psig}$, $\phi = 1$ condition is $U_{CJ} = 2.88\,\text{km/s}$, in the range of the secondary wave speeds observed.

Though deflagrations are commonly cited as traveling on the order of meters per second, unlike detonations, they do not have a fixed propagation velocity. Instead, they tend to accelerate to a maximum velocity on the order of half the Chapman–Jouguet detonation speed [3]. Though this is supersonic relative to a fixed reference frame, it is subsonic relative to the precursor shock generated ahead of the reaction zone (as this shock is not accompanied by chemical reactions, it is not visible in the images generated). This appears to well-describe the "primary" combustion front observed here.

Additionally, the appearance of the so-called "secondary" wave in the unswirled spark plug ignition tests appears to be consistent with the detonation-to-deflagration phenomena described in Sec.1.1.3. The curved annular walls confine the combustion wave, promoting flame folding and allowing for plentiful transverse wave–flame interactions which promote transition. The unswirled cases tend to show the formation of the local explosion center earlier and closer to the point of ignition, implying that the

dominant transition mechanisms in such cases are those which result in a smaller explosion center occurring in the turbulent flame behind the precursor shock, creating a wave which accelerates and builds in strength through positive-feedback mechanisms until it couples with the precursor shock and forms a detonation.

However, in the cases with injector swirl, transition is observed to occur more abruptly and closer to the leading edge of the combustion front. This appears to be consistent with the detonation "bubble" phenomenon described by Lee [3, 46], wherein turbulent mixing behind the leading combustion front creates a hot spot and generates a strong explosion center, resulting in a blast wave which catches up to the precursor shock and forms an overdriven detonation wave. In combustion fronts traveling into the incoming flow, the relative velocity of the wave is higher, leading to increased turbulence behind the front and increasing the strength of the positive feedback mechanism between the precursor shock and combustion front. This promotes the formation of these local explosion centers, leading to earlier and more sharp transition to detonation. In contrast, combustion fronts traveling with the incoming flow have a lower relative velocity, which tends to dampen the feedback loop and suppress the conditions which might lead to the formation of a local explosion center. This results in transitions in these cases tending to occur later (or in one case not at all).

The deflagration-to-detonation process tends to result in the creation of an overdriven detonation [3, 47]. This is consistent with the observation of a secondary wave traveling at greater than the Chapman–Jouguet velocity, particularly when the combustion front is propagating into the swirled injection flow. In a sufficiently large annulus (or sufficiently long tube), the overdriven wave would then then decay into a CJ detonation, but this is prevented by the merging of the upper and lower combustion branches. The behavior of the combustion front in the predetonator

cases is also supportive of the diagnosis of an overdriven detonation: the mass flux into the annulus which accompanies the the ignition event creates a nonstationary rear boundary condition which drives the detonation initiated in the annulus above the CJ condition.

5.8 Damage to Engine Hardware

It is periodically necessary to disassemble the engine to change injector plates, and every time this is done, the engine is inspected to ensure it remains in good condition. Over the course of the test plan, very little damage is observed to Arthur. Figure 5.22, taken between Tests 575 and 576, shows the only noticable deterioration: discoloration to and pitting of the outer annular wall, and eroding of the spark plug insulator. The former is almost certainly due to the predetonator exhaust impinging on the wall, the latter due to exposure to repeated shock and detonation waves during the ignition process. No damage is observed on the centerbody (that is, the inner annular wall).

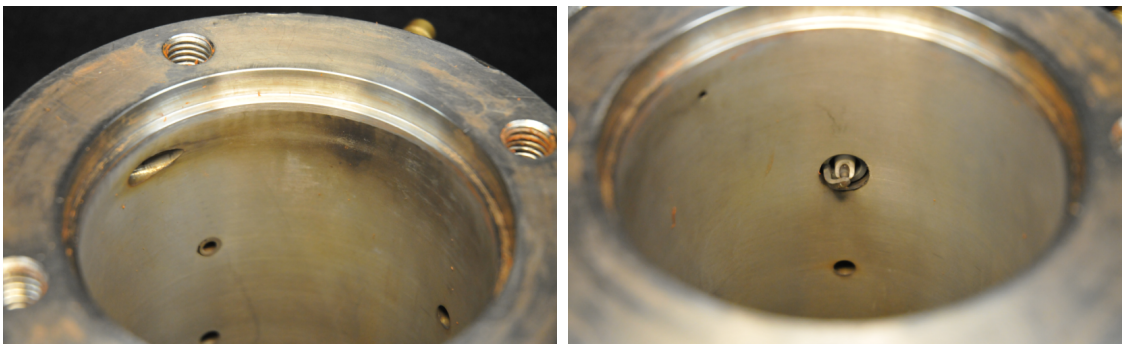

(a) Outer annular wall (b) Spark plug

Figure 5.22. Observed damage to engine.

There are also minor discolorations along the annular wall which correspond to the locations of injector ports. Previous RDE studies have reported damage to the annular walls due to the confined heat release of the detonation wave [156, 247, 248]. Though the test durations on Arthur are short, there are many of them, and the absence of any such damage or discoloration around the annulus provides another point of evidence that the engine is failing to sustain a detonation wave, and instead experiencing deflagration combustion.

5.9 On the Failure to Observe a Steadily-Propagating Detonation Wave

The totality of the pressure measurements (full and zoomed), high- and low-speed video (side-view and down-engine) and the inspection of the engine hardware leave little doubt that Arthur fails to sustain a steady detonation. It remains to discuss the observations from the experimental phase and, in particular, apparent failure to establish a detonation wave.

There are several possible reasons for this, but the most likely is the local equivalence ratio variation around the annulus. As discussed in Sec. 1.1.2, the rotating detonation is unstable, and its structure (as measured by the detonation cell size) is highly dependent on the equivalence ratio. As the detonation propagates through the annulus, variation of the equivalence ratio from strongly fuel rich to strongly fuel lean and back again would result in the wave oscillating between marginally unstable and strongly unstable states. This would prevent the strong transverse shock waves which are necessary to maintain the steady propagation of the wavefront from forming, destabilizing the detonation structure and leading to deterioration into a deflagration. It is also worth mentioning Bykovskii's criterion for minimum annular diameter, Eq. (3.7), is also a function of the detonation cell size. Local variations in the equivalence ratio could cause the cell size to increase to the point where the

channel is too narrow to sustain a detonation, leading to further destabilization of the detonation front.

However, in the ignition tests, two detonation waves are observed to form (by DDT in the spark ignition case, by apparent direct initiation in the predetonator case) which do not break down until after the counter-rotating detonations merge. (Described here as "canceling": a qualitative description, not a quantitative one). The counter-rotating or "slapping" mode of operation for RDEs has been observed in a number of studies, but the there is very little understanding of the phenomena by which this occurs. Further investigations of the mechanisms governing when two detonation waves are able to stably propagate through each other are necessary.

There remains finally the question of flowrates. Though the results of the model presented in Ch. 2 led to the conclusion that the plenum pressure—which governs mass flow rate—is not a factor in determining whether or not a detonation wave can propagate (the detonation wave never fell below the critical height for propagation), that model is idealized and assumes that the propellants are premixed. This is not the case in most detonation engines hitherto tested, which must account for diffusion and mixing of propellants. These have the effect of adding an additional timescale to the steady-operation problem. Increased mass flow rates can alleviate this problem by increasing injection velocities and creating a greater temporal margin of error for mixing prior to the arrival of the detonation wave. Low flow upstream pressures and flowrates can also cause the injection ports to fail to choke, which was observed by Fotia [168] to result in failure to achieve a steady detonation, instead resulting in a steady acoustic wave.

CHAPTER 6

CONCLUSIONS AND FUTURE WORK

6.1 Conclusions

The overwhelming majority of previous efforts in rotating detonation engine modeling have been directed to high-order computational models designed to investigate various features. However, these models are too computationally intensive to be of use for broad-spectrum parametric analysis. To that effect, a semi-empirical, control-volume approach was used to derive performance equations and construct a flexible, low-order model for the rotating detonation engine. The model was formulated to explicitly leave open the potential for exit-plane swirl and was used to conduct parametric analysis to determine the effect of a broad range of design parameters on performance. The model showed exit swirl to be nonzero for the majority of design iterations, yielding a resultant torque that was small compared to thrust, but not uniquely zero. However, some zero-torque points were observed, which may prove especially valuable in design optimization endeavors. Additionally, the case of zero net swirl (that is, spatially averaged circumferential velocity) was shown to occur separately from the case of zero resultant torque. For best performance, an RDE should have high propellant pressure, low propellant temperature, and zero injection swirl. Shorter and wider annuli offer both greater thrust and specific impulse. Fuel-rich mixtures offer greater performance for rocket applications; for airbreathing applications, fuel-lean mixtures are preferred. Results were shown to agree qualitatively with existing numerical simulations.

This model was then employed in concert with high-speed waverider forebodies to conduct parametric analysis of RDE and waverider design parameters to determine their effect on integrated performance. Peak performance was observed for waveriders with small cone angles and convex power-law body geometries, corresponding to the conditions of maximum forebody pressure recovery. Thrust and resultant torque were observed to be sensitive to body shape and freestream parameters while specific impulse and thrust-specific fuel consumption were not, though the latter result may be due to assumptions within the model; specifically, the absence of an inlet model to account for the effect of the Mach number (and dynamic pressure) at the exit of the waverider inlet. Higher Mach numbers were observed to have greater propulsive performance, but at the potential cost of inducing autoignition in the propellant mixture at freestream Mach numbers greater than 3.5 (and potentially lower for longer chain hydrocarbons).

A modular rotating detonation engine facility was constructed and used to perform a range of experiments. The engine was based on earlier-generation RDEs, while incorporating a number of design improvements intended to expand its effectiveness and operational capabilities. The facility was designed and instrumented to allow a resultant torque on the engine to be measured. A total of 350 tests were conducted using the facility at a range of injection pressures and equivalence ratios without observing a stable propagating detonation wave. Spectrograms of the high-speed pressure data showed the presence of a characteristic frequency inside the engine at approximately the expected detonation frequency that was not reflected in the thrust data, indicating the presence of a pressure-based periodic phenomenon inside the engine that is not fully understood.

Having failed to observe a steadily-propagating detonation wave by pressure, thrust, and torque measurements, a high-speed camera was used to visualize the ex-

haust plume and the annulus of the engine. This likewise failed to observe a rotating detonation, but did appear to show the presence of circumferential variation of the local equivalence ratio around the annulus, possibly explaining the failure to establish a detonation. Next, the high-speed camera was used to perform a series of qualitative and quantitative observations of the engine starting phenomena using both predetonator and spark plug ignition. Both methods initiated a pair of detonation waves which traveled in opposite directions around the annulus, intersecting on the opposite side of the chamber. The predetonator initiated these detonations directly, whereas the spark plug initiated a deflagration which underwent a transition to a detonation approximately one-quarter of the way around the annulus. The intersecting detonation waves appeared to cancel each other out upon intersecting, but a series of sub-detonation pressure waves were observed to propagate around the annulus several times before dying out. After the pressure waves died out, the predetonator case was observed to have a rotational flowfield; the spark plug case showed no such rotation. No steady detonation wave was observed using either ignition method. Data from the high-speed pressure transducers supports these visual observations.

More detailed visualizations were subsequently performed, focusing on the initial propagation of the combustion front around the annulus. The effect of positive and negative swirled injection was explored in addition to ignition method. Quantitative measurements of the combustion front were taken and used to determine the wave velocity. Predetonator ignition was observed to initiate a counter-rotating a pair of detonation waves. The branch propagating in the direction of the predeonator exit traveled at an approximately constant velocity whereas the opposing branch underwent a brief acceleration period. Swirl retarded the propagation velocity of the branch in the direction of the swirl, though to a greater degree in the branch opposed to the predetonator exit. Two types of combustion waves were observed in the spark

plug ignition cases, appearing to correspond to an initial deflagration wave which transitioned to a detonation wave. Transition occurred closer to the point of ignition for unswirled ignition, whereas swirled ignition resulted in transition closer to the deflagration wave front. While swirled injection initially increased the speed of the deflagration branch propagating in the direction of the swirl, branches propagating into the swirled flow transitioned to a detonation more rapidly. Detonations were observed to propagate at approximately Chapman–Jouguet velocity, though overdriven detonations were observed, particularly for predetonator ignition and spark plug ignition branches propagating into the swirl.

Finally, a series of possible reasons for the failure to establish a detonation wave was discussed. The leading culprit is believed to be equivalence ratio variation around the annulus causing a corresponding variation in the detonation cell size, leading to the breakdown of the detonation structure. Low propellant flow rates were also hypothesized to play a role.

6.2 Future Work

6.2.1 Low-Order RDE Model

The RDE model is suitable for follow-on studies, including nozzle imacts and investigating the effects of other fuel mixtures (including hydrocarbon fuels and air). Additionally, the model can be used to perform further integration studies with other fore- and aft-body geometries, including mission design studies and further investigations of Mach number and dynamic pressure effect. However, the addition of a diffuser model is strongly recommended for future integration studies.

It would be worthwhile to compare the effects of various types of RDE injection schemes. For example, the method outlined in Chapter 2 imposes a plenum stagnation

pressure, which was then used to iteratively determine the detonation wave height and the propellant mass flow rate. However, experimental analyses often describe the engine behavior in terms of the propellant mass flow rate. Therefore, it would be worthwhile to investigate an alternate inlet model which proscribes the mass flow rate and uses the characteristic period of the detonation wave to determine the detonation wave height. In addition, the the curvature of the oblique shock and slipline around the annulus can be determined by taking into account Mach number variation in the expansion of the combustion products. Further studies and improvements can also include the effect of sidewall injection, correction factors to account for mixing losses, the addition of a heat transfer model.

The model derives performance parameters by integrating over the annulus in three dimensions, but only models the flow in two dimensions. However, as shown in Section 5.2, the static pressure upstream of the detonation wave is less than the sonic condition because of the three-dimensional effect of the area change experienced by the propellants from the injector ports to the annular chamber. This first-order three-dimensional effect could be relatively easily added without relaxing the assumption of uniform radial property variation. This would also allow for a more realistic investigation of injector ports, discharge coefficient, and pressure recovery, and provide more realistic performance results.

6.2.2 Continuing Experiments

Continuing experimental efforts should concentrate on identifying and resolving factors which prevent the establishment of a steady detonation wave. These efforts fall in three broad categories: improving the quality and quantity of data acquired, improving the facility to increase propellant flow and remove internal friction, and improvements to the design of the engine itself.

6.2.2.1 Improvements to Data Acquisition

To gain a better understanding of the behavior inside the annulus, additional pressure transducers should be employed around the outer housing. One unfortunate consequence of re-using the housing is that, as they are restricted to the locations designed into Skittle, the number and placement of diagnostic locations are limited (and not well-suited to Arthur's design). That said, though, there are additional points available for pressure transducers. They have not been employed yet due to the limited supply of transducers and especially water cooling jackets. There are several water-cooling jackets in which transducers have become stuck: PCB classifies removing the stuck transducer as a transducer service, and while these are not inexpensive, they are less expensive than replacing the transducer and jacket with new ones. Additionally, if PCB cannot extract the transducer, they will replace them. Further, while putting additional holes in the housing is not desirable, there is space for one transducer closer to the injection plane, which would be of great benefit to describing the behavior of the mixing and diffusion zone.

6.2.2.2 Improvements to the Experimental Facility

The flow rates described in the experiment here are computed using a fairly rudimentary method that makes a number of assumptions about the behavior of the flow through the propellant lines and was fairly wasteful of the nitrogen gas used for calibration. The calibrations could be improved by redoing the calibrations using a mass flow meter with a range more appropriate for the actual flowrates or, ideally, employing dedicated flow meters on each propellant line to take dynamic flow rate measurements over the course of the experiment.

Measures should be taken to increase the flow rates that the facility is able to supply. Increased flow rates can most easily be obtained by increasing the area available to the flow, increasing the stagnation pressure, and decreasing the pressure drop through the lines. In the current experiments, the minimum areas in the flowpath are at either the bottle nipple or immediately downstream therefrom. Re-plumbing the facility with larger-diameter tubing, including at the bottles themselves, would significantly raise the available flow rates. The use of a single bottle on each line was also limiting. Flow rate could be increased by using multiple propellant bottles in parallel for both the fuel and oxidizer lines. Finally, the pressure drop in the system could be decreased most easily by reducing the length of tubing through which the propellants must pass. Locating the gas cart closer to the test stand could cut a significant amount of length out of the tubing (20–30 ft easily).

To improve the torque and thrust readings, the ball-spring plungers in the RDE clamps should be replaced with an alternative method of providing the rotational degree of freedom that has less internal friction. Lubricated bearings would be ideal, but a number of Hudson bearings of the sort used on roller-table conveyors have been procured, and with relatively basic modifications to the RDE clamps could significantly reduce friction in the system. In the same vein, replacing even a short segment of each 1/4 in oxygen line with flexible tubing would further reduce the internal resistance to torque. A calibration should be performed with the engine installed and all components in place to quantify this internal friction and its effect on the measured strain. The calibration of the rod itself has already been performed, so this is simply a case of either a small tweak to the existing torque calibration plate or the manufacture of a new one. The concept of the strain rod appears to be sound, but the rod used in the present experiments is not sensitive enough to capture small changes in strain response. A thinner torque rod or one made from a

material with lower torsional resistance should be built to improve the resolution of the torque measurements. Torque measurements could also be improved by constructing a lighter predetonator. The present design works well but is much longer and heavier than required, and a more compact design would decrease the torsional preload and improve system response. Additional steps can include an improved sandwich plate design to ensure proper transmission of thrust while maintaining rotational freedom, a more accurate method of determining that preload, and a more streamlined method of mounting and dismounting the engine.

Finally, to improve fit and alignment, the test stand could be re-built using improved materials. A large amount of quad-section t-slotted extrusion (t-slot) has been donated to the ARC, along with some brackets and fasteners. T-slotted extrusion is higher-quality and easier to align than C-channel, and would make a more secure and customizable platform on which to test. Aluminum t-slotted extrusion is easier to cut than uni-strut, and can be done so using a wood blade in a miter saw.

6.2.2.3 Improvements to Engine Design

Alterations to Arthur should focus on more uniform propellant distribution, the ability to accommodate greater mass flow rates, and ease of disassembly. A simple means of obtaining more uniform propellant distribution through the valve cavity can be accomplished by a number of means, including redesign of the injector isolator to prevent the propellant from having an unobstructed path from injector port to the annulus, and the installation of a mesh, foam, or other porous material in the fluidic valve chamber above the injector ports to distribute the propellant flow more evenly around the annulus. Other injection methods could also be employed, though any modifications towards sidewall injection would likely reduce or eliminate the ability to cool one or more of the annular surfaces. Greater flowrates could be accommodated

through more or larger propellant input ports, as well as a reconfigured injection system that makes use of upstream plenums to which larger propellant lines can be connected. The most difficult part of disassembling Arthur (for example, to change injector plates or access the fluidic valve chamber) is separating the housing and head mount. This process could be ameliorated by chamfering the edge between these two parts, a threaded hole in the head mount, or an internal lever.

APPENDIX A

DERIVATION OF THE CONSERVATION EQUATIONS FOR A ROTATING DETONATION ENGINE

A.1 Continuity

In vector form, the continuity equation is:

$$\frac{\partial \rho}{\partial t} + \nabla \cdot (\rho \vec{V}) = 0 \tag{A.1}$$

Integrating over the control volume $\mathscr{V}$:

$$\int_{\mathscr{V}} \frac{\partial \rho}{\partial t}\, d\mathscr{V} + \int_{\mathscr{V}} \nabla \cdot (\rho \vec{V})\, d\mathscr{V} = 0 \tag{A.2}$$

The first term simplifies by the Reynolds transport theorem and the second by the divergence theorem:

$$\frac{\partial}{\partial t} \int_{\mathscr{V}} \rho\, d\mathscr{V} + \int_S \rho \vec{V} \cdot \hat{n}\, dS = 0 \tag{A.3}$$

Assuming steady state, $\partial/\partial t = 0$, and Equation (A.3) simplifies to

$$\int_S \rho \vec{V} \cdot \hat{n}\, dS = 0 \tag{A.4}$$

Separating out the surfaces:

$$\int_{S_1} \rho \vec{V} \cdot \hat{n}\, dS_1 + \int_{S_2} \rho \vec{V} \cdot \hat{n}\, dS_2 + \int_{S_3} \rho \vec{V} \cdot \hat{n}\, dS_3 + \int_{S_4} \rho \vec{V} \cdot \hat{n}\, dS_4 = 0 \tag{A.5}$$

As there is no flow through S_3 or S_3, $\vec{V} \cdot \hat{n}_3 = \vec{V} \cdot \hat{n}_4 = 0$. Therefore, Equation (A.5) becomes:

$$\int_{S_1} \rho \vec{V} \cdot \hat{n}\, dS_1 + \int_{S_2} \rho \vec{V} \cdot \hat{n}\, dS_2 = 0 \tag{A.6}$$

From the definition of the control volume:

$$\vec{V} = V_r\, \hat{r} + V_\theta\, \hat{\theta} + V_z\, \hat{z} \tag{A.7}$$

Therefore:

$$\vec{V} \cdot \hat{n}_1 = -V_z$$

$$\vec{V} \cdot \hat{n}_2 = V_z$$

Then, Equation (A.6) simplifies to:

$$\int_{S_2} (\rho V_z)_2 \, dS_2 - \int_{S_1} (\rho V_z)_1 \, dS_1 = 0 \tag{A.8}$$

Expanding the integrals:

$$\int_0^{2\pi} \int_{r_i}^{r_o} (\rho V_z)_2 \, dr \, d\theta - \int_0^{2\pi} \int_{r_i}^{r_o} (\rho V_z)_1 \, dr \, d\theta = 0 \tag{A.9}$$

As property variation in the r-direction is neglected, the r-integrals can be computed:

$$\int_0^{2\pi} (\rho V_z)_2 \, dS_2 \left[\frac{1}{2} r_2\right]_{r_i}^{r_o} d\theta - \int_0^{2\pi} (\rho V_z)_1 \left[\frac{1}{2} r_1\right]_{r_i}^{r_o} d\theta = 0 \tag{A.10}$$

$$\frac{1}{2}\left(r_o^2 - r_i^2\right)_2 \int_0^{2\pi} (\rho V_z)_2 \, d\theta - \frac{1}{2}\left(r_o^2 - r_i^2\right)_1 \int_0^{2\pi} (\rho V_z)_1 \, d\theta = 0 \tag{A.11}$$

Noting that the annulus thickness δ_a and mean radius r_m are given by:

$$\delta_a = (r_o - r_i)$$
$$r_m = \frac{1}{2}(r_o + r_i)$$

therefore

$$\begin{aligned} \delta_a r_m &= \frac{1}{2}(r_o - r_i)(r_o + r_i) \\ &= \frac{1}{2}\left(r_o^2 - r_i^2\right) \end{aligned} \tag{A.12}$$

Substituting Equation (A.12) into Equation (A.11), and noting that for a straight annulus $r_{m_1} = r_{m_2}$ and $\delta_{a_1} = \delta_{a_2}$, the final continuity equation is

$$\delta_a r_m \left[\int_0^{2\pi} (\rho V_z)_2 \, d\theta - \int_0^{2\pi} (\rho V_z)_1 \, d\theta\right] = 0 \tag{A.13}$$

A.2 Energy

The differential vector form of the conservation of energy (from Lyman [170], who cites Liepmann and Roshko [249]) is

$$\rho \frac{Dh_0}{Dt} = \frac{\partial P}{\partial t} + \nabla \cdot \left(\boldsymbol{\tau}_{ij} \cdot \vec{V} - \vec{q}\right) + \rho \vec{f} \vec{V} \tag{A.14}$$

However, this equation does not allow for any internal heat release, such as that provided by the detonation wave. This is accounted for by the addition of a separate $\vec{q}_{det}$ term. Expanding the material derivative, noting that the total specific enthalpy is an intensive property and the General Property Balance [250] applies

$$\rho\left[\frac{\partial h_0}{\partial t}+\nabla\cdot\left(h_0\vec{V}\right)\right]=\frac{\partial P}{\partial t}+\nabla\cdot\left(\boldsymbol{\tau}_{ij}\cdot\vec{V}-\vec{q}\right)+\rho\vec{f}\vec{V}-\vec{q}_{det} \tag{A.15}$$

Assuming:

1. Steady State: $\partial/\partial t=0$
2. Inviscid: $\boldsymbol{\tau}_{ij}=0$
3. No body forces: $\vec{f}_b=0$

Equation (A.15) becomes

$$\rho\nabla\cdot\left(h_0\vec{V}\right)=-\nabla\cdot\vec{q}-\vec{q}_{det} \tag{A.16}$$

Integrating over the control volume

$$\int_{\mathscr{V}}\rho\nabla\cdot\left(h_0\vec{V}\right)d\mathscr{V}=-\int_{\mathscr{V}}\nabla\cdot\vec{q}\,d\mathscr{V}-\int_{\mathscr{V}}\vec{q}_{det}\,d\mathscr{V} \tag{A.17}$$

Applying the divergence theorem to both terms, and noting that $\int_{\mathscr{V}}\vec{q}_{det}\,d\mathscr{V}=\vec{Q}_{det}$

$$\int_S\rho\left(h_0\vec{V}\right)\cdot\hat{n}\,dS=-\int_S\vec{q}\cdot\hat{n}\,dS-\vec{Q}_{det} \tag{A.18}$$

Expanding over the surfaces:

$$\begin{aligned}\int_{S_1}(\rho h_0\vec{V}\cdot\hat{n})_1\,dS_1+&\int_{S_2}(\rho h_0\vec{V}\cdot\hat{n})_2\,dS_2\\+\int_{S_3}(\rho h_0\vec{V}\cdot\hat{n})_3\,dS_3+&\int_{S_4}(\rho h_0\vec{V}\cdot\hat{n})_4\,dS_4\\&=-\int_{S_1}(\vec{q}\cdot\hat{n})_1\,dS_1-\int_{S_2}(\vec{q}\cdot\hat{n})_2\,dS_2\\&\quad-\int_{S_3}(\vec{q}\cdot\hat{n})_3\,dS_3-\int_{S_4}(\vec{q}\cdot\hat{n})_4\,dS_4-Q_{det}\end{aligned} \tag{A.19}$$

Again assuming no flow through surfaces S_3 and S_4

$$\vec{V} \cdot \hat{n}_1 = -V_z \qquad \vec{V} \cdot \hat{n}_3 = 0$$
$$\vec{V} \cdot \hat{n}_2 = V_z \qquad \vec{V} \cdot \hat{n}_4 = 0$$

There is no heat transfer through surfaces S_1

$$\vec{q} \cdot \hat{n}_1 = 0 \qquad \vec{q} \cdot \hat{n}_2 = 0$$
$$\vec{q} \cdot \hat{n}_3 = 0 \qquad \vec{q} \cdot \hat{n}_4 = 0$$

so Equation (A.19) simplifies to:

$$\begin{aligned} -\int_{S_1} (\rho h_0 V_z)_1 \, dS_1 + \int_{S_2} (\rho h_0 V_z)_2 \, dS_2 \\ = -\int_{S_3} (\vec{q} \cdot \hat{n})_3 \, dS_3 - \int_{S_4} (\vec{q} \cdot \hat{n})_4 \, dS_4 - Q_{det} \end{aligned} \tag{A.20}$$

The two heat flux terms are calculated by a separated heat transfer analysis, and can be represented as $\int_{S_{3,4}} (\vec{q} \cdot \hat{n})_{3,4} \, dS_{3,4} = Q_{3,4}$. As these are cooling flows, the direction of heat transfer is in line with the normal vector: $\vec{q} \cdot \hat{n} = q$, and as a source term, the sign on Q_{det} is opposite that of the cooling flows. Thus Equation (A.20) becomes:

$$\int_{S_2} (\rho h_0 V_z)_2 \, dS_2 - \int_{S_1} (\rho h_0 V_z)_1 \, dS_1 + Q_3 + Q_4 - Q_{det} = 0 \tag{A.21}$$

Completing the r-integral as before, the final Energy equation is

$$\delta_a r_m \left[\int_0^{2\pi} (\rho h_0 V_z)_2 \, d\theta - \int_0^{2\pi} (\rho h_0 V_z)_1 \, d\theta \right] + Q_3 + Q_4 - Q_{det} = 0 \tag{A.22}$$

A.3 Momentum

The differential vector form of the Navier–Stokes equation is:

$$\rho \frac{D\vec{V}}{Dt} = -\nabla \cdot (\boldsymbol{P}_{ij} + \boldsymbol{\tau}_{ij}) + \rho \left(\vec{f_b} + \vec{f} \right) \tag{A.23}$$

Where $\boldsymbol{P}_{ij} + \boldsymbol{\tau}_{ij} = \boldsymbol{\sigma}_{ij}$ are the normal and shear stress components of the Cauchy stress tensor, $\vec{f}_b$ is the specific body force, and $\vec{f}$ is the specific resultant force. Integrating over the control volume $\mathscr{V}$ and expanding the material derivative:

$$\begin{aligned}\int_{\mathscr{V}} \rho \frac{\partial \vec{V}}{\partial t}\, d\mathscr{V} + \int_{\mathscr{V}} \rho \left(\vec{V} \cdot \nabla\right) \vec{V}\, d\mathscr{V} \\ = \int_{\mathscr{V}} \nabla \cdot \left(-\boldsymbol{P}_{ij} + \boldsymbol{\tau}_{ij}\right)\, d\mathscr{V} + \int_{\mathscr{V}} \rho \vec{f}_b\, d\mathscr{V} + \int_{\mathscr{V}} \rho \vec{f}\, d\mathscr{V}\end{aligned} \tag{A.24}$$

Assuming:

1. Steady State: $\partial/\partial t = 0$
2. Inviscid: $\boldsymbol{\tau}_{ij} = 0$
3. No body forces: $\vec{f}_b = 0$

and noting that the total resultant force can be simply rendered as $\vec{f}$, Equation (A.24) becomes

$$\int_{\mathscr{V}} \rho \left(\vec{V} \cdot \nabla\right) \vec{V}\, d\mathscr{V} = -\int_{\mathscr{V}} \nabla \cdot \boldsymbol{P}\, d\mathscr{V} + \vec{F} \tag{A.25}$$

By the divergence theorem of Gauss, the second term can be converted from a volume integral to a surface integral

$$\int_{\mathscr{V}} \rho \left(\vec{V} \cdot \nabla\right) \vec{V}\, d\mathscr{V} = -\int_{S} \boldsymbol{P}_{ij} \cdot \hat{n}\, dS + \vec{F} \tag{A.26}$$

Solving for $\vec{F}$ and breaking by component

$$F_i = \int_{\mathscr{V}} \rho \left(\vec{V} \cdot \nabla\right) V_i\, d\mathscr{V} + \int_{S} P \cdot \hat{n}\, dS \tag{A.27}$$

where $i = r,\, \theta,\, z$. The first term simplifies by the following identity[1]

$$\int_{\mathscr{V}} \nabla \phi\, d\mathscr{V} = \int_{S} \phi\, dS$$

where ϕ is a scalar field. So, Equation (A.24) becomes

$$F_i = \int_{S} \rho V_i \left(\vec{V} \cdot \hat{n}\right) dS + \int_{S} P_i \cdot \hat{n}\, dS \tag{A.28}$$

[1]Proof follows from the divergence theorem [251].

From the definition of the control volume:

$$\vec{V}\cdot\hat{n}_1 = -V_z\,\hat{z} \qquad \vec{V}\cdot\hat{n}_2 = V_z\,\hat{z} \qquad \vec{V}\cdot\hat{n}_3 = 0 \qquad \vec{V}\cdot\hat{n}_4 = 0$$

$$P\,\hat{n}_1 = -P_1\,\hat{z} \qquad P\,\hat{n}_2 = (P_2 - P_\infty)\,\hat{z} \qquad P\,\hat{n}_3 = P_3\,\hat{r} \qquad P\,\hat{n}_4 = -P_4\,\hat{r}$$

where P_∞ is the atmospheric pressure. Substituting these into Equation (A.28) yields expressions for the resultant forces:

$\hat{\boldsymbol{r}}$:

$$\begin{aligned} F_r &= \int_{S_4} P_4\,dS_4 - \int_{S_3} P_3\,dS_3 \\ &\approx 0 \end{aligned}$$

This is assumed to be small, and is not of interest for this analysis.

$\hat{\boldsymbol{\theta}}$:

$$F_\theta = \int_{S_2} (\rho V_\theta V_z)_2\; dS_2 - \int_{S_1} (\rho V_\theta V_z)_1\; dS_1$$

Completing the r-integrals yields the final expression for the resultant force in the circumferential direction

$$F_\theta = \delta_a r_m \left[\int_0^{2\pi} (\rho V_\theta V_z)_2\; d\theta - \int_0^{2\pi} (\rho V_\theta V_z)_1\, d\theta\right] \tag{A.29}$$

$\hat{\boldsymbol{z}}$:

$$F_z = -\int_{S_1} \left(\rho V_z^2\right)_1\; dS_1 + \int_{S_2} \left(\rho V_z^2\right)_2\; dS_2 - \int_{S_1} P_1\,dS_1 + \int_{S_2} (P_2 - P_\infty)\; dS_2$$

Again completing the r-integrals, we have the final expression for the resultant force in the axial direction

$$F_z = \delta_a r_m \left[\int_0^{2\pi} \left(\rho V_z^2 + P_2 - P_\infty\right)_2\, d\theta - \int_0^{2\pi} \left(\rho V_z^2 + P\right)_1\, d\theta\right] \tag{A.30}$$

However, it is convention, particularly in rocket propulsion contexts, to draw the control volume such that mass flux into the system is zero. If the control volume

is extended to encompass the propellant plenum (at stagnation conditions), $V_{z_1} = V_{\theta_1} = 0$, and Equations (A.29) and (A.30) reduce to

$$F_\theta = \delta_a r_m \int_0^{2\pi} (\rho V_\theta V_z)_2 \, d\theta \tag{A.31}$$

$$F_z = \delta_a r_m \int_0^{2\pi} \left(\rho V_z^2 + P_2 - P_\infty\right)_2 \, d\theta \tag{A.32}$$

APPENDIX B

ADDITIONAL RDE-WAVERIDER FIGURES

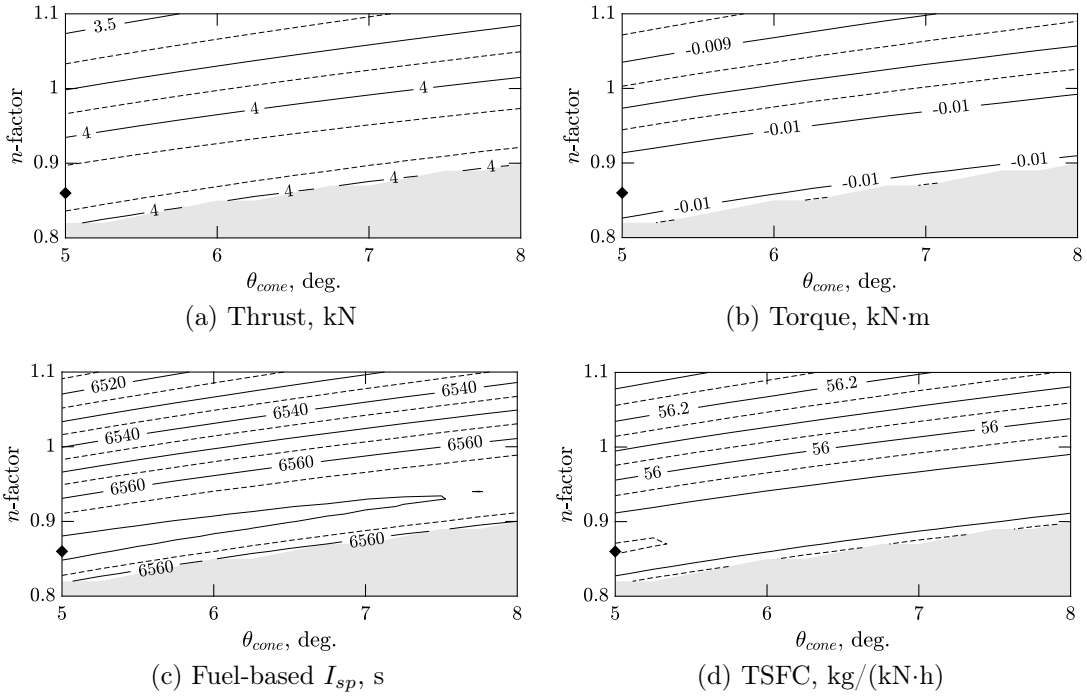

(a) Thrust, kN (b) Torque, kN·m

(c) Fuel-based I_{sp}, s (d) TSFC, kg/(kN·h)

Figure B.1. Integrated RDE performance map, Mach 3, $\overline{q} = 500\,\text{psf}$, hydrogen fuel.

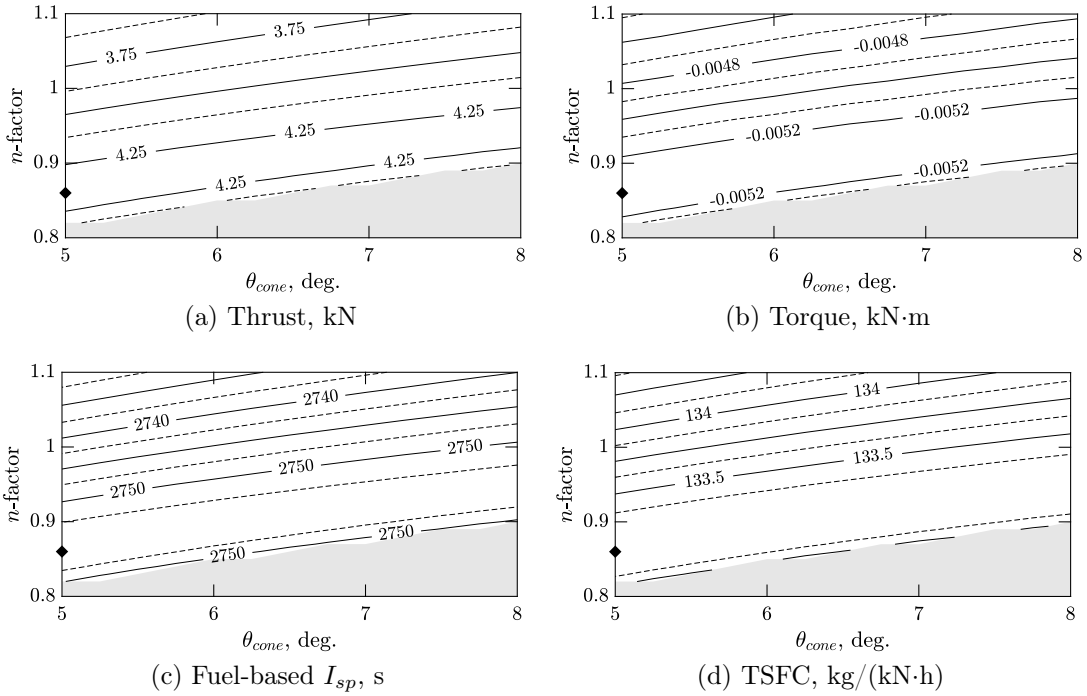

(a) Thrust, kN (b) Torque, kN·m

(c) Fuel-based I_{sp}, s (d) TSFC, kg/(kN·h)

Figure B.2. Integrated RDE performance map, Mach 3, $\overline{q} = 500\,\text{psf}$, propane fuel.

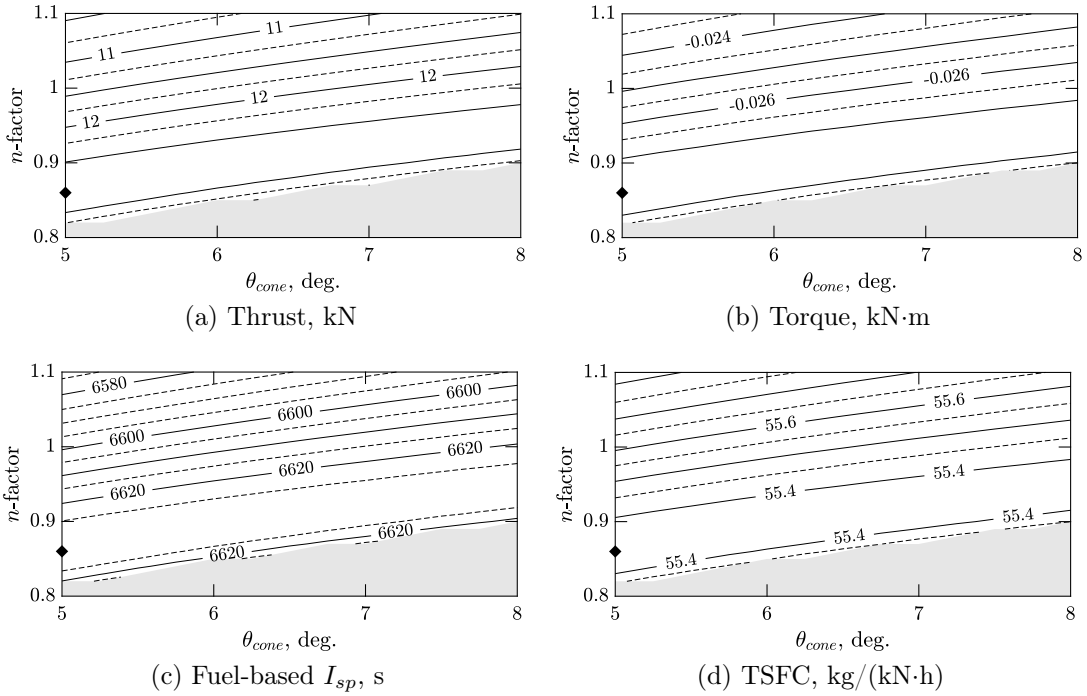

(a) Thrust, kN (b) Torque, kN·m

(c) Fuel-based I_{sp}, s (d) TSFC, kg/(kN·h)

Figure B.3. Integrated RDE performance map, Mach 3, $\overline{q} = 1500\,\text{psf}$, hydrogen fuel.

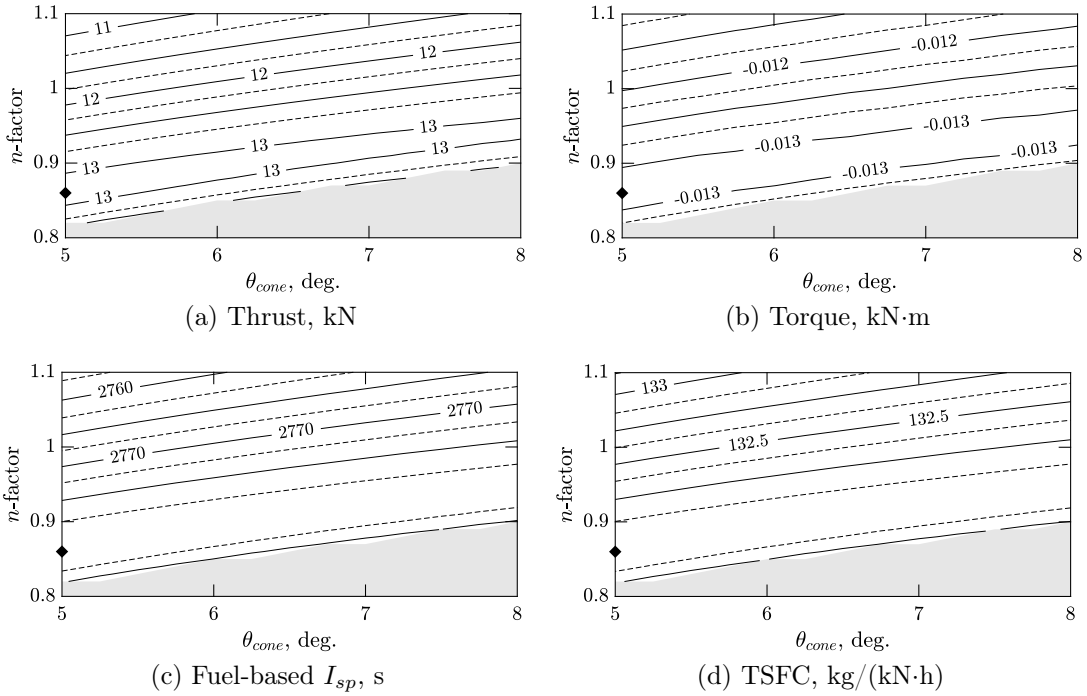

(a) Thrust, kN (b) Torque, kN·m

(c) Fuel-based I_{sp}, s (d) TSFC, kg/(kN·h)

Figure B.4. Integrated RDE performance map, Mach 3, $\overline{q} = 1500\,\text{psf}$, propane fuel.

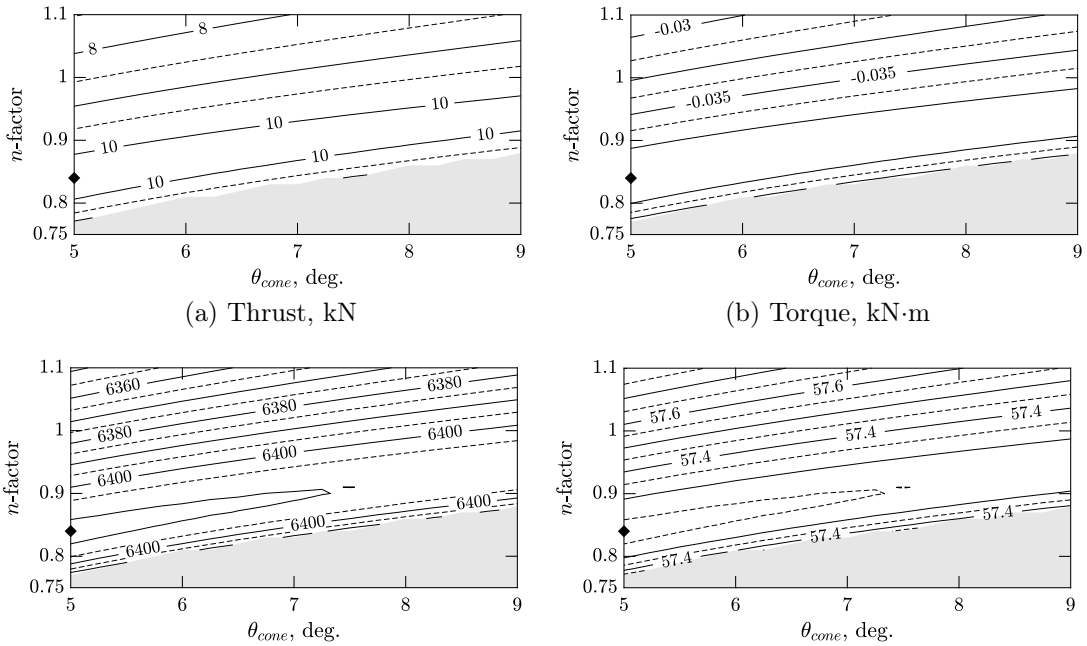

(a) Thrust, kN (b) Torque, kN·m

(c) Fuel-based I_{sp}, s (d) TSFC, kg/(kN·h)

Figure B.5. Integrated RDE performance map, Mach 3.5, $\overline{q} = 1000\,\text{psf}$, hydrogen fuel.

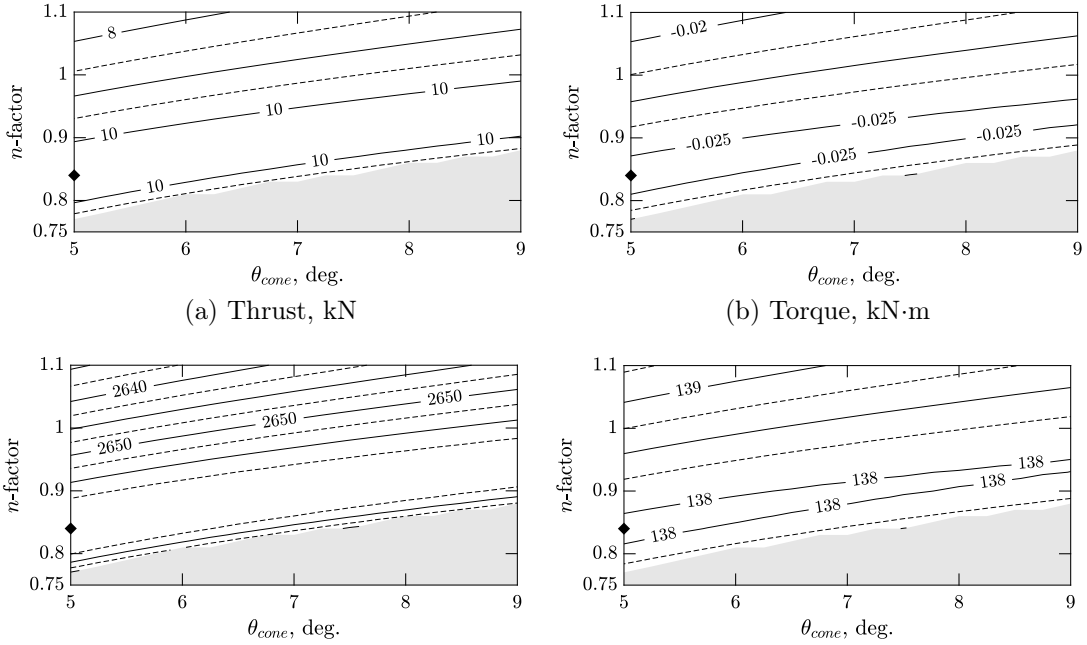

(a) Thrust, kN (b) Torque, kN·m

(c) Fuel-based I_{sp}, s (d) TSFC, kg/(kN·h)

Figure B.6. Integrated RDE performance map, Mach 3.5, $\overline{q} = 1000\,\text{psf}$, propane fuel.

APPENDIX C

CYCLE TIMING

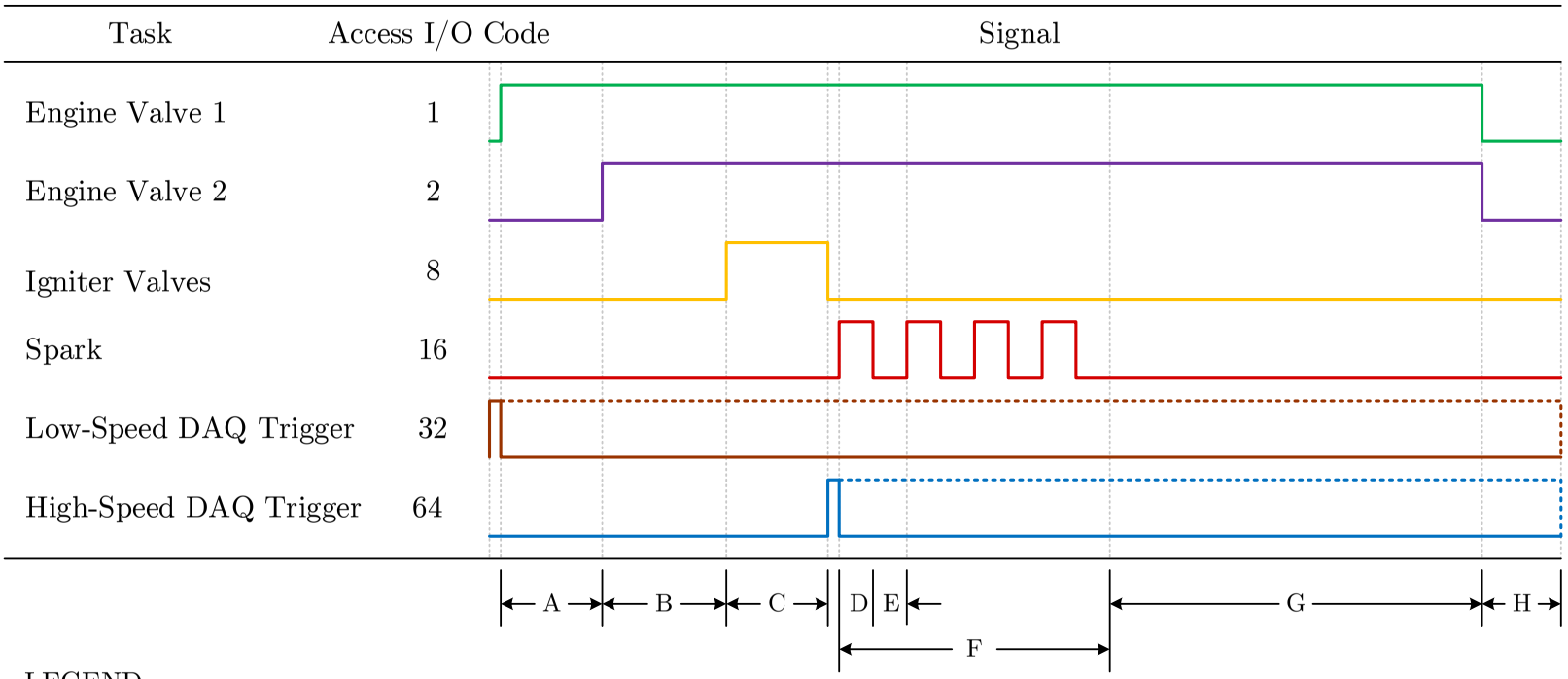

LEGEND

A Engine Valve Delay (t_{evd})	D Spark High Time (t_{sph})	G Test Duration (t_{test})
B Igniter Valve Delay (t_{ivd})	E Spark Low Time ($t_{spl} = t_{sph}$)	H Tail (t_{tail})
C Igniter Valve Open Time (t_{ivo})	F Spark Duration (t_{sp})	

Figure C.1. Cycle timing diagram.

Table C.1. Test pressure and timing matrix

				Predetonator		Spark Plug				
P_{0_f} (psig)	ϕ	$P_{0_{ox}}$ (psig)	t_{evd} (ms)	t_{ivd} (ms)	t_{iot} (ms)	t_{ivd} (ms)	t_{iot} (ms)	t_{sht} (ms)	n_{sp}	t_{sp} (ms)
15	0.5	61.0	0	24	16	42	0	5	4	80
	0.75	39.9	0	26	16	44	0	5	4	80
	1.0	30.5	0	29	17	48	0	5	4	80
	1.5	20.7	0	35	18	55	0	5	4	80
	2.0	15.3	0	40	19	61	0	5	4	80
30	0.5	122.5	0	25	14	41	0	5	4	80
	0.75	76.8	0	25	14	42	0	5	4	80
	1.0	54.3	0	24	15	41	0	5	4	80
	1.5	36.3	0	37	17	46	0	5	4	80
	2.0	27.8	0	31	17	50	0	5	4	80
45	0.5	> 150	N/A	N/A	N/A	N/A	N/A	N/A	N/A	N/A
	0.75	112.6	0	25	15	42	0	5	4	80
	1.0	80.7	0	25	15	42	0	5	4	80
	1.5	50.1	0	25	16	43	0	5	4	80
	2.0	37.8	0	27	16	45	0	5	4	80
60	0.5	> 150	N/A	N/A	N/A	N/A	N/A	N/A	N/A	N/A
	0.75	144.7	0	26	14	42	0	5	4	80
	1.0	104.7	0	25	15	42	0	5	4	80
	1.5	64.9	0	24	16	42	0	5	4	80
	2.0	47.0	0	25	16	43	0	5	4	80

APPENDIX D

CIRCUIT DIAGRAMS

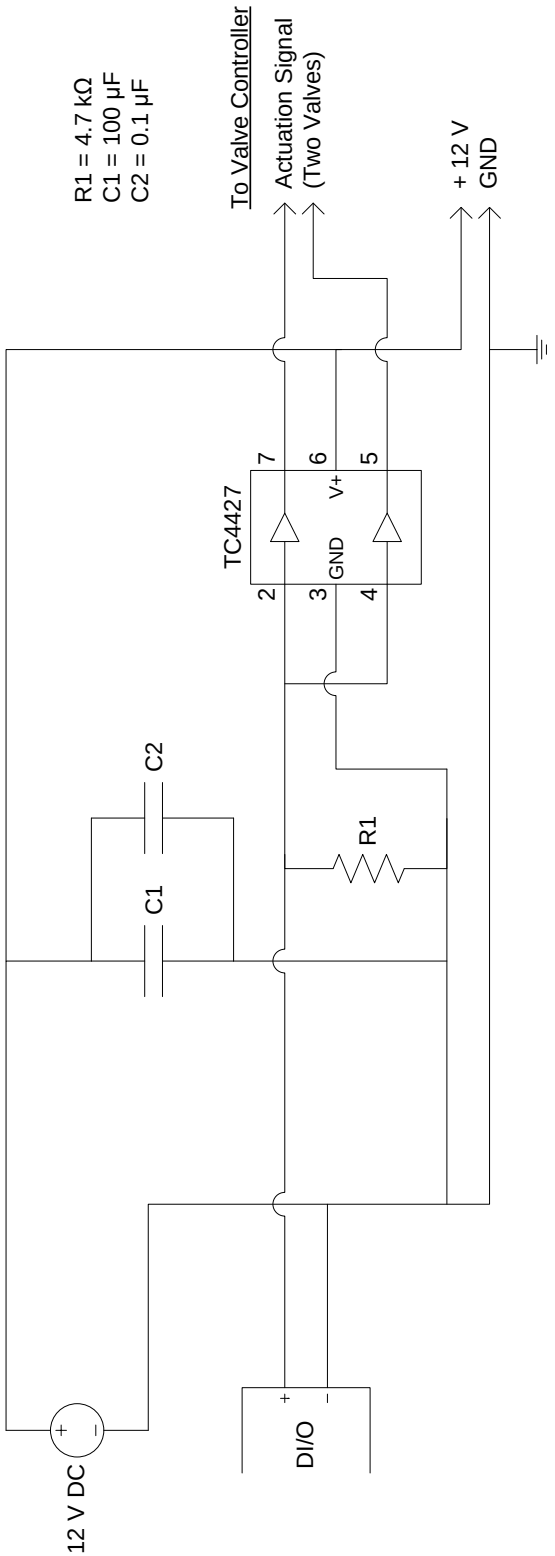

Figure D.1. Circuit diagram for injector trigger box.

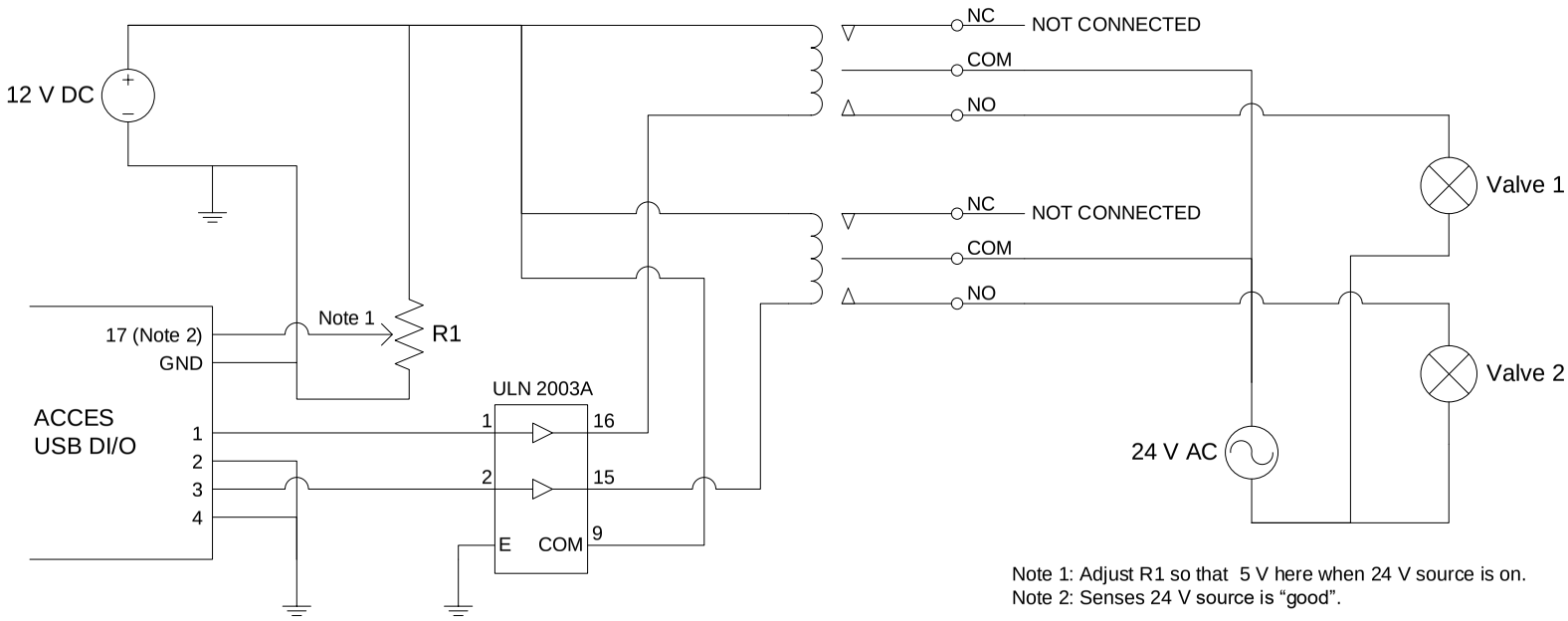

Figure D.2. Circuit diagram for engine valve control system.

APPENDIX E

PLUMBING AND INSTRUMENTATION DIAGRAMS

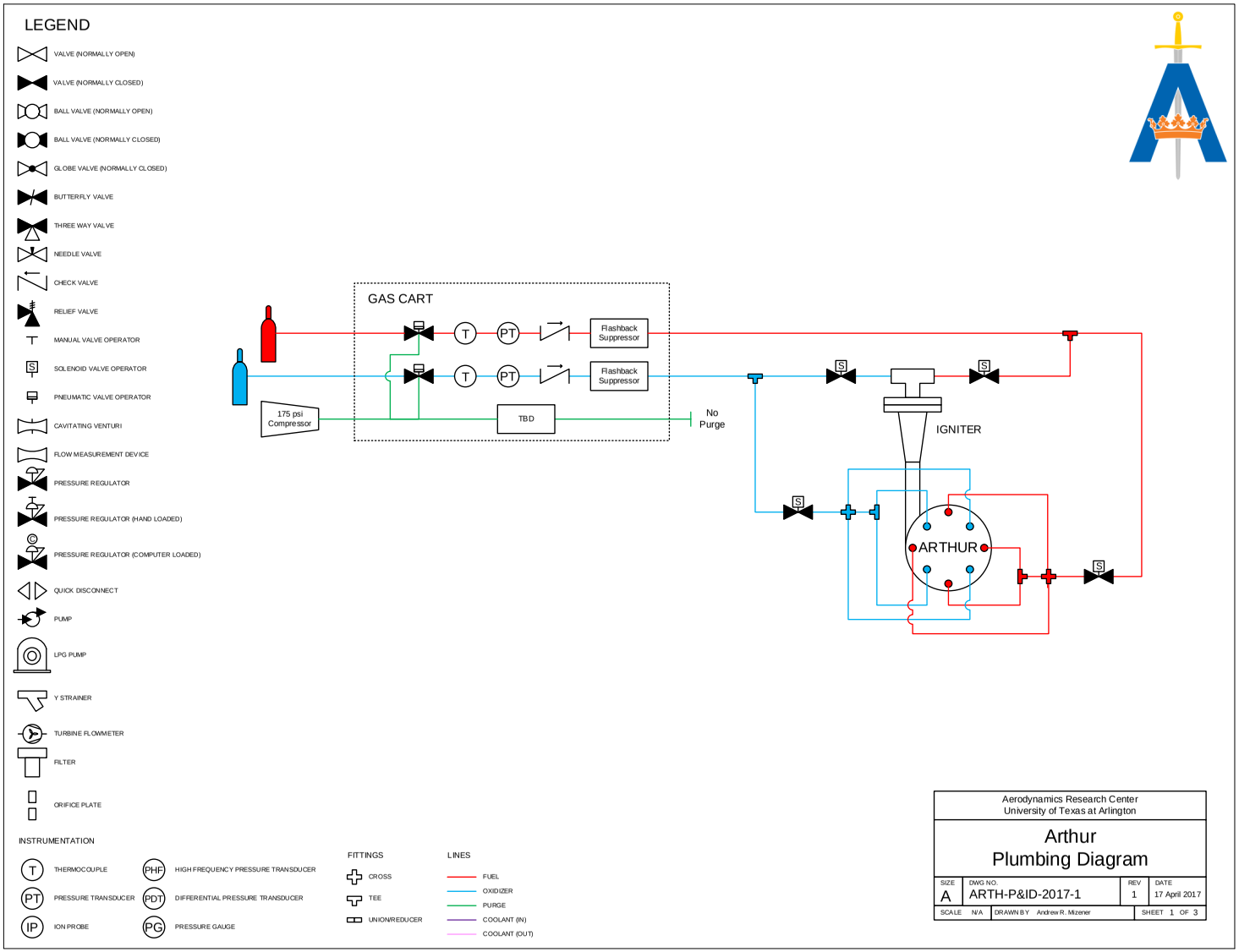
LEGEND
VALVE (NORMALLY OPEN)
VALVE (NORMALLY CLOSED)
BALL VALVE (NORMALLY OPEN)
BALL VALVE (NORMALLY CLOSED)
GLOBE VALVE (NORMALLY CLOSED)
BUTTERFLY VALVE
THREE WAY VALVE
NEEDLE VALVE
CHECK VALVE
RELIEF VALVE
MANUAL VALVE OPERATOR
SOLENOID VALVE OPERATOR
PNEUMATIC VALVE OPERATOR
CAVITATING VENTURI
FLOW MEASUREMENT DEVICE
PRESSURE REGULATOR
PRESSURE REGULATOR (HAND LOADED)
PRESSURE REGULATOR (COMPUTER LOADED)
QUICK DISCONNECT
PUMP
LPG PUMP
Y STRAINER
TURBINE FLOWMETER
FILTER
ORIFICE PLATE
INSTRUMENTATION
T THERMOCOUPLE
PT PRESSURE TRANSDUCER
IP ION PROBE
PHF HIGH FREQUENCY PRESSURE TRANSDUCER
PDT DIFFERENTIAL PRESSURE TRANSDUCER
PG PRESSURE GAUGE
FITTINGS
CROSS
TEE
UNION/REDUCER
LINES
FUEL
OXIDIZER
PURGE
COOLANT (IN)
COOLANT (OUT)
GAS CART
T
PT
Flashback Suppressor
Flashback Suppressor
175 psi Compressor
TBD
No Purge
S
IGNITER
ARTHUR
Aerodynamics Research Center
University of Texas at Arlington
Arthur
Plumbing Diagram
SIZE A
DWG NO. ARTH-P&ID-2017-1
REV 1
DATE 17 April 2017
SCALE N/A
DRAWN BY Andrew R. Mizener
SHEET 1 OF 3

LEGEND

- VALVE (NORMALLY OPEN)
- VALVE (NORMALLY CLOSED)
- BALL VALVE (NORMALLY OPEN)
- BALL VALVE (NORMALLY CLOSED)
- GLOBE VALVE (NORMALLY CLOSED)
- BUTTERFLY VALVE
- THREE WAY VALVE
- NEEDLE VALVE
- CHECK VALVE
- RELIEF VALVE
- MANUAL VALVE OPERATOR
- SOLENOID VALVE OPERATOR
- PNEUMATIC VALVE OPERATOR
- CAVITATING VENTURI
- FLOW MEASUREMENT DEVICE
- PRESSURE REGULATOR
- PRESSURE REGULATOR (HAND LOADED)
- PRESSURE REGULATOR (COMPUTER LOADED)
- QUICK DISCONNECT
- PUMP
- LPG PUMP
- Y STRAINER
- TURBINE FLOWMETER
- FILTER
- ORIFICE PLATE

INSTRUMENTATION

- (T) THERMOCOUPLE
- (PT) PRESSURE TRANSDUCER
- (IP) ION PROBE
- (PHF) HIGH FREQUENCY PRESSURE TRANSDUCER
- (PDT) DIFFERENTIAL PRESSURE TRANSDUCER
- (PG) PRESSURE GAUGE

FITTINGS

- CROSS
- TEE
- UNION/REDUCER

LINES

- FUEL
- OXIDIZER
- PURGE
- COOLANT (IN)
- COOLANT (OUT)

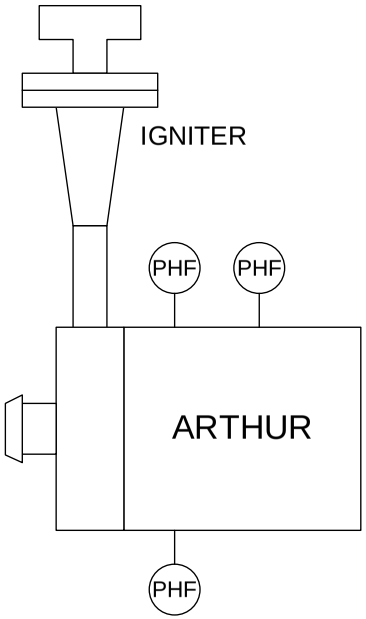

Aerodynamics Research Center
University of Texas at Arlington

Arthur
Instrumentation Diagram

SIZE	DWG NO.	REV	DATE
A	ARTH-P&ID-2017-1	1	17 April 2017

SCALE	DRAWN BY	SHEET
N/A	Andrew R. Mizener	2 OF 3

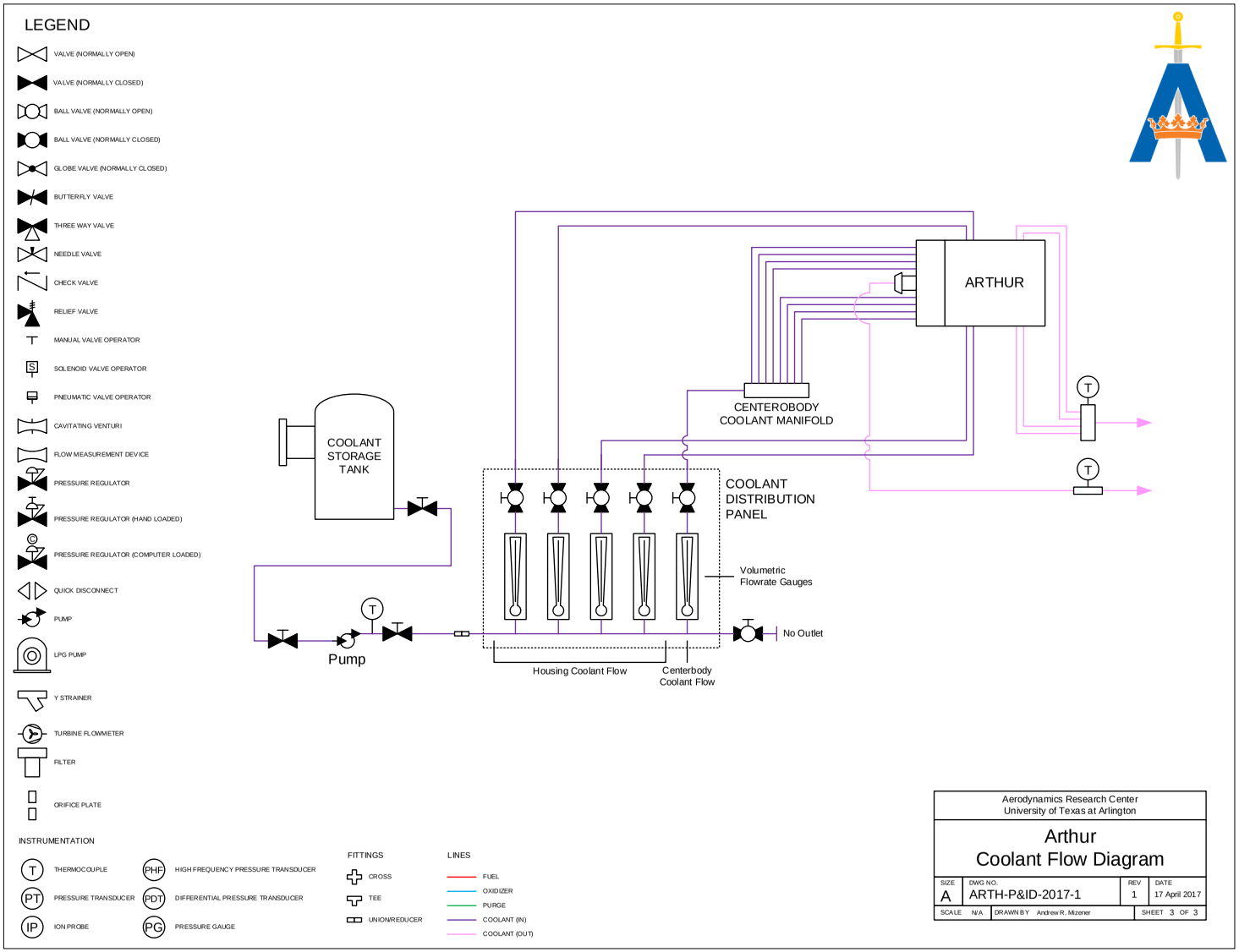
LEGEND
VALVE (NORMALLY OPEN)
VALVE (NORMALLY CLOSED)
BALL VALVE (NORMALLY OPEN)
BALL VALVE (NORMALLY CLOSED)
GLOBE VALVE (NORMALLY CLOSED)
BUTTERFLY VALVE
THREE WAY VALVE
NEEDLE VALVE
CHECK VALVE
RELIEF VALVE
MANUAL VALVE OPERATOR
SOLENOID VALVE OPERATOR
PNEUMATIC VALVE OPERATOR
CAVITATING VENTURI
FLOW MEASUREMENT DEVICE
PRESSURE REGULATOR
PRESSURE REGULATOR (HAND LOADED)
PRESSURE REGULATOR (COMPUTER LOADED)
QUICK DISCONNECT
PUMP
LPG PUMP
Y STRAINER
TURBINE FLOWMETER
FILTER
ORIFICE PLATE
INSTRUMENTATION
T THERMOCOUPLE
PT PRESSURE TRANSDUCER
IP ION PROBE
PHF HIGH FREQUENCY PRESSURE TRANSDUCER
PDT DIFFERENTIAL PRESSURE TRANSDUCER
PG PRESSURE GAUGE
FITTINGS
CROSS
TEE
UNION/REDUCER
LINES
FUEL
OXIDIZER
PURGE
COOLANT (IN)
COOLANT (OUT)
ARTHUR
CENTEROBODY
COOLANT MANIFOLD
COOLANT
STORAGE
TANK
COOLANT
DISTRIBUTION
PANEL
Volumetric
Flowrate Gauges
No Outlet
Pump
Housing Coolant Flow
Centerbody
Coolant Flow
T
T
T
Aerodynamics Research Center
University of Texas at Arlington
Arthur
Coolant Flow Diagram
SIZE A
DWG NO. ARTH-P&ID-2017-1
REV 1
DATE 17 April 2017
SCALE N/A
DRAWN BY Andrew R. Mizener
SHEET 3 OF 3

APPENDIX F

IMPROVED HIGH-SPEED IGNITION VISUALIZATION FIGURES

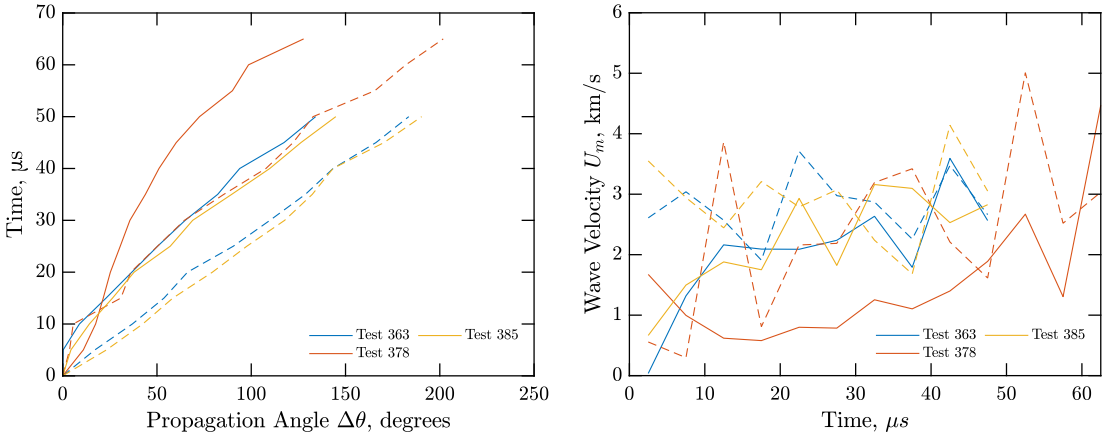

(a) θ–t wave diagram (b) Wave velocity

Figure F.1. Wave propagation results: 0° swirl, predetonator ignition. Solid lines indicate the upper combustion branch, dashed lines indicate the lower combustion branch.

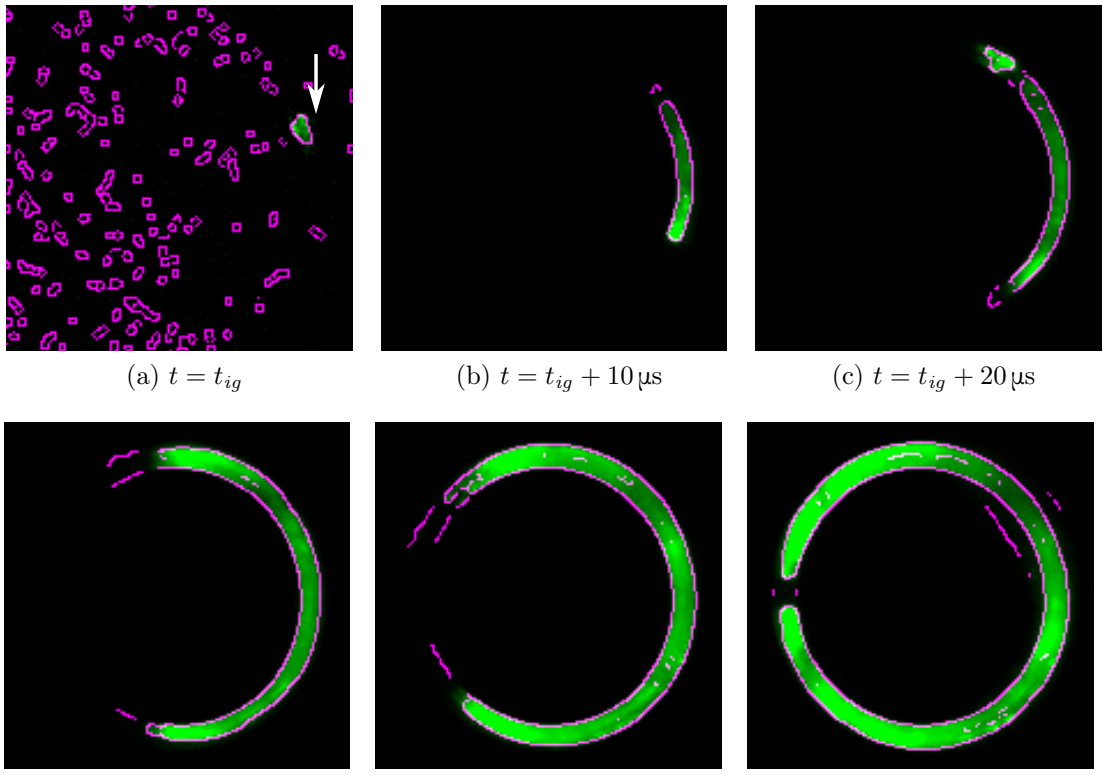

(a) $t = t_{ig}$ (b) $t = t_{ig} + 10\,\mu s$ (c) $t = t_{ig} + 20\,\mu s$

(d) $t = t_{ig} + 30\,\mu s$ (e) $t = t_{ig} + 40\,\mu s$ (f) $t = t_{ig} + 50\,\mu s$

Figure F.2. Selected frames, Test 385: 0° swirl, predetonator ignition.

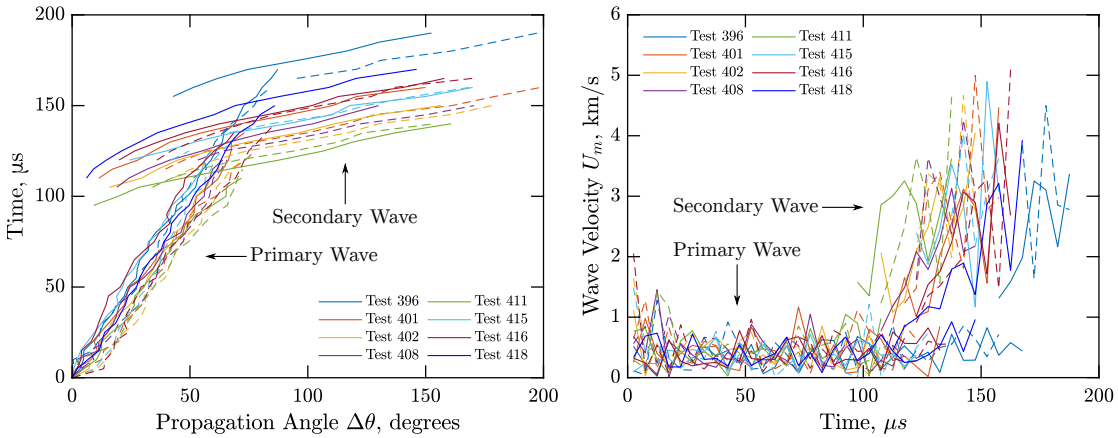

(a) θ–t wave diagram (b) Wave velocity

Figure F.3. Wave propagation results: 0° swirl, spark plug ignition. Solid lines indicate the upper combustion branch, dashed lines indicate the lower combustion branch.

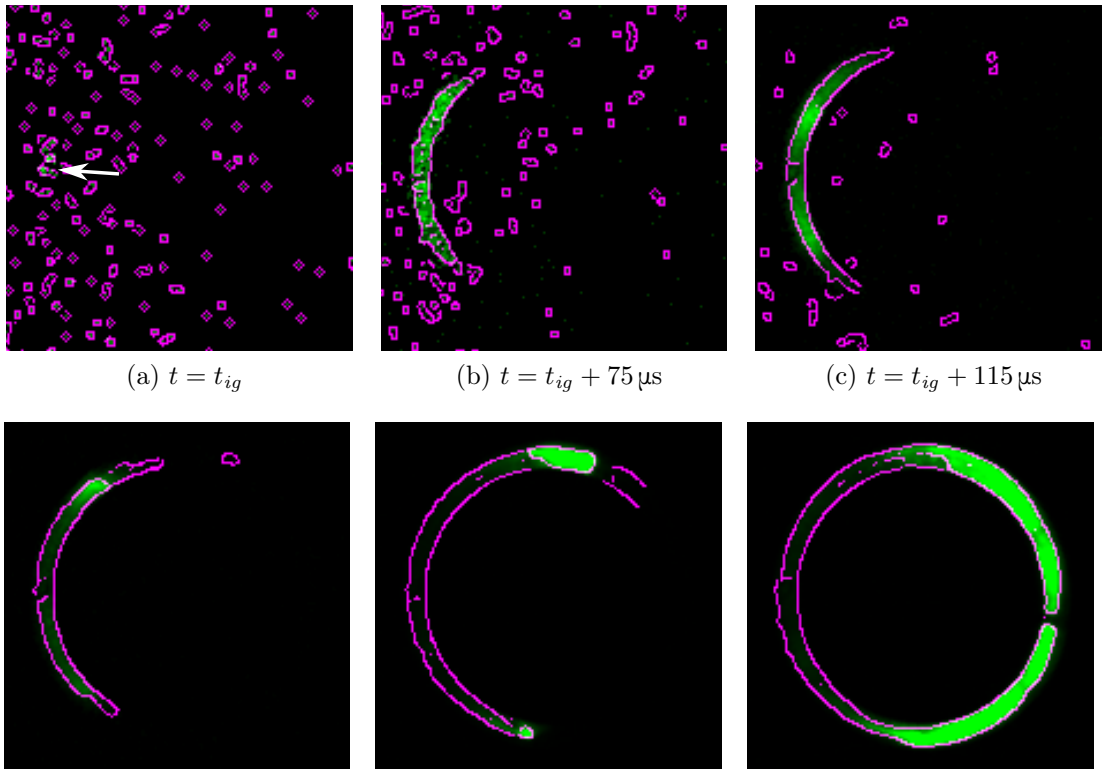

(a) $t = t_{ig}$ (b) $t = t_{ig} + 75\,\mu s$ (c) $t = t_{ig} + 115\,\mu s$

(d) $t = t_{ig} + 125\,\mu s$ (e) $t = t_{ig} + 140\,\mu s$ (f) $t = t_{ig} + 160\,\mu s$

Figure F.4. Selected frames, Test 415: 0° swirl, spark plug ignition.

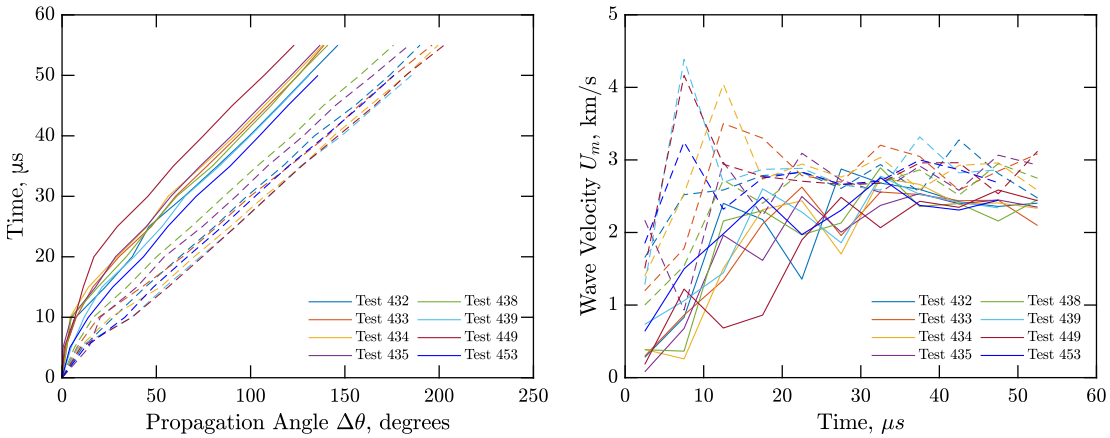

(a) θ–t wave diagram (b) Wave velocity

Figure F.5. Wave propagation results: +30° swirl, predetonator ignition. Solid lines indicate the upper combustion branch, dashed lines indicate the lower combustion branch.

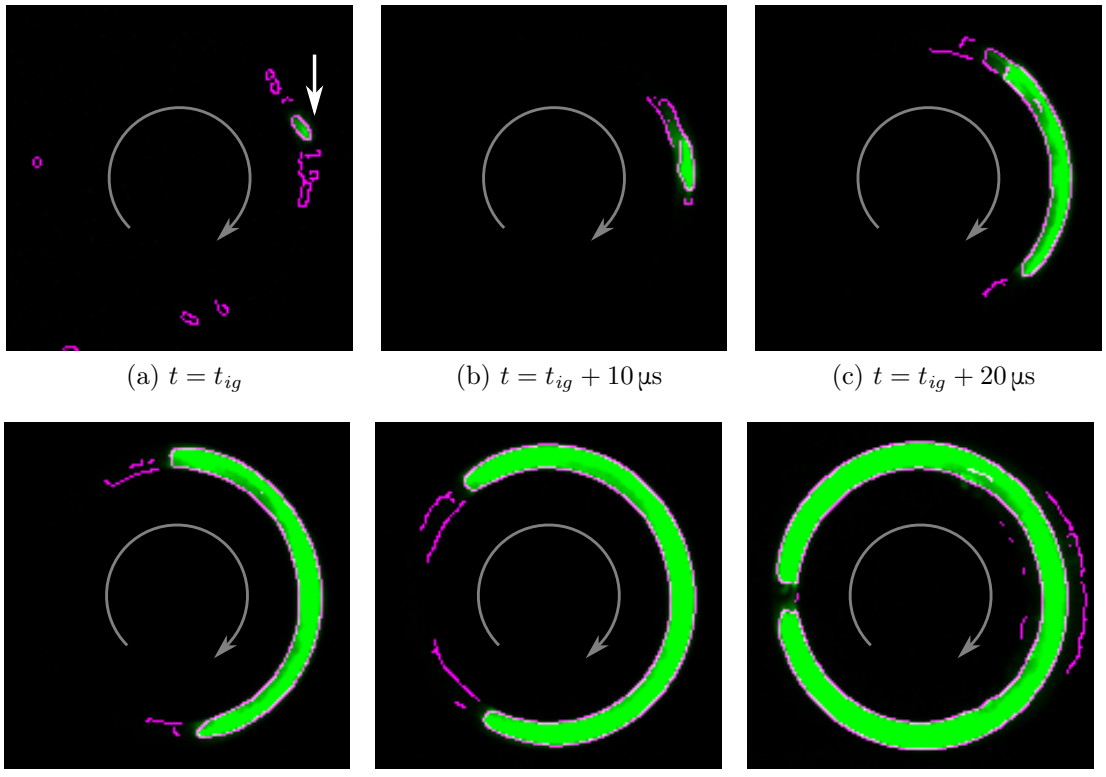

(a) $t = t_{ig}$ (b) $t = t_{ig} + 10\,\mu s$ (c) $t = t_{ig} + 20\,\mu s$

(d) $t = t_{ig} + 30\,\mu s$ (e) $t = t_{ig} + 40\,\mu s$ (f) $t = t_{ig} + 55\,\mu s$

Figure F.6. Selected frames, Test 432: +30° swirl, predetonator ignition.

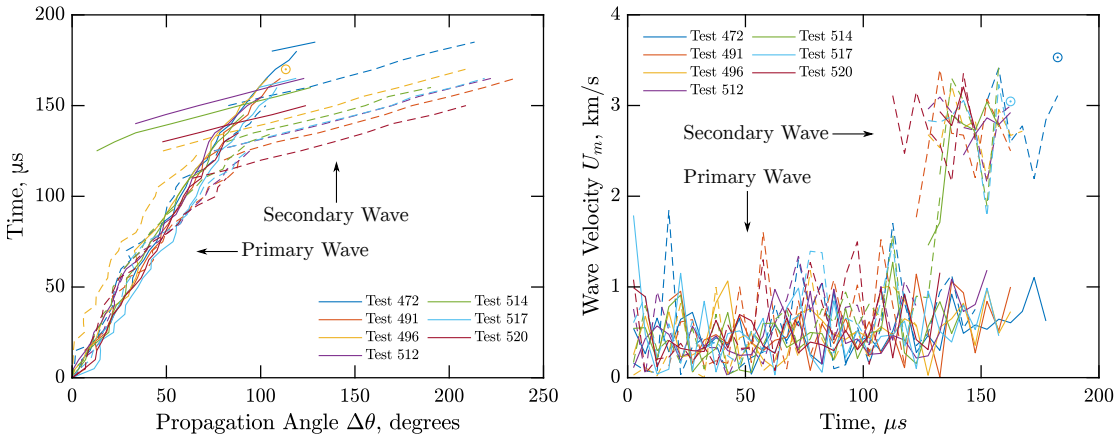

(a) θ–t wave diagram (b) Wave velocity

Figure F.7. Wave propagation results: +30° swirl, spark plug ignition. Solid lines indicate the upper combustion branch, dashed lines indicate the lower combustion branch.

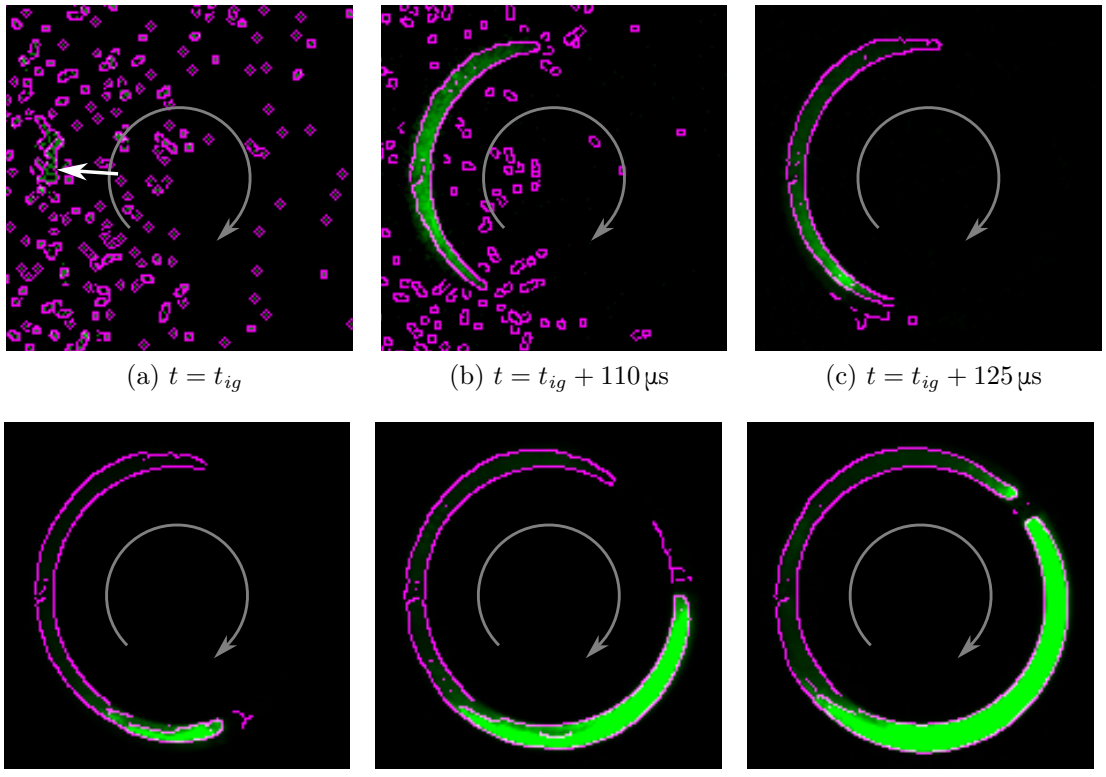

(a) $t = t_{ig}$ (b) $t = t_{ig} + 110\,\mu s$ (c) $t = t_{ig} + 125\,\mu s$

(d) $t = t_{ig} + 140\,\mu s$ (e) $t = t_{ig} + 160\,\mu s$ (f) $t = t_{ig} + 170\,\mu s$

Figure F.8. Selected frames, Test 496: +30° swirl, spark plug ignition.

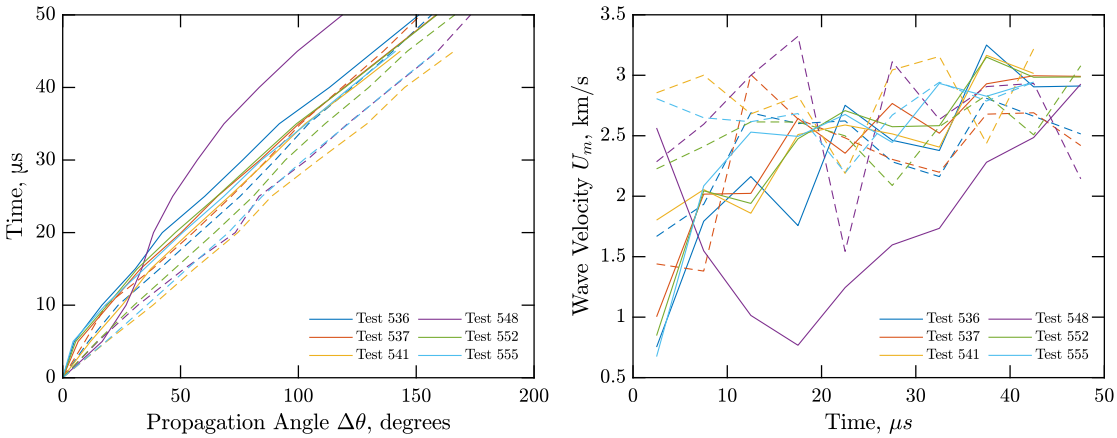

(a) θ–t wave diagram (b) Wave velocity

Figure F.9. Wave propagation results: $-30°$ swirl, predetonator ignition. Solid lines indicate the upper combustion branch, dashed lines indicate the lower combustion branch.

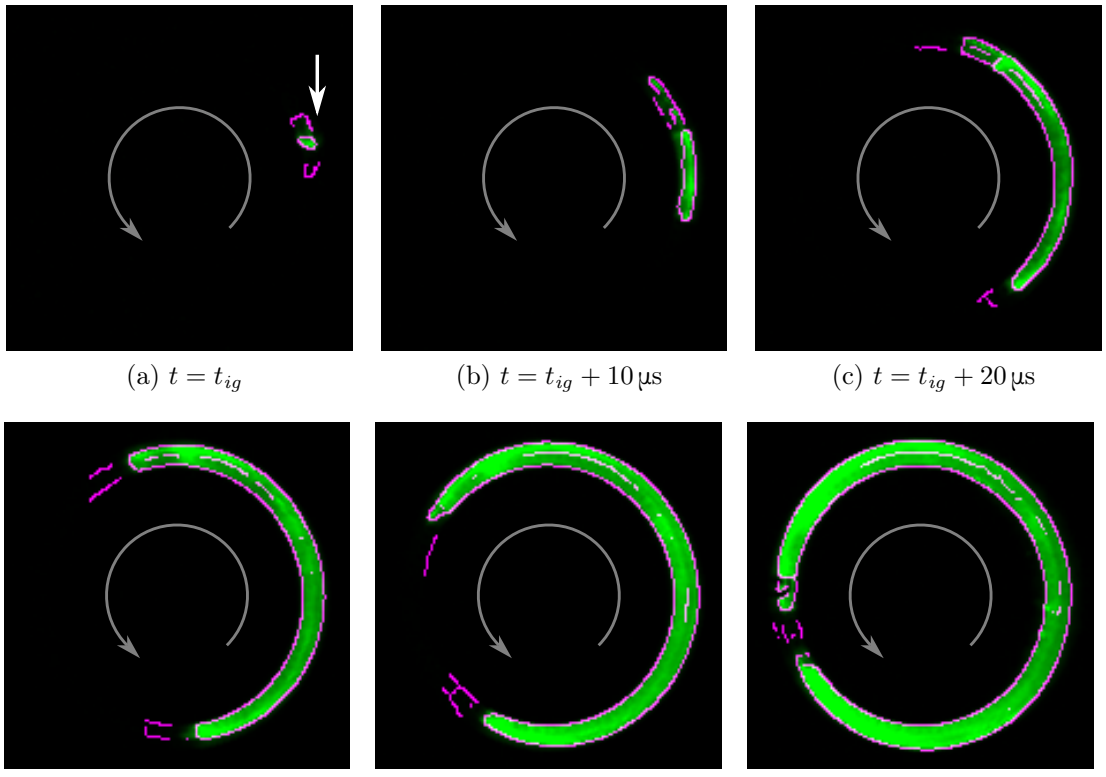

(a) $t = t_{ig}$ (b) $t = t_{ig} + 10\,\mu s$ (c) $t = t_{ig} + 20\,\mu s$

(d) $t = t_{ig} + 30\,\mu s$ (e) $t = t_{ig} + 40\,\mu s$ (f) $t = t_{ig} + 50\,\mu s$

Figure F.10. Selected frames, Test 552: $-30°$ swirl, predetonator ignition.

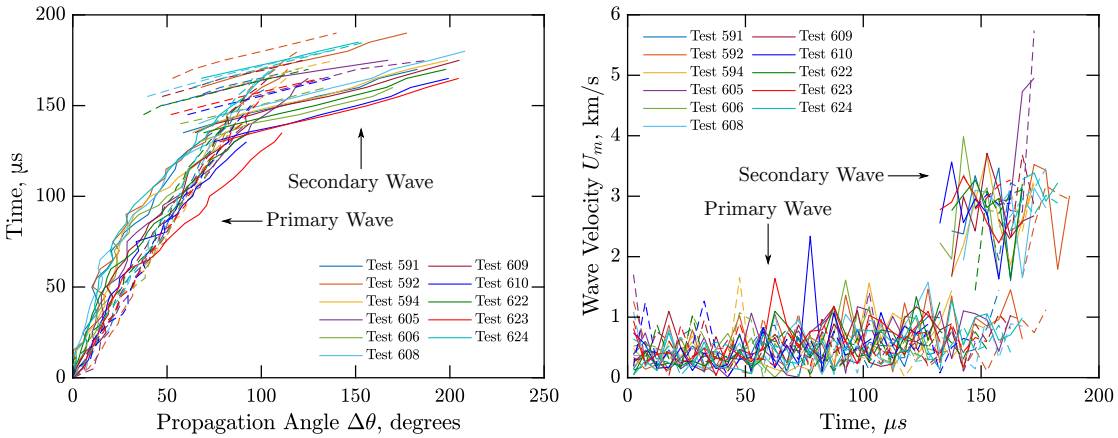

(a) θ–t wave diagram (b) Wave velocity

Figure F.11. Wave propagation results: −30° Swirl, Spark Plug Ignition. Solid lines indicate the upper combustion branch, dashed lines indicate the lower combustion branch.

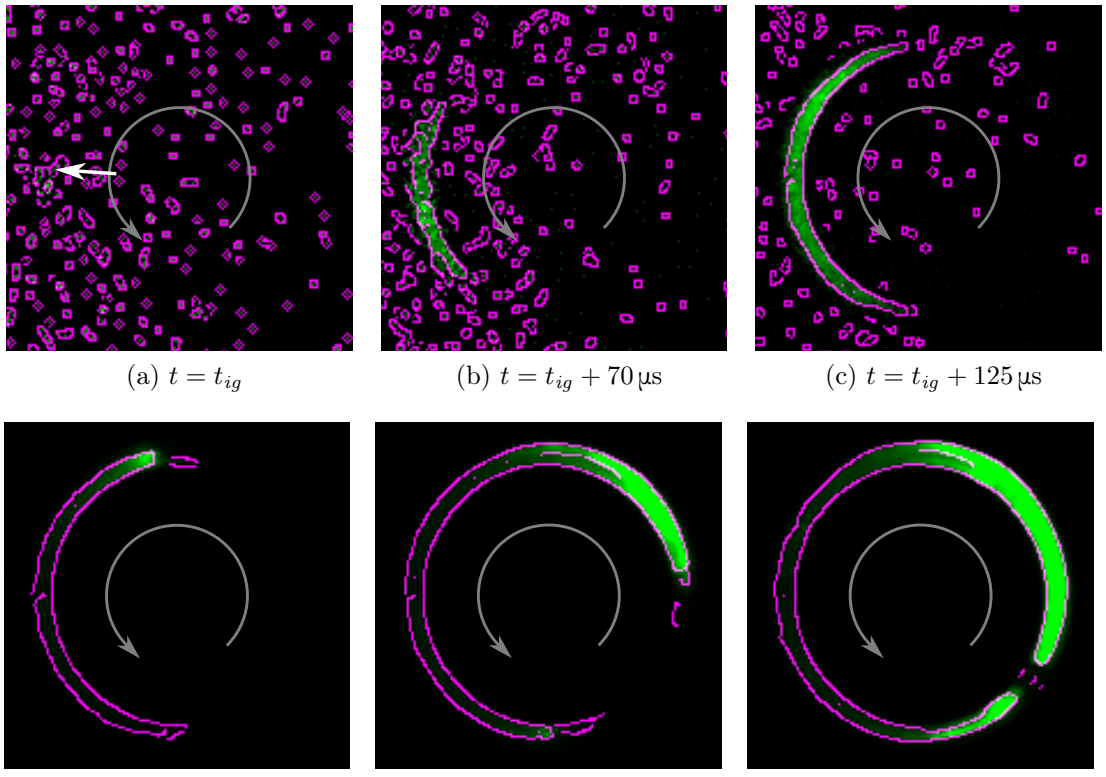

(a) $t = t_{ig}$ (b) $t = t_{ig} + 70\,\mu s$ (c) $t = t_{ig} + 125\,\mu s$

(d) $t = t_{ig} + 140\,\mu s$ (e) $t = t_{ig} + 165\,\mu s$ (f) $t = t_{ig} + 175\,\mu s$

Figure F.12. Selected frames, Test 609: −30° swirl, spark plug ignition.

REFERENCES

[1] Glassman, I. and Yetter, R. A., *Combustion*, 2nd ed., Academic Press, Amsterdam, 2008.

[2] Turns, S. R., *An Introduction to Combustion: Concepts and Applications*, 2nd ed., McGraw-Hill, Boston, 2006.

[3] Lee, J. H. S., *The Detonation Phenomenon*, Cambridge University Press, Cambridge, UK, 2008.

[4] Agrawal, J. P., *High Energy Materials: Propellants, Explosives and Pyrotechnics*, John Wiley & Sons, Hoboken, NJ, 2010.

[5] "Detonation," in *The Oxford English Dictionary*, Oxford University Press, Oxford, UK, 1933, vol. 3, p. 273.

[6] Berthelot, M. and Vieille, P., "Sur la Vitesse de Propogation des Phénomènes Explosifs dans les Gaz," *Comptes Rendus de l'Académie des Sciences*, vol. 93, pp. 18–23, 1881.

[7] Berthelot, M. and Vieille, P., "L'Ondé Explosive," *Annales de Chimie et de Physique*, vol. 28, no. 5, pp. 599–601, 1883.

[8] Mallard, E. and Le Châtelier, H., "Recherches Expérimentales et Théoriques sur le Combustion des Mélanges Gazeux Explosifs," *Annales des Mines*, pp. 274–568, 1883.

[9] Krehl, P. O. K., *History of Shock Waves, Explosions and Impact: A Chronological and Biographical Reference*, Springer, Berlin, 2009.

[10] Salas, M. D., "The Curious Events Leading to the Theory of Shock Waves," *Shock Waves*, vol. 16, no. 6, pp. 477–487, 2007. doi: 10.1007/s00193-007-0084-z

[11] Hugoniot, H., "Sur la Propagation du Mouvement dans les Corps et Spécialement dans les Gaz Parfaits, Première Partie," vol. 57, pp. 3–97, 1887.

[12] Hugoniot, H., "Sur la Propagation du Mouvement dans les Corps et Spécialement dans les Gaz Parfaits, Deuxième Partie," *Journal de l'École Polytechnique*, vol. 58, pp. 1–125, 1889.

[13] Chapman, D. L., "On the Rate of Explosion in Gases," *Philosophical Magazine*, vol. 47, pp. 90–104, 1889.

[14] Mikelson, V. A., "On the Normal Ignition Velocity of Explosive Gaseous Mixtures," Ph.D. dissertation, Moscow University, Moscow, Russian Empire, 1890.

[15] Jouguet, É., "Sur l'Onde Explosive," *Comptes Rendus de l'Académie des Sciences*, vol. 140, p. 121, 1904.

[16] Jouguet, É., "Sur la Propagation des Réactions Chimiques dans les Gaz," *Journal des Mathématiques Pures et Appliquées, Series 6*, vol. 1, pp. 347–425, 1905.

[17] Jouguet, É., "Sur la Propagation des Réactions Chimiques dans les Gaz," *Journal des Mathématiques Pures et Appliquées, Series 6*, vol. 2, pp. 5–85, 1906.

[18] Rankine, W. J. M., "On the Thermodynamic Theory of Waves of Finite Longitudinal Disturbance," *Philosophical Transactions of the Royal Society of London*, vol. 160, pp. 277–288, 1870. doi: 10.1098/rstl.1870.0015

[19] Fickett, W. and Davis, W. C., *Detonation: Theory and Experiment*, Dover, Mineola, New York, 2000.

[20] Crussard, J. C., "Sur Quelques Propriétés de l'Onde Explosive," *Comptes Rendus de l'Académie des Sciences*, vol. 144, pp. 417–420, 1907.

[21] Nordeen, C. A., "Thermodynamics of a Rotating Detonation Engine," Ph.D. dissertation, University of Connecticut, Stoors, Connecticut, 2013.

[22] Zel'dovich, Ya. B., "К Теории Распространения Детонации в Газообразных Системах," *Zhurnal Éksperimental'noĭ i Teoreticheskoĭ Fiziki*, vol. 10, no. 5,

pp. 542–568, 1940. English: “On the Theory of the Propagation of Detonation in Gaseous Systems”.

[23] Zel’dovich, Ya. B., “On the Theory of the Propagation of Detonation in Gaseous Systems,” NACA Tech. Mem. 1261, 1950. English Translation.

[24] von Neumann, J., “Theory of Detonation Waves,” O.S.R.D. Rep. 542, 1942.

[25] Döring, W., “Über Detonationsvorgang in Gasen,” *Annalen der Physik*, vol. 43, no. 6-7, pp. 421–436, 1943. doi: 10.1002/andp.19434350605

[26] Powers, J. M., *Combustion Thermodynamics and Dynamics*, Cambridge University Press, Cambridge, UK, 2016.

[27] Peace, J. T., “Experimental Detonation Schematic,” Illustration, 2018.

[28] Wintenberger, E., “Application of Steady and Unsteady Detonation Waves to Propulsion,” Ph.D. dissertation, California Institute of Technology, Pasadena, California, 2004.

[29] Lee, J. H. S., “Dynamic Parameters of Gaseous Detonations,” *Annual Review of Fluid Mechanics*, vol. 16, no. 1, pp. 311–336, 1984. doi: 10.1146/annurev.fl.16.010184.001523

[30] Austin, J. M., “The Role of Instability in Gaseous Detonation,” Ph.D. dissertation, California Institute of Technology, Pasadena, California, 2003.

[31] Mach, E. and Sommer, J., “Über die Fortpflanzungsgeschwindigkeit von Explosionsschallwellen,” *Sitzungsberichte der Akademie der Wissenschaftenn, Wien*, vol. 75, pp. 101–130, 1877.

[32] Denisov, Yu. N. and Troshin, Ya. K., “Пульсирующая и Спиновая Детонация Газовых Смесей в Трубах,” *Doklady Akademii Nauk SSSR*, vol. 125, pp. 110–113, 1959. English: “Pulsating and Spin Detonation of Gas Mixtures in Pipes”.

[33] Denisov, Yu. N. and Troshin, Ya. K., "Механизм Детонационного Сгорания," *Zhurnal Prikladnaya Mekhanika i Tekhnicheskaya Fizika*, vol. 1, no. 1, pp. 21–35, 1960. English: "The Mechanism of Detonation Combustion".

[34] Denisov, Yu. N. and Troshin, Ya. K., "On the Mechanism of Detonative Combustion," *Eighth Symposium (International) on Combustion*, vol. 8, no. 1, pp. 600–610, 1960. doi: 10.1016/S0082-0784(06)80551-5

[35] Shepherd, J. E., "Detonation Database," 2005. [Online]. URL: http://shepherd.caltech.edu/detn_db/html/db.html. Accessed 30 August 2018.

[36] Kaneshige, M. and Shepherd, J. E., "Detonation Database," GALCIT Explosion Dynamics Laboratory Report FM97-8, 1997.

[37] Lefebvre, M. H., Oran, E. S., Kailasanath, K., and Van Tiggelen, P. J., "The Influence of the Heat Capacity and Diluent on Detonation Structure," *Combustion and Flame*, vol. 95, no. 1-2, pp. 206–218, 1993. doi: 10.1016/0010-2180(93)90062-8

[38] Oran, E. S., Weber, J. W., Stefaniw, E. I., Lefebvre, M. H., and Anderson, J. D., "A Numerical Study of a Two-Dimensional H_2-O_2-Ar Detonation Using a Detailed Chemical Reaction Model," *Combustion and Flame*, vol. 113, no. 1-2, pp. 147–163, 1998. doi: 10.1016/S0010-2180(97)00218-6

[39] Gavrikov, A. I., Efimenko, A. A., and Dorofeev, S. B., "A Model for Detonation Cell Size Prediction from Chemical Kinetics," *Combustion and Flame*, vol. 120, no. 1-2, pp. 19–33, 2000. doi: 10.1016/S0010-2180(99)00076-0

[40] Ng, H. D., "The Effect of Chemical Reaction Kinetics on the Structure of Gaseous Detonations," Master's thesis, McGill University, Montréal, Québec, Canada, 2005.

[41] Mével, R., Davidenko, D., Lafosse, F., Dupré, G., and Paillard, C., "Experimental and Numerical Detonation Cell in H_2-N_2O-Ar Mixtures," in *European Combustion Meeting*, 2009.

[42] Eaton, R., Zhang, B., Bergthorson, J. M., and Ng, H. D., "Measurement and Chemical Kinetic Model Predictions of Detonation Cell Size in Methanol–Oxygen Mixtures," *Shock Waves*, vol. 22, no. 2, pp. 173–178, 2012. doi: 10.1007/s00193-012-0359-x

[43] Khasainov, B., Virot, F., Presles, H.-N., and Desbordes, D., "Parametric Study of Double Cellular Detonation Structure," *Shock Waves*, vol. 23, no. 3, pp. 213–220, 2013. doi: 10.1007/s00193-012-0419-2

[44] Yu, J., Hou, B., Lelyakin, A., Xu, Z., and Jordan, T., "Gas Detonation Cell Width Prediction Model Based on Support Vector Regression," *Nuclear Engineering and Technology*, vol. 49, no. 7, pp. 1423–1430, 2017. doi: 10.1016/j.net.2017.06.014

[45] Malik, K., Żbikowski, M., and Teodorczyk, A., "Detonation Cell Size Model Based on Deep Neural Network for Hydrogen, Methane and Propane Mixtures with Air and Oxygen," *Nuclear Engineering and Technology*, In Press (published online 10 November 2018). doi: 10.1016/j.net.2018.11.004

[46] Lee, J. H. S. and Moen, I. O., "The Mechansm of Transition from Deflagration to Detonation in Vapor Cloud Explosions," *Progress in Energy and Combustion Science*, vol. 6, no. 4, pp. 359–389, 1980. doi: 10.1016/0360-1285(80)90011-8

[47] Urtiew, P. A. and Oppenheim, A. K., "Experimental Observations of the Transition to Detonation in an Explosive Gas," *Proceedings of the Royal Society A*, vol. 295, no. 1440, pp. 13–28, 1966. doi: 10.1098/rspa.1966.0223

[48] Shchelkin, K. I., *Быстрое Горение и Спиновая Детонация Газов*, Voenizdat, Mosow, 1949. English: "Rapid Combustion and Spin Detonation of Gases".

[49] Lee, J. H., Knystautas, R., and Yoshikawa, N., "Photochemical Initiation of Gaseous Detonations," *Acta Astronautica*, vol. 5, no. 11-12, pp. 971–982, 1978. doi: 10.1016/0094-5765(78)90003-6

[50] Knystautas, R., Lee, J. H., Moen, I., and Wagner, H. G., "Direct Initiation of Spherical Detonation by a Hot Turbulent Gas Jet," *Seventeenth Symposium (International) on Combustion*, vol. 17, no. 1, pp. 1235–1245, 1979. doi: 10.1016/S0082-0784(79)80117-4

[51] Nicholls, J. A., Wilkinson, H. R., and Morrison, R. B., "Intermittent Detonation as a Thrust-Producing Mechanism," *Journal of Jet Propulsion*, vol. 27, no. 5, pp. 534–541, 1957. doi: 10.2514/8.12851

[52] Roy, M., "Propulsion par Statoréacteur à Détonation," *Comptes Rendus de l'Académie des Sciences*, vol. 222, pp. 31–32, 1946.

[53] Goddard, R. H., "Reaction Combustion Chamber for Unconfined Charges of Detonative Fuel Fed Intermittently to the Combustion Chamber," U.S. Patent 2,465,525, 1949.

[54] Dunlap, R., Brehm, R. L., and Nicholls, J. A., "A Preliminary Study of the Application of Steady-State Detonative Combustion to a Reaction Engine," *Jet Propulsion*, vol. 26, pp. 451–456, 1958.

[55] Nicholls, J. A., Cullen, R. E., and Ragland, K. W., "Feasibility Studies of a Rotating Detonation Wave Rocket Motor," *Journal of Spacecraft and Rockets*, vol. 3, no. 6, pp. 893–898, 1966. doi: 10.2514/3.28557

[56] Adamson, T. C. and Olsson, G. R., "Performance Analysis of a Rotating Detonation Wave Rocket Engine (Rotating Detonation Wave Rocket Engine Performance Analyzed and Compared to Conventional Rocket Engines)," *Astronautica Acta*, vol. 14, no. 4, pp. 405–415, 1967.

[57] Voitsekhovskii, B. V., "Stationary Spin Detonation," *Soviet Journal of Applied Mechanics and Technical Physics*, vol. 3, pp. 157–164, 1960.

[58] Bollay, W., "Pulse Detonation Jet Propulsion," U.S. Patent 2,942,412, 1960.

[59] Morrison, R. B. and Hays, P. O., "Rotary Detonation Power Plant," U.S. Patent 3,240,010, 1966.

[60] Lange, O. H., Stein, R. J., and Tubbs, H. E., "Detonation Reaction Engine," U.S. Patent 3,263,418, 1966.

[61] Lange, O. H., Stein, R. J., and Tubbs, H. E., "Continuous Detonation Reaction Engine," U.S. Patent 3,336,754, 1967.

[62] Spindler, C. L., "Standing Detonation Wave Rocket Engine," U.S. Patent 3,423,942, 1969.

[63] Helman, D., Shreeve, R., and Eidelman, S., "Detonation Pulse Engine," AIAA Paper 1986–1683, 1986. doi: 10.2514/6.1986-1683

[64] Cambier, J.-L. and Adelman, H. G., "Preliminary Numerical Simulations of a Pulsed Detonation Wave Engine," AIAA Paper 1988–2960, 1988. doi: 10.2514/6.1988-2960

[65] Eidelman, S., Grossman, W., and Lottati, I., "A Review of Propulsion Applications of the Pulsed Detonation Engine Concept," AIAA Paper 1989–2446, 1989. doi: 10.2514/6.1989-2446

[66] Eidelman, S., Grossman, W., and Lottati, I., "Review of Propulsion Applications and Numerical Simulations of the Pulsed Detonation Engine Concept," *Journal of Propulsion and Power*, vol. 7, no. 6, pp. 857–865, 1991. doi: 10.2514/3.23402

[67] Eidelman, S. and Grossman, W., "Pulsed Detonation Engine Experimental and Theoretical Review," AIAA Paper 1992–3168, 1992. doi: 10.2514/6.1992-3168

[68] Bussing, T. R. A., Bratkovich, T. E., and Hinkley Jr., J. B., "Practical Implementation of Pulse Detonation Engines," AIAA Paper 1997–2748, 1997. doi: 10.2514/6.1997-2748

[69] Eidelman, S., "Pulse Detonation Engine: A Status Review and Technology Development Road Map," AIAA Paper 1997–2740, 1997. doi: 10.2514/6.1997-2740

[70] Kailasanath, K., "Review of Propulsion Applications of Detonation Waves," *AIAA Journal*, vol. 38, no. 9, pp. 1698–1708, 2000. doi: 10.2514/2.1156

[71] Kailasanath, K., "Recent Developments in the Research on Pulse Detonation Engines," *AIAA Journal*, vol. 41, no. 2, pp. 145–159, 2003. doi: 10.2514/2.1933

[72] Wolański, P., "Detonative Propulsion," *Proceedings of the Combustion Institute*, vol. 34, no. 1, pp. 125–158, 2013. doi: 10.1016/j.proci.2012.10.005

[73] Ostrander, M. J., Hyde, J. C., Young, M. F., Kissinger, R. D., and Pratt, D. T., "Standing Oblique Detonation Wave Engine Performance," AIAA Paper 1987–2002, 1987. doi: 10.2514/6.1987-2002

[74] Adelman, H. G., Cambier, J.-L., Menees, G. P., and Balboni, J. A., "Analytical and Experimental Validation of the Oblique Detonation Wave Engine Concept," AIAA Paper 1988–97, 1988. doi: 10.2514/6.1988-97

[75] Wang, Y.-y., Fujiwara, T., Aoki, T., Arakawa, H., and Ishiguro, T., "Three-Dimensional Standing Oblique Detonation Wave in a Hypersonic Flow," AIAA Paper 1988–478, 1988. doi: 10.2514/6.1988-478

[76] Bogdanoff, D. W. and Brackett, D. C., "Computational Investigation of Oblique Detonation Ramjet-in-Tube Concepts," *Journal of Propulsion and Power*, vol. 5, no. 3, pp. 276–281, 1989. doi: 10.2514/3.23149

[77] Cambier, J.-L., Adelman, H. G., and Menees, G. P., "Numerical Simulations of Oblique Detonations in Supersonic Combustion Chambers," *Journal of Propulsion and Power*, vol. 5, no. 4, pp. 482–491, 1989. doi: 10.2514/3.23180

[78] Cambier, J.-L., Adelman, H. G., and Menees, "Numerical Simulations of an Oblique Detonation Wave Engine," *Journal of Propulsion and Power*, vol. 6, no. 3, pp. 315–323, 1990. doi: 10.2514/3.25436

[79] Pratt, D. T., Humphrey, J. W., and Glenn, D. E., "Morphology of Standing Oblique Detonation Waves," *Journal of Propulsion and Power*, vol. 7, no. 5, pp. 837–845, 1991. doi: 10.2514/3.23399

[80] Dabora, E. K. and Broda, J.-C., "Standing Normal Detonations and Oblique Detonations for Propulsion," AIAA Paper 93–2325, 1993. doi: 10.2514/6.1993-2325

[81] Ashford, S. A., "Oblique Detonation Waves, With Application to Oblique Detonation Wave Engines, and Comparison of Hypersonic Propulsion Engines," Ph.D. dissertation, University of Oklahoma, Norman, Oklahoma, 1994.

[82] Menees, G. P., Adelman, H. G., Cambier, J.-L., and Bowles, J. V., "Wave Combustors for Trans-Atmospheric Vehicles," *Journal of Propulsion and Power*, vol. 8, no. 3, pp. 709–713, 1992. doi: 10.2514/3.23536

[83] Nordeen, C. A., Schwer, D. A., Schauer, F. R., Hoke, J., Barber, T. *et al.*, "Energy Transfer in a Rotating Detonation Engine," AIAA Paper 2011–6045, 2011. doi: 10.2514/6.2011-6045

[84] Braun, E. M., "New Detonation Concepts for Propulsion and Power Generation," Ph.D. dissertation, University of Texas at Arlington, Arlington, Texas, 2012.

[85] Voytsekhovskiy, B. V., "Stationary Detonation," *Doklady Akademii Nauk SSSR*, vol. 129, no. 5, pp. 1254–1256, 1959.

[86] Lavrentyev Institute of Hydrodynamics, "About the Institute." [Online]. URL: http://www.hydro.nsc.ru/institute/about/. Accessed 8 August 2016.

[87] Clayton, R. M. and Rogero, R. S., "Experimental Measurements on a Rotating Detonation-Like Wave Observed During Liquid Rocket Resonant Combustion," JPL Tech. Rep. 32-788, 1965.

[88] Mikhailov, V. V. and Topchiyan, M. E., "Study of Continuous Detonation in an Annular Channel," *Combustion, Explosion, and Shock Waves*, vol. 1, no. 4, pp. 12–14, 1965. doi: 10.1007/BF00748805

[89] Bykovskii, F. A. and Mitrofanov, V. V., "Detonation Combustion of a Gas Mixture in a Cylindrical Chamber," *Combustion, Explosion, and Shock Waves*, vol. 16, no. 5, pp. 570–578, 1980. doi: 10.1007/BF00794937

[90] Zhdan, S. A., Mardashev, A. M., and Mitrofanov, V. V., "Calculation of the Flow of Spin Detonation in an Annular Chamber," *Combustion, Explosion, and Shock Waves*, vol. 26, no. 2, pp. 210–214, 1990. doi: 10.1007/BF00742414

[91] Bykovskii, F. A., "Thermal Fluxes in Combustion Chamber Walls in the Detonation and Turbulent Combustion Modes," *Combustion, Explosion, and Shock Waves*, vol. 27, no. 1, pp. 66–71, 1991. doi: 10.1007/BF00785359

[92] Bykovskii, F. A., Vasil'ev, A. A., Vedernikov, E. F., and Mitrofanov, V. V., "Explosive Combustion of a Gas Mixture in Radial Annular Chambers," *Combustion, Explosion, and Shock Waves*, vol. 30, no. 4, pp. 510–516, 1994. doi: 10.1007/BF00790158

[93] Bykovskii, F. A. and Vedernikov, E. F., "Continuous Detonation Combustion of an Annular Gas-Mixture Layer," *Combustion, Explosion, and Shock Waves*, vol. 32, no. 5, pp. 489–491, 1996. doi: 10.1007/BF01998570

[94] Bykovskii, F. A., Mitrofanov, V. V., and Vedernikov, E. F., "Continuous Detonation Combustion of Fuel–Air Mixtures," *Combustion, Explosion, and Shock Waves*, vol. 33, no. 3, pp. 344–353, 1997. doi: 10.1007/BF02671875

[95] Bykovskii, F. A. and Vedernikov, E. F., "Continuous Detonation of a Subsonic Flow of a Propellant," *Combustion, Explosion, and Shock Waves*, vol. 39, no. 3, pp. 323–334, 2003. doi: 10.1023/A:1023800521344

[96] Bykovskii, F. A., Zhdan, S. A., and Vedernikov, E. F., "Continuous Spin Detonations," *Journal of Propulsion and Power*, vol. 22, no. 6, pp. 1204–1216, 2006. doi: 10.2514/1.17656

[97] Zhdan, S. A., Bykovskii, F. A., and Vedernikov, E. F., "Mathematical Modeling of a Rotating Detonation Wave in a Hydrogen–Oxygen Mixture," *Combustion, Explosion, and Shock Waves*, vol. 43, no. 4, pp. 449–459, 2007. doi: 10.1007/s10573-007-0061-y

[98] Bykovskii, F. A. and Vedernikov, E. F., "Continuous Spin Detonation of Hydrogen–Oxygen Mixtures. 3. Methods of Measuring Flow Parameters and Flow Structure in Combustors of Different Geometries," *Combustion, Explosion, and Shock Waves*, vol. 44, no. 4, pp. 451–460, 2008. doi: 10.1007/s10573-008-0072-3

[99] Bykovskii, F. A., Zhdan, S. A., and Vedernikov, E. F., "Continuous Spin Detonation of Hydrogen–Oxygen Mixtures. 1. Annular Cylindrical Combustors," *Combustion, Explosion, and Shock Waves*, vol. 44, no. 2, pp. 150–162, 2008. doi: 10.1007/s10573-008-0021-1

[100] Bykovskii, F. A., Zhdan, S. A., and Vedernikov, E. F., "Continuous Spin Detonation of Hydrogen–Oxygen Mixtures. 2. Combustor with an Expanding Annular Channel," *Combustion, Explosion, and Shock Waves*, vol. 44, no. 3, pp. 330–342, 2008. doi: 10.1007/s10573-008-0041-x

[101] Zhdan, S. A., "Mathematical Model of Continuous Detonation in an Annular Combustor with a Supersonic Flow Velocity," *Combustion, Explosion, and Shock Waves*, vol. 44, no. 6, pp. 690–697, 2008. doi: 10.1007/s10573-008-0104-z

[102] Bykovskii, F. A., Zhdan, S. A., and Vedernikov, E. F., "Realization and Modeling of Continuous Spin Detonation of a Hydrogen–Oxygen Mixture in Flow-Type Combustors. 1. Combustors of Cylindrical Annular Geometry," *Combustion, Explosion, and Shock Waves*, vol. 45, no. 5, pp. 606–617, 2009. doi: 10.1007/s10573-009-0089-2

[103] Lentsch, A., Bec, R., Serre, L., Falempin, F., Daniau, E. *et al.*, "Overview of Current French Activities on PDRE and Continuous Detonation Wave Rocket Engines," AIAA Paper 2005–3232, 2005. doi: 10.2514/6.2005-3232

[104] Daniau, E., Falempin, F., and Zhdan, S., "Pulsed and Rotating Detonation Propulsion Systems: First Step Toward Operational Engines," AIAA Paper 2005–3233, 2005. doi: 10.2514/6.2005-3233

[105] Canteins, G., "Etude de la Détonation Continue Rotative: Application à la Propulsion," Ph.D. dissertation, Université de Poitiers, Poitiers, France, 2006.

[106] Falempin, F., Daniau, E., Getin, N., Bykovskii, F. A., and Zhdan, S. A., "Toward a Continuous Detonation Wave Rocket Engine Demonstrator," AIAA Paper 2006–7956, 2006. doi: 10.2514/6.2006-7956

[107] Daniau, E., Falempin, F., Getin, N., Bykovskii, F. A., and Zhdan, S. A., "Design of a Continuous Detonation Wave Engine for Space Application," AIAA Paper 2006–4794, 2006. doi: 10.2514/6.2006-4794

[108] Davidenko, D. M., Gökalp, I., and Kudryavtsev, A. N., "Numerical Simulation of the Continuous Rotating Hydrogen–Oxygen Detonation with a Detailed Chemical Mechanism," in *West-East High Speed Flow Field Conference*, Moscow, 2007.

[109] Falempin, F. and Daniau, E., "A Contribution to the Development of Actual Continuous Detonation Wave Engine," AIAA Paper 2008–2679, 2008. doi: 10.2514/6.2008-2679

[110] Falempin, F., "Continuous Detonation Wave Engine," in *Advances on Propulsion Technology for High-Speed Aircraft*, NATO RTO-EN-AVT-150, 2007, pp. 8-1–8-16.

[111] Davidenko, D. M., Gökalp, I., and Kudryavtsev, A. N., "Numerical Study of the Continuous Detonation Wave Rocket Engine," AIAA Paper 2008–2680, 2008. doi: 10.2514/6.2008-2680

[112] Falempin, F. and Le Naour, B., "R&T Effort on Pulsed and Continuous Detonation Wave Engines," AIAA Paper 2009–7284, 2009. doi: 10.2514/6.2009-7284

[113] Wolański, P., Kindracki, J., Fujiwara, T., Oka, Y., and Katsuyuki, S.-u., "An Experimental Study of Rotating Detonation Engine," in *20th International Colloquium on the Dynamics of Explosions and Reactive Systems*, Montréal, Canada, 2005.

[114] Hishida, M., Fujiwara, T., and Wolanski, P., "Fundamentals of Rotating Detonations," *Shock Waves*, vol. 19, no. 1, pp. 1–10, 2009. doi: 10.1007/s00193-008-0178-2

[115] Hayashi, A. K., Kimura, Y., Yamada, T., Yamada, E., Kindracki, J. *et al.*, "Sensitivity Analysis of Rotating Detonation Engine with a Detailed Reaction Model," AIAA Paper 2009–0633, 2009. doi: 10.2514/6.2009-633

[116] Lee, S.-H., Cho, D.-R., and Choi, J.-Y., "Effect of Curvature on the Detonation Wave Propagation Characteristics in Annular Channels," AIAA Paper 2008–988, 2008.

[117] Braun, E. M., Dunn, N. L., and Lu, F. K., "Testing of a Continuous Detonation Wave Engine with Swirled Injection," AIAA Paper 2010–0146, 2010. doi: 10.2514/6.2010-146

[118] Lu, F. K. and Braun, E. M., "Rotating Detonation Wave Propulsion: Experimental Challenges, Modeling, and Engine Concepts," *Journal of Propulsion and Power*, vol. 30, no. 5, pp. 1125–1142, 2014. doi: 10.2514/1.B34802

[119] Zhou, R., Wu, D., and Wang, J., "Progress of Continuously Rotating Detonation Engines," *Chinese Journal of Aeronautics*, vol. 29, no. 1, pp. 15–29, 2016. doi: 10.1016/j.cja.2015.12.006

[120] Kailasanath, K., "Recent Developments in the Research on Rotating-Detonation-Wave Engines," AIAA Paper 2017–0784, 2017. doi: 10.2514/6.2017-0784

[121] Schwer, D. A. and Kailasanath, K., "Numerical Study of the Effects of Engine Size on Rotating Detonation Engines," AIAA Paper 2011–0581, 2011. doi: 10.2514/6.2011-581

[122] Schwer, D. A. and Kailasanath, K., "Effect of Inlet on Fill Region and Performance of Rotating Detonation Engines," AIAA Paper 2011–6044, 2011. doi: 10.2514/6.2011-6044

[123] Nordeen, C. A., Schwer, D., and Corrigan, A., "Area Effects on Rotating Detonation Engine Performance," AIAA Paper 2014–3900, 2014. doi: 10.2514/6.2014-3900

[124] Nordeen, C. A. and Schwer, D., "Radial Effects on Rotating Detonation Engine Swirl," AIAA Paper 2015–3781, 2015. doi: 10.2514/6.2015-3781

[125] Zhdan, S. A. and Syryamin, A. S., "Numerical Modeling of Continuous Detonation in Non-Stoichiometric Hydrogen–Oxygen Mixtures," *Combus-*

tion, Explosion, and Shock Waves, vol. 49, no. 1, pp. 69–78, 2013. doi: 10.1134/S0010508213010085

[126] Braun, E. M., Lu, F. K., Wilson, D. R., and Camberos, J. A., "Airbreathing Rotating Detonation Wave Engine Cycle Analysis," *Aerospace Science and Technology*, vol. 27, no. 1, pp. 201–208, 2013. doi: 10.1016/j.ast.2012.08.010

[127] Braun, E. M., Lu, F. K., and Wilson, D. R., "Airbreathing Rotating Detonation Wave Engine Cycle Analysis," AIAA Paper 2010–7039, 2010. doi: 10.2514/6.2010-7039

[128] Braun, E. M., Lu, F. K., Wilson, D. R., and Camberos, J. A., "Detonation Engine Performance Comparison Using First and Second Law Analyses," AIAA Paper 2010–7040, 2010. doi: 10.2514/6.2010-7040

[129] Endo, T. and Fujiwara, T., "A Simplified Analysis on a Pulse Detonation Engine Model," *Transactions of The Japan Society for Aeronautical and Space Sciences*, vol. 44, no. 146, pp. 217–222, 2002. doi: 10.2322/tjsass.44.217

[130] Endo, T., Kasahara, J., Matsuo, A., Sato, S., Inaba, K. *et al.*, "Pressure History at the Thrust Wall of a Simplified Pulse Detonation Engine," *AIAA Journal*, vol. 42, no. 9, pp. 1921–1930, 2004. doi: 10.2514/1.976

[131] Fievisohn, R. T. and Yu, K. H., "Quasi-Steady Modeling of Rotating Detonation Engine Flowfields," AIAA Paper 2015–3616, 2015. doi: 10.2514/6.2015-3616

[132] Fievisohn, R. T. and Yu, K. H., "Parametric Study of an Ethylene–Air Rotating Detonation Engine Using an Ideal Model," AIAA Paper 2016–1403, 2016. doi: 10.2514/6.2016-1403

[133] Fievisohn, R. T. and Yu, K. H., "Steady-State Analysis of Rotating Detonation Engine Flowfields with the Method of Characteristics," *Journal of Propulsion and Power*, vol. 33, no. 1, pp. 89–99, 2017. doi: 10.2514/1.B36103

[134] Yi, T.-H., Lou, J., Turangan, C., Choi, J.-Y., and Wolański, P., "Propulsive Performance of a Continuously Rotating Detonation Engine," *Journal of Propulsion and Power*, vol. 27, no. 1, pp. 171–181, 2011. doi: 10.2514/1.46686

[135] Schwer, D. A. and Kailasanath, K., "Numerical Investigation of the Physics of Rotating-Detonation-Engines," *Proceedings of the Combustion Institute*, vol. 33, no. 2, pp. 2195–2202, 2011. doi: 10.1016/j.proci.2010.07.050

[136] Nordeen, C. A., Schwer, D. A., Schauer, F. R., Hoke, J., Cetegen, B. *et al.*, "Thermodynamic Modeling of a Rotating Detonation Engine," AIAA Paper 2011–0803, 2011. doi: 10.2514/6.2011-803

[137] Paxson, D. E., "Numerical Analysis of a Rotating Detonation Engine in the Relative Reference Frame," AIAA Paper 2014–0284, 2014. doi: 10.2514/6.2014-0284

[138] Tobita, A., Fujiwara, T., and Wolański, P., "Detonation Engine and Flying Object Provided Therewith," U.S. Patent 7,784,267 B2, 2010.

[139] Wolański, P., Kalina, P., Balicki, W., Rowiński, A., Perkowski, W. *et al.*, "Development of Gasturbine with Detonation Chamber," in *Detonation Control for Propulsion: Pulse Detonation and Rotating Detonation Engines*, Springer, Berlin, 2018, ch. 2, pp. 23–37.

[140] Rankin, B. A., Fotia, M. L., Naples, A. G., Stevens, C. A., Hoke, J. L. *et al.*, "Overview of Performance, Application, and Analysis of Rotating Detonation Engine Technologies," *Journal of Propulsion and Power*, vol. 33, no. 1, pp. 131–143, 2017. doi: 10.2514/1.B36303

[141] Frolov, S. M., Zvegintsev, V. I., Ivanov, V. S., Aksenov, V. S., Shamshin, I. O. *et al.*, "Demonstrator of Continuous-Detonation Air-Breathing Ramjet: Wind Tunnel Data," *Doklady Physical Chemistry*, vol. 474, no. 1, pp. 75–79, 2017. doi: 10.1134/S0012501617050013

[142] Frolov, S. M., Zvegintsev, V. I., Ivanov, V. S., Aksenov, V. S., Shamshin, I. O. *et al.*, "Wind Tunnel Testing of a Detonation Ramjet Model at Approach Air Stream Mach Number 5.7 and a Stagnation Temperature of 1500 K," *Doklady Physical Chemistry*, vol. 481, Part 1, pp. 100–103, 2018. doi: 10.1134/S0012501618070035

[143] Liu, S., Liu, W., Wang, Y., and Lin, Z., "Free Jet Test of Continuous Rotating Detonation Ramjet Engine," AIAA Paper 2017–2282, 2017. doi: 10.2514/6.2017-2282

[144] Schwer, D. A., Kaemming, T. A., and Kailasanath, K., "Pressure Feedback in the Diffuser of a Ram–RDE Propulsive Device," AIAA Paper 2017–1061, 2017. doi: 10.2514/6.2017-1061

[145] Nakagami, S., Matsuoka, K., Kasahara, J., Kumazawa, Y., Fujii, J. *et al.*, "Experimental Visualization of the Structure of Rotating Detonation Waves in a Disk-Shaped Combustor," *Journal of Propulsion and Power*, vol. 33, no. 1, pp. 80–88, 2017. doi: 10.2514/1.B36084

[146] Rankin, B. A., Richardson, D. R., Caswell, A. W., Naples, A., Hoke, J. *et al.*, "Imaging of OH* Chemiluminescence in an Optically Accessible Non-premixed Rotating Detonation Engine," AIAA Paper 2015–1604, 2015. doi: 10.2514/6.2015-1604

[147] Cho, K. Y., Codoni, J. R., Rankin, B. A., Hoke, J., and Schauer, F., "High-Repetition-Rate Chemiluminescence Imaging of a Rotating Detonation Engine," AIAA Paper 2016–1648, 2016. doi: 10.2514/6.2016-1648

[148] Rankin, B. A., Codoni, J. R., Cho, K. Y., Hoke, J., and Schauer, F. R., "Mid-Infrared Imaging of an Optically Accessible Non-Premixed Hydrogen–Air Rotating Detonation Engine," AIAA Paper 2017–0370, 2017. doi: 10.2514/6.2017-0370

[149] Codoni, J. R., Cho, K. Y., Hoke, J. L., Rankin, B. A., and Schauer, F. R., "Simultaneous mid-IR Emission and OH Chemiluminesence Measurements Within a RDE Operating with and without Backpressure," AIAA Paper 2018–1882, 2018. doi: 10.2514/6.2018-1882

[150] Frolov, S. M., Aksenov, V. S., and Shamshin, I. O., "Shock Wave and Detonation Propagation Through U-Bend Tubes," *Proceedings of the Combustion Institute*, vol. 31, no. 2, pp. 2421–2428, 2007.

[151] Kudo, Y., Nagura, Y., Kasahara, J., Sasamoto, Y., and Matsuo, A., "Oblique Detonation Waves Stabilized in Rectangular-Cross-Section Bent Tubes," *Proceedings of the Combustion Institute*, vol. 33, no. 2, pp. 2319–2326, 2011. doi: 10.1016/j.proci.2010.08.008

[152] Nakayama, H., Moriya, T., Kasahara, J., Matsuo, A., Sasamoto, Y. *et al.*, "Stable Detonation Wave Propagation in Rectangular-Cross-Section Curved Channels," *Combustion and Flame*, vol. 159, no. 2, pp. 859–869, 2012. doi: 10.1016/j.combustflame.2011.07.022

[153] Bedick, C., Sisler, A., Ferguson, D. H., and Strakey, P., "Development of a Lab-Scale Experimental Testing Platform for Rotating Detonation Engine Inlets," AIAA Paper 2017–0785, 2017. doi: 10.2514/6.2017-0785

[154] Schwinn, K., Gejji, R., Kan, B., Sardeshmukh, S., Heister, S. *et al.*, "Self-Sustained, High-Frequency Detonation Wave Generation in a Semi-Bounded Channel," *Combustion and Flame*, vol. 193, pp. 384–396, 2018. doi: 10.1016/j.combustflame.2018.03.022

[155] Balicki, W., Irzycki, A., Lukasik, B., and Snopkiewicz, K., "Testing of Initiation of Rotating Detonation Process in Hydrogen–Air Mixtures," *Journal of KONES Powertrain and Transport*, vol. 19, no. 2, 2012. doi: 10.5604/12314005.1137887

[156] Zhu, Y., Anand, V., Jodele, J., Knight, E., Gutmark, E. J. *et al.*, "Plasma-Assisted Rotating Detonation Combustor Operation," AIAA Paper 2017–4742, 2017. doi: 10.2514/6.2017-4742

[157] Kindracki, J., Wolański, P., and Gut, Z., "Experimental Research on the Rotating Detonation in Gaseous Fuels–Oxygen Mixtures," *Shock Waves*, vol. 21, no. 2, pp. 75–84, 2011. doi: 10.1007/s00193-011-0298-y

[158] Miller, S. J., "Design and Testing of an H_2/O_2 Predetonator for a Simulated Rotating Detonation Engine Channel," Master's thesis, Air Force Institute of Technology, Wright–Patterson Air Force Base, Ohio, 2013.

[159] St. George, A., Randall, S., Anand, V., Driscoll, R., and Gutmark, E., "Characterization of Initiator Dynamics in a Rotating Detonation Combustor," *Experimental Thermal and Fluid Science*, vol. 72, pp. 171–181, 2016. doi: 10.1016/j.expthermflusci.2015.11.002

[160] Yang, C., Wu, X., Ma, H., Peng, L., and Gao, J., "Experimental Research on Initiation Characteristics of a Rotating Detonation Engine," *Experimental Thermal and Fluid Science*, vol. 71, pp. 154–163, 2016. doi: 10.1016/j.expthermflusci.2015.10.019

[161] Yoshida, A., Okuda, Y., Yatsufusa, T., Endo, T., Taki, S. *et al.*, "Detonation Properties of Mixed-Fuel-and-Air Gas Mixtures," in *20th International Colloquium on Dynamics of Explosions and Reactive Systems*, Montréal, Canada, 2005.

[162] Boening, J. A., Heath, J. D., Byrd, T. J., Koch, J. V., Mattick, A. T. *et al.*, "Design and Experiments of a Continuous Rotating Detonation Engine: a Spinning Wave Generator and Modulated Fuel/Oxidizer Mixing," AIAA Paper 2016–4966, 2016. doi: 10.2514/6.2016-4966

[163] Knowlen, C., Wheeler, E., Mendez, D., and Kurosaka, M., "Thrusting Pressure and Supersonic Exhaust Velocity in a Rotating Detonation Engine," AIAA Paper 2018–0884, 2018. doi: 10.2514/6.2018-0884

[164] Miller, S. J., King, P. I., Schauer, F. R., and Hoke, J. L., "Ignition Design for a Rotating Detonation Engine," AIAA Paper 2013–1174, 2013. doi: 10.2514/6.2013-1174

[165] Bykovskii, F. A., Zhdan, S. A., and Vedernikov, E. F., "Initiation of Detonation of Fuel–Air Mixtures in a Flow-Type Annular Combustor," *Combustion, Explosion, and Shock Waves*, vol. 50, no. 2, pp. 214–222, 2014. doi: 10.1134/S0010508214020130

[166] Peng, L., Wang, D., Wu, X., Ma, H., and Yang, C., "Ignition Experiment with Automotive Spark on Rotating Detonation Engine," *International Journal of Hydrogen Energy*, vol. 40, no. 26, pp. 8465–8474, 2015. doi: 10.1016/j.ijhydene.2015.04.126

[167] St. George, A. C., Driscoll, R. B., Anand, V., and Gutmark, E. J., "Starting Transients and Detonation Onset Behavior in a Rotating Detonation Combustor," AIAA Paper 2016–0126, 2016. doi: 10.2514/6.2016-0126

[168] Fotia, M., Hoke, J., and Schauer, F. R., "Experimental Study of the Ignition Process in Rotating Detonation Engines," AIAA Paper 2017–1928, 2017. doi: 10.2514/6.2017-1928

[169] Wu, C.-H., "Discussion on 'A Practical Solution of a Three-Dimensional Flow Problem of Axial-Flow Turbomachinery' by Smith, Traugott, and Wislicenus," *Transactions of the ASME*, vol. 75, no. 5, pp. 789–803, 1953.

[170] Lyman, F. A., "On the Conservation of Rothalpy in Turbomachines," *Journal of Turbomachinery*, vol. 115, no. 3, pp. 520–525, 1993. doi: 10.1115/1.2929282

[171] Nordeen, C. A., Schwer, D. A., Schauer, F. R., Hoke, J. J., Barber, T. *et al.*, "Divergence and Mixing in a Rotating Detonation Engine," AIAA Paper 2013–1175, 2013. doi: 10.2514/6.2013-1175

[172] Schwer, D. A. and Kailasanath, K., "On Reducing Feedback Pressure in Rotating Detonation Engines," AIAA Paper 2013–1178, 2013. doi: 10.2514/6.2013-1178

[173] "Standard Thermodynamic Properties of Chemical Substances," in *CRC Handbook of Chemistry and Physics*, 96th ed., Haynes, W. M., Ed., CRC Press, Boca Raton, FL, 2015, ch. 5, pp. 5-4–5-42.

[174] Gurvich, L. V., Iorish, V. S., Yungman, V. S., and Dorofeeva, O. V., "Thermodynamic Properties as a Function of Temperature," in *CRC Handbook of Chemistry and Physics*, 96th ed., Haynes, W. M., Ed., CRC Press, Boca Raton, FL, 2015, ch. 5, pp. 5-43–5-65.

[175] "U.S. Standard Atmosphere, 1976," NASA Tech. Mem. X-74335, 1976.

[176] Goodwin, D. G., Moffat, H. K., and Speth, R. L., "Cantera: An Object-Oriented Software Toolkit for Chemical Kinetics, Thermodynamics, and Transport Processes," Version 2.3.0, 2016. [Online]. URL: http://www.cantera.org. Accessed 31 May 2017.

[177] "Shock & Detonation Toolbox," California Institute of Technology Explosion Dynamics Laboratory, 2014. [Online]. URL: http://shepherd.caltech.edu/EDL/PublicResources/cantera/html/SD_Toolbox/. Accessed 15 March 2016.

[178] Schwer, D. A. and Kailasanath, K., "Fluid Dynamics of Rotating Detonation Engines with Hydrogen and Hydrocarbon Fuels," *Proceedings of the Combustion Institute*, vol. 34, no. 2, pp. 1991–1998, 2013. doi: 10.1016/j.proci.2012.05.046

[179] Sichel, M. and Foster, J. C., "The Ground Impulse Generated by a Plane Fuel-Air Explosion with Side Relief," *Acta Astronautica*, vol. 6, no. 3, pp. 243–256, 1979. doi: 10.1016/0094-5765(79)90096-1

[180] Sutton, G. P. and Biblarz, O., *Rocket Propulsion Elements*, 7th ed., John Wiley & Sons, New York, 2001.

[181] Schwer, D. A. and Kailasanath, K., "Numerical Investigation of Rotating Detonation Engines," AIAA Paper 2010–6880, 2010. doi: 10.2514/6.2010-6880

[182] Mizener, A. R. and Lu, F. K., "Low-Order Parametric Analysis of a Rotating Detonation Engine in Rocket Mode," *Journal of Propulsion and Power*, vol. 33, no. 6, pp. 1543–1554, 2017. doi: 10.2514/1.B36432

[183] "Perseus – 2011," MBDA Missile Systems, 2011. [Online]. URL: http://www.mbda-systems.com/innovation/concept-visions/perseus-2011/. Accessed 10 June 2017.

[184] Henry, J. R. and Anderson, G. Y., "Design Considerations for the Airframe-Integrated Scramjet," NASA Tech. Mem. X-2895, 1973.

[185] Kumar, A. J., "Numerical Simulations of Scramjet Inlet Flow Fields," NASA Tech. Pap. 2517, 1986.

[186] Curran, E. R., "Scramjet Engines: The First Forty Years," *Journal of Propulsion and Power*, vol. 17, no. 6, pp. 1138–1148, 2001. doi: 10.2514/2.5875

[187] Blevins, R. D., Bofilios, D., Holehouse, I., Hwa, V. W., Tratt, M. D. *et al.*, "Thermo-Vibro-Acoustic Loads and Fatigue of Hypersonic Flight Vehicle Structure," AFRL Tech. Rep. AFRL-RB-WP-TR-2009-3139, 2009.

[188] Rodi, P. E., "On Using Upper Surface Shaping to Improve Waverider Performance," AIAA Paper 2018–0554, 2018. doi: doi.org/10.2514/6.2018-0554

[189] Eggers, A. J., Resknioff, M. M., and Dennis, D. H., "Bodies of Revolution Having Minimum Drag at High Supersonic Airspeeds," NACA Tech. Rep. 1306, 1957.

[190] Eggers, A. J., Ashley, H., Springer, G. S., Bowles, J. V., and Ardema, M. D., "Hypersonic Waverider Configuration from the 1950's to the 1990's," in *1st International Hypersonic Waverider Symposium*, 1990.

[191] Ding, F., Liu, J., Shen, C.-b., Liu, Z., Chen, S.-h. *et al.*, "An Overview of Research on Waverider Design Methodology," *Acta Astronautica*, vol. 140, pp. 190–205, 2017. doi: 10.1016/j.actaastro.2017.08.027

[192] Bowcutt, K. G., Anderson, J. D., and Capriotti, D., "Viscous Optimized Hypersonic Waveriders," AIAA Paper 87–0272, 1987. doi: 10.2514/6.1987-272

[193] Corda, S. and Anderson, J. D., "Viscous Optimized Hypersonic Waveriders Designed from Axisymmetric Flow Fields," AIAA Paper 88–0369, 1988. doi: 10.2514/6.1988-369

[194] Center, K. B., Sobieczky, H., and Doughtery, F. C., "Interactive Design of Hypersonic Waverider Geometries," AIAA Paper 91–1697, 1991. doi: 10.2514/6.1991-1697

[195] Miller, R. W., Argrow, B. M., Center, K. B., Brauckmann, G. J., and Rhode, M. N., "Experimental Verification of the Osculating Cones Method for Two Waverider Forebodies At Mach 4 and 6," AIAA Paper 98–0682, 1998. doi: 10.2514/6.1998-682

[196] Jones, K. D. and Center, K. B., "Waverider Design Methods for Non-Conical Shock Geometries," AIAA Paper 2002–3204, 2002. doi: 10.2514/6.2002-3204

[197] Rodi, P. E., "The Osculating Flowfield Method of Waverider Geometry Generation," AIAA Paper 2005–0511, 2005. doi: 10.2514/6.2005-511

[198] Rodi, P. E. and Genovesi, D., "Engineering-Based Performance Comparisons Between Osculating Cone and Osculating Flowfield Waveriders," AIAA Paper 2007–4344, 2007. doi: 10.2514/6.2007-4344

[199] Rodi, P. E., "Preliminary Ramjet/Scramjet Integration with Vehicles Using Osculating Flowfield Waverider Forebodies," AIAA Paper 2012–3223, 2012. doi: 10.2514/6.2012-3223

[200] Voland, R. T., Huebner, L. D., and McClinton, C. R., "X-43A Hypersonic Vehicle Technology Development," *Acta Astronautica*, vol. 59, no. 1–5, pp. 181–191, 2006. doi: 10.1016/j.actaastro.2006.02.021

[201] Sziroczak, D. and Smith, H., "A Review of Design Issues Specific to Hypersonic Flight Vehicles," *Progress in Aerospace Sciences*, vol. 84, pp. 1–28, 2016. doi: 10.1016/j.paerosci.2016.04.001

[202] Neer, M. A., "Autoignition of Flowing Hydrogen-Air Mixtures," *AIAA Journal*, vol. 13, no. 7, pp. 924–928, 1975. doi: 10.2514/3.60471

[203] Conti, R. S. and Hertzberg, M., "Thermal Autoignition Temperatures for Hydrogen-Air and Methane-Air Mixtures," *Journal of Fire Sciences*, vol. 6, no. 5, pp. 348–355, 1988. doi: 10.1177/073490418800600503

[204] Furno, A. L., Imhof, A. C., and Kuchta, J. M., "Effect of Pressure and Oxidant Concentration on Auto-Ignition Temperatures of Selected Combustibles in Various Oxygen and Dinitrogen Tetroxide Atmospheres," *Journal of Chemical & Engineering Data*, vol. 13, no. 2, pp. 243–249, 1968. doi: 10.1021/je60037a032

[205] Bounaceur, R., Glaude, P.-A., Sirjean, B., Fournet, R., Montagne, P. *et al.*, "Prediction of Auto-Ignition Temperatures and Delays for Gas Turbine Applications," *Journal of Engineering for Gas Turbines and Power*, vol. 138, no. 2, pp. 021 505-1–021 505-7, 2016. doi: 10.1115/1.4031264

[206] Speight, J. G., "Flammability Properties," in *Lange's Handbook Of Chemistry*, 16th ed., McGraw-Hill, New York, 2005, ch. 2.6, pp. 2.351–2.434.

[207] Chen, C. C., Liaw, H. J., Shu, C. M., and Hsieh, Y. C., "Autoignition temperature data for methanol, ethanol, propanol, 2-butanol, 1-butanol, and 2-methyl-2,4-pentanediol," *Journal of Chemical and Engineering Data*, vol. 55, no. 11, pp. 5059–5064, 2010. doi: 10.1021/je100619p

[208] Coordinating Reseach Council, "Handbook of Aviation Fuel Properties," CRC Rep. 530, 1983. [Online]. URL: http://www.dtic.mil/dtic/tr/fulltext/u2/a132106.pdf. Accessed 9 June 2016.

[209] Seddon, J. and Goldsmith, E. I., *Intake Aerodynamics*, 1st ed., AIAA Educational Series, New York, 1985.

[210] "Engines, Aircraft, Turbojet and Turbofan, General Specification For," United States Department of Defense, Military Specification MIL-E-5007D, 1973.

[211] Heiser, W. H., Pratt, D. T., Daley, D. H., and Mehta, U. B., *Hypersonic Airbreathing Propulsion*, AIAA Educational Series, Washington, D.C., 1994.

[212] Smart, M. K., "Design of Three-Dimensional Hypersonic Inlets with Rectangular-to-Elliptical Shape Transition," *Journal of Propulsion and Power*, vol. 15, no. 3, pp. 408–416, 1999. doi: 10.2514/2.5459

[213] Suraweera, M. V. and Smart, M. K., "Shock Tunnel Experiments with a Mach 12 Rectangular-to-Elliptical Shape-Transition Scramjet at Off-Design Conditions," *Journal of Propulsion and Power*, vol. 25, no. 3, pp. 555–564, 2009. doi: 10.2514/1.37946

[214] Smart, M. K., "Scramjet Inlets," in *High Speed Propulsion: Engine Design - Integration and Thermal Management*, NATO RTO-EN-AVT-185, 2010, pp. 9-1–9-24.

[215] Maikapar, G. I., "Lift-to-Drag Ratio at Supersonic Speeds," *Fluid Dynamics*, vol. 28, no. 5, pp. 696–701, 1993. doi: 10.1007/BF01050055

[216] Fry, R. S., "A Century of Ramjet Propulsion Technology Evolution," *Journal of Propulsion and Power*, vol. 20, no. 1, pp. 27–58, 2004. doi: 10.2514/1.9178

[217] "Missiles de Croisière," Ministère de la Défense (France), 17 November 2014. [Online]. URL: https://www.defense.gouv.fr/marine/equipements/missiles/missiles-de-croisiere. Accessed 2 December 2018.

[218] Lewis, J., "Sokov on Russian Cruise Missiles," Arms Control Wonk, 25 August 2015. [Online]. URL: http://www.armscontrolwonk.com/archive/207801/sokov-on-russian-cruise-missiles/. Accessed 2 December 2018.

[219] Bana, S., "Armed to the Hilt: Indian Navy's Anti-Ship Missiles," *Vayu Aerospace & Defense Weekly*, pp. 67–70, iss. III, May–June 2017.

[220] Grossel, S. S., "Overview of Combustion and Flame Propagation Phenomena Related to DDAs," in *Deflagration and Detonation Flame Arresters*, Wiley, Hoboken, NJ, 2002, ch. 4, pp. 51–75.

[221] Diakow, P. A., "Detonation Characteristics Of Dimethyl Ether, Methanol and Ethanol Air Mixtures," Master's thesis, Queen's University, Kingston, Ontario, Canada, 2012.

[222] Wang, H., You, X., Joshi, A. V., Davis, S. G., Laskin, A. *et al.*, "USC Mechanism Version II: High-Temperature Combustion Reaction Model of H_2/CO/C_1–C_4 Compounds," 2007. [Online]. URL: http://ignis.usc.edu/USC_Mech_II.htm. Accessed 17 May 2017.

[223] Leyes II, R. A. and Fleming, W. A., *The History of North American Small Gas Turbine Aircraft Engines*, American Institute of Aeronautics and Astronautics, Reston, VA, 1999.

[224] "The Market for Missile/Drone/UAV Engines," Forecast International, Tech. Rep., 2010. [Online]. URL: http://www.forecastinternational.com/samples/F655_CompleteSample.pdf. Accessed 5 June 2017.

[225] Bertin, J. J., *Hypersonic Aerothermodynamics*, AIAA Educational Series, New York, 1993.

[226] Lu, F. K. and Dunn, N. L., "Continuous Detonation Wave Engine with Quenching Structure," U.S. Patent 8,544,280 B2, 2013.

[227] Gere, J. M., *Mechanics of Materials*, 6$^{\text{th}}$ ed., Thomson, Toronto, 2006.

[228] Radulescu, M. I., "The Propagation and Failure Mechanism of Gaseous Detonations: Experiments in Porous-Walled Tubes," Ph.D. dissertation, McGill University, Montréal, Québec, Canada, 2003.

[229] Gao, Y., Ng, H. D., and Lee, J. H. S., "Minimum Tube Diameters for Steady Propagation of Gaseous Detonations," *Shock Waves*, vol. 24, no. 4, pp. 447–454, 2014. doi: 10.1007/s00193-014-0505-8

[230] Ishii, K. and Monwar, M., "Detonation propagation with Velocity Deficits in Narrow Channels," *Proceedings of the Combustion Institute*, vol. 33, no. 2, pp. 2359–2366, 2011. doi: 10.1016/j.proci.2010.07.051

[231] Nishimura, J., Ishihara, K., Goto, K., Matsuoka, K., Kasahara, J. *et al.*, "Experimental Research on a Long Duration Operation of a Rotating Detonation Engine," in *Proceedings of the 31st International Symposium on Shock Waves*, Nagoya, Japan, 2017.

[232] Braun, E. M., Balcazar, T. S., Wilson, D. R., and Lu, F. K., "Experimental Study of a High-Frequency Fluidic Valve Fuel Injector," *Journal of Propulsion and Power*, vol. 28, no. 5, pp. 1121–1125, 2012. doi: 10.2514/1.B34442

[233] Peace, J. T., Joshi, D. D., and Lu, F. K., "Experimental Study of High-Frequency Fluidic Valve Injectors for Detonation Engine Applications,"

in *52nd Aerospace Sciences Meeting*, AIAA Paper 2014–1318, 2014. doi: 10.2514/6.2014-1318

[234] Belles, F. E. and Simon, D. M., "Variation of the Pressure Limits of Flame Propagation with Tube Diameter for Propane-Air Mixtures," National Advisory Committee for Aeronautics, NACA Research Mem. E51J09, 1951.

[235] Joshi, D. D., "Unsteady Thrust Measurement Techniques for Pulse Detonation Engines," Ph.D. dissertation, University of Texas at Arlington, Arlington, Texas, 2014.

[236] Bello, A. T., "Exergy Analysis of a Pulse Detonation Engine Linear Power Generator," Ph.D. dissertation, University of Texas at Arlington, Arlington, Texas, 2016.

[237] Goodwin, G. B., Houim, R. W., and Oran, E. S., "Shock Transition to Detonation in Channels with Obstacles," *Proceedings of the Combustion Institute*, vol. 36, no. 2, pp. 2717–2724, 2017. doi: 10.1016/j.proci.2016.06.160

[238] Porel, K. S. and Attia, M. S., "Effect of Axial Spacing and Blockages on the Deflagration to Detonation Transition in a Pulse Detonation Engine," AIAA Paper 2018–1609, 2018. doi: 10.2514/6.2018-1609

[239] Bickford, J., *Handbook of Bolts and Bolted Joints*, CRC Press, Boca Raton, FL, 1998.

[240] "The TDMS File Format," National Instruments, 2 November 2017. [Online]. URL: http://www.ni.com/white-paper/3727/en/. Accessed 1 June 2018.

[241] Figliola, R. S. and Beasley, D. E., *Theory and Design for Mechanical Measurements*, 4th ed., John Wiley & Sons, Hoboken, NJ, 2006.

[242] Press, W. H., Vetterling, W. T., Teukolsky, S. A., and Flannery, B. P., "Minimization or Maximization of Functions," in *Numerical Recipes in Fortran 77:*

The Art of Scientific Computing, 2nd ed., Cambridge University Press, Cambridge, UK, 1992, ch. 10, pp. 387–448.

[243] Shank, J. C., "Development and Testing of a Rotating Detonation Engine Run on Hydrogen and Air," Master's thesis, Air Force Institute of Technology, Wright–Patterson Air Force Base, Ohio, 2012.

[244] Smith, R. D. and Stanley, S., "Experimental Investigation of Continuous Detonation Rocket Engines for In-Space Propulsion," AIAA Paper 2016–4582, 2016. doi: 10.2514/6.2016-4582

[245] Bluemner, R., Bohon, M. D., Paschereit, C. O., and Gutmark, E. J., "Single and Counter-Rotating Wave Modes in an RDC," AIAA Paper 2018–1608, 2018. doi: 10.2514/6.2018-1608

[246] Canny, J., "A Computational Approach to Edge Detection," *IEEE Transactions on Pattern Analysis and Machine Intelligence*, vol. PAMI-8, no. 6, pp. 679–698, 1986. doi: 10.1109/TPAMI.1986.4767851

[247] Le Naour, B., Falempin, F., and Miquel, F., "Recent Experimental Results Obtained on Continuous Detonation Wave Engine," AIAA Paper 2011–2235, 2011. doi: 10.2514/6.2011-2235

[248] Ishihara, K., Nishimura, J., Goto, K., Nakagami, S., Matsuoka, K. *et al.*, "Study on a Long-time Operation Towards Rotating Detonation Rocket Engine Flight Demonstration," AIAA Paper 2017–1062, 2017. doi: 10.2514/6.2017-1062

[249] Liepmann, H. W. and Roshko, A., *Elements of Gasdynamics*, John Wiley & Sons, New York, 1957.

[250] Granger, R. A., *Fluid Mechanics*, Dover, New York, 1995.

[251] Lim, H. S., "Line, Surface and Volume Integrals," Department of Physics, National University of Singapore. [Online]. URL: http://www.physics.nus.edu.sg/~phylimhs/LineSurfVolInt2.pdf. Accessed 8 August 2016.

BIOGRAPHICAL STATEMENT

Andrew R. Mizener was born in Nürnberg, Germany, in 1986. He received a B.S. degree in Aeronautical and Astronautical Engineering in 2009 and a M.S. degree in Aeronautics and Astronautics in 2011, both from Purdue University. He attended the University of Texas at Arlington for his doctoral degree due to its strong history in detonation research, in particular for its position as a pioneer in rotating detonation engines in the United States. He was a recipient of an Enhanced Graduate Teaching Assistantship and the Summer 2018 Dissertation Fellowship at UT Arlington and taught multiple courses as an Adjunct Professor while conducting his doctoral research. He is a member of the AIAA, and in his free time, he enjoys the works of Joachim Myer, Terry Pratchett, John Williams, and the Marvel canon.